H-SPACE 2024

8TH INTERNATIONAL CONFERENCE
ON RESEARCH, TECHNOLOGY AND EDUCATION OF SPACE

Selected papers of the 8th International Conference on Research, Technology and Education of Space

April 25-26, 2024, Budapest, Hungary
at Budapest University of Technology and Economics

Organized by
Faculty of Electrical Engineering and Informatics
Budapest University of Technology and Economics
and
Hungarian Astronautical Society

Editors
László Bacsárdi and Kálmán Kovács

MANT 2024

Selected papers of the 8th International Conference on Research, Technology and Education of Space (H-SPACE2024)
April 25-26, 2024, Budapest, Hungary
BME building 'I', Hall IB.027 and online
Budapest University of Technology and Economics
Magyar tudósok krt. 2., Budapest, H-1117 Hungary

This publication has been supported by BME VIK, MANT and KKM

Editors: László Bacsárdi and Kálmán Kovács

Publisher (Kiadó):
Hungarian Astronautical Society (MANT, Magyar Asztronautikai Társaság)
1044 Budapest, Ipari park u. 10.
www.mant.hu
Budapest, 2024

Responsible publisher:
István Arnócz, Secretary General

ISBN 978-963-7367-35-9

Welcome from the Organizing Committee

On April 25-26, the 8th International Conference on Research, Technology and Education of Space (H-SPACE) conference was held in Budapest.

The event was organized by the Faculty of Electrical Engineering and Informatics at the Budapest University of Technology and Economics (BME) – in cooperation with the Hungarian Astronautical Society (MANT), which is the oldest space association in Hungary. The organization of the conference series started in 2015, at a time of growing opportunities arising from ESA recently granting membership to Hungary and the need for a joint presentation of space activities pursued at BME. The selection of the date for the first occasion of our conference series was a tribute to the successful mission of the first Hungarian satellite, Masat-1, launched on February 13, 2012.

A lot has happened in space since the last H-SPACE conference in 2022. We would like to highlight a few Hungarian achievements between April 2022 and April 2024.

Our companies and research institutions are actively participating in different European and international space programs. The recently published Hungarian Space Kaleidoscope 2023/2024 contains more than 60 companies, research institutions and university departments working in the Hungarian space sector.

Our national astronaut program – the Hungarian to Orbit (HUNOR) – selected four astronaut candidates and one of them will conduct experiments on the International Space Station with Axiom Space.

Researchers from the HUN-REN Astronomy and Earth Science Research Center (HUN-REN CSFK) are participating in the PRIDE (Planetary Radio Interferometry and Doppler Experiment) experiment of the JUICE (Jupiter Icy Moons Explorer) program, one of the most important interplanetary missions of the European Space Agency (ESA). The spacecraft was launched in April 2023 towards the largest giant planet in our solar system, Jupiter.

The newest satellite of the Budapest University of Technology and Economics (BME) has been launched in June 2023. The MRC-100 is named in honor of the university’s radio club (Műegyetemi Rádió Club) 100th anniversary in 2024. MRC-100 is a 5*5*15 cm size PocketQube satellite. One of its tasks is to measure electrosmog, but it also carries instruments for experiments of teams from University of Debrecen, Széchenyi István University (Győr) and the University of Szeged.

In September 2022, BME started the first class of its space engineering MSc program, and the first students will graduate this June.

In line with the objectives of Hungary's Space Strategy adopted by the Hungarian government in 2021, 17 Hungarian universities have entered into a consortium agreement to launch 4 separated but coordinated space related postgraduate training program under the national UniSpace education program. These includes Space Technology Specialist, Innovative Nutrition and Health Sciences Specialist, Space Science Specialist and Space Policy Advisor Training Program. The 3-semester program started in September 2022 and the first class graduated this February.

In this Aprill, Iván Almár, honorary president of the Hungarian Astronautical Society became the first Hungarian who has been recognized with the IAF Hall of Fame award by the International Astronautical Federation.

The topic of this year’s H-SPACE conference is “Cooperation in the space sector”. The agenda of the conference addresses scientific, technological, and educational issues of space research and space activities. The conference is open for both local and international professionals and provides an opportunity to showcase Hungarian scientific, technological, educational and outreach activities related to space.

The Organizing Committee has internationally recognized members: Dr. Balázs Bartóki-Gönczy, Dr. Tibor Bálint, Ferenc Horvai, Prof. János Lichtenberger, Dr. Lóránt Földváry, Prof. László Pap, Dr. Andrea Pődör, Prof. Gábor Stépán, Dr. Szabolcs Rózsa. We are grateful for their contributions to the success of the conference.

We had five keynote and highlights talks:

- *Small satellites - Finnish road from education to science and business*
  Jaan Praks, Aalto University, Finland
- *PocketQubes: A New Frontier in Space Education*
  Caius Reza, Alba Orbital, Glasgow, United Kingdom
- *Hungarian participation in the European Space Agency's JUICE (Jupiter Icy Moons Explorer) mission*
  Pál Gábor Vizi, HUN-REN Centre for Energy Research, Budapest, Hungary
- *Innovation at the European Union Agency for Space Programme*
  Christina Giannopapa, European Union Agency for Space Programme (EUSPA)
- *Educational and incubation practices in the emerging space - an association perspective*
  István Arnócz, Hungarian Astronautical Society, Budapest, Hungary

On the first day, we hosted in person presentations which will be live streamed for online participants. The second day we hosted online presentations (oral and posters). The conference had four main sections: a Plenary with invited presentations. Session Science and Technology I-II and Session Education and Outreach.

In April 2024, we published a book of abstracts for the conference. In that book, we published all the abstracts of the conference. During the event, we had five highlight and invited lectures, 21 oral technical presentations and 32 poster presentations. 23 authors submitted a full paper which went through a rigours review process and has been reviewed by two reviewers. After the review process, these papers are included in these proceedings.

We appreciated all the positive and constructive feed-back from the participants from all aspects. We look forward to organizing the upcoming event of our conference series in 2026.

Dr. László Bacsárdi
co-chair
Vice President of MANT

Dr. Kálmán Kovács
co-chair
President of MANT

Highlights of selected papers from the H-SPACE 2024 Conference

In this proceeding, we present 23 papers prepared by the speakers and their co-authors based on the conference podium presentations and poster sessions.

Let us introduce the papers of the Research Section of the Conference with three thematic focuses, as **communication and space technology; space exploration missions**; and s**ustainability and extraterrestrial adaptations**. These articles collectively underscore the multidisciplinary nature of space research presented at H-SPACE 2024. From advances in communication technology to groundbreaking planetary missions and sustainable food systems, the conference highlights humanity's commitment to innovation and adaptation in space exploration. The key themes emerging from the studies include enhancing technological efficiency, fostering international collaborations, and ensuring the sustainable use of space resources for future generations.

Papers dealing with innovations and challenges in space communication systems form the **communication and space technology** topic. The article of Csurgai-Horváth and Csala focuses on improving the reliability of millimeter-wave satellite and terrestrial radio connections, particularly in the Ka (19.7 GHz) and Q-band (39.4 GHz), where rain-induced signal fading poses significant challenges. They introduce a method using rain sensors and automated detection algorithms to identify rain events and generate precise attenuation statistics, enhancing fade margin design. Their findings, based on Alphasat satellite and terrestrial link data, underscore the importance of localized, long-term measurements for robust communication system planning. The study of Kovács at al. examines the impact of optical background radiation on the performance of free-space quantum key distribution (QKD) links, focusing on wavelengths of 810 nm and 1550 nm. It contrasts the operational parameters of the Chinese satellite Micius at 810 nm with the planned Eagle-1 mission at 1550 nm, evaluating how these differences affect QKD link quality. Insights from this research aim to optimize QKD systems, supporting the advancement of secure quantum communication networks like EuroQCI within the EU. Meanwhile, the BME Suborbitals team (Dobay at al.) has developed an innovative CubeSat payload capable of enduring high acceleration and radiation. This payload incorporates fungal sporulation studies, atmospheric channel characterization using OFDM links, and greenhouse gas analysis. It also features a camera for horizon detection, expanding its research and educational potential. These advancements demonstrate the utility of sounding rockets as cost-effective platforms for cutting-edge experiments.

In the **space exploration missions** topic we put projects aim to deepen our understanding of celestial bodies and environments. One such initiative is Hungary's contribution to ESA's *Comet Interceptor* mission. This mission, as discussed by Kereszturi and colleagues, will explore a dynamically new comet from the Oort Cloud, with Hungarian entities involved in developing the CoCa imaging system and the digital processing module. Their work highlights Hungary's growing presence in advanced space exploration efforts. Another work of Kereszturi and colleagues tries to better understand how space weathering driven infrared spectral changes modify the observability of specific infrared spectral fingerprints of meteorite minerals. Similarly, Steinmann's research develops a GIS-based hydrological model for arid environments on Earth, like the Negev desert, and Mars, specifically Oxia Planum. By integrating terrain, precipitation, and flow data, the model identifies sedimentary targets for future Martian missions, enhancing our approach to planetary exploration.

Research addressing critical challenges related to preserving the Earth's orbital environment and ensuring resource sustainability has been grouped under the sustainability and extraterrestrial adaptations topic. Khan and Ntantis present a comprehensive review of the growing issue of space debris, a consequence of decades of satellite launches and emerging megaconstellations. They evaluate various debris removal technologies, including laser-based methods and net capture, alongside the importance of regulatory measures and international collaboration. Their work emphasizes preventing scenarios like the Kessler Syndrome, where debris collisions could render Low Earth Orbit unusable. In another article J. Elbo and E.L. Ntantis explor the theoretical and practical applications of of Lagrangian points, including asteroid observation, climate change solutions, and space transportation infrastructure. Notably, L1 is proposed for a sunshade to reduce global warming, while L2 hosts the James Webb Space Telescope for deep space exploration. Lagrangian points also hold promise for spaceports, orbital shipyards, quarantine stations, and space colonies, particularly at L4 and L5. These locations offer unique advantages for manufacturing, research, and long-term space missions. The study concludes that Lagrangian points are essential for advancing humanity's space exploration, offering strategic positions for satellites, space stations, and future megastructures like the InterPlanetary Superhighway. Additionally, Meier et al. explore sustainable food production for space environments. Their study examines the effects of plant-based diets on mealworm larvae, demonstrating high survival rates and enhanced protein content. By combining innovative agricultural techniques with entomophagy, the research highlights strategies to address food sustainability for both terrestrial and extraterrestrial applications.

The articles presented for the H-Space 2024 conference in the Technology Section can be classified into three thematic topics based on their focus: **quantum and communication technologies**, **propulsion and space system optimization**, and **remote sensing and environmental analysis**. Each focus encapsulates research advancements tailored to the exploration and development of space technologies, highlighting their significance in both theoretical and practical realms.

The articles of **quantum and communication technologies** topic encompass cutting-edge research in satellite-based quantum communication, secure information transfer, and advanced routing mechanisms. Galambos et al. investigate the synchronization of clocks using GPS-disciplined oscillators (GPSDOs) and a free-space laser system, demonstrating their potential in applications like quantum key distribution, with particular challenges arising from optical turbulence at greater distances. Mihály and Bacsárdi introduce a novel algorithm for routing in entanglement-based satellite networks, showcasing its efficiency and adaptability in securing communication in a quantum internet infrastructure. Oláh and Bacsárdi explore the role of quantum entanglement in the development of a satellite-based quantum internet, emphasizing the integration of quantum memories to overcome the limitations imposed by atmospheric conditions in free-space communication systems. These studies collectively underline the transformative potential of quantum technologies in achieving unprecedented levels of security and connectivity in space.

In the **propulsion and space system optimization** topic, papers focus on improving the efficiency and sustainability of space propulsion systems and mission-critical devices. Mulki and Ntantis delve into the capabilities of Microwave Electrothermal Thrusters (MET), which utilize plasma for heating propellants, achieving high specific impulse and thrust, marking a significant step in sustainable propulsion for space exploration. Hegedűs and Tölgyesi introduce a MATLAB-based optimization program for solid-fueled suborbital rocket engines, targeting improved grain geometries and cost-effective performance for rocket launches. Meanwhile, Vizi and Nagy discuss the development of a Direct Current Converter for ESA's JUICE mission, a power system critical for studying Jupiter's plasma environment and its moons, showcasing advanced engineering tailored to extreme environments. These projects underscore the importance of propulsion advancements and power system innovations in advancing exploratory and operational capacities in space.

Lastly, the **remote sensing and environmental analysis** group highlights innovative approaches to Earth observation and atmospheric studies. Gaskó et al. present a cost-efficient GNSS reflectometry method for hydrological parameter measurement, such as water levels and soil moisture, leveraging environmental signal interference patterns to provide continuous and precise data. Borsi et al. focus on radiation measurements in the altitude range of 30–90 km using a sounding rocket experiment. This initiative aims to fill the data gap in ionizing radiation studies at high altitudes, offering insights critical to the safety of human spaceflight and the design of space technologies. Both studies reflect the pivotal role of Earth observation and environmental monitoring in understanding and addressing challenges related to Earth's surface and atmospheric conditions. In a complementary analysis, Arguello and Toth explore the establishment of reliable radiocommunication systems between Earth and the International Space Station (ISS), addressing technical challenges such as noise levels and geo-redundancy to optimize connectivity. Kertész analyzes the strategic sovereignty of Europe in space activities, emphasizing the importance of autonomous launch capabilities for maintaining Europe’s role in the global space sector. Together, these efforts contribute to a holistic understanding of space technologies, spanning communication, propulsion, environmental sensing, and strategic policy.

These studies, diverse yet interconnected, demonstrate the breadth of technological innovation at the forefront of modern space exploration and utilization, positioning the conference as a beacon for pioneering research in the domain.

The four articles we presented here from the **Education Section** of H-SPACE 2024 conference belong to two professional topics: collaborative models and historical replication and innovative educational initiatives. Each group underscores the critical role of cooperation, hands-on engagement, and educational evolution in fostering the next generation of space exploration and technology experts.

The papers of collaborative models and historical replication cluster focus on leveraging collective efforts and commemorating past achievements to drive progress in the space domain. Koulaouzos’s analysis, Assessment of Cooperation in the Space Sector, explores the advantages of collaborative frameworks within the evolving New Space era. Using examples like the Apollo program and the European Space Agency (ESA), Koulaouzos articulates the strategic benefits of alliances among large enterprises and small to medium-sized enterprises (SMEs). These benefits include risk reduction, cost-sharing, resource optimization, and improved market reach. However, the study also delves into challenges, such as integrating SMEs into larger networks due to their restricted capital and limited track record. The article presents models like Coopetition and business clusters as solutions for fostering partnerships that optimize outcomes through trust and structured governance. Similarly, the work of Pataki and Németh, Reproduction of the Lunar Radar Experiment Failure and Success During Implementation, bridges historical and contemporary space research. By replicating Zoltán Bay’s groundbreaking lunar radar experiment at Széchenyi István University, this study not only pays tribute to a pivotal moment in radar astronomy but also demonstrates how modern adaptations of past technologies can yield significant results. The experiment’s success, achieved through contemporary instrumentation and modifications, underscores the importance of revisiting historical achievements as a foundation for advancing education and technical capabilities.

The other cluster, innovative educational initiatives, highlights the transformative role of academic and practical initiatives in preparing future professionals for the complexities of the space industry. Nagy et al., in The Educational and Awareness-Raising Activities of BME Suborbitals, describe the Budapest University of Technology and Economics’ (BME) hands-on approach to aerospace education. Flagship projects like Prometheus, Kratos, and Athena exemplify the integration of theoretical and practical learning, offering students real-world engineering experience. Beyond technical skill development, these projects also inspire public interest and foster a culture of innovation. The work emphasizes the broader adoption of experiential learning models, showcasing how university-led initiatives can bridge gaps between academia and industry. Complementing this, Matevska et al.'s article, Engineering and Management of Space Systems, tackles the evolving educational demands of the space sector. The authors critique traditional aerospace programs for their limited focus on mechanical engineering and propose an interdisciplinary approach that addresses the life cycle of space systems. Their international, double-degree Master's program, developed by Bremen City University of Applied Sciences and Gdańsk University of Technology, integrates agile methods, stakeholder management, and industry collaboration with companies like Airbus and OHB. This forward-thinking curriculum equips graduates with the multifaceted competencies required to navigate the dynamic demands of space missions and manage the increasing complexity of space systems.

Together, these studies underline the necessity of blending historical insights, collaborative strategies, and innovative education to empower the next generation of space professionals. They reflect a shared vision: advancing the space sector through cooperation, practical engagement, and comprehensive training programs that adapt to both historical legacies and future challenges.

Dr. Kálmán Kovács

Final Conference Program

In this program, the name and affiliation of the presenter author is listed.
For detailed information about authors and their affiliations, see the book of abstracts of the conference.

April 25, Thursday

Location: Building I, ground floor, IB.027
Budapest University of Technology and Economics
Magyar tudósok krt. 2., Budapest, H-1117

The first day was live streamed for online participants.

Master of the ceremony: László Bacsárdi

14:00 Opening ceremony
Orsolya Ferencz, Ministerial Commissioner, Ministry of Foreign Affairs and Trade
Hassan Charaf, Dean, Faculty of Electrical Engineering and Informatics, BME
Kálmán Kovács, President, Hungarian Astronautical Society

14:20 Keynote talk
Small satellites - Finnish road from education to science and business
Jaan Praks, Aalto University, Finland

14:50 Keynote talk
PocketQubes: A New Frontier in Space Education
Caius Reza, Alba Orbital, Glasgow, United Kingdom

15:20 Poster highlight talks

16:00 Coffee break and poster session

Session Chair: Lóránt Földváry

16:45-18:45: Technical presentations – Session Science and Technology I

The future of satellite frequency usage satellite agenda items for WRC-23 and WRC-27
Péter Vári, National Media and Infocommunication Authority, Budapest, Hungary

Hungarian participation in the Comet Interceptor mission
Ákos Kereszturi, Konkoly Observatory, HUN-REN Research Centre for Astronomy and Earth Sciences, Budapest, Hungary

Radio interferometric observations of the JUICE spacecraft en route to Jupiter
Judit Fogasy, Konkoly Observatory, HUN-REN Research Centre for Astronomy and Earth Sciences, Hungary

SPECTRE, a self-deploying bi-stable composite tape-spring mechanism for future nanosatellite missions
Sara Sanchis Climent, KTH, Royal Institute of Technology, Stockholm, Sweden

FOTEC's Testing and Qualification Capabilities for Small Satellites
Laura Bettiol, FOTEC Forschungs-und Technologietransfer GmbH, Wiener Neustadt, Austria

Thermal performance characterization of battery insulation on ATL-1 picosatellite mission
Zoltán Tóth, H-ION Research, Development and Innovation Ltd., Budapest, Hungary

Fast and flexible developments of digital logics: applications in the first Hungarian astrophysical satellite, GRBAlpha
András Pál, Konkoly Observatory, HUN-REN Research Centre for Astronomy and Earth Sciences, Budapest, Hungary

Testing remote clock synchronization with GPSDO-s and a free space laser communication system
Máté Galambos, Budapest University of Technology and Economics, Hungary

18:45: Wrap up of the first day - *László Bacsárdi*

April 26, Friday

Location: online

Session Chair: Kálmán Kovács

9:00: Welcome of the second day

9:05: Highlight talk

Hungarian participation in the European Space Agency's JUICE (Jupiter Icy Moons Explorer) mission
Pál Gábor Vizi, HUN-REN Centre for Energy Research, Budapest, Hungary

9:30-12:00: Technical presentations – Session Science and Technology II

The Space Weather Monitoring and Data Service at HUN-REN Institute of Earth Physics and Space Science (EPSS)
Árpád Kis, HUN-REN Institute of Earth Physics and Space Science, Sopron, Hungary

Reproduction of the Lunar Radar experiment failure and success during implementation
Péter Pataki, Széchenyi István University, Győr, Hungary

Review of Lagrangian Points and Scope of Stationary Satellites
Joel Eldo, Amity University Dubai, UAE

Space Debris: Overview and Mitigation Strategies
Mohammed Vaseeq H. Khan, Amity University Dubai, UAE

The Expected Impact of SysML v2 to Cooperation in the Space Sector
Vince Molnár, Budapest University of Technology and Economics, Hungary

EON: The first year of the re-started optical tracking of artificial satellites at Baja
Tibor Hegedüs, Baja Observatory of the University of Szeged, Baja, Hungary

Study of Microwave Electrothermal Propulsion System
Rhea Ranjit Mulki, University of Southern California, Los Angeles, USA

Assessing Natural and Anthropogenic Ground Deformation Using Sentinel-1 PSI in the Region of Cluj-Napoca, Romania
Péter Farkas, Geo-Sentinel Kft., Hungary

11:45: Highlight talk

Innovation at the European Union Agency for Space Programme
Christina Giannopapa, European Union Agency for Space Programme (EUSPA)

12:05 Lunch break

Session Chair: Dorottya Milánkovich

13:15: Opening of the afternoon session

13:20: Invited talk

Educational and incubation practices in the emerging space - an association perspective
István Arnócz, Hungarian Astronautical Society, Budapest, Hungary

13:40-15:00: Presentations – Session Education and Outreach

Assessment of Cooperation in the Space Sector
Don Koulaouzos, Skytrek Ltd, London, United Kingdom

Engineering and Management of Space Systems (EMSS) - an International Joint Master's Double-Degree Programme
Jasminka Matevska, City University of Aplied Sciences, Bremen, Germany

Space Science in the Classroom
Annamária Komáromi, Balassi Bálint Eight Grade Secondary Grammar School, Hungary

The educational and awareness-raising activities of BME Suborbitals
Bence Csaba Kováts, Budapest University of Technology and Economics, Hungary

Introduction of space science in higher education: space science in BSc engineering
Szilárd Takács, Széchenyi István University, Győr, Hungary

15:00 Closing remarks

April 25 – Poster presentations

Probing Low Mass Neutrinos in Gravitational Wave Environments: A Novel Approach with Feynman Diagrams & Applications In Space Sciences
Panta Sasikanth, N.B.K.R Institute of Science and Technology, Nellore, India

Fast Routing in Entanglement-based Satellite Networks
András Mihály, Budapest University of Technology and Economics, Hungary

Circular food production in space environment – Insect protein production by supplementing green biomass in feed
Orsolya Meier, University of Debrecen, Debrecen, Hungary

Thermal properties of heterogeneous materials using extended heat equations
Anna Fehér, Budapest University of Technology and Economics, Hungary

Spectral instrument optimization for asteroid missions by space weathering simulation
Ákos Kereszturi, Konkoly Observatory, HUN-REN Research Centre for Astronomy and Earth Sciences, Budapest, Hungary

RTK GNSS monitoring under high ionospheric activity
Bence Takács, Budapest University of Technology and Economics, Hungary

High-redshift radio quasars from ground and space
Máté Kreizinger, Eötvös Loránd University, Budapest, Hungary

Investigation of Glass-foam systems as Insulation materials for Space applications
Kinga Tamási, Ludovika University of Public Service, Budapest, Hungary

MAUVE – UV-Vis Spectroscopy of Stars by a 16U CubeSat
Gergő Mezőhegyi, C3S Electronics Development LLC., Budapest, Hungary

Comprehensive analysis of the ionospheric response to the largest geomagnetic storms from solar cycle 24 over Europe
Kitti A. Berényi, ELKH-ELTE Space Research Group, Budapest, Hungary

Proposal of a Hybrid CSNN-PSO Algorithm For Improving Space Debris Identification and Classification
Hanga Katreiner, Technische Universität Berlin, Berlin, Germany

Transparent Planetary Polished Thin Section Rock Sample Maker for Hungarian Hunveyor Educational Space Probe
Pál Gábor Vizi, HUN-REN Centre for Energy Research, Budapest, Hungary

Remote sensing of hydrological parameters by GNSS reflectometry
János Gaskó, Budapest University of Technology and Economics, Hungary

Development of GIS software based spatial ejecta estimation algorithm to support the NASA-ESA Artemis program
Richárd Krisztián Tomka, Konkoly Observatory, HUN-REN Research Centre for Astronomy and Earth Sciences, Budapest, Hungary

Distributed Intelligence and Sensor Network in the Power Systems of MRC-100 Satellite
Péter Püspöki, Budapest University of Technology and Economics, Hungary

The Hungarian contribution to the T-FORS Horizon Europe project
Kitti A. Berényi, ELKH-ELTE Space Research Group, Budapest, Hungary

Application of Rain Sensor Device in Reliable Attenuation Statistics Calculations on Satellite and Terrestrial Radio Connections
László Csurgai-Horváth Budapest University of Technology and Economics, Hungary

Simulating Solar Particle Events: New advances in Proton irradiation techniques for biological samples at ATOMKI
Máté Szarka, HUN-REN Institute for Nuclear Research

Radiation characteristics measurement on a sounding rocket near the Kármán line
Bence Csaba Kováts, Budapest University of Technology and Economics, Hungary

CubeSim - A Simulation Framework for small Satellites
Bernhard Seifert, FOTEC Forschungs- und Technologietransfer GmbH, Wiener Neustadt, Austria

An event-based hydrological model for arid/hyper-arid and Martian environments
Vilmos Steinmann, Konkoly Observatory, HUN-REN Research Centre for Astronomy and Earth Sciences, Budapest, Hungary

The role of entanglement in the development of satellite-based quantum internet
Kitti Oláh, Budapest University of Technology and Economics, Hungary

Preliminary design of payload for sounding rockets
Ádám Dobay, Budapest University of Technology and Economics, Hungary

Fuel consumption optimization for suborbital solid fuelled rocket engines
Gergely Márk Tölgyesi, Budapest University of Technology and Economics, Hungary

Numerical investigation of the spanwise mean velocity gradient method for transition delay
Márton Kulcsár, Budapest University of Technology and Economics, Hungary

Radiocommunications with the International Space Station (ISS)
Katherine Cazco, Széchenyi István University, Győr, Hungary

Class-Space: From the classroom to space!
Anna Pántya, HUN-REN Centre for Energy Research, Budapest, Hungary

The perspective of launch capacity and strategic sovereignty of European space activity
Bence Kertész, Ludovika University of Public Service, Budapest, Hungary

Space Awareness: latest fireball events and the independent allsky7/8 network of Hungary
Tibor Hegedüs, Baja Observatory of the University of Szeged, Baja, Hungary

Data processing from weather satellites
Benedikta Rédling, Széchenyi István University, Győr, Hungary

The first module in space by SZESAT
Barnabás Zoltán Baranyai, Széchenyi István University, Győr, Hungary

Daytime Optical Background Radiation
Dóra Borbála Kovács, Budapest University of Technology and Economics, Hungary

Selected papers

Content

Orsolya Meier, Éva Domokos-Szabolcsy, Milán Fehér

„Circular food production in space environment Insect protein production by supplementing green biomass in feed"

HSPACE2024-FP-09

Máté Galambos, Gergely Jánosi, Márton Czermann, Barna Kirchhof, László Bacsárdi

„Testing Clock Synchronization with GPSDOs and a Free-Space Laser Communication System"

HSPACE2024-FP-10

András Mihály, László Bacsárdi

„Fast Routing in Entanglement-based Satellite Networks"

HSPACE2024-FP-11

Kitti Oláh, László Bacsárdi

„The role of entanglement in the development of satellite-based quantum internet"

HSPACE2024-FP-12

Rhea R. Mulki, Efstratios L. Ntantis

„Study of Microwave Electrothermal Propulsion System"

HSPACE2024-FP-13

Hegedűs András, Tölgyesi Gergely Márk

„Fuel consumption optimization for suborbital solid fuelled rocket engines"

HSPACE2024-FP-14

Pál Gábor Vizi, Janos Nagy

„DCC Direct Current Converter development for PEP experiment of ESA's JUICE (Jupiter Icy Moons Explorer) mission"

HSPACE2024-FP-15

János Gaskó, Dániel Fátay, Bence Dávid Turák, Szabolcs Rózsa

„Remote sensing of hydrological parameters by GNSS reflectometry"

HSPACE2024-FP-16

Szilárd Borsi, Richárd Huba Bezzegh, Dominik Gábor Nagy, Bence Csaba Kováts

„Radiation characteristics measurement on a sounding rocket near the Kármán line”

HSPACE2024-FP-17

Katherine Alexandra Cazco Arguello, Máté Péter Toth

„Radiocommunications with the international space station (ISS)”

HSPACE2024-FP-18

Bence Kertész

„The perspective of launch capacity and strategic sovereignty of European space activity”

HSPACE2024-FP-19

Don Koulaouzos

„Assessment of Cooperation in the Space Sector”

HSPACE2024-FP-20

Péter Pataki, Péter Németh

„Reproduction of the Lunar Radar experiment failure and success during implementation”

HSPACE2024-FP-21

Ádám Nagy, Bence Ujhegyi, Bence Csaba Kováts

„The educational and awareness-raising activities of BME Suborbitals”

HSPACE2024-FP-22

Jasminka Matevska, Marek Chodnicki, Zbigniew Łubniewski

„Engineering and Management of Space Systems - an International Joint Master's Double-Degree Programme”

HSPACE2024-FP-23

Application of Rain Sensor Device in Reliable Attenuation Statistics Calculations on Satellite and Terrestrial Radio Connections

László Csurgai-Horváth
Budapest University of Technology and Economics
Faculty of Electrical Engineering and Informatics,
Department of Broadband Infocommunications and
Electromagnetic Theory, Hungary
csurgai-horvath.laszlo@vik.bme.hu

Benedek Mihály Csala
Budapest University of Technology and Economics
Faculty of Electrical Engineering and Informatics,
Department of Broadband Infocommunications and
Electromagnetic Theory, Hungary
csala.benedekmihaly@edu.bme.hu

Abstract—**In the case of satellite and terrestrial radio connections operating in the millimeter wavelength range, it is well known that fading phenomena are primarily caused by precipitation, especially liquid water (rain). As a result, when planning these radio connections, a sufficient amount of fade margin must be included in order to ensure that the availability of the connection is adequate. The sizing of the fade margin is supported by rain attenuation models based on long-term measurements, both for terrestrial [1] and satellite [2] connections.**

The above models take into account the geographical location of the installation of the connections, the frequency range used and other characteristics of the transmission, such as the polarization and the elevation angle of the received satellite. At the same time, even in the case of small geographical distances, varied meteorological conditions occur, so statistics based on specific, local measurements are also of great importance. In the case of satellite connections, the Q (33-50 GHz) and V band (40-75 GHz), which are intensively researched today, still have relatively little measurement data, and during the processing of the measurement data, it is particularly difficult to identify fading phenomena, which is necessary for the production of accurate statistical data.

In our article, we present the attenuation measurements of the Ka (19.7 GHz) and Q-band (39.4 GHz) beacon signals of the Alphasat satellite [3], as well as a terrestrial 57.725 GHz connection [4] installed in the same location. We also describe a signal detection based on a rain sensor device, and a fading phenomenon selection method, which is suitable for accurately identifying rain events and thus forming reliable attenuation statistics (distributions). The method greatly speeds up rain event detection, which is traditionally done mostly by manual work, and makes the results of attenuation statistics more accurate.

Keywords—Ka/Q band, 58GHz, LOS, Correlation, Attenuation, Statistics, Millimeter wave, Rain

I. INTRODUCTION

Rain intensity is a significant physical quantity whose measurement is fundamental in many ways. Meteorological observations, agricultural purposes, flight safety, or even the quality of terrestrial or satellite radio communication at millimeter wavelengths are closely related to the amount of liquid precipitation [5]. Many types of measurement devices are suitable for measuring precipitation, including rain intensity, from simple tipping bucket gauges or drop counter sensors to present-time sensors or radar-based measurements [6]. In general, the devices for measuring rain intensity work with a certain integration time, which can be several minutes. The measurement result provided by these devices is expressed as the rain intensity in [$mm\cdot h^{-1}$] detected at the geographic location of the measuring system. In the case of radio connections at millimeter wavelengths, the power of the received signal at the receiver is affected by precipitation, especially the intensity of the rain. On the other hand, this phenomenon can be used to determine the magnitude of the rain intensity from the change in free space loss [7], for which the appropriate calculations can be found in the relevant recommendations of ITU [8]. On longer radio connections, we have to account for the difference between the effective and the real path length, but on very short connections, it can be assumed that the rain affects on whole path length with a non-various attenuation. We base the findings of our article on this relating to the terrestrial link. We present the method based on a computation of rain intensity from the change in signal level, measured on a short radio connection operating at 58 GHz. The great advantage of the method is that the instantaneous rain intensity can be determined with high resolution, which is limited by the sampling rate of the received signal level. The process provides a solution for the rapid detection of precipitation conditions and many practical application possibilities can be assigned for our new detection process.

The statistical properties of the path attenuation are also an important measure of the radio link. As we mentioned, there are ITU recommendations to determine the long-term distribution of the attenuation [1], [2]. Nevertheless, the rain attenuation statistics of measured time series plays also a key role in the design of radio links. To support this process, we apply an additional rain sensor device to detect the rainy periods and improve the resulting statistics.

The rest of the paper is organized as follows. Section II and III briefly introduces the applied measurement setup, while Section IV explains the methods to utilize the measured attenuation time series for rain intensity calculation. Section V introduces the application of a rain sensor device. Section VI explains the result regarding correlation calculation, while Section VII. describe the results regarding cumulative distribution calculation. Section VIII. presents final remarks, conclusions and application areas.

II. THE TERRESTRIAL MEASUREMENT SETUP

One objective of this paper is to study rain fading effects by analysing the received signal power of terrestrial and satellite radio links.

The terrestrial measurements are carried out by an experimental full duplex radio link built up with Nokia MetroHopper wireless excess link devices, that were originally designed for dense microcellular networks [9] . This radio is set up to function over short distances to establish a low-latency connection to Nokia base stations using the 58GHz band. The parameters of the link are listed in Table I., while the location and the outdoor radio unit can be seen in Fig. 1.

TABLE I. LINK PARAMETERS

Location	Path length [m]	Frequency [GHz]	TX power [dBm]	TX/RX antenna gain [dB]
Budapest	118	57.725	5	34

FIU19 indoor units are also installed at both ends of the link, providing a local management interface and 4 x 2 Mbit/s capacity channel. In our experimental setup no data transmission was carried out, only the received signal strength in [dBm] was monitored and logged with 1 sample/sec via the scripting tool of the management interface.

Fig. 1. MetroHopper link between two buildings.

The free space loss according to ITU-R P.525 [10] is 41dB, while the attenuation of the atmospheric gases, especially the effect of oxygen adds further 1.1dB [11]. The typical and non-adjustable TX power of the radio unit is 5dBm [9] and the polarization is vertical. After the final alignment of the radio units, with the device parameters according to Table I., with clear sky conditions the received signal power level is roughly –56dBm at the receiver side. According to the User's Manual of the MetroHopper Radio the minimal received power level is –75 dBm (BER = 10^{-3}), resulting in a 19 dB fade margin for the measurement setup. By taking into account the short path length, this fade margin is sufficiently high to detect even the most intensive rain events.

III. THE SATELLITE MEASUREMENT SETUP

Alphasat Scientific Experiment transmitting coherent beacon signals at Ka-band (19.701 GHz) and Q-band (39.402 GHz). The geosynchronous Alphasat satellite, located at 25°E supports a Europe-wide experiment to investigate the atmospheric propagation effects occurring in Ka and Q bands. The Department of Broadband Infocommunications and Electromagnetic Theory at Budapest University of Technology and Economics designed and installed a receiver station for both beacons, operating since 2014.

The receiver station is installed on the flat roof of the department's building at 120 m above sea level with 47.48°N latitude and 19.06°E longitude coordinates. As the orbit inclination of the satellite can reach 3°, the receiver is equipped with a step-tracking system to track the satellite.

The Cassegrain antennas are equipped with the Out-Door Units (ODU) on the back of the reflector dishes. The High Performance Antennas are originally manufactured for the backbone network of terrestrial mobile radio systems, but considering their high interference protections and excellent radiation characteristics they are appropriate to receive the Ka and Q-band beacon frequencies of the Alphasat satellite. Fig. 2 depicts the complete outdoor system.

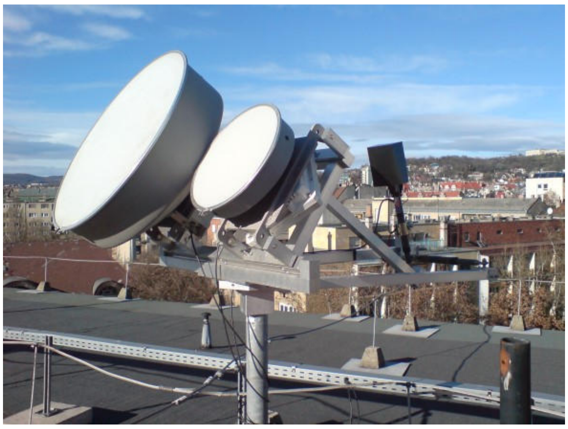

Fig. 2. High performance antennas and the tracking system

The antennas are manufactured by GRANTE Antenna Development and Production Corporation. We selected a 0.3 m antenna for the Q-band and a 0.6 m antenna for the Ka-band that have similar gain and half-power beam widths and ensure almost equal received signal power on the IF band.

TABLE II. ANTENNA PARAMETERS

	Ka-band	Q-band
Frequency range	17.7-23.6 GHz	37-39.5 GHz
Diameter	0.6 m	0.3 m
Mid band gain	39.5 dBi	39.2 dBi
Polarization	Linear V	Linear tilted 45°
Half-power beam width	1.6°	1.7°

The measurement setup ensures 29dB fade margin in both frequency bands.

IV. DETECTING RAIN ATTENUATION WITH HIGH RESOLUTION

A short distance millimeter wavelength radio link can be utilized to sense the momentary rain intensity by measuring the received signal power and converting it to rain intensity time series by using the following equation, based on the relevant ITU recommendation [8]:

$$R_i^{[\mathrm{mm/h}]} = 10^{\frac{\log\left(\frac{A_i}{d\cdot k}\right)}{\alpha}} \tag{1}$$

where A_i is the i^{th} value of the path attenuation time series in [dB]. A calibration process using the measurement of a meteorological station nearby [12] ensure the validity of the transformed rain intensity data. The most important advantage of the method is that the sampling rate of the resultant rain intensity time series is identical to the sampling rate of the received power over the radio link. Actually, this is 1 sample/sec, therefore the fast changes in the rain intensity can be also detected, contrarily to the conventional sensors, that usually smoothing the peaks due to their integrating behaviour.

Fig. 4. depicts a typical rain event in January, 2023 with approx. 5 min. length. In the centre of the event a fast increase of the rain intensity is observable, whose duration is only 15 sec.

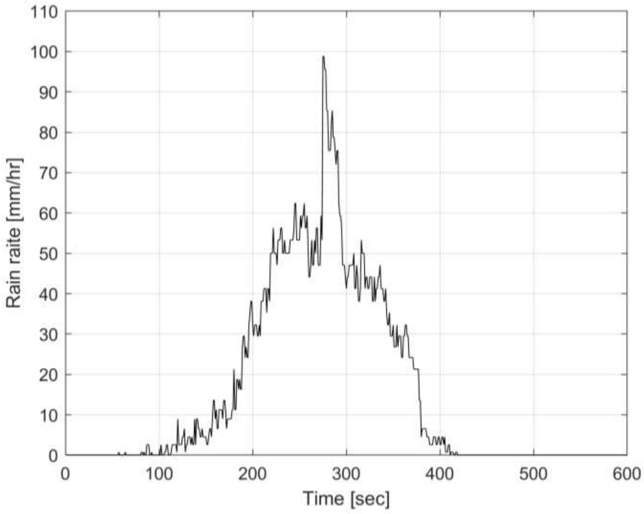

Fig. 3. Single rain event with high peak intensity. Measured on 13th of January 2023.

There could be several application areas of this kind of rain intensity sensing. In case of adaptive control of the modulation and coding over terrestrial or satellite communication links [13] high resolution and fast information about the momentary rain intensity may support the adaptive algorithm and higher throughput can be achieved. In case of a diversity system, when several radio stations are operated at multiple geographical locations, the perfect knowledge about the local rain rate changes may be very advantageous. Similarly, if diversity radio and optical links are concurrently operated at the same path, the fast switching control of the two different media may increase the channel capacity.

V. SENSING RAIN EVENTS

A. *Rain sensor*

A rain sensor device is installed next to the terrestrial and satellite radio connection receiver antennas, see Fig. 4. The sensor was adapted to a meteorological station in a way, that the sensor gives binary 1 when rain is present otherwise binary 0. The sensor data is sampled every 1 minute. The sensor surface is tilted by 45 degrees and heated when it is raining, to avoid false sensor data because water remaining on the detector surface.

Fig. 4. The rain sensor device

B. *Selecting fading events*

The rain sensor data were interpolated to adjust it to the 1-second sampling rate of the radio links. For every minute the corresponding rain data sample was taken for the corresponding 60 seconds. The sensor data gave a shorter time period for a rain event than the data of the radio links. That's why data signaling a rain event was extended by 12 minutes both before and after to minimize data loss caused by excluding the beginning and the end of a fading event.

The average level of RPWR was calculated by omitting measurement data taken during fading events using the extended rain sensor data.

After selecting the fading events caused by rain the RPWR of the fading events were matched to the average of RPWR to minimize the impact of offsets in attenuation on statistical data. Only those fading events were matched, which beginning and end samples were 0.4 dB higher or lower than the average RPWR. The average RPWR for the given day *avg_RPWR*, a compensation constant *CC* and the maximum RPWR of the fading event *max{data}* were used to match the data of each fading event separately using the following equation:

$$matched\_data(i) = data(i) - max\{data\} + avg\_RPWR + CC \tag{2}$$

Where i is the index of the sample of the given fading event, $min\{i\}$ is the beginning and $max\{i\}$ is the end of the fading event. The *CC*'s goal is to minimize the impact of the noise affecting the measurement. The *CC*'s value is determined by the noise affecting the measurement in rainless periods. The *CC*s were determined for each radio link separately using the following equation:

$$CC = 1.5\cdot\sigma(data) \tag{3}$$

$\sigma(.)$ refers to the standard deviation of the argument. In the case of terrestrial radio connection data refers to the RPWR samples for rainless days during the measurement period. In the case of satellite links data refers to samples, which fulfil the following criteria: they are within the range of the average RPWR of samples ±0.8dB, the time on which samples were taken is continuous and at least 1 hr.

Fig. 5 is showing the results of the aforementioned method:

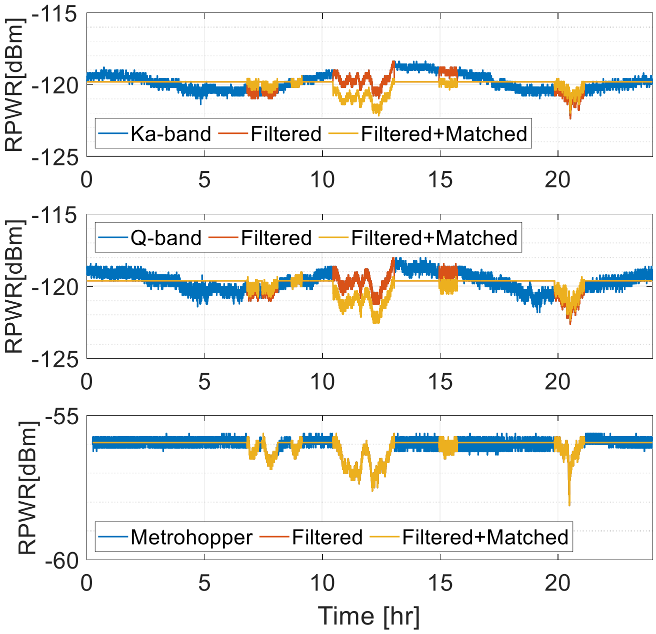

Fig. 5. Measurement and processed data for different radio links (March 1.)

VI. CORRELATION BETWEEN RADIO LINKS

The correlation between the Ka-, Q-band and terrestrial 58GHz connections and in multiple cases were analyzed. The correlation was calculated separately for days, on which at least one fading event occurred. The average correlation was calculated from the corresponding daily correlations by performing a Fisher transformation [14] on all correlations, then the mean was calculated and an inverse Fisher transformation was done.

A. Raw measurement data

The correlations were calculated directly, without any processing, from the measurement data:

TABLE III. CORRELATIONS OF RAW MEASUREMENT DATA

Correlation	**Ka-Terrestrial**	**Q-Terrestrial**	**Ka-Q band**
min. value	–10.26%	–11.56%	86.51%
max. value	90.08%	90.51%	98.14%
average	44.82%	49.24%	95.39%

The correlation between the two satellite links is notably higher than between a satellite and the terrestrial radio link.

B. Filtered measurement data

The correlations were calculated from the filtered fading events concatenated with the average RPWR:

TABLE IV. CORRELATIONS OF FILTERED MEASUREMERNT DATA

Correlation	**Ka-Terrestrial**	**Q-Terrestrial**	**Ka-Q band**
min. value	–9.94%	–13.11%	88.37%
max. value	92.37%	92.08%	99.43%
average	52.22%	56.86%	96.46%

The correlation between the two satellite links is still higher than between a satellite and the terrestrial radio link, but both have increased mainly because the noisy rainless periods were replaced by a constant value.

C. Filtered and matched to average RPWR measurement data

The correlations were calculated from the filtered and then matched to average RPWR fading events concatenated with the average RPWR:

TABLE V. CORRELATIONS OF FILTERED AND MATCHED TO AVERAGE DATA

Correlation	**Ka-Terrestrial**	**Q-Terrestrial**	**Ka-Q band**
min. value	43.04%	38.55%	81.34%
max. value	88.31%	88.17%	99.28%
average	76.25%	75.19%	94.93%

The correlation between the two satellite links is slightly lower compared to filtered measurement data. The correlation between a satellite and the terrestrial radio link increases by about 20% compared to filtered measurement data. Also, the minimum values changed from a negative correlation to about positive 40% on a satellite and the terrestrial comparison.

D. Rain intensities

The correlations were calculated from rain intensities calculated from filtered and matched to average RPWR measurement data using [15]:

TABLE VI. CORRELATIONS OF RAIN INTENSITIES

Correlation	**Ka-Terrestrial**	**Q-Terrestrial**	**Ka-Q band**
min. value	11.96%	4.84%	92.29%
max. value	90.87%	90.17%	99.13%
average	57.67%	59.49%	96.78%

The correlation between rain intensities calculated from filtered than matched to average level fading events is higher about 2% than the correlation between the data it was calculated from in the case of comparing the Ka- and Q-bands. The average rain intensity correlation between a satellite and the terrestrial link decreases significantly. This phenomenon requires further research.

VII. CUMULATIVE DISTRIBUTIONS OF ATTENUATION

The complementary cumulative distribution function (CCDF) was calculated from 3 data: raw measurement, filtered data, filtered and matched to average RPWR data. The cumulative distributions were compared with the corresponding ITU recommendation [1] for terrestrial and [2] for satellite links. In the case of raw measurement data, the 0dB attenuation equals the median of the measurement data. In the case of filtered data attenuation was calculated relative to the average RPWR from the rainless periods of the given day. However, when calculating from filtered and matched to average RPWR data always the actual attenuation was used thanks to the level matching. Fig. 6 shows the CCDFs for the terrestrial 58 GHz link, while Fig. 7 shows the CCDFs for the Ka-band satellite radio connection.

In the case of satellite links, a significant improvement was made by filtering and matching the data to the average level compared to raw data. The cause of this is mainly the elimination of the signal fluctuation caused by the tracking of the geosynchronous satellite seen in Fig. 5. In the case of the terrestrial link CCDF from the filtered and matched to average level data is roughly identical to the CCDF calculated from the raw data.

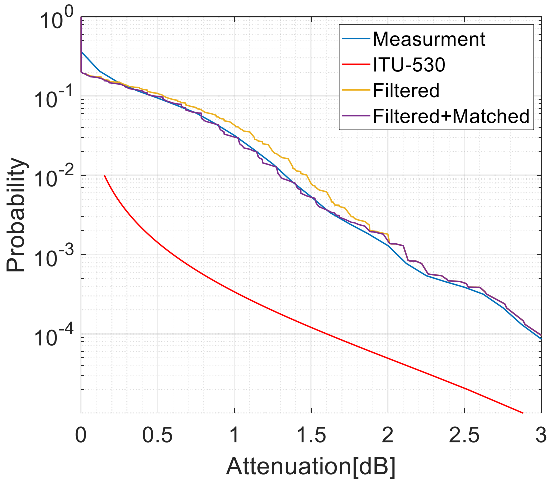

Fig. 6. CCDF of attenuation on the terrestrial 58 GHz link

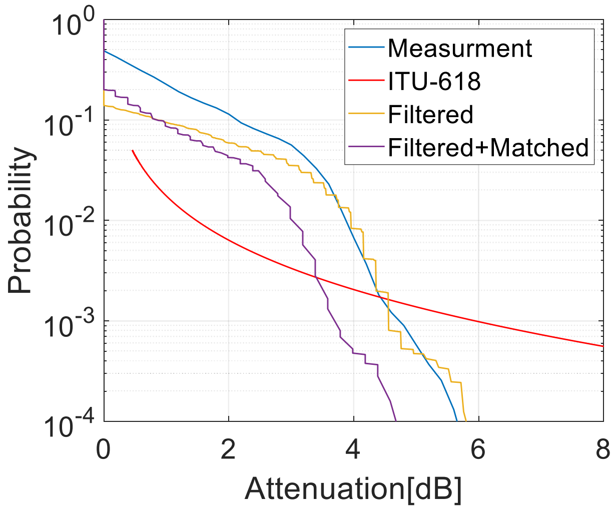

Fig. 7. CCDF of attenuation on the Ka-band satellite radio connection

VIII. CONCLUSION

In our paper, we discuss in detail the deterioration of terrestrial and satellite communication links as a result of increasingly frequent heavy rains in recent years. In our opinion, precise and adequately frequent measurement of rainfall rate and rain intensity is becoming more important from a scientific and economic point of view. To detect the rain events a rain sensor device was applied to investigate the fade events on a short-range radio connection in a 58GHz frequency band and on a Ka and Q-band satellite channel.

We calculated the correlation between different measurements and compared the statistical properties of the measurements with the relevant ITU-R recommendation. Based on the high correlation achieved between satellite and terrestrial links by filtering the fading events and matching them to the average RPWR in the future a method could be worked out to predict fading events and thus the cumulative distribution of attenuation on a satellite link using data from a terrestrial connection and vice versa. The calculated CCDF can be closer to the corresponding CCDF determined by ITU-R recommendation when filtering the fading events out and matching them to the average RPWR. This method calculates always with actual attenuation and eliminates the problem of choosing the 0dB attenuation, which significantly influences the result of the CCDF.

In order to improve the results, we are collecting more measurement data to be able to calculate attenuation statistics for longer measurement time series. Also, the detection of fading caused by rain on satellite connections could be improved by placing more rain sensor devices along the path of the radio signal.

REFERENCES

[1] ITU-R Rec. P.530-18. Propagation data and prediction methods required for the design of terrestrial line-of-sight systems. ITU, 2021.

[2] Recommendation ITU-R P.618-14. Propagation data and prediction methods required for the design of Earth-space telecommunication systems. ITU, 2023.

[3] Kelmendi, A., Csurgai-Horvath, L., Svigelj, A., Mohorcic, M., Javornik, T., & Hrovat, A. (2023). Site Diversity Experiment in Q-Band Satellite Communications in Slovenia and Hungary. IEEE ANTENNAS AND WIRELESS PROPAGATION LETTERS, 22(8), 1967–1971. http://doi.org/10.1109/LAWP.2023.3270839

[4] Andrea Farkasvölgyi, László Csurgai-Horváth, Attila Hilt (2024). High Resolution Rain Intensity Sensing with Millimeter Wavelength Radio Link, Journal of Microelectronics, Electronic Components and Materials (under review)

[5] Rodda, J.C., Dixon, H., "Rainfall measurement revisited," *Weather 2012*, *67*, pp. 131–136.

[6] Vuerich E., Monesi C., Lanza L.G., Stagi L., Lanzinger E.: Instruments and observing methods, report No. 99. World Meteorological Organization. Italy, Germany, 10.2007-04.2009.

[7] Goldshtein, O.; Messer, H.; Zinevich, A. Rain rate estimation using measurements from commercial telecommunications links. IEEE Trans. Signal Process. 2009, 57, 1616–1625.

[8] ITU. Recommendation ITU-R P.838-3. Specific Attenuation Model for Rain for Use in Prediction Methods; ITU: Geneva, Switzerland, 2005.

[9] Nokia: Nokia MetroHopper Radio, User Manual.

[10] RECOMMENDATION ITU-R P.525-4. Calculation of free-space attenuation, 2019.

[11] Recommendation ITU-R P.676-13, „Attenuation by atmospheric gases and related effects", P Series, Radiowave propagation, Aug. 2022.

[12] MetNet Hungary Ltd., https://www.metnet.hu/

[13] Csurgai-Horváth, L. Receiver station in Budapest for Q/V band satellite site diversity and adaptive coding and modulation experiments with Alphasat. Int J Satell Commun Networking. 2019; 37: 149– 162.

[14] Silver, N. C., & Dunlap, W. P. (1987). Averaging correlation coefficients: Should Fisher's *z* transformation be used? *Journal of Applied Psychology, 72*(1), 146–148. https://doi.org/10.1037/0021-9010.72.1.146

[15] Csurgai-Horváth, László & Bito, Janos. (2018). Rain Intensity Estimation Using Satellite Beacon Signal Measurements A Dual Frequency Study. 1-5. 10.1109/ISNCC.2018.8530986.

Daytime Optical Background Radiation

Dóra Borbála Kovács, Eszter Udvary, Ágoston Schranz, Balázs Matolcsy
Department of Networked Systems and Services,
Faculty of Electrical Engineering and Informatics,
Budapest University of Technology and Economics,
Műegyetem rkp 3, Budapest, 1111, Hungary

Abstract—
The quality of free-space optical quantum key distribution (QKD) links is significantly influenced by optical background radiation. This study was motivated by the need to understand and mitigate the effects of optical background radiation, a critical parameter shaping transmission quality in quantum-based free-space communication. Our investigation focuses on wavelengths within the 810 and 1550 nm band, which are commonly utilized in optical communications. Specifically, we explore how Eagle-1's planned operation at 1550 nm, in contrast to the Chinese satellite Micius at 810 nm, impacts the optical background radiation and subsequently affects the performance of QKD links. This research provides insights crucial for optimizing QKD systems and advancing the development of secure quantum communication infrastructures such as EuroQCI (European Quantum Communication Infrastructure) within the European Union.

Keywords—optical background radiation, free-space quantum key distribution

I. INTRODUCTION

A. *Challenges in Free-Space Quantum Key Distribution*

Since the advent of the internet at the user level, networks have evolved rapidly, and in less than three decades we have gone from dial-up modem solutions to stable wireless networks. However, the demand to communicate at the highest possible data rates in the most secure way has driven the need to research and develop quantum-based solutions. These technologies would revolutionize data transmission compared to current solutions. Satellites capable of optical communication and Quantum Key Distribution (QKD) are becoming the key infrastructure of the near future.

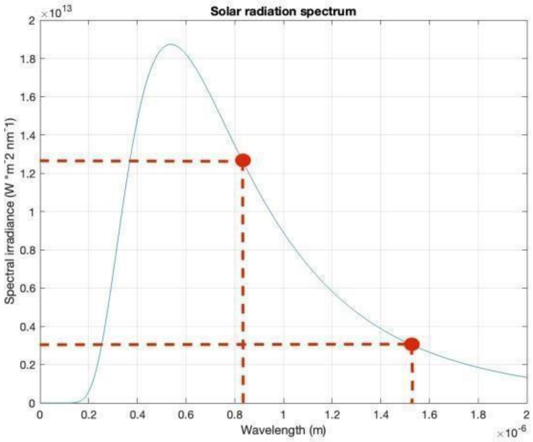

Figure 1. Solar radiation marked at the searched values

Privacy and security have been intrinsic to humans since ancient times. Thus, the emergence of quantum computing could influence classical key cryptography in the upcoming decades, potentially rendering a significant portion of cryptosystems insecure. The invention of Shor's algorithm ensures that some of today's classical public key algorithms will become obsolete [1]. Quantum key distribution [2] uses single-photon communications (QKD systems that operate with weak-coherent light sources, where multiple photons may be present in a pulse) to generate and transfer new keys on- demand with security based on fundamental quantum principles in concert with information-theoretically secure protocols [3]. Since the emergence of the first QKD protocol in 1984 [4], rapid progress has been made in the last decade, resulting in increases of transmission distances and key rates [5]. The real challenge is to increase the communication range to large distances, eventually on a global scale, because of photon losses in the channel [6]. Generally, the attenuation in free-space is lower than that in fiber for optical signals, the free-space channel shows advantage for a distance over ~ 70 km [6]. For instance, values of 0.07 dB/km can be achieved at 2400 m above sea level with higher absorption attenuations at lower altitudes [7]. In order to maximize the benefits of free-space connections, it's crucial to leverage space and satellite technologies effectively. One of the main problems is that optical satellite *communication links are strongly dependent on free-space* channel conditions [8]. Among the atmospheric phenomena that degrade optical satellite links, cloud coverage is also a dominant one, which causes the blockage of the link [9]. Even under cloud-free line-of-sight conditions, optical satellite links are mainly affected by atmospheric turbulence, absorption and scattering, high background solar noise, and pointing losses [10]. The maximal communication distance of a discrete-variable QKD system is limited by the above mentioned background noise that causes the typical sharp cutoff in the rate-distance dependency. This consists of the intrinsic detector dark count rate (DCR) and extrinsic noise sources such as the Sun during daylight. The latter is the dominant term (at least during daytime) and depends on the operational setting (e.g., time of the day and direction of the link), as well as the receiver's aperture size A and incoming light intensity I_0. Many QKD systems use temporal filtering [11], which reduces background noise as the detectors are only active for a time Δt when a photon from the sender is expected (in practice, this is often done by post-selection). The solar background depends on the wavelength λ and spectral filter bandwidth $\Delta\lambda$. [12].

The sunlight intensity at 1550 nm is ~4 times weaker than that at 800 nm, so it is justified to design the quantum channel on the wavelength of 1550 nm in order to decrease losses caused by solar radiance. This fact is visible in Figure 1. Atmospheric transmittance is diminished due to both air absorption and the scattering of the propagating beam. The atmospheric composition primarily consists of gas molecules and small particles, including water droplets, dust, and aerosols. Gas molecules possess specific absorption lines, while scattering can be explained by Rayleigh scattering. The classic electrodynamic explanation is that light passing through a transparent medium oscillates in time with the electric field of the atoms or molecules, which act on the charges of the scattering centers. These tiny dipoles then emit electromagnetic radiation. The interaction between light and particles involves elastic scattering, resulting in an identical frequency determined by the wavelength and size of the particles. This main type of scattering of solar noise for links between a satellite and Earth or between two satellites is proportional to [12]: $I(\lambda)$ for proportionality $\frac{I_0(\lambda)}{\lambda^4}$ for the incident light intensity $I_0(\lambda)$. Therefore, Rayleigh scattering at 1550 nm is only 7% of its value at 800 nm. During our measurements we were focusing on the above mentioned two main factors of channel loss.

B. *Previous experiments*

After addressing the challenges posed by the free-space quantum channel, we will now discuss several distinct experiments conducted as part of the satellite development process.

After the satellite Micius was launched, the first goal was to establish a space-ground quantum link and perform QKD from satellite to ground. The typical LEO (Low Earth orbit) satellite-to-ground channel attenuation was calibrated during one orbit and varied from 29 dB at 530 km to 44 dB at 1600 km and the loss due to atmospheric absorption was 3–8 dB [13]. The second planned mission of the Micius satellite was a bidirectional distribution of its spaceborne entangled photons to two distant locations on Earth [14]. The physical distance between the two ground stations was 1203 km. The separation between Micius and these ground stations varies from 500 to 2000 km. Using a reference laser on the satellite, the overall two-downlink channel attenuation was measured in real time, which varied from 64 to 82 dB, a significant part of it due to atmospheric transmittance. The Greek QCI (Quantum Communication Infrastructure) contributed to this research by analysing a LEO satellite-to-ground BB84 QKD link over a turbulent atmospheric channel under daytime and nighttime conditions [15]. Based on the set of the reported numerical results, the establishment of the QKD downlink is hard to accomplish in daylight conditions, but a sufficient amount of quantum keys can be distilled during nighttime. The link to Micius was only operational during the night to avoid sunlight saturating the single-photon detectors in the ground station [16].

A more ambitious quantum communication infrastructure project is taking shape in Europe. The European Quantum Communication Infrastructure (EuroQCI) initiative aims to build a secure quantum communication infrastructure that will span the entire European Union (EU), including its overseas territories [17]. One project involves building a fully operational, secure, and effective quantum satellite system capable of distributing QKD quantum keys in Europe, known as Eagle-1. Based on all of this, it is important to have knowledge about optical background noise.

Figure 2. Photo of the device

II. DAYTIME MEASUREMENTS

A. *Device used for measurements*

In the Budapest University of Technology and Economics (BME) Mobile and Quantum Communication laboratory, a portable ambient light measurement station had already been developed which was adequate to measure optical background radiation. The station encompasses the optical components, a camera for capturing snapshots of the sky, a system for data acquisition and storing using a Raspberry Pi as the central computer, and the necessary power supplies with cabling within a weather-resistive housing. These units are illustrated in Fig. 2. We can measure the optical power in four distinct sectors labeled from 0 to 3, all in different wavelength bands. Each of them contains a low-noise photodetector and an aspheric condenser lens. Sectors 1 and 2 also include optical band-pass filters (OBPFs), resulting in narrowband operation, focusing on noise in the 850 nm-band and the C-band (1530–1565 nm), respectively. The filters in use have their central wavelengths at 810 nm and 1540 nm [18]. These two wavelengths could be of interest in the process of Eagle-1 mentioned in Sec. 1/B. Sectors 0 and 3 provide extra information about the total amount of incoming optical power in the visible (sector 0) and the near-infrared (sector 3) bands without filtering [18]. The data acquisition (DAQ) device processes four new values every 60 milliseconds and stores them in a comma-separated text file, including a timestamp and a new line character for each entry. It opens a new file every hour to avoid reading from huge files. Saving in this form simplifies data storage and makes data processing after/during measurement convenient. Every ten minutes, the device takes a picture of the sky to capture visual information alongside the numerical data.

B. Measurement

We positioned the measuring instrument on the rooftop terrace of Building BME I, located on the 5th floor. The primary rationale for this decision is to conduct measurements in the area most shielded from artificial light sources. The surface of the terrace has a slope angle of approximately 4.5 degrees. Apart from this slight incline, the detectors were oriented to face roughly directly upward throughout the observation period. The elevation above sea level is roughly 107 meters, excluding the building's height. While the highest level of the building from the southeast could potentially block incoming light to some extent, this was not a significant issue due to the distance and angle of the detectors and lenses. In Figure 3 the device is situated at the location marked with a red symbol, and power was supplied directly from the network to the device via an extension cord.

The measurement results have been saved to a shared folder starting from March 14, 2023. As detailed above, the data are stored in the described format, organized accordingly. we developed a program using Matlab software to analyse and graphically represent these data. This program enables a simpler overview of the differences and similarities between individual channels. For clarity, we simultaneously displayed the voltage measured by all four channels on the graphs. However, these voltages are not directly comparable to the detected optical power due to several factors influencing it. These factors include the sensitivity and internal amplification of the detectors, current-voltage conversion, and the efficiency of the lenses in focusing. We labeled the voltage values on the Y-axis of the graphs as OPI, which stands for Optical Power Indicator, with units in volts (V), while the X-axis represents time. Each channel's signal was plotted in a different color for clarity and distinction.

C. Results

The graphical representation of data saved by the instrument suitable for measuring background radiation is shown in the following figures (Figures 4-6), created using the mentioned Matlab programs. Cloud cover, appearing intermittently, results in higher peaks on the graph, while lower OPI (Optical Power Indicator) values occur when light transmission is less obstructed, indicating relatively clearer skies. This might seem contradictory at first glance, but the explanation is straightforward. When the sky is clear, and the Sun is not directly overhead the detector, most of the incoming light is from the blue end of the visible spectrum, which is a relatively narrow band comparing where detectors are sensitive. However, when the Sun is behind clouds, light scatters and reflects over a wider range of wavelengths. Generally speaking, although the sensors are not precisely calibrated, it's evident that the background radiation measured by Channel 0 is significantly higher than Channel 3. This aligns with the previous knowledge described earlier; the Sun's spectrum contains stronger visible components than infrared ones, and the noise power at 1550 nm is much lower than that at 810 nm. This statement is supported by all measurement results, indicating that designing for 1550 nm quantum channels is more favorable in terms of noise compared to designs based on 810 nm. Data from different channels correlate significantly, with differences appearing in the amplitudes of the OPI. During the night, the signal fluctuates around the dark noise values specific to each channel, attributed to the coarser quantization levels of the DAQ (Data Acquisition) system. These levels are insufficient for effective noise measurement during darker hours when photons are detected. In Figure 5, a graph of a day is shown where OPI values exhibit significantly high peaks at one point (12:32), with the function otherwise monotonically increasing, then decreasing with minor fluctuations to the dark voltage level. The lines described by the functions coincide with the apparent movement of the Sun. The "A" marker indicates the brightest time point. On each picture the attached three photographs were taken by the device at times labeled A, B, and C. The camera is aligned identically to the detectors and is set to capture images of the sky at regular intervals. Although these photos offer only limited weather information, they are valuable for assessing cloud cover levels. It's evident why the OPI values are higher at 12:20 compared to 13:10 or 14:30, as the average brightness is highest in the image at that time. Labels D, E, and F correspond to times 12:10, 13:00, and 14:20; the corresponding images show a gradually darkening sky due to cloudy weather. Figure 6, for instance, illustrates values measured on a rainy day graphically. The thick rain clouds, less transparent to light, obstruct significant light from reaching the detectors, resulting in a highly fluctuating graph. The graph also shows that the appearance of clouds increases the level of scattered light. Where the Sun emerges, the intensity falls back to levels comparable to a clear sky, and in strong darkness, it almost falls to values similar to those measured under night conditions. During the analysis, I did not consider the wavelength dependence of lens focal length since within the critical 1540 nm sector, there is a consistent 10 nm width filter. In the laboratory earlier, using a tunable laser, I coupled light into the detector equipped with the filter within the specified 10 nm range, thus obtaining the characteristic of the filter. It was observed that there is no significant wavelength dependence in

Figure 2. Placement of the device

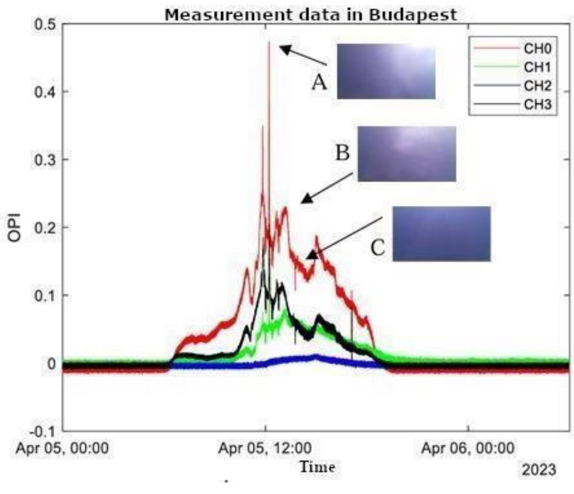

Figure 4. Results on a clear day

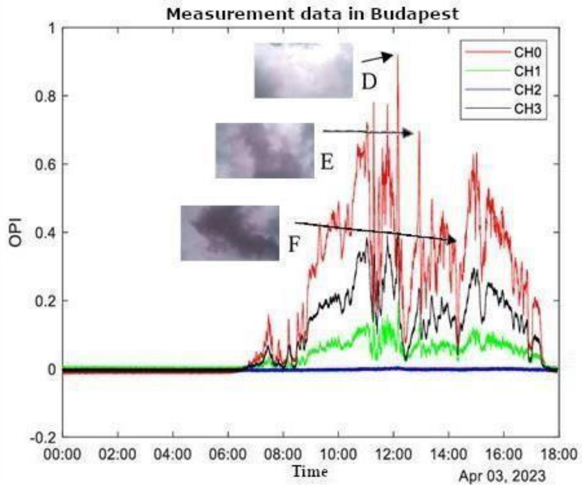

Figure 5. Results on a rainy day

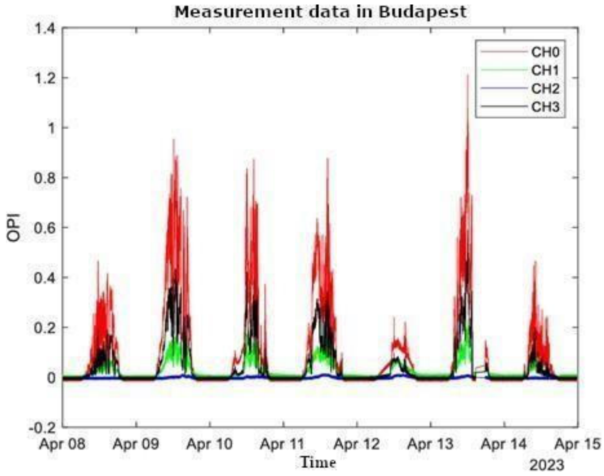

Figure 6. A week-long measurement

the filter's and the detector's response. Additionally, it can be stated that the detector surface, which is on the order of several mm^2, proves to be of sufficient size optically. Therefore, the values read from the graph can be considered real results. The graph depicting measurements taken over the course of a week clearly shows which days were rainy and cloudy, and which ones were sunny.

III. OUTLOOK

The measured data indicates that a sky with light cloud cover has dual negative impacts. It significantly reduces the strength of signals both incoming and outgoing between the ground station and satellite, while also amplifying noise levels at the receiver. The dynamic movement of clouds contributes to rapid fluctuations in the signal-to-noise ratio. Additionally, dense rain clouds can effectively block a substantial portion of sunlight, affecting transmission. In terms of infrared channels, the 1550 nm channel exhibits lower noise compared to the 810 nm channel, aligning with expectations based on solar emission and Rayleigh scattering. However, when evaluating the quantum channel, the quantity of noise photons may be a more crucial metric to consider.

Results are supporting the fact that implementing quantum communication in bad weather is not possible with current technology. However, we note that there will be no turbulence or bad weather between satellites. Only when considering quantum communication between a satellite and the ground must bad weather be taken into account [19]. One of the main drawbacks of the current satellite-based quantum communication missions is that they work only at night, which greatly limits their practical applications [20]. It is necessary to measure daytime background radiation values to ensure the proper functioning of quantum-enabled satellites and receiver stations planned for future implementation.

IV. CONCLUSIONS

In this work we have discussed the significance of measuring background noise and subsequently conducted measurements in relation to this topic. The results show that for minimizing photon loss due to solar radiance, 1550 nm is an ideal choice. The values of the solar background radiance during the day depend on the position of the satellite relative to the sun azimuth as well as on the Optical Ground Station's location [21]. Further measurements are needed in this regard, with the optical fiber placed outdoors at different positions and secured using a movable connector.

V. Acknowledgements

This project has received funding from the European Union under grant agreement No 101081247 (QCIHungary project) and has been implemented with the support provided by the Ministry of Culture and Innovation of Hungary from the National Research, Development and Innovation Fund.

[1] Shor, P.W. Algorithms for quantum computation: Discrete logarithms and factoring. In Proceedings of the 35th Annual Symposium on Foundations of Computer Science, Santa Fe, NM, USA, 20–22 November 1994; pp. 124–134.

[2] Bennett C H and Brassard G 1984 Proc. IEEE Int. Conf. on Computers, Systems, and Signal Processing (Bangalore, India) p 175

[3] Bennett, Charles H., et al. "Generalized privacy amplification." IEEE Transactions on Information theory 41.6 (1995): 1915-1923.

[4] Bennett, C.H.; Gilles, B. Proceedings of the IEEE International Conference on Computers, Systems and Signal Processing, Bangalore, India, 9–12, December 1984; IEEE: Piscataway, NJ, USA, 1984.

[5] Pirandola, S.; Andersen, U.L.; Banchi, L.; Berta, M.; Bunandar, D.; Colbeck, R.; Englund, D.; Gehring, T.; Lupo, C.; Ottaviani, C.; et al. Advances in quantum cryptography. Adv. Opt. Photonics 2020, 12, 1012.

[6] LU, Chao-Yang, et al. "Micius quantum experiments in space." Reviews of Modern Physics, 2022, 94.3: 035001.

[7] Schmitt-Manderbach, T., et al., 2007, "Experimental Demonstration of Free-Space Decoy-State Quantum Key Distribution over 144 km," Phys. Rev. Lett. 98, 010504

[8] Kaushal, H.; Kaddoum, G. Optical Communication in Space: Challenges and Mitigation Techniques. IEEE Commun. Surv. Tutor. 2016, 19, 57–96.

[9] Lyras, N.K.; Kourogiorgas, C.I.; Panagopoulos, A.D. Cloud Attenuation Statistics Prediction from Ka-Band to Optical Frequencies: Integrated Liquid Water Content Field Synthesizer. IEEE Trans. Antennas Propag. 2016, 65, 319–328.

[10] Kaushal, H.; Kaddoum, G. Optical Communication in Space: Challenges and Mitigation Techniques. IEEE Commun. Surv. Tutor. 016, 19, 57–96

[11] H. Ko, K.-J. Kim, J.-S. Choe, B.-S. Choi, J.-H. Kim, Y. Baek, and C. J. Youn, Experimental filtering effect

[12] LIAO, Sheng-Kai, et al. Long-distance free-space quantum key distribution in daylight towards inter-satellite communication. Nature Photonics, 2017, 11.8: 509-513.

[13] Liao, S.-K., et al., 2017a, "Satellite-to-ground quantum key distribution," Nature (London) 549, 43

[14] Yin, J., et al., 2017a, "Satellite-based entanglement distribution over 1200 kilometers," Science 356, 1140

[15] Giannopappa, C. 5G, Fibre in the Sky and beyond. In Proceedings of the ScyLight Workshop on Optical and Quantum Communication, Online Event, 8–9 June 2021.

[16] ABASIFARD, Mostafa, et al. The ideal wavelength for daylight free-space quantum key distribution. arXiv preprint arXiv:2303.02106, 2023.

[17] Scudo, Petra F., and Adam M. Lewis, 2021, "Quantum communications infrastructure architecture: Theoretical background, network structure and technologies. A review of recent studies from a European public infrastructure perspective," arXiv:2110.06762.

[18] Á. Schranz, E. Udvary, B. Matolcsy, L. Bacsárdi and A. Nagy, "A Portable Ambient Optical Noise Measurement Station," 2023 23rd International Conference on Transparent Optical Networks (ICTON), Bucharest, Romania, 2023

[19] Liao, Shengkai et al. “Long-distance free-space quantum key distribution in daylight towards inter-satellite communication.” Nature Photonics 11 (2017): 509 - 513

[20] Pratt, S. R., R. A. Raines, C. E. Fossa, and M. A. Temple, 1999, "An operational and performance overview of the iridium low Earth orbit satellite system"

[21] Ntanos, A.; Lyras, N.K.; Zavitsanos, D.; Giannoulis, G.; Panagopoulos, A.D.; Avramopoulos, H. LEO Satellites Constellation-to-Ground QKD Links: Greek Quantum Communication Infrastructure Paradigm. *Photonics* 2021

Preliminary design of payload for sounding rockets

András Ádám Dobay, Ábrók László Patrik, Gábor Kreinicker, Bálint Gábriel
BME Suborbitals
Budapest University of Technology and Economics
Budapest, Hungary
dobay.adam@bmesuborbitals.com

Zoltán Petrovics, Máté Albert, Ferenc Dániel Békési, Noel Nataniel Bozó, Csaba Velich, Kornél Dobos
BME Suborbitals
Budapest University of Technology and Economics
Budapest, Hungary

***Abstract*—Many prominent academy and industry players have the desire to experiment under high acceleration and elevated radiation within the uppermost troposphere. This demand can be satisfied with sounding rocket satellites developed by university students and research groups. BME Suborbitals is a team of STEM students, who develop their rockets and a solid-propellant engine for various competitions. Recently our team began developing scientific and technological experiments for payload applications. The payload will be encapsulated in a CubeSat format of 10x10x20 cm (2U) design conforming to CP-CDS-R14.1. The frame has been designed by the team to specifically comply with the experiments on-board, which include a Fungal Sporulation experiment (FSE) in collaboration with Szeged Biological Research Centre (SZBK) to aid space mycology, an Aeronautical-Ground channel (AGC) study with OFDM link for channel characterization and finally a monochromator to study greenhouse gas concentration at various altitudes. The CubeSat will also be capable of filming the entire descent with an on-board camera, which will be analyzed as its secondary purpose of horizon detection.**

I. INTRODUCTION

Sounding rockets have the advantage of return capabilities compared to traditional satellite systems. To expand this idea, our team devised a payload specifically targeted at reusability and adapted to simple ground-based evaluation. In this paper, we present current advances in some of our scientific and technological experiments, including an *atmospheric spectroscopic measurement with an acousto-optical deflector* to detect harmful greenhouse gases, *Orthogonal frequency division multiplexing (OFDM) channel characterisation*; rocket travel-induced effects on *Coprinopsis cinerea mushroom's sporulation* and *Horizon detection technological demonstration* using commercially available cameras.

II. MONOCHROMATOR

A. Experiment overview and relevance

The Earth's atmosphere consists predominantly of nitrogen (approximately 78%) and oxygen (about 21%), alongside trace amounts of other gases. The relevant layer of the atmosphere for this measurement is the troposphere, which is right below the tropopause region approximately 0-10 km above the surface. In this region, a variety of gas components can be found in a dynamic equilibrium with each other. Widely known for the so-called greenhouse gases that greatly damage the ozone layer that protects the Earth, such as CO_2, CH_4, N_2O, and halogenated gases, like SF_6, Halons, chlorofluorocarbons (CFCs). Nitrous oxide is also naturally present in the atmosphere as part of the Earth's nitrogen cycle and has a variety of natural sources, but agriculture, land use, and transportation as anthropogenic emissions can affect the environment. From human-related activities, the halogenated organic gases (halons) are the most harmful representatives of which are CFCs also commonly called Freons have no significant natural sources and have been widely used as refrigerants, propellants, and fire extinguishing agents [3]. Emissions of N_2O from NO production are expected to remain the largest threat to ozone throughout the 21st century. Consequently, monitoring these halocarbons and N_2O is still a crucial process to observe, and to track the recovery of the stratospheric ozone layer [4].

By measuring the spectrum of sunlight filtering through the Earth's atmosphere, the monochromator could help us identify the presence and abundance of different gases like ozone, water vapor, or pollutants. This data can be used to monitor air quality, track changes in atmospheric composition, and improve our understanding of climate change.

This experiment will specifically measure H_2O, O_2, O_4 (O_2 dimer), OBrO, OClO, $(CHO)_2$, CH_3OOH, OIO, I_2, Br_2, NO_2, NO_3, O_3 (Figure 1) as these chemical compounds' absorption spectra were within the spectral response of the chosen photodiode system. For further optimizations, it is imperative to carry out ground experiments with laboratory circumstances to choose the best candidates for measuring.

B. Engineering challenges

Traditional monochromators utilize bulky optical components that won't fit within the confined space of a 2U CubeSat. Overcoming this limitation requires innovative miniaturization techniques. We proposed the two following resolutions:

- *Miniaturized Optics*: Advanced fabrication methods like thin-film optics, optical cables and micromachining can be used to create miniaturized versions of essential optical components. These miniaturized components can achieve similar performance to their larger counterparts while fitting comfortably within the CubeSat's tight space constraints.

- *Diffractive Optics*: Diffractive optics, which employ gratings to manipulate light, offer a promising alternative due to their inherently compact design. These gratings can perform the same function as traditional lenses and prisms while requiring significantly less space. This should be solved by using acousto-optics methods which are less sensitive to high-frequency vibration and do not require a large amount of power for operation.

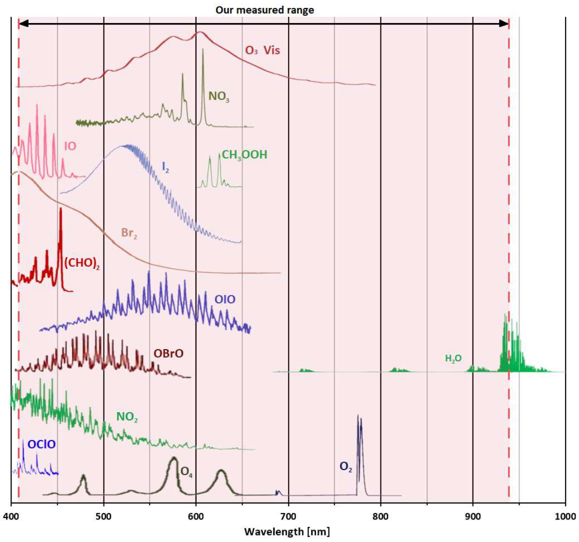

Fig. 1. Graphical illustration of our measurable wavelength range (reddish) and within the observable components (colored spectrums). (The shown absorption cross sections are not proportional.) [2]

Another critical challenge is the intense vibration that occurs during the operational phase of a CubeSat. These vibrations can damage the delicate optical components within the monochromator, causing misalignment or even permanent damage. A single misplaced component counts as a single-point failure. To mitigate the effects of vibrations, several techniques can be employed, such as passive damping utilizing elastomeric isolators strategically placed between the monochromator and the CubeSat frame to passively absorb vibrations, dampening their impact on the delicate optics. Another approach is a stiff and lightweight frame design to improve its overall resistance to vibrations.

Another significant issue is prevalent in this case, as a diffraction grating needs to be capable of sweeping through a predefined range of wavelengths. It requires its optical properties; in particular, its diffraction index to vary controllably. This issue is traditionally solved with motor-controlled optics, but due to size constraints and vibration sensitivity, our team opted to use an acousto-optical deflector.

C. The Acousto Optical Deflector

The photo-elastic effect is the change in the optical properties of a material due to mechanical strain. We are particularly interested in the connection between the diffraction index (n) and the mechanical deformation (S) which can be formulated in Equation 1.

$$\Delta n \;=\; \frac{1}{2}n^3 pS \;=\; n_0 S \qquad (1)$$

where p is the photo-elastic constant. In practice the mechanical deformation is caused by a sound wave characterized by angular frequency Ω, and speed v. Then it can be easily seen that the change in the diffraction index is also harmonic, and takes the form presented in Equation 2.

$$\Delta n \;= n_0 sin(\Omega(t - \frac{x}{v}) \qquad (2)$$

If we investigate an electromagnetic wave, the diffraction index has a harmonic spatial dependence, so by straightforward calculation one can show that the EM wave is a phase-modulated optical lattice, which moves in the direction parallel to the sound waves. Because of this, the dispersion of the EM wave can be observed.

In this application, the main focus is on the Bragg diffraction. If $L \gg \lambda$, we can only observe the 0th and the 1st order diffraction (Figure 2). But to see a diffracted beam the Bragg condition must be met, which is $sin\,\alpha \;= \frac{\lambda}{2\Lambda}$. This can be derived from the following conditions: firstly, we model the material as semipermeable mirrors, secondly, we need constructive interference between the different reflections. Accounting for the refraction on the surface of the crystal for Θ, we get Equation 3.

$$\Theta = \omega\left(t - \frac{y\cdot n(x)}{c}\right) = \omega t - \omega y \frac{n_0 sin\,\Omega(t - x/v)}{c} \qquad (3)$$

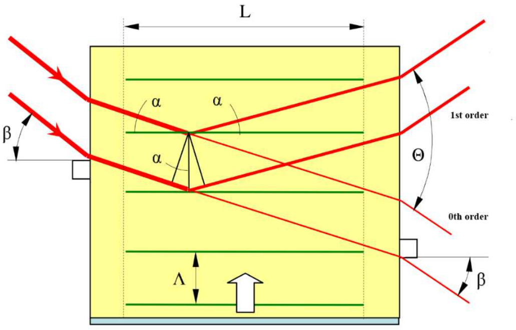

Fig. 2. Bragg diffraction and the transmitted beam [1]

III. Coprinopsis cinerea mushroom’s sporulation experiment

A. Scientific Background of Coprinopsis cinerea

Coprinopsis cinerea, commonly known as the gray shag mushroom, is a fascinating organism widely studied in mycology due to its unique characteristics and various applications. Here, we present some key points about *Coprinopsis cinerea*.

Coprinopsis cinerea, classified within the kingdom Fungi, phylum Basidiomycota, class Agaricomycetes, and order Agaricales, is a heterotrophic, saprotrophic mushroom that decomposes organic matter while constructing its structure. Its fruiting bodies are characterized by small to medium-sized mushrooms with distinctive cylindrical caps that gradually dissolve into black, inky liquid as they mature. Initially white, the gills of this mushroom turn black as the spores mature, eventually leading to the liquefaction of the entire mushroom through autolysis.

Ecologically, *Coprinopsis cinerea* plays a vital role in ecosystem functioning by participating in the decomposition of plant material, particularly lignocellulose, thereby contributing to nutrient cycling and soil formation. In terms of research significance, its rapid growth, well-characterized genome, and susceptibility to genetic manipulation make *Coprinopsis cinerea* an ideal model organism for studying various biological processes, such as fungal development, metabolism, and environmental responses.

B. Experiment Overview and Relevance

In this experiment, we aim to investigate the effects of high altitude on Coprinopsis cinerea fungi by subjecting them to the effects of a rocket launch and flight. The experiment will consist of two stages: first, the fungi will be launched to an altitude of 3000 meters, followed by a second launch to an altitude of 9000 meters. We will observe any changes in the fungi's morphology, physiology, or gene expression post-flight compared to control samples kept at ground level.

Currently, we have performed inoculation experiments in the laboratory of Biological Research Center of Szeged (SZBK), during which the yeast extract-malt extract-glucose (YMG) medium proved to be the most suitable.

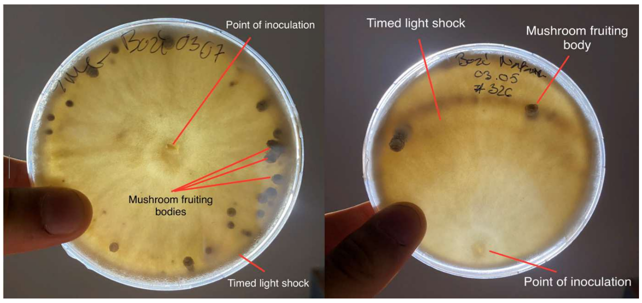

Fig. 3. Mushroom inoculated center and at the side of the petri dish

In the first experimental phase, we tried to determine the optimal location of the mushroom inoculation. We observed that inoculating the mushroom on the side of the petri dish did not always bring reliable results [5], however, the central location proved to be more effective (Figure 3). Thanks to this, the fungi showed central growth in the petri dish, which was of paramount importance for the success of the experiments.

During the second series of experiments, we performed synchronization experiments that spanned a long period of time (Figure 5). Our goal was to prepare the mushrooms for fruiting body formation in a timed manner, thereby promoting the achievement of more accurate research results and the reliability of the experiments.

At last, we devised a custom parametric design of a petri dish with thicker walls to adapt to the challenges present throughout the rocket launch and mounting solution on the printed circuit board (PCB) (Figure 4). The design also accompanies two sensors to measure temperature, pressure and humidity within the experiment chamber.

Exposure to high altitudes can significantly influence the growth and development of *Coprinopsis cinerea*. One key area of interest is whether the morphology of the mushrooms undergoes changes in response to altitude-induced stress.

Fig. 4. Custom design of a petri dish with sensor adaptation

Additionally, researchers are curious about any alterations in the expression of genes related to stress response, metabolism, or growth regulation in the fungi following exposure to high altitudes. Another aspect of investigation involves understanding the impact of high altitude on the reproductive capacity and spore production of *Coprinopsis cinerea*. Furthermore, scientists aim to discern any observable differences between the fungi subjected to 3000 meters and those exposed to 9000 meters of altitude. Through these inquiries, we can deepen our understanding of how environmental factors, such as altitude, shape the biology of *Coprinopsis cinerea*.

C. Future Results and Implications

The findings of this experiment will contribute to our understanding of how fungi, particularly Coprinopsis cinerea, respond to extreme environmental conditions such as high altitudes, pressure and acceleration. The results may have broader implications for fungal ecology, adaptation to environmental stressors, and the potential effects of climate change on fungal communities. Additionally, insights gained from this study could inform future research on space biology, astrobiology, and the cultivation of fungi in extraterrestrial environments.

By conducting this experiment, we aim to shed light on the resilience and adaptability of fungi in the face of environmental challenges, ultimately advancing our knowledge of fungal biology and its applications in various fields.

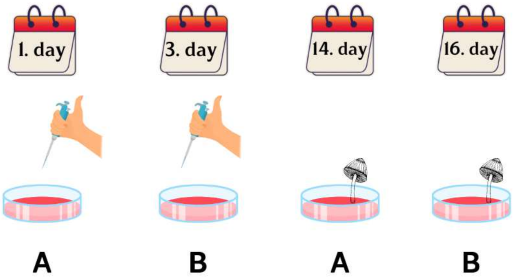

Fig. 5. The synchronization experiments timeline

IV. HORIZON DETECTION CAMERAS

Since there are direction-sensitive experiments on the payload, it is essential to determine the exact attitude. There will be four cameras, placed perpendicular to each other on the four sides of the CubeSat so that the sensors of each camera are perpendicular to the plane of the Earth. After a successful mission, the complete flight recording will be post-processed. The Sun and the Earth's horizon will be detected, from which the satellite's attitude can be determined using mathematical tools.

A. Camera calibration

For the camera, we chose a First-person view (FPV) camera whose small size, wide angle of view and 4k resolution are suitable for the experiment. The large field of view, although it allows to maximize the area under investigation, causes a significant barrel distortion in the image, which makes it difficult to apply various edge detection algorithms. However, camera calibration can be used to reduce this distortion.

A checkerboard pattern board was used to calibrate the camera (Figure 6). The purpose of this is to use image processing to detect the corner points of each square, the physical distance of which can be used to determine the distortion parameters: the radial distortion and the intrinsic matrix. By subsequently applying these parameters to any image taken with the same camera, we can minimize the distortion.

The calibration was done in MATLAB, but due to the large angle of view, manual parameter optimization was also needed. The result is not optimal, as shown in the figure, while the distortion in the center of the image is reduced, there is still some anomaly at the edges of the image.

B. Post-processing methods

To process the full mission record, we need to detect the Sun and the Earth's horizon. The detection of the former one is more straightforward due to its brightness as it is more separable from the background. However, finding the horizon is more laborious. We worked with two methods: one is edge detection, and the other is iteration. Edge detection and line fitting is a resource-intensive and slow process. A given frame is converted to HSV from RGB channels and then binarized in the channel where the Earth and sky are separated. An edge detection is done on this image and then a straight line is fitted to the horizon using the Hough transform. This step is an important precondition for camera calibration. The vector perpendicular to this line defines the normal vector of the horizon in the image coordinate system.

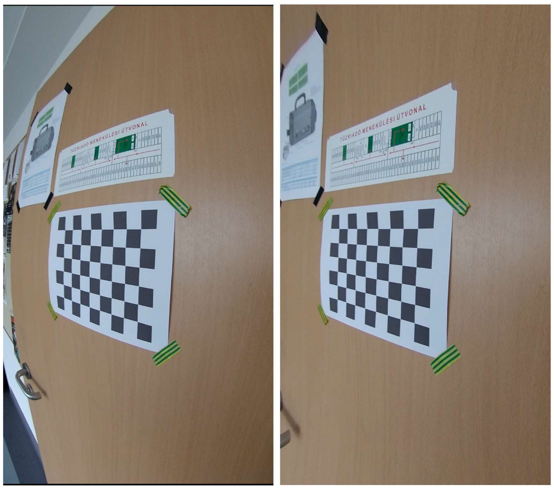

Fig. 6. Camera calibration with checkerboard pattern: original image (left), calibrated image (right)

The iteration method is a faster solution than the straight-line fitting (Figure 7). The average value of the pixels of the Earth and space is determined and a threshold is defined based on these values. Next, we determine which corners of the image exceed this value. Accordingly, we can determine which edges of the image should be used to find the intersection of the horizon. By iterating along the edges of the image, we obtain the two intersections of the horizon, from which we obtain the normal vector of the horizon in the coordinate system of the image.

This iteration process can be further accelerated by using interval halving instead of iteration, or by reducing the resolution of the image. The latter will reduce the accuracy of positioning but may allow real-time positioning in later missions using a lower power on-board computer. This method also has a significant drawback: if the Sun is close to both the horizon and the edge of the image, it will not be possible to detect the second intersection and an incorrect normal vector may be calculated.

Knowing these vectors in a base fixed to the Earth, we can determine the rotation matrix to move from the satellite base highlighted by the images to this base. This rotation matrix will form the satellite position we intend to determine.

V. OFDM CHANNEL CHARACTERISATION

During flight, real-time transmission of telemetry and other measurement results increase the reliability of experiments conducted from the rocket. However, it hasn’t been explicitly measured what data rate can be reliably achieved between the rocket and the ground station. To study this matter, an experiment aimed at measuring the radio frequency channel will be included on the research rocket, to determine the radio frequency channel between the ground base station(s) and the rocket. For the implementation of communication at this stage, frequencies in the Industrial, Scientific and Medical (ISM) radio band are designated.

For the air-ground channel, not many comprehensive studies were performed with wideband communication systems. The reason behind this is that most avionics systems use narrowband signals for communication. However, with the introduction of commercial flying products like drones, experimental rockets and balloons there is an increasing need for high-speed wireless communication to support functions such as live video streaming.

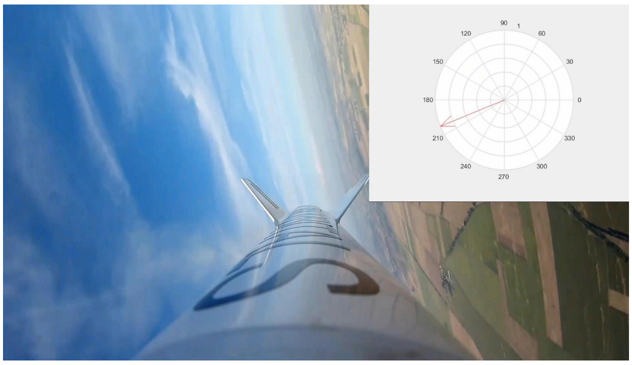

Fig. 7. The horizon detection iteration algorithm was tested on images captured during the flight of the Athena rocket. The diagram in the upper right corner shows the direction of the vector perpendicular to the horizon determined by the algorithm.

We assume that between the transmitter and the receiver, the signal propagates through multiple paths due to the physical environment, including reflections from various terrain features and the ground. Additionally, the channel becomes time-invariant between moving objects relative to each other. The effects of the radio channel on the baseband signal are demonstrated by Equation 4.

$$h(t, \tau) = \sum_{i=1}^{N} \alpha\left(d_i\right) e^{j(2\pi f_c + 2\pi f_{D,i} t)} \cdot \delta(\tau - \tau_i) \quad (4)$$

where N is the number of different propagation paths, $\alpha(d_i)$ is the free-space path loss on the i-th path, $exp(j(2\pi f_c)$ is the baseband signal, $2\pi f_{D,i} t$ is the Doppler-spread and $\delta(\tau - \tau_i)$ is the delay of the i-th path, $h(t, \tau)$ is the time-varying weight function of the radio channel. The transmitted signal can be affected by the channel with delay, which appears as phase shift, attenuation, and frequency offset. From the weight function, with appropriate mathematical steps, the transfer function of the channel can also be obtained, which is a parameter that can be measured and estimated. Based on this, the distortions of the received signal can be eliminated during channel estimation.

For successful channel estimation, several key signal parameters must be considered. Firstly, high bandwidth is crucial, as the coherence bandwidth of the channel significantly influences communication link design. A signal with a broad bandwidth enables the accurate representation of the channel, enhancing estimation precision. Additionally, power distribution is vital. Optimal measurement signals should possess a high Peak-to-Average Power Ratio (PAPR). This high PAPR facilitates an expanded dynamic range, particularly advantageous in fading channels where signal strength can vary dramatically. Moreover, the duration of the signal is critical. Similar to coherence bandwidth, coherence time is paramount in fading environments. To ensure channel stability, the signal duration should be shorter than the coherence time, preventing signal degradation and maintaining reliable estimation.

For all the above reasons OFDM was chosen as the modulation in the payload subsystem. OFDM-based systems are widely used in spread spectrum communication systems. OFDM also benefits from its multicarrier scheme, which is highly sensitive to Doppler spreading. Measuring and comparing Doppler spreading to simulation results in such a high-speed case provides valuable information on designing communication systems for this type of application.

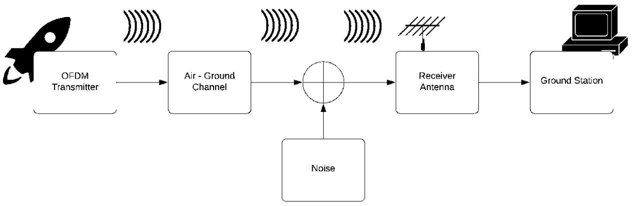

Fig. 8. The proposed block diagram of the experiment

The experiment (Figure 8) includes simulating OFDM signal propagation for the air-ground channel, designing a transmitter module capable of transmitting the desired OFDM signal with appropriate power, designing a receiver antenna and creating an SDR-based receiver on the ground station, where the received data can be processed and stored for further evaluation.

ACKNOWLEDGMENT

Nataniel Bozó thanks Máté Virágh PhD for enabling him to work in the lab of SZBK and for guiding the work with his expertise. Dániel Békési would like to thank Péter Bálint Horváth PhD for his guidance.

REFERENCES

[1] Sándor Lenk, “Akusztooptikai fénydiffrakció vizsgálata”, BME fizipedia, Retrieved: 2024-04-22

[2] E. Gordon, L.S. Rothman, R.J. Hargreaves et al. "The HITRAN2020 molecular spectroscopic database" *JQSRT* 277 (2022) 107949. doi:10.1016/j.jqsrt.2021.107949

[3] "NOAA Global Monitoring Laboratory - CFCs and their substitutes in stratospheric ozone depletion". *gml.noaa.gov*. Retrieved 2024-04-22.

[4] “U.S. Environmental Protection Agency - Overview of Greenhouse Gases”. *epa.gov*. Retrieved 2024-04-22.

[5] H. Muraguchi, K. Umezewa, M. Niikura et al., “Strand-Specific RNA-Seq Analyses of Fruiting Body Development in Coprinopsis cinerea”, PLoS One, 2015, vol. 10

Hungarian participation in the Comet Interceptor mission

Ákos Kereszturi
Konkoly Thege Miklos Astronomical Institute,
Research Centre for Astronomy and Earth Sciences,
HUN-REN, Budapest, Hungary
e-mail: kereszturi.akos@csfk.org

Tibor Diós
REMRED Ltd., Budapest, Hungary

Gergely Gutay
REMRED Ltd., Budapest, Hungary

Zoltán Magari
REMRED Ltd., Budapest, Hungary

Hunor Makkai
REMRED Ltd., Budapest, Hungary

Bálint Sódor
SGF Ltd., Budapest, Hungary

Gábor Tróznai
SGF Ltd., Budapest, Hungary

Sándor Szalai
HUN-REN Wigner Research Centre for Physics
Budapest, Hungary

Abstract— **Comet Interceptor is an exciting new mission that will be launched before its target is known. The mission is foreseen for launch together with ESA's ARIEL spacecraft, both to be delivered to the Sun-Earth Lagrange point L2. Comet Interceptor will wait there in space until a new Dynamically New Comet (DNC) from the Oort cloud is identified on its way into the inner Solar System. The primordial target will be recorded by the Comet Camera (CoCa) imaging system, provided by a consortium led by the University of Bern in Switzerland including DLR Adlershof, LAM Marseille, CSFK CSI (HUN-REN) and industrial partners REMRED Ltd. and SGF Ltd., while independently Admatis Ltd. and Wigner RCP also contributes in the mission from Hungary. CoCa is designed to provide high resolution imaging of the selected comet with 4 filters at broadband optical wavelengths.**

Keywords—Comet Intereptor missions, ESA, spaceprobe, Comet Camera, CoCa, Digital Processing Module, DPM

I. INTRODUCTION

The mission of ESA's Comet Interceptor (C-I) spacecraft [1] is to visit a comet that is on its first to approach to the inner Solar System after its formation between the giant planets and its ejection into the distant cometary cloud (Figure 1). However, an already known Long Period Comet (LPC) could be a secondary target if ideal primordial originated object cannot be found during the mission lifetime. The characteristics and composition of its surface can provide more new knowledge about the primordial material of the Solar System than ever before. Such a celestial body has never been examined by a spacecraft, since after its discovery any visit would require barely a year to prepare and launch the spacecraft. Accordingly, this mission after launch will wait at the L2 Lagrange point until the Large Synoptic Survey Telescope (LSST, Vera C. Rubin Observatory) telescope discovers such a comet moving in a favorable orbit that the probe can reach. Lagrangian points, discovered by mathematician Joseph Louis Lagrange. which are locations in space where gravitational forces and the orbital motion of different bodies balance each other. Therefore, they can be used by spacecraft to 'hover'. L2 is located 1.5 million kilometers directly 'behind' the Earth as viewed from the Sun.

The F-category i.e. fast Comet Interceptor mission has a maximum cost of 150 million euros (excluding launch), together with the Ariel space telescope, in 2028 or 2029 with an Ariane 62 launch vehicle from the Kourou spaceport (French Guiana), from the ELA-4 launchpad. Comet Interceptor is foreseen for launch as co-passenger with ESA's exoplanet-studying Atmospheric Remote-sensing Infrared Exoplanet Large-survey (ARIEL) space telescope. Both missions will be delivered to L2 and from there Comet Interceptor will journey onwards to the chosen target using its own propulsion system. The main difficulty of planning Comet Interceptor is that the parameters of the target and those of the rendezvous are not yet known, however the spacecraft's instrumentation and observation routines must be designed and created now. The rendezvous can take place at a relative speed of up to 70 km/s (a dust shield similar to that of the Giotto probe protects the spacecraft), with previously unknown orbital elements [2, 3, 4]. The probe can wait a maximum of 5 years in space, if it does not find an ideal target by then, it will visit a previously known comet. But with luck, the target object could even be an interstellar comet that is currently passing through the Solar System.

The observations target the characteristics of the coma and nuclei along three orbits: the main unit (A), a Japanese (B1) and a European (B2) CubeSats. The Hungarian role in the space probe is the design and manufacture of the Digital Processing Module (including Data Recorder unit) of the CoCa optical camera (REMRED Ltd., SGF Ltd., Konkoly Thege Astronomical Institute, CSFK, HUN-REN), the design and manufacture of the thermal insulation (ADMATIS Kft.), and some plasma physical instruments (HUN-REN Wigner RCP).

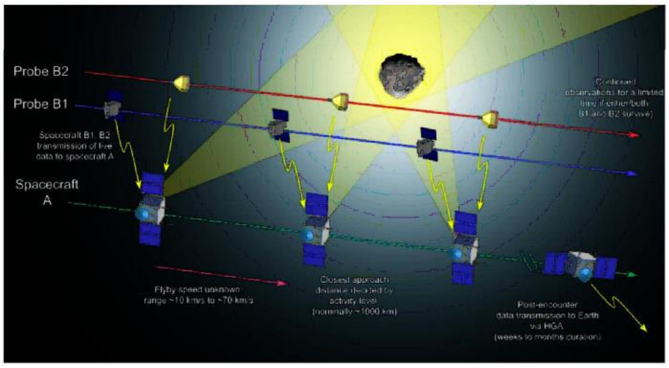

Figure 1. Schematic presentation of the three probes (A, B1 B2) flies through the target comet (ESA C-I Mission)

II. SEARCH FOR THE TARGET COMET

The survey for the target dynamically new comet will be done by the Large Synoptic Survey Telescope (LSST) instrument's wide-field, high-sensitivity state-of-the-art detector scans the sky quickly enough, so a faint moving object can be discovered by regular monitoring of the sky with trajectory determination.

According to the statistical estimations so far, the LSST telescope will be able to discover a long-period comet heading toward the interior of the solar system as a suitable object available for the C-I probe considering orbital elements in the first 3 years. The earlier the object become discovered the more time exists for proper orbit determination and orbital maneuver of the C-I probe trio in ideal case with a time advantage of 6-12 months, to make a safe flyby.

III. THE SPACEPROBE

The total mass of the probe is 800 kg, which includes the mass of its body, equipment and scientific instruments, as well as the fuel required for orbital maneuvers. Its energy supply is provided by solar panels that can be opened to the side. According to the 2019 plan, it is cylindrical, but in 2021, the plans already include a cube.

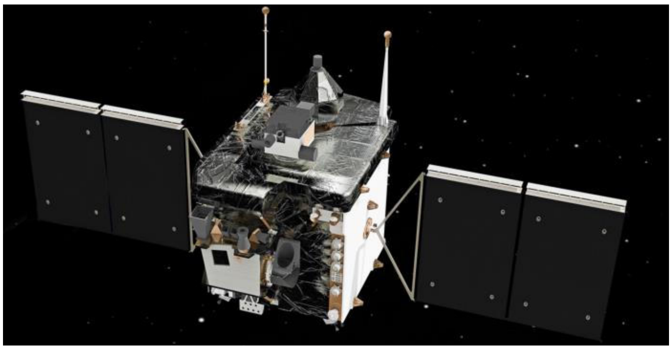

Figure 2. C-I combination of three space-probes *(A, B1 & B2)*

On top of the probe A are the two small probes B1 and B2, which after determining the trajectory of the target comet selected on pictures of Earth telescopes, they will separate to observe the comet's nucleus from a closer view (Figure 1). The CoCa is on the main probe A (Figure 2 and 3).

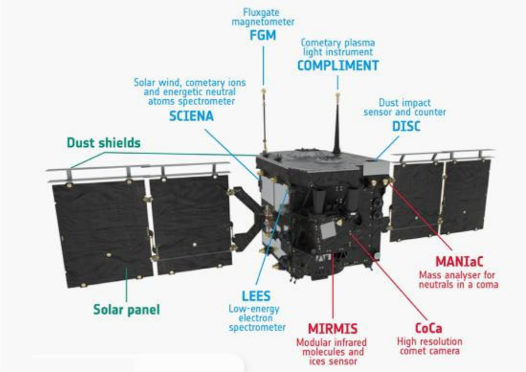

Figure 3. Scientific instruments positions on the main probe A

TABLE I. INTRUMENTS OF THE PAYLOAD ON THE MAIN PROBE A

Acronym	**Instrument**	**Observation targets**
CoCa	Comet Camera	Optical and near infrared image detector for the nuclei and coma observations.
MANIaC	Mass Analyzer for Neutrals and Ions at Comets	Neutral and charged particle analysis of the coma targeting gas density and composition, including D/H isotopic rations (plus some isotopes of O, C, S elements), linked to Earth based observations to deduce production rates.
MIRMIS	Modular InfraRed Molecules and Ices Sensor	Recording the surface composition and thermal properties of the nuclei plus the gas in the coma, in the near and middle infrared region (0.9-25 µm), identifying various ices, minerals, gases (e.g., H_2O, CO_2, CH_4 etc.).

DFP	Dust Field and Plasma package	Surveying ionized and dusty environments in the coma surrounding space environment, including magnetic field, electric field, plasma parameters (density, temperature, speed), distribution of electrons, ions, energetic neutrals, spacecraft potential, and cometary dust.

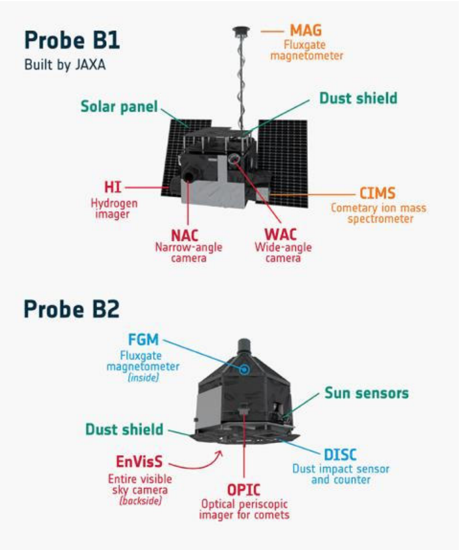

Figure 4. Instruments on Probe B1 and Probe B2

IV. SCIENCE-TECHNOLOGY SYNERGY

The camera aims to observe both the coma and the nucleus. Importanat heritage in the backgound comes from the Colour and Stereo Surface Imaging System (CaSSIS) [5] instument onboard Mars on the European Space Agency's ExoMars Trace Gas Orbiter (TGO) orbiter, and also form the detector system of the JANUS instrument from ESA's JUICE mission (Figure 5).

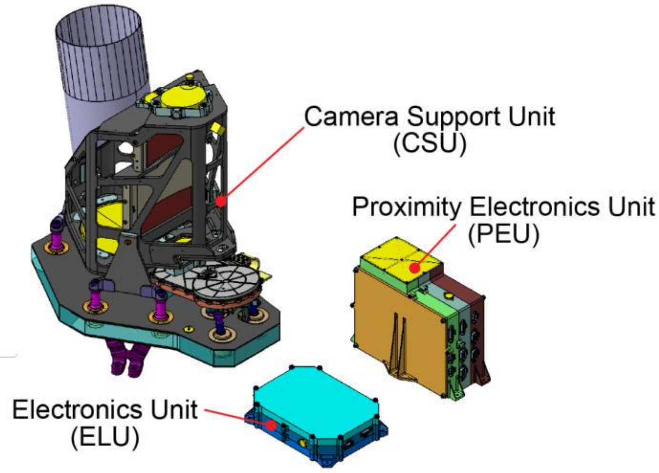

Figure 5. Main parts of the camera system (ESA)

The diameter of the camera main mirror is 135 mm, focal distance 875 mm, the optical systems project the 0.69° x 0.92° sized image to a 2000 x 1504 pixel sized E2V CMOS detector. The images are coded with 14 bites and could be recorded in a range of exposure times between 220 µs and 15 minutes. The data is recorded in the 256 Gb memory with ~120 Gb redundance.

A wide range of activities have been realized in the last years by the Hungarian contributors and will be continued till the production of the final probe. Among the works, the Digital Processor Module (DPM) breadboard was mostly finished (Figure 6), SDM, EM, EFM models have been tested, PFM model will be tested in 2024. Improvement of operational requirements and proposed sequence for CoCa are being done.

Parts procurement issues are present due to lead times but have been managed till now, with early procurement, close monitoring of the supplier and risk to consider. However, it is difficult to identify tradeoff between lead times, cost and parts quality. Prototyping was completed and based on the tests, new protection mechanism against, input voltage issues have been implemented. Radiation tests have been realized, leading to updated layout, electrical interface and redundancy were also updated.

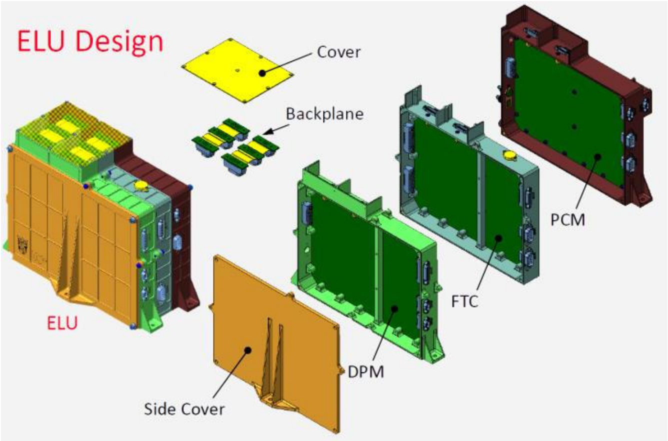

Figure 6. Structure and components of the Electronic Unit (ELU)

Regarding the synergy between scientific and engineering , among others activities have been recently realized such as specifcation of the 4 color filters based on former experiences with other comets was realized. Imaging of hypothetical nucleus with a different albedo and color, as well as of a coma optical recording were consedered and modelled, where even 10-time overexposure might happen and could be compensated for the nucleus.

The frequency of image creation was considered and selected, as well as the need regarding the target tracking where the smear should be below 1 px. Modeling of ideal image readout and compression methods were estimated for different target and observatonal conditions. Requirements for calibration was defined and various documents supporting the mission were made, including the compilation of the 110 page long Red Book for Comet Interceptor.

V. CONCLUSIONS AND OUTREACH

The Hungarian contribution to the CoCa and it's DPM are progressing according to the schedule and working on the Phase C-D currently. For scientific aspects recent results and the progress with the LSST supports the original aims, and a new aspect has also been emerged the possible visit of an interstellar object, even if it has a small chance but should be considered. For the technical realization the lead times become long in the last years might forced the designers toward further improved protocols. It also turned out that even if non-European suppliers provide some risk, it is difficult to avoid any non-European contribution in small parts. Regardless possible difficulties the companies were able to realize the work had to be done till now.

Further activities beside engineering works are panned to improve the scheduling of observations by simulations of various orbital parameters [6], recording under different illumination geometries [7] and expectations on surface reflectance from potential analogue simulant materials [8].

In order to support the teaching and public relations in scientific topics we advise the following public articles with respect to the Comet Interceptor Mission and research of comets related to the Hungarian space research: Tóth & Kereszturi [9, 10], Kereszturi [11], Szalai & Nagy [12].

ACKNOWLEDGMENT

The realization of DPM related to the CoCa instrument of is supported by the Ministry of Foreign Affairs and Trade through a PRODEX grant. The C-I contribution of mission coordinators Geraint H. Jones, (University College London), and Colin Snodgrass (University of Edinburgh), as well as the support from the former and current project managers: Kristin Wirth, Thomas Beck, Atakan Sirin are also acknowledged.

REFERENCES

[1] Snodgrass, C., Jones G.H. The European Space Agency's Comet Interceptor lies in wait. Nat Commun 10, 5418. 2019.

[2] Tóth, I., Az üstökösök megismerésének mérföldkövei 2. Üstököskutatás az űrkorszakban. Meteor Csillagászati Évkönyv 2016, szerk.. J. Benkő, A. Mizser, MCSE, Budapest, 2015, 243-281.

[3] Levison, H.F., Comet taxonomy. In. Completing the Inventory of the Solar System, Astronomical Society of the Pacific Conference Proceedings 107, Eds: T. W. Rettig and J. M. Hahn, 1996.pp. 173-191.

[4] Érdi, B. Égi mechanika. Csillagászat. Szerk.: M. Marik. Budapest, 1989. Akadémiai Kiadó, Szegedi Nyomda, 111-237.

[5] Thomas, N. at al: The Colour and Stereo Surface Imaging System (CaSSIS). Space Sci. Rev. (2017 issue). doi:10.1007/s11214-017-0421-1

[6] Halasz, H. 2022. "Üstökösmag megfigyelhetőség szimuláció a Comet Interceptor űrszondához." ELTE TTK, BSc thesis work.

[7] Penttilä, A., Palos, M., Näsilä, A., Kohout T. 2022. Blender modeling and simulation testbed for solar system object imaging and camera performance. 16th EPSC, id.EPSC2022-788

[8] Amiko, T., Naoya, S., Hideaki, M., Tomohiro, U., Takafumi, N., Pál, B., Takahiro I. 2020. Experimental study on thermal properties of high porosity particles for understanding physical properties of Phobos surface. JpGU-AGU Joint Meeting, PPS08-P01

[9] Tóth, I., Kereszturi, Á. 2022. Vadászat egy nagyon messziről érkező üstökösre. Új európai üstökösprogram magyar részvétellel (1. rész) Természet Világa Természettudományi Közlöny, 153. évf. 2022. június 6. sz., pp. 254-258.

[10] Tóth, I., Kereszturi, Á. 2022. Zöld utat kapott egy új európai üstökösprogram. Egy nagyon távolról érkező üstökös vizsgálatára (2. rész). Természet Világa Természettudományi Közlöny, 153. évf. 2022. július 7. sz., pp. 313-316.

[11] Kereszturi, Á. 2023. A Comet Interceptor küldetés. Fizikai Szemle, 73. évf. 2023. júl-aug. 7-8. sz. pp. 245-248.

[12] Szalai, S,, Nagy, J. 2023. Fejlesztések Naprendszer-kutatási missziókban. Fizikai Szemle, 73. évf. 2023. júl.-aug. 7-8. sz. pp. 267-274.

Spectral instrument optimization for asteroid missions by space weathering simulation

Ákos Kereszturi
Konkoly Thege Miklós Astronomical Institute, CSFK,
HUN-REN, Budapest, Hungary
e-mail: kereszturi.akos@csfk.org

Pál Bernadett
Konkoly Thege Miklós Astronomical Institute, CSFK,
HUN-REN, Budapest, Hungary
e-mail: pal.bernadett@csfk.org

Asteroid surfaces are heavily affected by space weathering effects. These cause darkening and reddening of the targets and diminishing of the infrared spectral bands of local minerals. Artificial simulation of meteorites was conducted by proton irradiation tests provided by HUN-REN ATOMKI (to mimic the space weathering consequences, with specific focus on mineral band changes of the irradiated NWA 10580 meteorite. Changes of olivine, pyroxene feldspar and spinel detectability was surveyed. Based on the findings: a detector with a resolution between 50 - 80 cm^{-1} could be sufficient to detect the main peaks of feldspar, spinel and pyroxene. The peak that remained observable the longest was the feldspar peak, which was indicated even at 115 cm^{-1} resolution.

Keywords—NWA10580; meteorite, space weathering, infrared spectra, detector resolution

I. INTRODUCTION

The aim of this work is to better understand how space weathering driven infrared spectral changes modify the observability of specific infrared spectral fingerprints of meteorite minerals, and using such knowledge to estimate which wavelengths and detector channel / filter arrangement support identification of heavily space weathered asteroid surfaces by next space missions with sophisticated detectors.

II. METHODS

A. Sample and irradiation

FA 11×8×2 mm sized thick section of the NWA 10580 CO3 chondrite meteorite was exposed to irradiation. It is a poorly weathered primitive meteorite, composed of forsteritic olivine, enstatite, and diopside, with small chondrules, few CAIs, sulphide blobs, engulfed in a fine-grained matrix. The plain surface was cut but not polished.

B. Used infrared detectors

The infrared spectroscopic measurements were done with a Vertex 70 FTIR spectrometer scanning 32 times for each measured site in the 400–4000 cm−1 range, with 30 s duration at 4 cm−1 spectral resolution. Later the Bruker Optics' Opus 5.5. software was used to manipulate the spectra. Minerals were identified by the RUFF Database and the Crystal Sleuth software [1], as well as by the relevant publications.

For the DRIFTS measurements a Praying Mantis diffuse reflectance accessor was attached to the Vertex 70 FTIR. The spectra of the bulk meteorite were recorded with spectral resolution of 4 cm−1, using sample scan time of 512 s.

C. Used irradiation facility

The space weathering simulating irradiation was done by 1 keV protons produced by the electron cyclotron resonance (ECR) ion source at HUN-REN ATOMKI (Institute for Nuclear Research) with three different levels of fluence values. These were: 10^{11} ion cm$^{-2,}$ 10^{14} ion cm^{-2}and 10^{17} ion cm^{-2} under vacuum conditions (pressure < 1×10^{-7} mbar).

D. Spectral coarsening

To simulate how a spectral detector with different resolutions would see the spectrum of the meteorite in question, we used a simple mathematical averaging method to artificially degrade the resolution of our data. The original resolution data was read in and then new wavenumber – reflectance values were calculated with the following formula:

$$x_d = \frac{\sum_{n=1}^{d} x}{d}$$

where x_d represents the new datapoint with the chosen resolution, x the original data point and d the degradation factor (or resolution divisor). The new wavenumber values were calculated similarly:

$$v_d = \frac{\sum_{n=1}^{d} v}{d}$$

where $ν_d$ stands for the wavenumber of the new datapoint and ν is the wavenumber of the original data point.

The resolution was recalculated in each step as:

$$res_d = v_d^1 - v_d^0$$

where res_d is the new reduced resolution, $ν^0_d$ and $ν^1_d$ are two consecutive wavenumber values.

We are also noting the resolution in wavelength ranges in the figures by converting the wavenumber to wavelength. In this work we are focusing on the wavenumber range from 1500 cm^{-1} to 600 cm^{-1}. When calculating the reduced resolution in wavelength, we took the difference between two consecutive wavelength-reflectance values at the beginning and at the end of the chosen wavenumber range.

III. RESULTS

A. *Mineral identification*

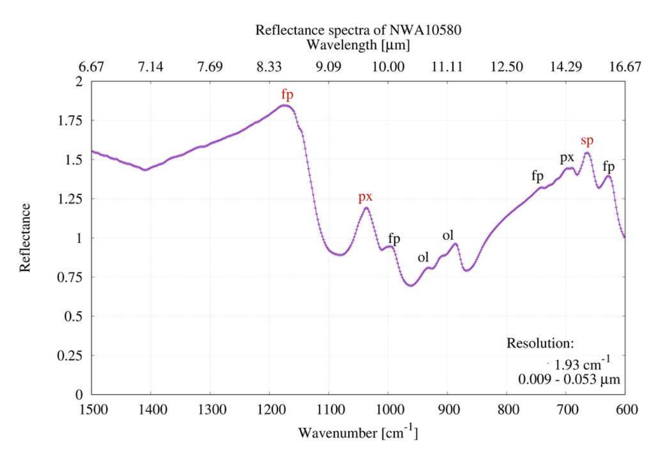

Fig. 1. *The original spectrum of the NWA10580 meteorite with a resolution of 1.93 cm^{-1}.*

The original spectrum of the NWA 10580 meteorite can be seen in Fig. 1. The main peaks of minerals are noted in red and minor peaks are noted in black. The used abbreviations for minerals through all figures are the following: fp – feldspar, px – pyroxene, ol – olivine, sp – spinel. In the original resolution dataset the main peaks of feldspar, pyroxene and spinel are visible, as well as three minor feldspar, two minor olivine and one minor pyroxene peaks.

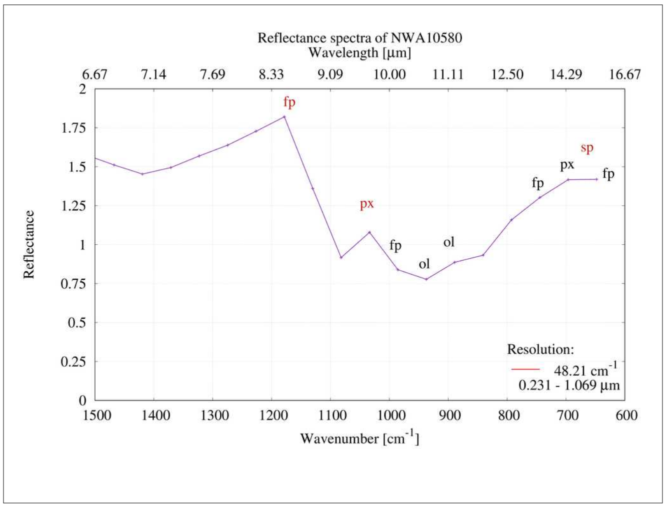

Fig. 2. *Degraded spectrum of the NWA10580 meteorite with a resolution of 48.21 cm^{-1}. The main peak of spinel disappears, along with the minor peaks of feldspar, olivine and pyroxene.*

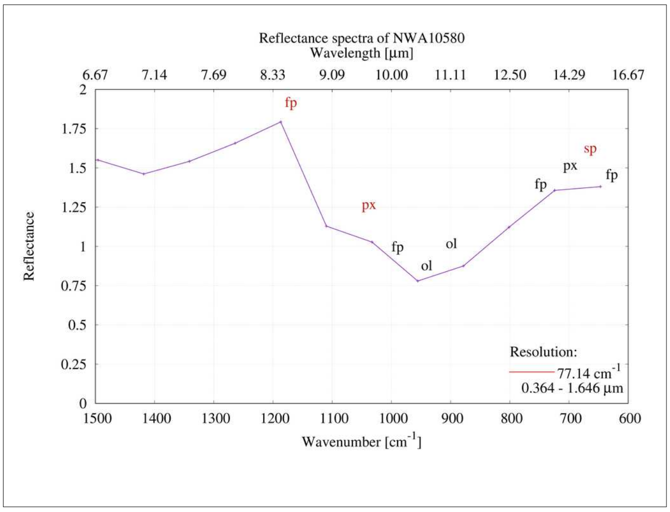

Fig. 3. *Degraded spectrum of the NWA10580 meteorite with a resolution of 77.14 cm-1. The main peak of pyroxene is not visible anymore.*

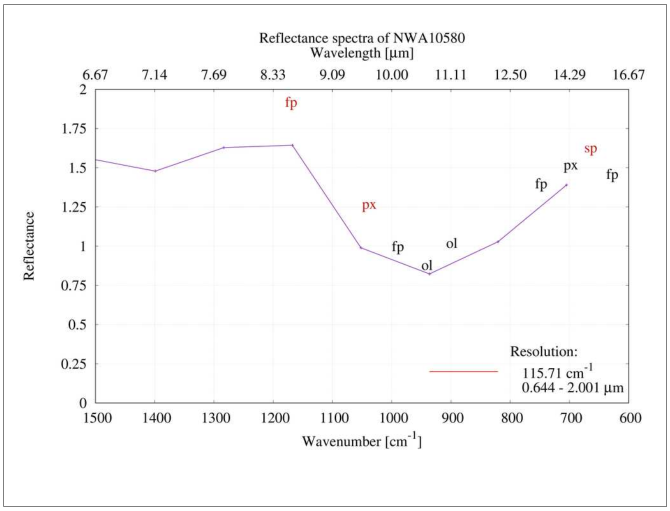

Fig. 4. *Degraded spectrum of the NWA 10580 meteorite with a resolution of 115.71 cm^{-1}. The existence of the feldspar main peak around 1180 cm^{-1} is indicated, but not clearly detectable.*

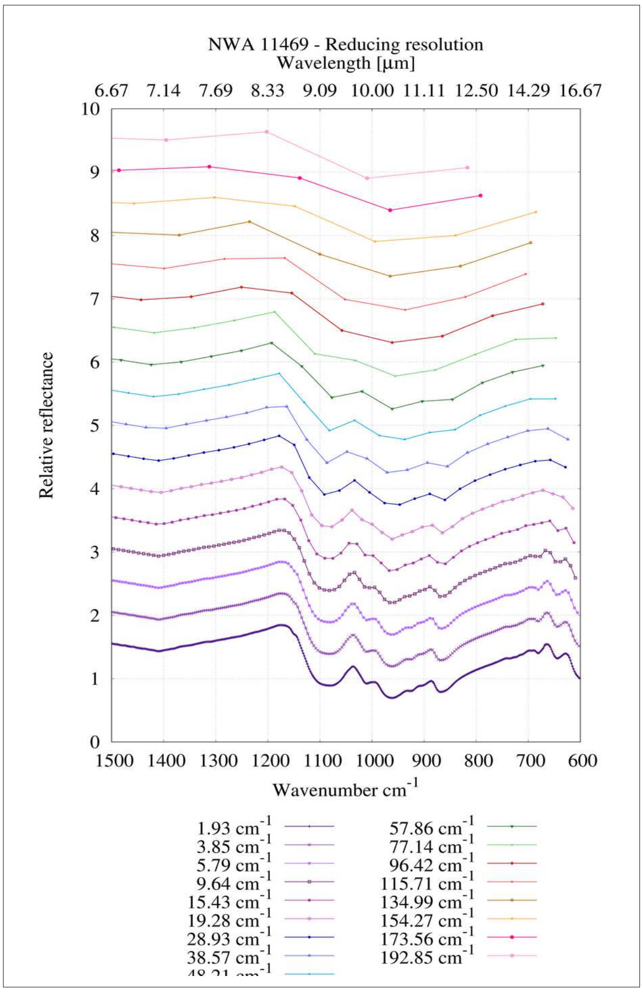

Fig. 5. *Reducing the resolution of the original NWA10580 meteorite spectrum with a resolution of 1.93 cm^{-1} (bottom) to 192.85 cm^{-1} (top). At the lowest resolutions no peaks remain observable.*

IV. DISCUSSION

In the original resolution data with a resolution of 1.93 cm^{-1} (Fig. 1) there are 3 main peaks and 6 minor peaks visible. As the resolution of the data is degraded we see these peaks gradually vanish. The minor peak of feldspar around 720 cm^{-1} and pyroxene around 690 cm^{-1} are the first to vanish. These are barely visible at 9.64 cm^{-1} resolution and not observable at lower resolutions.

At 19.28 cm^{-1} spectral resolution the minor peaks of feldspar around 990 cm^{-1}, olivine at 940 cm^{-1} and feldspar around 620 cm^{-1} are not observable anymore. The only minor peak that remains visible is the olivine peak around 890 cm-1, which disappears at 48.21 cm^{-1} resolution (Fig. 2). At this resolution the first main peak disappears, this is the spinel at around 660 cm^{-1}. However, as there is little data below 600 cm^{-1}, this is mainly due to mathematical averaging. If we had observations from lower wavenumbers, most likely this spinel peak would remain detectable at lower resolutions too.

The main peak of pyroxene around 1040 cm^{-1} disappears at 77.14 cm^{-1} resolution (Fig. 3.). The main peak of feldspar around 1180 cm-1 remains somewhat observable until 115.71 cm^{-1} (Fig. 4.), but the exact position of the peak is not clearly visible after the 77.14 cm^{-1} resolution. Fig. 5. shows the degradation process from the original resolution (bottom) to a resolution of 192.85 cm^{-1}(top).

V. CONCLUSION

The minor peaks of minerals disappear first, as expected, but the main peaks remain observable at lower resolutions as well (Tab. 1). Since the main peak of spinel vanished in our data mainly due to the degradation method, this peak might be visible with an actual detector that has a resolution around or better than 50 cm^{-1}. This resolution should be sufficient to detect the main peaks of feldspar, spinel and pyroxene. A detector with a resolution of approximately 70 cm^{-1} should still be able to detect the main peaks of feldspar and pyroxene, and a poor resolution around 115 cm^{-1} should still be enough to observe the existence of feldspar with an approximate peak position.

In this work, the potential for mineral identification of meteorites in the mid-infrared range was investigated as a function of spectral resolution, in order to evaluate the potential for similar observations of asteroid surfaces by future space missions. These results may be of particular relevance for cubesats, as this class of probes is increasingly involved in space missions. On-board low-cost infrared detectors on cubesats can provide optimal data if the location of filters or bands is carefully chosen.

TABLE 1: Observability of main (in bold) and minor mineral peaks in the degraded spectra. A + sign means observable, a – sign means not observable at the given resolution.

Resolution [cm^{-1}]	**Feldspar (1170 cm^{-1})**	Feldspar (993 cm^{-1})	Feldspar (745 cm^{-1})	Feldspar (625 cm^{-1})	**Pyroxene (1033 cm^{-1})**	Pyroxene (695 cm^{-1})	**Spinel (663 cm^{-1})**	Olivine (933 cm^{-1})	Olivine (892 cm^{-1})
1.93	+	+	+	+	+	+	+	+	+
3.85	+	+	+	+	+	+	+	+	+
5.79	+	+	+	+	+	+	+	+	+
9.64	+	+	+	+	+	+	+	+	+
15.43	+	+	-	+	+	-	+	-	+
19.28	+	-	-	-	+	-	+	-	+
28.93	+	-	-	-	+	-	+	-	+
38.57	+	-	-	-	+	-	+	-	+
48.21	+	-	-	-	+	-	-	-	-
57.86	+	-	-	-	+	-	-	-	-
77.14	+	-	-	-	+	-	-	-	-
96.42	+	-	-	-	-	-	-	-	-
115.71	+	-	-	-	-	-	-	-	-
134.99	-	-	-	-	-	-	-	-	-
154.27	-	-	-	-	-	-	-	-	-
173.56	-	-	-	-	-	-	-	-	-
192.85	-	-	-	-	-	-	-	-	-

ACKNOWLEDGMENT

This project was supported by the K_138594 project of NKFIH. The authors acknowledge the from the Europlanet 2024 RI which has been funded by the European Union's Horizon 2020 Research Innovation Program under grant agreement No. 871149. Z.J. is grateful for the support of the Hungarian Academy of Sciences through the János Bolyai Research Scholarship. The authors thank the work of Juhász Z., Gyollai I., Rácz R., Rezes D., Sulik B., Szabó M., Szalai Z., Szávai P. in this research project.

REFERENCES

[1] B. Lafuente, R.T. Downs, H. Yang, N. Stone 2016, The Power of Databases The RRUFF Project, eds. T. Armbruster, & R. M. Danisi (Berlin, München, Boston: De Gruyter)

An event-based hydrological model for arid/hyper-arid and Martian environment

Vilmos Steinmann
HUN-REN Research Centre for Astronomy and Earth Sciences
Konkoly Thege Miklós Astronomical Institute
Budapest, Hungary
steinmann.vilmos@csfk.hun-ren.hu

Eötvös Loránd University, Faculty of Science
Department of Physical Geography
Science Doctoral School of Earth Science
Budapest, Hungary

Abstract— **Understanding hydrological processes in extreme environments, such as arid and hyper-arid areas, is crucial for studying the evolution of Martian valley systems as part of planetary exploration. The aim of this research is to develop a raster-based hydrological model for this type of environment, capable of estimating the steady-state flow characteristics of the area under study. The model has been tested on the Zafit watershed, which is a sub-basin of the Zin basin in the Negev desert, Israel. This part of the Negev desert can be a potential Mars analogue field due to its low vegetation cover and arid climate. The model has been also tested on a Martain area, which can be found at the Oxia Planum region, which is the landing site of the ExoMars2020 rover mission. The model, which is built into and runs under the open source geoinformatics software QGIS, uses flow accumulation tool (targeting the catchment area) and surface-related environmental variables such as slope and aspect, as well as precipitation data for the study area. The results could support in-situ targeting of next Mars surface missions, identifying areas of sediment accumulation.**

Keywords—Mars;GIS;hydrology, discarge modelling

I. INTRODUCTION

Watershed modelling is a challenging task due to the wide range of factors that influence the results. It is not possible to perfectly represent the processes that occur, even under optimal conditions. Despite covering less than a third of the Earth's surface, arid regions can still experience heavy episodic rainfall events that are accompanied by flash floods [1]. Accurate hydrological models can help us to understand what happens on the surface during such an event and how it affects and changes the landscape. The prevailing hypothesis is that such events may have occurred during early wet periods on Mars. While there are significant differences between Earth and Mars, the mechanics of heavy rainfall and subsequent flooding are partly similar. By conducting measurements and modelling in desert Martian analogue regions, it is possible to gain insight into how Martian flood battlements and valleys may have formed.

The model presented here estimates various hydrological parameters, such as water depth and velocity, which are important parameters for surface evolution models, from the physical properties (e.g. slope, roughness) of the surface and a specific precipitation event. The model can be applied not only to terrestrial areas but also to other celestial bodies, such as Mars, and thus helps to understand the morphology of the valleys and channels mentioned above and the process of their formation, erosion, and accumulation.

The occurrence of liquid water on Mars is an important topic for decades, as there are signatures of old fluvial systems, lakes, and shorelines [2], but more recent surface features indicate flows [3] and modelling also support microscopic scale liquid water formation [4] by increased humidity [5], with the help of the deliquescence process [6, 7] even supported by brines [8]. Martian meteorites also indicate liquid water in the subsurface in the past [9]. Although the estimation of past volume and duration of existence of liquid water is important for past environment reconstruction for astrobiology research [10, 11], interpretation of recent [12], and planning of next missions [14].

II. METHODS

A. Description of the analysed areas

The Zafit sub-basin is situated within the Zin basin in the Israelian Negev desert. The sample area is located to the south of the Dead Sea (N-31°1' E-35°12'). The area is characterized by strong aridity, with an average annual rainfall of less than 100 mm per year. The geology of the area is dominated by dolomite and marly dolomite [14]. The study area covers 35 km^2, with the longest valley measuring 17 km [15]. The Zafit sub-catchment is an excellent analogue for the Martian surface in terms of morphology and climate (Fig 1, inset a).

The area of interest, designated as Oxia Planum, is situated on the planet Mars. This region was the landing site of the ExoMars2020 mission [16]. Previous studies have indicated that the area was once covered with water [20.], as evidenced by the presence of clay minerals and phyllosilicates. The area exhibits rare cratering, with no prominent valley or gully (Fig 1, inset b). Craters in the target area would have been influence the flow but their depressions were filled artificially in the DTM in order to provide a free path for the water runoff.

B. Workflow

The primary input parameter of the model is a digital terrain model (DTM). For the terrestrial sample area, a Shuttle Radar

Topographic Mission (SRTM) DTM [15] with a spatial resolution of 30 meters per pixel (m/px) was utilized. For the Mars sample area, a High-Resolution Imaging Science Experiment (HiRISE) DTM with a spatial resolution of 0.5 m/px was employed [16].

In the initial stage, the model determines the catchment area (A) value for each pixel based on the user-defined surface. This value is equal to the catchment area above each pixel. Next, the model estimates the flow depth from the specified rainfall amount (i in mm) and the time of the rainfall event (t in minutes) [17, 18] utilizing the following modified Manning's formula:

$$h = \left(\frac{\frac{\frac{i}{1000}A^{0.5}}{0.595t3600}n}{S^{0.5}} \right)^{3/2} \tag{1}$$

where n is the dimensionless Manning roughness factor, S is the Slope in radian.

In the subsequent stage, the model determines the flow velocity [19] values for each pixel based on the previously calculated water depth, using the Darcy-Weisbach method, which necessitates the specification of a friction factor. To calculate the friction factor, the D_{50} (median) grain size must be defined within the model [18]. A median grain size of 1 mm was specified in the test:

$$F_v = \left(\frac{8ghS}{F_b} \right)^{0.5} \tag{2}$$

where g is the gravity of the celestial body, F_b is the friction factor. The acceleration of gravity was adjusted to be 9.807 m/s^2 for the Earth sample site and 3.72 m/s^2 for the Martian sample site.

The flow discharge values were determined using the following equation:

$$Q_f = A_w F_v \tag{3}$$

where Q_f is the flow discharge in m^3/s and A_w is the wetted area of the flow. The wetted area of the flow can be calculated with multiplying the flow width and the flow depth. For simplicity, the flow width is equal with the spatial resolution of the given DTM.

III. RESULTS AND DISCUSSION

Both the terrestrial and Martian 10 minute long events were simulated with the following precipitation intensities: 10 mm, 20 mm, 35 mm, 25 mm, 15 mm, 5 mm. The average of the events used is 18.3 mm/hr, which is the average of the observed storm event that occurred on the terrestrial surface there.Unfortunately poor knowledge exists on the characteristics of possible early precipitation events on Mars as the valley networks are partly in degraded state [21], paleodischarge values [22] and other characteristics, including the duration of their active period [23.] are poorly constrained. But climate might have not been so warm as earlier suggested and probably short wet periods produced most of the valleys occasionally by sudden events [24], confirming the need for further model based estimations, like those presented in this work.

The model initially calculated the water depths associated with each rainfall event and then accumulated them to estimate the water depth for the entire event. The maximum water depth was 0.63 m for the Earth sample area and 0.38 m for the Mars sample area. The average water depth at the Zafit sub-catchment was 0.016 m while the Martian sample site was 0.0014 m (Fig 2).

Precipitation (mm)	**Table 1: Results of the individual and the cumulated precipitation events. Every individual event held 10 minutes.**	
	Average depth of flow (m)	
	Terrestrial area	*Martian area*
10	0.012	0.0012
20	0.018	0.0015
35	0.025	0.002
25	0.021	0.0018
15	0.015	0.0013
5	0.008	0.0006
Cummulative	0.1	0.008

A discrepancy is observed in the magnitude of precipitation events and cumulative water depths occurring over a 10-minute period, with the terrestrial and Martian regions exhibiting disparate values (Table 1).

The flow velocity and flow discharge are determined from the accumulated water depth data previously mentioned. For the terrestrial sample area, the maximum flow velocity is 1.32 m/s, while the average velocity is 0.44 m/s (Fig 4, inset a). For the Mars sample area, the maximum flow velocity is 0.77 m/s, while the average velocity is 0.26 m/s (Fig 3 inset a).

The maximum flow discharge value for the Martian sample area is 0.059 m^3/s, while the average flow discharge is 0.002 m^3/s (Fig 3, inset b). In contrast, the maximum flow discharge for the terrestrial sample area is 5.6 m^3/s, with an average value of 0.28 m^3/s (Fig 4, inset b).

A comparison of the flow depth values clearly demonstrates the distinction between the Earth and the Martian sample areas, despite the utilisation of identical precipitation values in the simulation (Table 1). The discrepancy in flow depth values can be attributed to the disparate or fragmented morphologies of the two study areas. In the terrestrial sample area, the majority of precipitation accumulates in a primary valley. In contrast, the Martian sample area exhibits a fragmented valley network devoid of prominent channel that could collect precipitation from the surrounding area..

A significant disparity exists in the flow velocity values between the two study areas. The maximum flow velocity value in the Earth sample area is approximately two times higher than the highest value measured in the Martian sample area. In both cases, the same roughness values were employed, and the slope conditions are comparable. However, due to the nearly one-third lower gravity on Mars, the flow velocity peaks are considerably lower.

IV. CONCLUSION AND FUTURE DEVELOPMENT

The model has been tested on two sample sites on two different celestial bodies. The terrestrial sample site is a hyper-arid area in the Negev desert in Israel, and the Martian sample site is a once waterlogged area rich in clay minerals in the Oxia Planum region, which is the landing site for the ExoMars2020 rover mission. During the test, water depth values were estimated from the same precipitation intensity data, from which flow velocity and flow discharge values can be further calculated. The model is currently only capable of operating in a steady state, which means that it cannot handle dynamically changing data over time. The primary goal for further development is to ensure that the model can handle such data. Another primary objective is to create a version of the model that is not only capable of hydrological analysis but can also estimate the rate and location of surface evolution and hence erosion and accumulation from existing hydrological and other data. As with hydrological modelling, this is a complex and multi-variable process, the first tests of which are currently underway.

The long-term objective is to construct a sophisticated model that can process time-series data in order to estimate hydrological variables and the associated surface-forming processes, regardless of the topography of the study area. Surface evolution models optimized for terrestrial conditions are not applicable or inaccurate in the Martian environment. However, on Mars it is also important to know the work of water and precipitation that was once present to shape the surface. Using erosion/accumulation data, the location of sediment transported and deposited by former flowing water can be more accurately determined and missions can be better targeted. Of course, there are models that can be applied to Mars, but those estimates are derived from calculations based on cross-sectional studies. The principal disadvantage of this approach is that it infers large catchments from small samples, which can result inaccuracies. In contrast, a raster-based model calculates variables over the entire area, considering differences in the catchment area due to surface variability, which can vary significantly even over relatively short distances.

ACKNOWLEDGMENT

This work is part of the PhD thesis of the author at ELTE university.

REFERENCES

[1] N.Weiler, Y.Avin, M.Rosensaft, L.Olsving-Whittaker, “Variations in hillslope runoff as detected using geological strata coupled with vegetation patterns-implication on spatially distributed desert runoff agriculture”,Journal of Landscape Ecology, Vol 10, 2017

[2] H. Hargitai et al. 2019. Evolution of the Navua Valles region: Implications for Mars' paleoclimatic history. Icarus 330, 91-102

[3] A. Kereszturi et al. 2011. Possible role of brines in the darkening and flow-like features on the Martian polar dunes based on HiRISE images. Planetary and Space Science 59, 1413–1427.

[4] A. Kereszturi & E.G. Rivera-Valentin 2012. Locations of thin liquid water layers on present-day Mars. Icarus 221, 289-295.

[5] B. Pál et al. 2018. Seasonal changes of near-surface relative humidity on Mars. EPSC2018-51.

[6] B. Pal 2019. Global distribution of near-surface relative humidity levels on Mars. 50th LPSC #1831.

[7] B. Pál & A. Kereszturi 2017. Possibility of microscopic liquid water formation at landing sites on Mars and their observational potential. Icarus 282, 84–92.

[8] B. Pál & A. Kereszturi 2021. Trends and key limiting factors of calcium perchlorate deliquescence on the surface of Mars. EPSC2021-162.

[9] I. Gyollai et al. 2023. Multiple generation magmatic and hydrothermal processes in a Martian subvolcanic environment based on the analysis of Yamato-000593 nakhlite meteorite. MAPS 58, 218-240.

[10] H.G. Changela et al. 2021. Mars: New insights and unresolved questions. International Journal of Astrobiology 20, 394-426.

[11] M. Marschall et al. 2012. Migrating and UV screening subsurface zone on Mars as target for the analysis of photosynthetic life and astrobiology. Planetary and Space Science 71, 146-153.

[12] B. Pal & A. Kereszturi 2020. Annual and daily ideal periods for deliquescence at the landing site of InSight based on GCM model calculations. Icarus 340, 113639.

[13] C. Orgel et al. 2014: Scientific Results and Lessons Learned from an Integrated Crewed Mars Exploration Simulation at the Rio Tinto Mars Analogue Site. Acta Astronautica 94(2), 736–748.

[14] Y.Rinat, F.Marra, M.Armon, A.Metzger, Y.Levi, P.Khain, E.Vadislavsky,M.Rosensaft, E.Morin,”Hydrometeorological analysis and forecasting of a 3d flash-flood-triggering desert rainstrom”, Natural Hazard and Earth System Sciences, Vol 21, 2021.

[15] T.G.Farr, M.Kobrock, “Shuttle Radar Topography Mission procedures a welth of data”, AGU,2000.

[16] Y.Tao, J-P. Muller, S.J. Conway, S.Xiong, “Large Area High-Resolution 3D Mapping of Oxia Planum: The Landing Site for the ExoMars Rosalind Franklin Rover”, Remote Sensing, Vol 13, 2021.

[17] H. Mitasova, C.M.Barton, I.I.Ullah, J. Hofierka, R.S. Harmon, “Gis-based soil erosion modeling” Remote Sensing and GIScience in Geomorphology, edited by J. Shroder and M.P.Bishop, pp228-258,2013.

[18] M.G. Kleinhans, H.E. van der Kasteele, E. Hauber, “Paleoflow reconstruction from fan delta morphology on Mars”, Earth and Planetary Science Letters, Vol 294, pp 378-392, 2010.

[19] M.G.Kleinhans, “Flow discharge and sediment transport models for estimating a minimum timescale of hydrological activity and channel and delta formation on Mars”, Journal of Geophysical Research, Vol 110, Issue E12, 2005.

[20] Quantin-Nataf C, Carter J, Mandon L, Thollot P, Balme M, Volat M, Pan L, Loizeau D, Millot C, Breton S, Dehouck E, Fawdon P, Gupta S, Davis J, Grindrod PM, Pacifici A, Bultel B, Allemand P, Ody A, Lozach L, Broyer J. Oxia Planum: The Landing Site for the ExoMars "Rosalind Franklin" Rover Mission: Geological Context and Prelanding Interpretation. Astrobiology. 2021 Mar;21(3):345-366. doi: 10.1089/ast.2019.2191. Epub 2021 Jan 5. PMID: 33400892; PMCID: PMC7987365

[21] Baker, V.R., Partridge, J.B., Small martian valleys: pristine and degraded morphology. J. Geophys. Res. 91, 3561–3572, 1986.

[22] Irwin, R.P., Craddock, R.A., Howard, A.D., Interior channels in Martian valley networks: discharge and runoff production. Geology 33 (6), 489–492, 2005.

[23] Kereszturi, A.,. Review of wet environment types on mars with focus on duration and volumetric issues. Astrobiology 12 (6), 586–600, 2012

[24] Kite E.S., Rafkin S., Michaels T.I., Dietrich W.E., Manga M. . Chaos terrain, storms, and past climate on Mars. JOURNAL OF GEOPHYSICAL RESEARCH, VOL. 116, E10002, doi:10.1029/2010JE003792, 2011

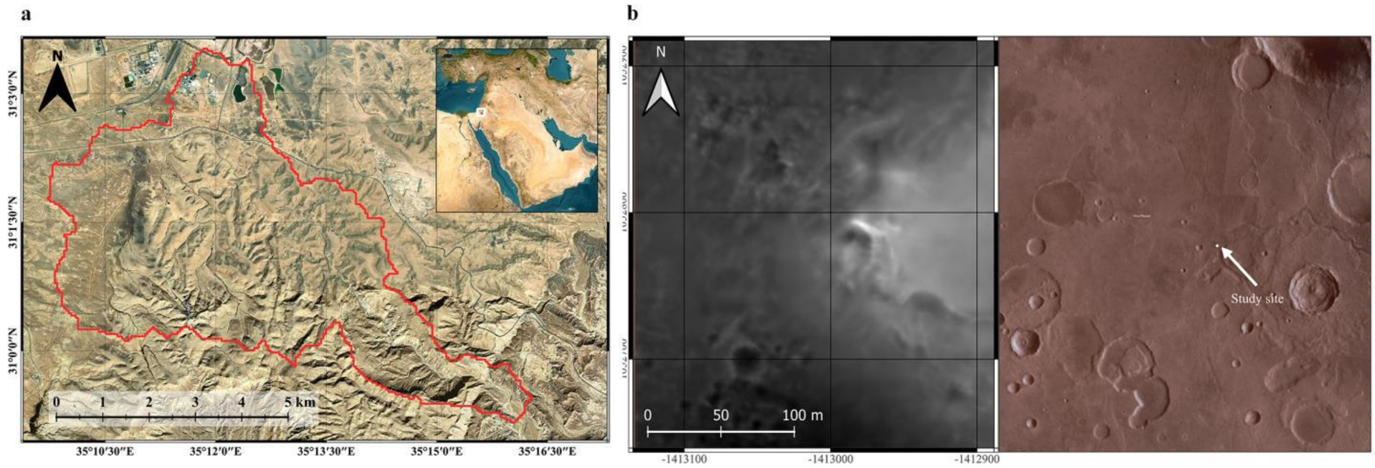

Fig 1: Overview of the analyzed areas. Inset a shows the terrestrial area, inset b shows the Martian area of interest.

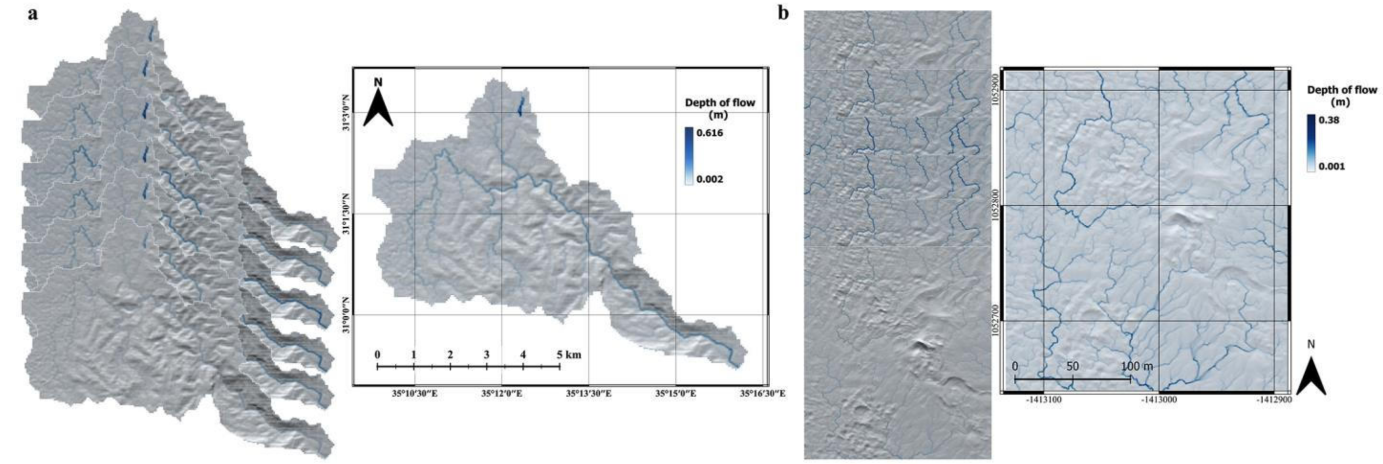

Fig 2: Results of flow depth estimation. The left side of inset a shows the sub-results of the different rain intensities, the right side of inset a show the accumulated flow depth of the terrestrial area. The left side of inset b shows the sub-results of the different rain intensities, the right side of inset b show the accumulated flow depth of the Martian area.

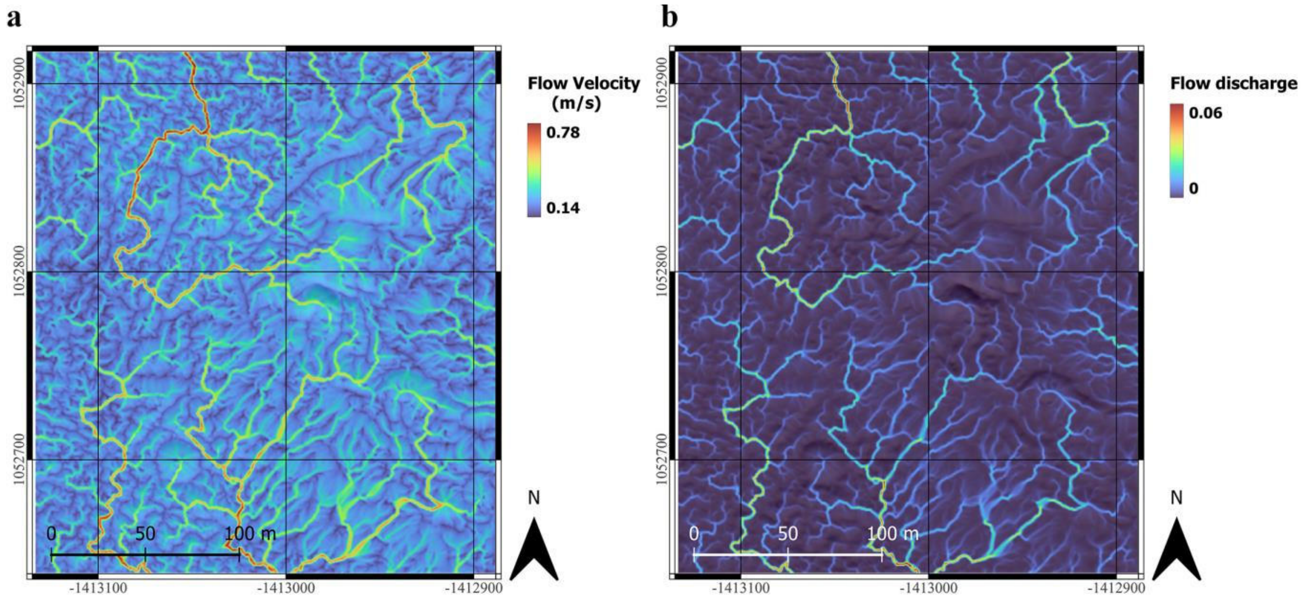

Fig 3: Results of flow velocity (inset a) and flow discharge (inset b) estimation on the Martian area of interest.

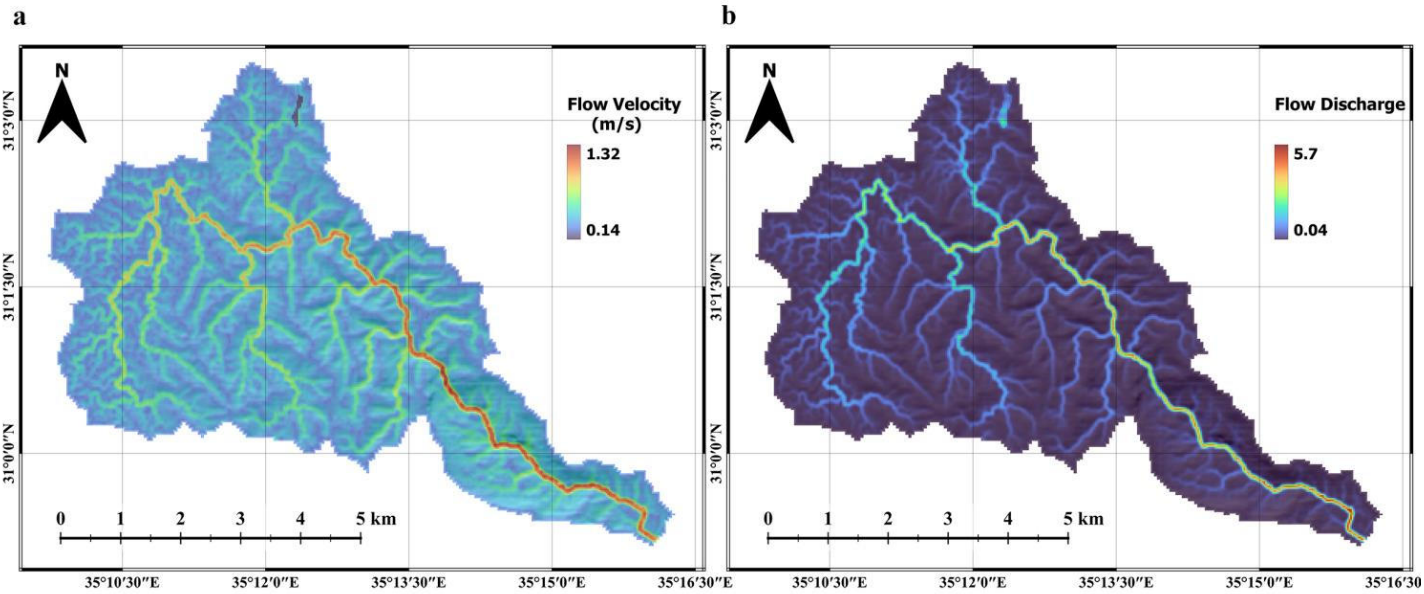

Fig 4: Results of flow velocity (inset a) and flow discharge (inset b) estimation at the terrestrial area of interest.

Space Debris: Overview and Mitigation Strategies

Mohammed Vaseeq Hussain Khan
Department of Aerospace Engineering
Amity University Dubai
Dubai, United Arab Emirates
vaseeqhkhan@gmail.com

Efstratios L. Ntantis
Department of Aerospace Engineering
Amity University Dubai
Dubai, United Arab Emirates
entantis@amityuniversity.ae

Abstract—**The space industry has experienced exponential growth since humanity's inaugural foray into space over six decades ago, heralding a new era of technological prowess and scientific achievements. However, this progress has brought forth significant challenges, chief among them being the proliferation of space debris. Advancements in rocket technology have led to reduced launch costs, resulting in an extensive network of more than 9,000 active satellites orbiting the Earth. Yet, alongside these operational satellites, approximately 12,000 trackable and an estimated 1 million non-trackable space debris objects exist, including defunct satellites, all hurtling through space at extreme velocities. This debris poses grave threats to functioning satellites, spacecraft, and astronauts, with frequent collisions exacerbating the issue by generating further debris. As nations and private entities intensify their investments in space exploration, the impending deployment of mega-constellations raises concerns of triggering the Kessler Syndrome—a chain reaction of collisions rendering Low Earth Orbit impassable. This paper critically evaluates existing literature on space debris, scrutinizing its origins, associated risks, and the prevailing legal frameworks governing debris mitigation. It underscores the imperative of international collaboration to safeguard the sustainability of our celestial environment, particularly amidst the surge of planned mega-constellations. Various active debris removal techniques, such as laser-based removal, net capture, harpooning, and passive methods like Drag Augmented Sails, are investigated for efficacy and feasibility within current technological constraints. Moreover, regulatory measures are analyzed to underscore their role in complementing technological innovations and fostering international cooperation. A holistic approach integrating regulatory frameworks, collaborative efforts, and technological advancements is advocated to address the escalating threat of space debris and ensure the long-term viability of space exploration endeavors. In summary, this paper offers a comprehensive examination of the space debris landscape, its perils, and a spectrum of mitigation strategies geared toward preserving the integrity of space exploration.**

Keywords—space sustainability, space pollution, space industry, Kessler syndrome, debris removal

I. INTRODUCTION

Humanity's first venture into the vast unknown of space began in 1957 when the Soviets launched the first artificial satellite, Sputnik 1. Over the past six decades, about 6,500 rockets (excluding failures) have been launched, placing about 16,990 satellites in Earth's orbit. Of these 16,990 satellites, roughly 11,500 are still orbiting in space, while just 9,000 are still functioning [1], highlighting the importance of effective satellite management and utilization [2]. Forecasts depict scenarios of high demand, base-case demand, and low demand. In the base case alone, an anticipated 27,000 active satellites will be in orbit by the end of 2030, almost a threefold increase from today. To maintain that number at the assumed lifespan, 4,000 to 5,000 satellites must be launched annually [3].

The exponential rise in satellite launches can be primarily attributed to increased cost efficiency. The cost of space launch has been substantially reduced due to constantly evolving technology. This expands opportunities to exploit space for commercial users, the military, and space agencies [4]. The remarkably swift progression of space exploration is nothing short of fascinating, but it is accompanied by dangerous by-products that are commonly overlooked, namely space debris. As the number of satellites constantly increases, so does the probability of collisions between other satellites or space debris. Maintaining sustainability in the Earth's orbit is vital to allow safe space operations and minimize the risk to interplanetary exploration efforts. Space traffic management and debris mitigation form a critical pillar to ensure the increasing use of space remains safe and sustainable. All spacefaring nations and organizations need to acknowledge that Earth's orbits are the pathway to the unknown beyond, and it must be kept open and safe if we wish to continue in our exploration. Mitigating space debris is imperative to achieve sustainability in Earth's orbit.

II. CURRENT LANDSCAPE

In the early days of space exploration, space debris was not paid much attention, with nations prioritizing short-term advantages over long-term shared goals. The prevailing belief was that the vast expanse of space could accommodate all objects without reaching capacity. However, as the foray into space deepens, acknowledging and addressing the issue regarding space debris is of utmost importance. This issue is becoming increasingly pertinent as private space ventures prioritize profitability over the responsible and sustainable use of space. Megaconstellations, particularly large satellite networks like SpaceX's Starlink and Amazon's Kuiper, are driving a rapid increase in the number of satellites orbiting Earth. These systems promise to revolutionize global communication but come with the significant downside of increased congestion in Low Earth Orbit (LEO). With SpaceX alone planning over 42,000 satellites, the risk of accidental collisions rises substantially, jeopardizing the safety of space operations [5].

By definition, space debris is "all man-made objects, including fragments and elements thereof, in Earth orbit or re-entering the atmosphere, that are non-functional" [6].

Space debris can generally be classified into three groups: small objects smaller than 1cm, medium objects of 1-10 cm, and large debris greater than 10cm [1]. Small debris objects are challenging to track and numerous but relatively easy to shield against. Medium Debris objects have a large population, making keeping track of them all very demanding. They are difficult and expensive to protect against. Large debris objects are relatively smaller in number and are regularly tracked by entities like the European Space Agency (ESA) and the Space Surveillance Network (SSN). Satellites cannot defend against these objects and must perform avoidance maneuvers.

The problem of space debris is essentially one of pollution since we actively pollute the orbital environment via our orbital activities. This issue has persisted since the very beginning, when we used to discard spent rocket stages, bolts, screws, and other elements when stage separation was occurring. Additionally, there have been cases where astronauts have lost tools and equipment during space walks [7]. Furthermore, non-operational satellites also contribute to the space debris ecosystem.

Space debris mostly populates regions with active satellites, and these orbits are:

- Low Earth Orbit (LEO): Up to 2000km above Earth's surface
- Medium Earth Orbits: 19000-23000 km above Earth's surface
- Geostationary Orbit (GEO): Around 36000 km above the Equator

Objects in LEO typically experience some level of atmospheric drag due to their proximity to Earth. This means that as the object falls closer to Earth, the heat generated due to friction with air molecules will incinerate it. However, if the object is too large to be burnt, it is bought down at Point Nemo, also known as the “Oceanic Point of Inaccessibility”. It is the most remote location in the world’s oceans, inaccessible to the general public. This is done to avoid the satellite potentially causing harm to the surrounding population where it lands. It is estimated that Point Nemo houses 264 retired spacecraft [8].

Satellites in geostationary orbits cannot be brought down to Earth and must be 'pushed back' to a higher orbit, the graveyard orbit, situated about 300km above GEO, to prevent interference with the functioning of operational GEO satellites [9].

Space debris can range in size from minuscule paint flecks to massive metal chunks. Since the first satellite launch in 1957, there has been more debris in orbit than operational satellites.

According to information released by the Space Debris Office of ESA (last updated on December 6, 2023), the total mass of all space objects in Earth's orbit exceeds 11,500 tons. It is estimated that around 130 million pieces of trim, untraceable debris, and over 1,000,000 medium-sized space debris objects exist [1].

Previous research shows that at least five large debris objects must be removed from orbit annually to stabilize the space debris situation. This conservative estimate presumes optimal conditions where no incident explosion occurs and post-mission disposal achieves a success rate of over 90% [10]. However, this conservative estimate predates the advent of mega-constellations, suggesting that the actual requirement may now be significantly higher, given the current and planned proliferation of satellites in Low Earth Orbit.

III. DANGERS OF SPACE DEBRIS

In 1978, a NASA scientist named Donal J Kessler described a phenomenon involving a self-sustaining cascading collision involving space debris. Essentially, two objects that collide in space break up into smaller fragments, and these smaller fragments collide with other objects, thus forming more debris. This cycle continues until Earth's orbit is filled with impassable debris, consequently confining humans to Earth. This effect was dubbed "The Kessler Syndrome" [11].

This theory has gained traction in recent years, mainly due to the growing interest in space operations in organizations, such as plans for constellations from significant companies like SpaceX, Amazon, and Apple. These constellations could act as catalysts for the scenario described in the Kessler Syndrome, raising concerns, mainly due to the lack of steps to mitigate and remediate existing and new space debris.

For instance, the accidental collision of American and Russian satellites, Iridium 33 and Kosmos 2251, in 2009 and the deliberate destruction of the Chinese Fengyun-1C spacecraft in 2007 alone have increased the sizeable orbital debris population in LEO by approximately 25%, posing more significant collision risks for spacecraft operating in low Earth orbit [12]. Additionally, Anti-Satellite (ASAT) tests are one of the most damaging contributors to space debris, as they deliberately destroy functioning or defunct satellites, creating thousands of debris fragments. The United States has also conducted ASAT tests, most notably in 2008 with Operation Burnt Frost, where the USA-193 satellite was intercepted to prevent it from crashing back to Earth [13]. In 2019, India conducted Mission Shakti, a test that destroyed one of its satellites, generating significant concern about the escalation of space debris risks [14]. Such tests dramatically increase the density of debris in LEO and further complicate efforts to sustain a debris-free orbital environment.

Furthermore, it is estimated that over 640 cases of explosions, collisions, break-ups, or anomalous events lead to fragmentation, and this number only accounts for the objects we can keep track of. The actual number is bound to be higher if we take smaller or unidentified objects into account as well [1]. Furthermore, over 11 non-deliberate fragmentations have occurred in the space environment over the past two decades, contributing to the increasing number of space debris in orbit [15].

Most "space junk" is moving extremely fast and can reach 18,000 miles per hour, dubbed hypervelocity, which is almost seven times faster than a bullet. Due to the rate of speed and volume of debris in Low Earth Orbit (LEO), current and future space-based services, explorations, and operations pose a safety risk to people and property in space and on Earth. For instance, numerous space shuttle windows were damaged by what was found to be tiny flecks of paint [16].

Crewed spacecraft such as the International Space Station (ISS) face this threat. The ISS can shield itself against particles up to 3mm in size using Whipple shields comprising multiple layers. The first layer breaks apart the debris object into fragments. The second layer breaks these fragments into even smaller ones until the fragments become too small to penetrate further layers [17].

However, almost 670,000 pieces of orbiting space debris 1-10cm big can destroy the onboard shielding system and penetrate the ISS's body [18]. The only way to avoid these is to perform avoidance maneuvers, which prove to be high economic burdens, especially considering spacecraft have limited propellants. Between 2010 and 2014, two European meteorological satellites had to perform five avoidance maneuvers to avoid fatal collisions with space debris [19]. The annual cost of losses due to space debris in 2020 alone was roughly $100 million, projected to rise only from here on out [20]. Microwave Electrothermal Propulsion Systems (MEPS) present a promising, relatively cost-effective prospect for satellite propulsion, offering a potential solution for precise maneuvering to avoid collisions with space debris. By effectively converting electrical energy into thrust, MEPS could facilitate the adjustment of spacecraft trajectories to navigate safely amidst the hazards of space debris, potentially minimizing the need for excessive propellant consumption [21].

IV. THREATS TO SCIENTIFIC RESEARCH DUE TO SPACE DEBRIS

The number of active space entities globally, including nations, private companies, and ventures, is continually increasing, meaning that the number of spacecraft, and subsequently the amount of space debris, is also growing. This increase collectively causes some degree of light pollution. Though the interference caused by large, active satellites may not disrupt astronomical observations much, only appearing as light streaks in the sky, the cumulative effect of millions of debris pieces has the potential to have a much more significant impact. Spread-out debris clouds can cause noise by reflecting and scattering incoming light waves, increasing the overall sky brightness to levels similar to urban centers. However, this increase in sky brightness is not limited to urban regions and will cover the entire globe. If the number of debris in orbit keeps increasing, it could become practically impossible to find Bortle One skies except in highly remote locations during deep winter nights [22].

Additionally, growing space debris poses severe threats to our scientific endeavors, such as the ISS and Hubble telescope, which can impact all the subsequent research we can only perform in those environments. Suppose we reach the tipping point, and our orbits become unusable. In that case, we will lose the opportunity to continue using the existing infrastructure to learn more and lose the potential to send any replacement [23].

Furthermore, the proliferation of space debris and the advancement of the Kessler Syndrome could endanger access to Lagrange points, vital for conducting various scientific endeavors such as deep space observation or asteroid observation [24].

V. LEGAL REGULATIONS CONCERNING SPACE DEBRIS

As of the time of this paper, there are no internationally enforced space laws to clean up debris in our orbits. Numerous legal and geopolitical challenges present themselves regarding active debris removal.

From a legal perspective, the Outer Space Treaty of 1967 and the Liability Convention of 1973 establish a robust framework regarding ownership rights over space objects. These treaties specify that no nation can salvage or retrieve space objects belonging to another country without explicit consent from the registered national owner. Security concerns are also relevant since debris retrieval entails sharing potentially sensitive information regarding the object's designs, implicating foreign policies and intellectual property rights [19].

Additionally, uncertain financial accountability further complicates the landscape for active debris removal, mainly because many debris are not traceable back to a specific object or fragmentation level. This adds another layer of complexity to the legal circumstances of debris removal, contributing to a sense of reluctance within the space community to undertake space debris removal options. This leads to the debris population within our orbits simply rising.

LEO, in particular, is now viewed as the World's largest “space junk zone”. Removing space debris from LEO is expensive because the problem of space junk is vast—there are nearly 6,000 tons of materials in LEO alone [22]. To curb the escalation of space debris, all newly launched satellites in LEO must incorporate a mechanism for controlled re-entry, ensuring their destruction within 25 years following the cessation of operations [25].

Space junk is not one country's responsibility but the responsibility of every country with spacefaring ambitions. The problem of managing space debris is both an international challenge and an opportunity to preserve the space environment for future space exploration missions [26].

To this end, numerous voluntary standards and guidelines have already been formulated, mirroring the national legislation and documentation of space agencies:

- Inter-Agency Space Debris Coordination Committee (IADC) Space Debris Mitigation Guidelines, 2021 [25].
- The European Code of Conduct for Space Debris Mitigation [25] was written and approved by five European agencies [27].
- Space Debris Mitigation Guidelines by the UN Committee on the Peaceful Uses of Outer Space [28].
- Recommendation of the International Telecommunication Union ITU ITU-R S.1003 "Protection of the geostationary satellite orbit as an environment".
- Space Debris Mitigation Guidelines and Regulatory Framework of the UAE Space Agency [29].
- ISO 24113 "Space systems: Space debris mitigation requirements" [30].

The IADC Space Debris Mitigation guidelines, resulting from the collaboration of 13 spacefaring nations, have served as a base for all the documents above. According to recommendations from the IADC guidelines, every organization must develop a Space Debris Mitigation Plan when developing a new spacecraft or mission. This document must include the following components:

1. Space Debris Mitigation Management Plan.
2. Plan to assess and mitigate risks related to space debris, applying relevant standards.
3. Disposal plan for spacecraft/orbital stages.
4. Measures highlighting any hazards that could generate space debris.
5. Justify choices when alternative options are available.
6. Compliance matrix addressing the Guideline recommendations.

The International Organization for Standardization (ISO) has been publishing a list of standards for space debris mitigation since 2010. In particular, the ISO 24113 document, which outlines the space debris mitigation requirements, has had a third edition published in 2019. This edition has enforced stricter requirements to guide countries and organizations in their space endeavor [31]. Most notably, limitations more stringent on the ejection of slag from solid rocket motors, limiting the number of debris objects released by a launch vehicle, and collision avoidance systems in satellites were made necessary. These standards will continually evolve to reflect the fast-paced changes shaping the space industry. ISO 24113 has a revised edition published in 2023, and all space industry members must operate while observing the set standards [32].

The European Space Agency (ESA) recently launched the ‘Zero Debris Charter,’ which aims to ensure that no new debris is generated from space missions by 2030. This initiative minimizes debris creation during satellite operations and actively removes existing debris. The charter reflects a bold step toward international collaboration and sustainable space exploration, emphasizing that future missions must prioritize the long-term health of the orbital environment [33].

A significant milestone in space regulation occurred when the Federal Communications Commission of the United States fined DISH Network for improperly disposing of their retired satellite, EchoStar-7, to a designated graveyard orbit. The FCC's imposition of a $150,000 fine underscores the increasing importance placed on responsible space management and planning and the enforcement of regulatory measures to mitigate the proliferation of space debris [34].

VI. SPACE DEBRIS MITIGATION

Space debris mitigation can be categorized into short-term and long-term risk reduction strategies. Short-term mitigation involves spacecraft executing Just-in-time collision avoidance maneuvers to minimize the likelihood of impact and subsequent debris generation. However, this approach does not address the underlying long-term risk of collisions. Long-term space debris risk reduction encompasses active debris removal, space debris remediation measures, the deliberate de-orbiting of decommissioned satellites into the Earth's atmosphere, or the relocation of debris or satellites to designated graveyard orbits. The space community is reluctant when it comes to implementing active debris removal methods, and this reluctance stems from four factors, as highlighted in [35]:

- High costs of missions. It is estimated that for satellites intended for geostationary orbits, 5-10% of the mission cost is attributed to debris protection and mitigation systems, and the percentage is even higher for satellites in LEO [19].
- Legal complexities involve ambiguity regarding ownership and access rights to manipulate/remove space objects registered with other countries physically.
- Lack of consensus on target selection.
- Potential for unintentional further debris generation during attempts at debris removal.

Despite these challenges, there is a growing awareness within the space community regarding the urgency of space debris mitigation. As a result, concentrated efforts are being made to explore and implement various methods to reduce the proliferation of space debris.

A. Drag Augmented Sails (DAS)

This method of space debris remediation offers a practical and effective manner for small satellites in LEO to operate sustainably. This involves including a compact sail that can be installed onto the satellite. Once the satellite reaches the end of its mission, the sail is deployed. This causes an increase in the area-mass ratio of the satellite with a minimal increase in the satellite's mass, thereby causing an increase in drag. This causes a reduction in the satellite's orbital speed and accelerates the satellite's re-entry into the atmosphere, where it can burn up. A functional advantage of DAS is that it requires no power or fuel. However, research is needed for the sail material, which should be capable of withstanding collisions with orbiting space debris.

Although the 25-year deorbiting timeframe is an arbitrary guideline set by space debris mitigation standards, research suggests that satellites in a 650-700 km orbit can de-orbit naturally within this period, provided they have a typical area-to-mass ratio (0.005 to 0.015 m^2/kg) [36]. However, by using drag augmentation sails (DAS) with an increased area-to-mass ratio (0.1 m^2/kg), the re-entry times of satellites at altitudes up to approximately 800 km can be significantly reduced, helping to meet the goal of minimizing the remaining orbital lifetime after a satellite's operational phase is completed.

The most effective application of a drag sail is at altitudes up to 950km. However, beyond this threshold, the necessary drag area for de-orbiting becomes impractically large, particularly for heavier satellites. For instance, to facilitate the de-orbiting of a one-ton satellite from an altitude of 1000km within a 25-year timeframe, a drag sail measuring at least 20m by 20m would be required [37]. Three drag sails were designed and manufactured by Cranfield University and are currently onboard three orbiting satellites [38].

B. Laser-Based Systems

This is a prospective solution for creating a just-in-time collision avoidance system. It involves heating a space debris object by aiming a powerful ground-based or space-based laser at it. This laser vaporizes the surface layer of the debris. This forms plasma and an exhaust plume, which leaves the surface of the debris at sufficient velocities to change the object's trajectory. This method is one of the few suitable for debris objects with dimensions less than 10cm in the LEO. However, there is a risk of generating additional debris via this method. Additionally, accurate target acquisition and tracking technology is required to carry out these operations safely. However, international concerns about the potential development of a "space weapon" restrict how freely countries can research such technology [39].

The Laser Ablative Debris Removal by Orbital Impulse Transfer (L'ARDOIT) project is based on the ablation effect. It involves an active spacecraft in LEO equipped with a 100ps ultraviolet pulse laser that can affect objects up to 25 km away. The spacecraft also features an advanced optics system capable of detecting and identifying objects at a distance of 600 km, ensuring that only confirmed debris is targeted for removal. However, further research and development are needed to improve the accuracy of distinguishing space debris from active satellites or other operational objects in orbit. [40].

C. Net Capture Method

The active space debris removal method involves deploying a chaser satellite with a net installed. The net will have flying weights attached to each corner, called bullets, which wrap around the target once they come in contact. The chaser satellite tracks and follows a designated space debris object then launches a net to capture the target object. This process has three key steps: net deployment, target capturing, and target de-orbiting. This method has various inherent advantages associated with it. For instance, it allows for the flexibility to capture debris of varying shapes or dimensions. Additionally, this method allows for a relatively large distance to be maintained between the chaser satellite and the target, reducing the likelihood of a collision between the spacecraft and the debris. This solution can be applied only within LEO, wherein the net can burn up along with the debris upon atmospheric re-entry [39].

The LEO technology was successfully demonstrated in 2018 via the in-orbit space debris removal mission RemoveDEBRIS. The DebrisSat1 released a target Cubesat with inflatable boons reaching 1m in diameter. The target was designed to better represent a space debris object. This target was caught with a 5-meter net made with high-strength fibers and deployed with concentric weights and a central cover. After successfully capturing the target, motors and winches installed in the weights are used to close the net. However, further investigation is required into methods for disposing of the captured debris [41].

D. Harpoon Method

This solution is similar to the net capture solution; however, it uses a harpoon instead of a net. It involves a chaser satellite tracking a target and then firing a harpoon to penetrate and anchor onto the target. The harpoon is towed and can be pushed to the graveyard orbit or pulled in for atmospheric re-entry. Due to the relatively low mass and size of harpoons, multiple harpoons can be installed on a single host spacecraft.

This method can capture non-cooperative or tumbling debris or debris with irregular shapes that may be unapproachable with other mitigation methods. The critical challenge of using the harpoon method requires precise targeting and accuracy while hitting the target. This is to prevent the generation of any new debris in the process. Due to this, the harpoon method is unsuitable for debris with high tumbling rates since the risk of generating new debris is too high. However, experiments conducted by the ESA indicated that for capturing objects spinning up to 6deg/s, the generation of new debris is minimal and internalized within the target object [42]. Additionally, a harpoon hitting a space debris object can significantly alter its rotational parameters, so carefully choosing the point at which it is fired is crucial.

The possibility of using a harpoon tether system was experimentally explored in orbit as part of the RemoveDEBRIS mission, in which a square aluminum honeycomb panel was successfully pierced from a distance of 1.5m. However, as for the net, further investigations are required to assess the best methodology for disposing of the captured object [41].

VII. CONCLUSION

The rapid expansion of human activity in space over the past 65 years has significantly increased the population of objects in Earth's orbital environment, posing long-term risks to space operations. The threat posed by the Kessler Syndrome, along with the lack of insufficient action plans to mitigate space debris, highlights the urgency of addressing space debris. This paper has reviewed the current state of space debris, a few select mitigation strategies, and the guidelines set by various regulatory bodies. As the space industry continues its exponential growth, maintaining the sustainability of Earth's satellite orbits is critical to ensure safe and efficient operations. The space industry's growth offers substantial opportunities to humanity. Still, these can only be realized if global cooperation, strengthened by initiatives like the ESA's "Zero Debris Charter" is facilitated to sustain space usage and preserve and clear Earth orbits. Achieving a sustainable space environment will require collective efforts from all stakeholders, supported by robust regulatory frameworks and innovative technologies.

REFERENCES

[1] Space environment statistics (2023) Space Environment Statistics · Space Debris User Portal. Available at: https://sdup.esoc.esa.int/discosweb/statistics/

[2] Eldo, J., & Ntantis, E.L. (2024). Satellite mapping and demarcation analysis for coastal regulation zones assessment. Environmental Research Communications 6 075023. DOI:10.1088/2515-7620/ad58ad

[3] Daehnick, C., Gang, J., & Rozenkopf, I. (2023, April 17). Space launch: Are we heading for oversupply or a shortfall? McKinsey & Company. https://www.mckinsey.com/industries/aerospace-and-defense/our-insights/space-launch-are-we-heading-for-oversupply-or-a-shortfall

[4] Jones, H. W. (2018, July 8). The recent large reduction in space launch cost. NASA Technical Reports Server (NTRS). https://ntrs.Nasa.gov/citations/20200001093

[5] Pultarova, T. and Howell, E. (2022) Starlink Satellites: Facts, tracking, and impact on astronomy, Space.com. Available at: https://www.space.com/spacex-starlink-satellites.html (Accessed: 21 September 2024)

[6] Space Debris Mitigation Guidelines of the Committee on the Peaceful Uses of Outer Space. United Nations Office for Outer Space Affairs - UNOOSA. (n.d.). https://www.unoosa.org/pdf/publications/st_space_49\E.pdf

[7] Goodwin, G. E. (2023). 4 times NASA astronauts lost things in space. Business Insider. https://www.businessinsider.com/nasa-astronauts-lost-items-in-space-dropped-bag-2023-11

[8] Gorvett, Z. (2023, October 9). The ocean grave for 264 spacecraft. BBC News. Available at: https://www.bbc.com/future/article/20231006-the-soviet-spacecraft-cemetery-in-the-pacific#

[9] Boag, S. (2019). The Lifespan of Orbiting Satellites.

[10] J.-C. Liou, N.L. Johnson, N.M. Hill, Controlling the growth of future LEO debris populations with active debris removal, Acta Astronaut. 66 (2010) 648–653.

[11] D.J. Kessler, B.G. Cour-Palais, Collision frequency of artificial satellites: creating a debris belt, J. Geophys. Res. 83 (1978) 2637–2646.

[12] Pultarova, T. (2023, August 30). Old Soviet satellite breaks apart in orbit after space debris collision. Available at: https://www.space.com/soviet-satellite-breaks-apart-after-debris-strike

[13] Day, D.A. (2021) Burning frost, the view from the ground: Shooting down a spy satellite in 2008, The Space Review: Burning Frost, the view from the ground: shooting down a spy satellite in 2008. Available at: https://www.thespacereview.com/article/4198/1 (Accessed: 21 September 2024).

[14] Akhmetov, Vladimir & Savanevych, Vadym & Dikov, Evgen. (2019). Analysis of the Indian ASAT test on 27 March 2019. 10.48550/arXiv.1905.09659..

[15] (2023). Available at: https://www.sdo.esoc.esa.int/environment.report/SpaceEnvironment_Report_latest.pdf .

[16] 30, J. (2022) Space debris and human spacecraft, Brewminate. Available at: https://brewminate.com/space-debris-and-human-spacecraft/.

[17] Space debris 101: The Aerospace Corporation (2024) Aerospace Corporation. Available at: https://aerospace.org/article/space-debris-101

[18] Carpineti, Dr. A. (2022, August 10). Space debris has chipped one of the ISS's windows. IFLScience. https://www.iflscience.com/space-debris-has-chipped-one-isss-windows-35668

[19] Undseth M., Jolly C., Olivari M. (2020), Space sustainability. The economics of space debris in perspective, OECD Science, Technology and Industry Policy Papers, no. 87, OECD Publishing, Paris

[20] Adilov, N., Braun, V., Alexander, P., & Cunningham, B. (2023). An estimate of expected economic losses from satellite collisions with orbital debris. Journal of Space Safety Engineering, 10(1), 66-69.

[21] Mulki R.R. & Ntantis. E.L. (2024, April 26). *Study of Microwave Electrothermal Propulsion System* [Paper presentation]. 8th International Conference on Research, Technology and Education of Space (H-SPACE 2024), Budapest, Hungary.

[22] Hattenbach, J. (2023, March 29). Satellites and space debris are polluting our night skies. Sky & Telescope. https://skyandtelescope.org/astronomy ESA's annual Space environment report -news/satellites-and-space-debris-are-polluting-our-night-skies/

[23] Primack, J. R., & Abrams, N. E. (2023). Star Wars Forever?—A Cosmic Perspective.

[24] Eldo J. & Ntantis E.L. (2024, April 26). *Review of Lagrangian Points and Scope of Stationary Satellites* [Paper presentation]. 8th International Conference on Research, Technology and Education of Space (H-SPACE 2024), Budapest, Hungary.

[25] IADC, IADC Space Debris Mitigation Guidelines, third ed., 2021

[26] NASA. (2023, November 3). Space debris. NASA. Available at: https://www.nasa.gov/headquarters/library/find/bibliographies/space-debris/

[27] ESA, European Code of Conduct for Space Debris Mitigation, 2004, pp. 1-20. http ://www.unoosa.org/documents/pdf/spacelaw/sd/2004-B5-10.pdf.

[28] UNOOSA, Space Debris Mitigation Guidelines of the Committee on the Peaceful Uses of Outer Space, 2010. http://www.unoosa.org/pdf/publications/st_spac e_49E.pdf

[29] UAESA, Space Debris Mitigation Guidelines, 2022. Available at: https://space.gov.ae/Documents/PublicationPDFFiles/POLREG/SpaceDebrisMitigationGuidelines-EN.pdf

[30] ISO, ISO 24113:2019 Space Systems — Space Debris Mitigation Requirements, 2019.

[31] Jdelriov. (n.d.). United NationsOffice for Outer Space Affairs. Space Debris Mitigation Standards Compendium -Update. https://www.unoosa.org/oosa/en/ourwork/topics/ space-debris/compendium.html

[32] Stokes, H., Akahoshi, Y., Bonnal, C., Destefanis, R., Gu, Y., Kato, A., & Tang, M. (2020). Evolution of ISO's space debris mitigation standards. Journal of Space Safety Engineering, 7(3), 325-331.

[33] The zero debris charter (no date) ESA. Available at: https://www.esa.int/Space_Safety/Clean_Space/The_Zero_Debris_Charter (Accessed: 21 September 2024).

[34] Mayorquin, O. (2023) Dish is first company to be fined by FCC over space junk rule, The New York Times. Available at: https://www.nytimes.com/2023/10/03/ business/dish-fcc-space-debris-fine.html .

[35] D. McKnight, R. Witner, F. Letizia, S. Lemmens, L. Anselmo, C. Pardini, A. Rossi, C. Kunstadter, S. Kawamoto, V. Aslanov, J.-C. Dolado Perez, V. Ruch, H. Lewis, M. Nicolls, L. Jing, S. Dan, W. Dongfang, A. Baranov, D. Grishko, Identifying the 50 statistically-most-concerning derelict objects in LEO, Acta Astronaut. 181 (2021) 282–291, https://doi.org/10.1016/j.actaastro .2021.01.021.

[36] J.R. Wertz and W.J. Larson, Space Mission Analysis and Design, Microcosm, 1999.

[37] Lourens Visagie, Vaios Lappas, Sven Erb, Drag sails for space debris mitigation, Acta Astronautica, Volume 109, 2015, 65-75, ISSN 0094-5765, https://doi.org/10.1016/j. actaastro. 2014.12.013.

[38] Serfontein, Z., Kingston, J., Hobbs, S., Holbrough, I. E., & Beck, J. C. (2021). Drag augmentation systems for space debris mitigation. Acta Astronautica, 188, 278-288.

[39] Baba, M. H., Manzoor, M. M. M., Singh, A., Kumar, R., & Thakur, A. K. (2023). Review analysis of problems associated with the various space debris removal methods. Materials Today: Proceedings.

[40] C.R. Phipps, LADROIT - a spaceborne ultraviolet laser system for space debris clearing, Acta Astronaut. 104 (2014) 243–255, https://doi.org/10.1016/j. actaastro.2014. 08.007.

[41] Guglielmo S. Aglietti, Ben Taylor, Simon Fellowes, Thierry Salmon, Ingo Retat, Alexander Hall, Thomas Chabot, Aurélien Pisseloup, C. Cox, A., Zarkesh, A. Mafficini, N. Vinkoff, K. Bashford, Cesar Bernal, François Chaumette, Alexandre Pollini, Willem H. Steyn, The active space debris removal mission RemoveDebris. Part 2: In orbit operations, Acta Astronautica, Volume 168, 2020, Pages 310-322, ISSN 0094-5765, https://doi.org/10.1016/j.actaastro.2019.09.001

[42] Development of Harpoon System for Capturing Space Debris. Available at: https://conference.sdo.esoc.esa.int/ proceedings/sdc6/paper/27/SDC6-paper27.pdf

Review of Lagrangian Points and Scope of Stationary Satellites

Joel Eldo
Department of Aerospace Engineering
Amity University Dubai
Dubai, UAE
joel.eldo01@gmail.com

Efstratios L. Ntantis
Department of Aerospace Engineering
Amity University Dubai
Dubai, UAE
entantis@amityuniversity.ae

Abstract—**Lagrangian points represent unique positions in a two-body system where a particle placed at any of these points with zero initial velocity will maintain its position, assuming minimal interference from external forces. These points serve as gravitational equilibrium zones, commonly referred to as L1, L2, L3, L4, and L5. The collinear points (L1, L2, and L3) are inherently unstable due to gravitational perturbations from nearby celestial bodies, whereas the triangular points (L4 and L5) tend to be stable, offering favorable conditions for the placement of stationary satellites or space stations. The relative stability of these points requires reduced velocity adjustments (ΔV) and, consequently, less fuel consumption, which is advantageous for long-term spatial projects. This paper explores the theoretical underpinnings of Lagrangian points, focusing on their stability and practical applications in astronautics. The study investigates historical missions utilizing the Lagrangian points and discusses the orbital mechanics involved in transitioning spacecraft between these points within the Sun-Earth system. Emphasis will be placed on the potential of these points to host megastructures, which, while currently hypothetical, could be realized through advanced space engineering techniques.**

Keywords—Lagrangian points, orbital mechanics, spacecraft positioning, astrophysics research, sustainability in space

I. INTRODUCTION

Over two centuries ago, Leonard Euler theorized the existence of three collinear equilibrium points – L1, L2, and L3 – where the gravitational forces of two celestial bodies counterbalance each other. Subsequently, Joseph-Louis Lagrange identified two additional points, L4 and L5, completing the five equilibrium points in a two-body system. These points, now collectively known as Lagrange points, represent locations where the gravitational influences of the Earth and the Sun effectively cancel out, creating regions in space where objects can maintain stable positions. This discovery was a significant contribution to the solution of the restricted three-body problem, and in recognition of Lagrange's contributions, these points were named after him [1].

A critical condition for the practical application of Lagrange points is that the mass of any third object within the system must be negligible compared to the masses of the primary celestial bodies involved. For instance, a system comprising the Sun and Earth and a third object of insignificant mass relative to Earth will exhibit clearly defined Lagrange points.

Conversely, suppose a third celestial body has a mass comparable to Earth's. In that case, the system will not maintain distinct Lagrangian points, undermining the applicability of this model in such scenarios.

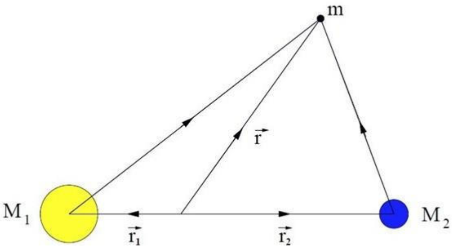

Fig. 1. The restricted three-body problem [2]

Lagrangian points, serving as regions of equilibrium in the gravitational interaction between two large bodies (*see* Fig.1), have profound applications across various space-related endeavors. These points enable the strategic positioning of spacecraft, such as space stations at stable towing points, relay satellites for enhanced communication capabilities, and surveillance satellites for defense purposes. Furthermore, they facilitate continuous monitoring of Earth from advantageous vantage points [3,4]. The mechanics underlying these points reveal that objects placed at these locations with negligible velocity relative to the system will remain stationary indefinitely. Among these, L1, L2, and L3 are collinear points that align directly with the vector connecting the Sun and the planet, inherently presenting instability, as shown in Figure 2. Conversely, L4 and L5 form the vertices of an equilateral triangle with the planet and the Sun, offering enhanced stability due to their relative positioning [5].

From a broader perspective, Lagrange points epitomize positions in space where the gravitational forces of two celestial bodies nullify each other, creating potential loci where spacecraft can significantly reduce fuel consumption for station-keeping. Such strategic placements allow for the extended observation of celestial and terrestrial domains from multiple perspectives.

The dynamics of these points also intertwine with fundamental principles of physics, such as the warping of the spacetime continuum under the influence of mass. The interaction of gravitational fields from rotating bodies introduces complexities like centripetal forces, further distorting spacetime. At Lagrange points, the gravitational pull from the involved bodies is effectively neutralized, creating zones where an object can exist in a state of zero gravitational force from both bodies. These characteristics make Lagrange points fascinating from a theoretical standpoint and invaluable for practical applications in space exploration and surveillance [6].

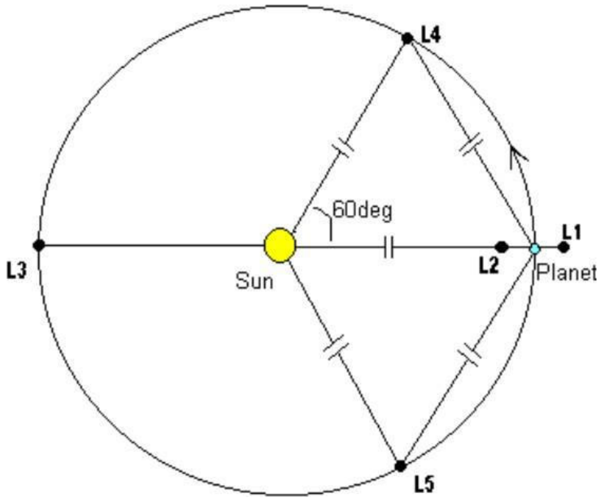

Fig. 2. Placement of Lagrange Points in the Sun-Earth System [7]

II. Types of Langrage Points

Based on their stability, Lagrange points are divided into two main spheres: *Meta Unstable Points* (L1, L2, L3) and *Stable Points* (L4, L5), as shown in Figure 3 and Figure 4.

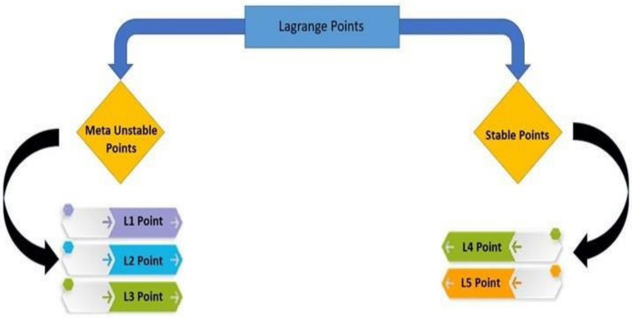

Fig. 3. Classification of Lagrange Points

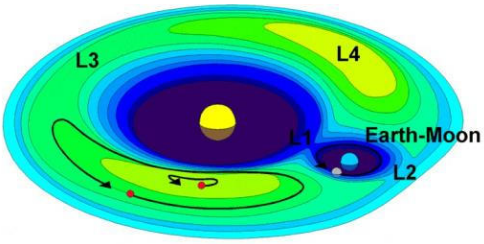

Fig. 4. Locations of Lagrange Points [8]

A. *Meta Unstable Lagrange Points*

L1, L2, and L3 points are meta-unstable Lagrange Points, as depicted in Figure 5. Objects positioned at these points will remain stable unless subjected to additional forces. However, practical observations show that the gravitational fields of celestial bodies like the Moon and other planets exert slight influences on these objects, causing deviations from their expected trajectories. Therefore, precise adjustments using instruments such as thrusters are necessary at these specific points to maintain desired trajectories. More specifically:

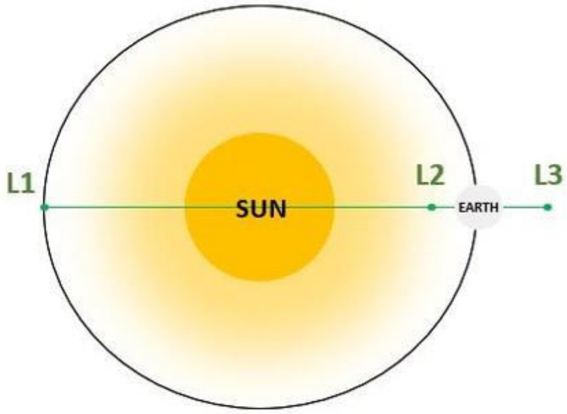

Fig. 5. Meta Unstable Lagrange Points

i. L1 Point

The L1 point, illustrated in Figure 6, lies along the vector connecting the Sun and Earth, approximately 1,000,000 miles from Earth. A key advantage of placing a satellite or spacecraft at this point is that it doesn't simply remain stationary; rather, it orbits in a small path, maintaining its position within the same general area. Some Lagrangian missions that have been successfully conducted include:

- Observation of the Sun
- Observation of the Earth's daytime side [9]

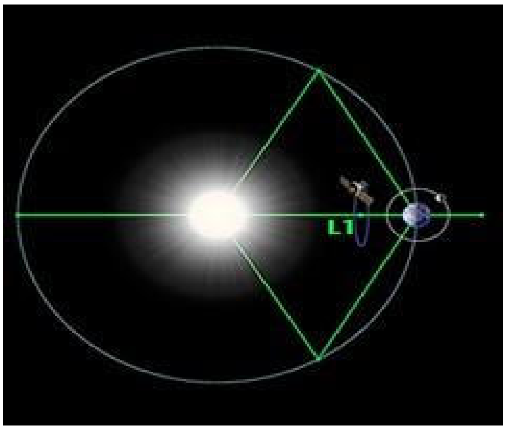

Fig. 6. L1 Lagrange Point [10]

An object cannot stagnate at a point such as L1 but follows a mini orbit and stays in the same region. Some examples of already carried out Lagrangian missions are:

- The Solar and Heliospheric Observatory (SOHO) (*see* Fig.7) was launched on a Lockheed Martin Atlas IIAS launch vehicle in December 1995. SOHO has been studying the Sun for its internal structure, extensive outer atmosphere, and the explanation for the origin of the solar wind [11].
- Other Sun observing satellites, such as the Advanced Composition Explorer (ACE) and the WING Satellite, make circuits around the L1 point and carry out detailed observations of the Sun.
- The First Satellite to be introduced into L1 Point is the International Sun-Earth Explorer, which collected samples from the Sun's solar winds to further analyze its composition [12].
- The European Space Agency's LISA Pathfinder Mission was scheduled to reach the L1 Lagrange point in early 2015. Its primary goal was to investigate the essential technologies required for a future space-based gravitational wave observatory, utilizing spacecraft to form a formation at these Lagrange points. The LISA has two Gold-platinum cubes, which were kept in a constant state of free-fall, isolated from all times of forces except the influence of gravity. The satellite constantly changed its orientation with the help of its thrusters [13].
- NASA's Deep Space Climate Observatory (DSCOVR), shown in Figure 8, is positioned at the L1 point. It serves a dual purpose for the space agency: monitoring the Sun for mass ejections such as solar flares that impact Earth's magnetic field, influencing the formation of the Aurora Borealis, and observing the Earth's daytime side for phenomena like Ozone Layer Depletion, Volcanic Eruptions, Weather changes, and more. [14].

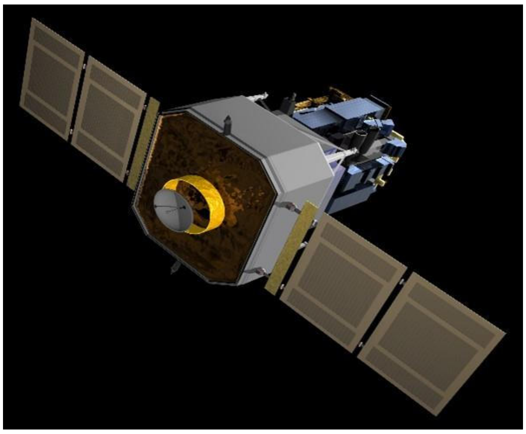

Fig. 7. Solar and Heliospheric Observatory [15]

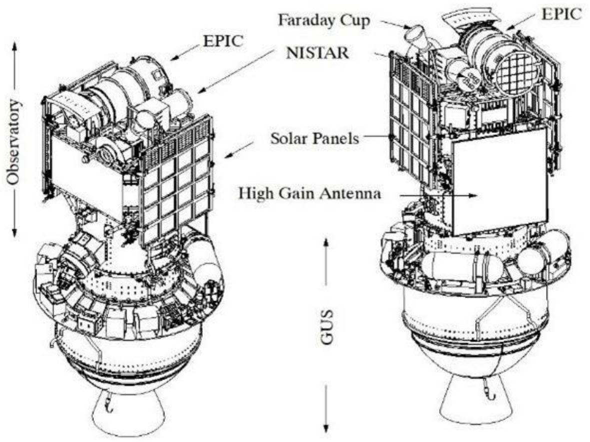

Fig. 8. Deep Space Climate Observatory [16]

ii. L2 Point

The L2 point is located beyond the Sun and the Earth's vector. It is about 1,000,000 miles above Earth. The main advantages of a satellite/spacecraft in this point are:

- Observation of Vast Space
- Observation of the Nighttime Side of the Earth. An object cannot be stagnant at a point such as L2, but it follows a mini orbit and stays in the same region. The Sun-Earth L2 point has many satellites and spacecraft. A telescope placed at L2 will have a continuous and uninterrupted view of the night sky because Earth has been reduced to almost the same size as the Moon in the night sky. Earth obstructs the view of observers in lower orbits, like Hubble Telescope observers. The Microwave Anisotropy Probe (MAP), depicted in Figure 9, achieved orbit around the L2 point in the Sun-Earth system. It conducted observations of the cosmic microwave background, as illustrated in Figure 10, providing insights into the image of the Big Bang's effects. The coverage area for the Sun-

Earth L2 is even broader than that for the Earth-Moon L2. By utilizing only 10% percent of its fuel, the Microwave Anisotropy Probe has enough fuel to be around this equilibrium point for quite a long time [17].

Some examples of already carried out Lagrangian missions are:

- NASA's Wilkinson Microwave Anisotropy Probe (WMAP) (*see* Fig.9).
- WING spacecraft was placed at the L2 point and later at the L1 point.
- ESA's Herschel Space Observatory: To identify and analyze objects across the Universe and our Solar System, particularly the formation and evolution of stars and galaxies and their interaction with the interstellar medium.
- ESA's Planck Satellite, a successor to the WMAP, was used to investigate the Universe's past even deeper using background radiation.
- ESA's Gaia Mission is intended to map out the entire Milky Galaxy, track 1% of the movement of celestial bodies, and detect white dwarfs and neutron stars.
- A German–Russian satellite is an X-ray observatory. It investigates high-energy zones such as supermassive black holes and merger galaxies.

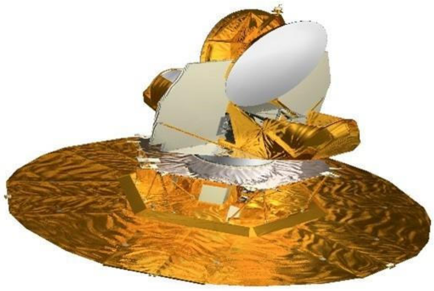

Fig. 9. Wilkinson Microwave Anisotropy Probe [18]

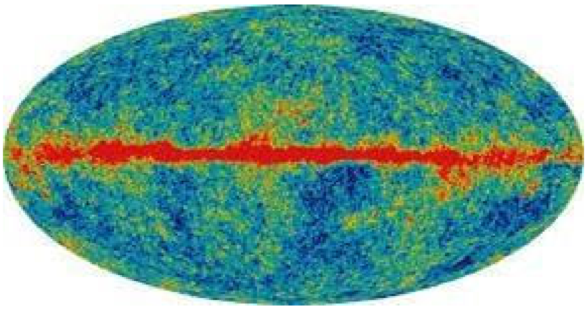

Fig. 10. The Cosmic Background of the Universe [19]

iii. L3 Point

L3 lies on the opposite side of the Sun, along the same orbital path as Earth but approximately 180 degrees out of phase (*see* Fig.11). This position places it at a distance from the Sun equal to Earth, about 150 million kilometers (93 million miles) away. However, unlike L4 and L5, which are stable due to the balancing of gravitational forces and the centripetal force of orbiting at the system's average angular velocity, L3 is inherently unstable.

The primary challenge of utilizing L3 is its instability and the consequent energy cost for maintaining a spacecraft's position. Any mission to L3 would require autonomous operation capabilities or the deployment of relay satellites to maintain communication with Earth.

Despite these challenges, exploring or utilizing L3 could provide unique scientific and strategic opportunities, particularly for missions that benefit from its unique orbital perspective.

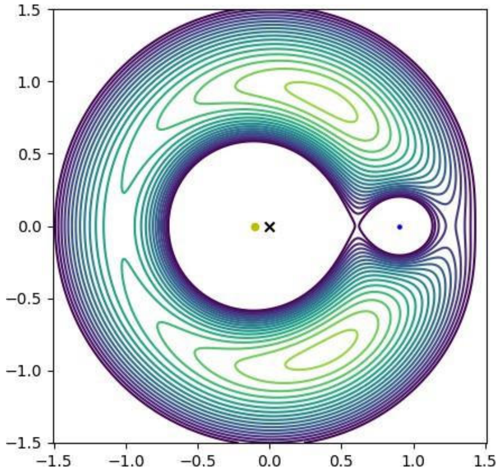

Fig. 11. L3 Lagrange Point [20]

B. Meta Stable Lagrange Points

Meta-stable Lagrange Points, as illustrated in Figure 12, are positions where objects placed will remain tethered. The slight influences of other gravitational fields or forces will not cause them to spiral off due to their inherent stability. These points require fewer altitude corrective measures; therefore, L4 and L5 are stable [21].

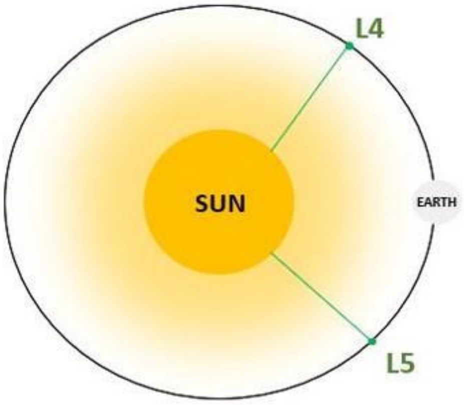

Fig. 12. Meta Stable Lagrange Points

III. NATURAL OCCURRENCES OF LAGRANGIAN POINTS

The L4 and L5 Lagrangian points, characterized by their high degree of orbital stability, naturally accumulate celestial bodies such as asteroids, commonly referred to as *Trojan* asteroids (*see* Fig.13). This propensity has been substantiated by the historical prediction and subsequent discovery of significant populations of such asteroids in the Lagrangian points of the Sun-Jupiter system, classified into the Trojan and Greek camps based on their respective positions [22]. These asteroids are effectively sequestered within these gravitational niches, a phenomenon that can be likened to ensnared in gravitational wells.

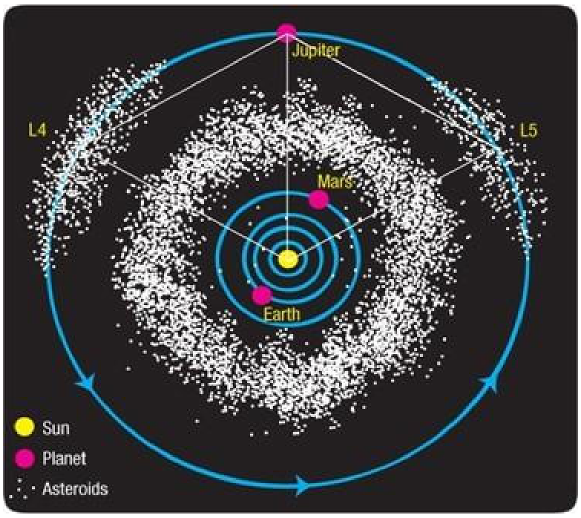

Fig. 13. Trojan and Greek Asteroids in Jupiter Lagrangian Points [23]

Despite the apparent peril these space-borne objects present, potentially complicating navigational efforts within their vicinities, the dynamic structure of the Lagrangian points provides a safeguarding mechanism, ensuring a maintained separation from the host planet by a process of continual orbital divergence. This intrinsic property diminishes the likelihood of collisions with the planet. Consequently, for terrestrial planets such as Earth, the L4 and L5 regions remain devoid of such risks, allowing for the unencumbered utilization of these regions for advanced space exploration initiatives and the emplacement of observational instruments. The scientific community continues to explore the potential these celestial anchor points offer, balancing the inherent risks against their considerable strategic advantages.

IV. FUTURE IMPLICATIONS OF LAGRANGIAN POINTS

A. *Asteroid Observatories*

One of the future advantages of exploiting the L1 point is the observation and study of asteroids from this Lagrange point. One of the main drawbacks that present-day astronomers face is that they cannot see space debris/objects such as asteroids heading toward Earth due to the Sun's glare, and it perfectly shadows the asteroid, making it nearly invisible. NASA will send a space telescope, Near-Earth Object Camera (NEOCam), to the Sun-Earth L1 Lagrange point to scout the sky for dangerous space debris. This point could act as a vantage point where we could pre-determine asteroids as close as 45 degrees to the Sun. In 4 years, NEOCam could find about 2/3rd of the potential asteroids in the sky, which could seriously threaten us. NEOCam (*see* Fig.14) is set to launch in 2025 [24].

NEOWISE is a satellite that scouts for asteroids near Earth using the Wide-field Infrared Survey Explorer, which orbits very close to Earth. An asteroid scouting spacecraft at a Lagrange point could pick up tiny infrared signals dispersed from the asteroids across a broad range of positions, except for those very close to the Sun, where intense glare posed challenges. Unlike WISE, NEOWISE did not rely on coolant to maintain a favorable temperature, benefiting from natural cooling at its location [25].

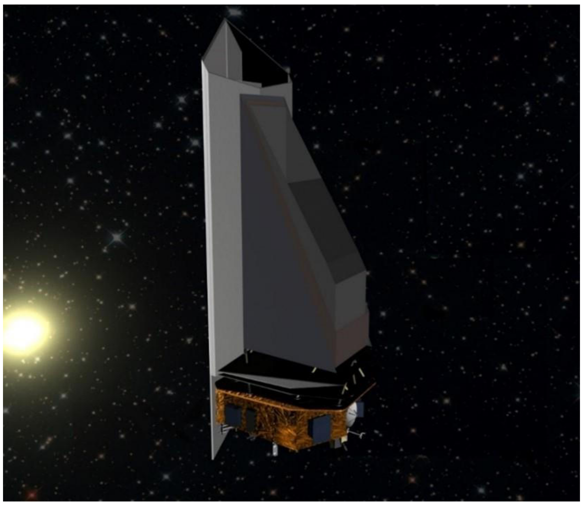

Fig. 14. NEOCam [26]

B. *Global Warming Solutions*

One of this point's most fascinating exploitations will be using the Sun-Earth L1 Lagrange point to slow climate change. A giant sunshade or Fresnel lens will distort the Sun's light, as illustrated in Figure 15.

This is one of the most ambitious uses of the L1 Lagrange point of the Sun-Earth system: It is an idea proposed by Roger Angel of the University of Arizona [27]. It is a megastructure idea beyond imagination, like the idea of a Dyson Sphere. According to [27], it should be possible to launch a tiny cloud of spacecraft into the L1 point and use it to block some of the Sun's harmful rays (*see* Fig.16). Each tiny spacecraft would measure 1m across and 1gr in weight. The problem with a considerable sunshade is that light pressure will be drastically high due to the enormous surface area.

However, the use of negligibly smaller objects, as proposed by Angel, can overcome this drawback while being as efficient as the sunshade. By implementing these structures into the L1 points, fuel will not be needed to keep these in place, i.e., L1. This idea will cool the Earth's atmosphere and surface, drastically reducing Global Warming and its effects.

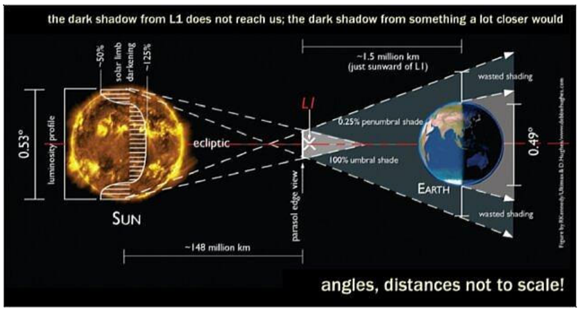

Fig. 15. Use of a large sunshade in the L1 Lagrange Point [28]

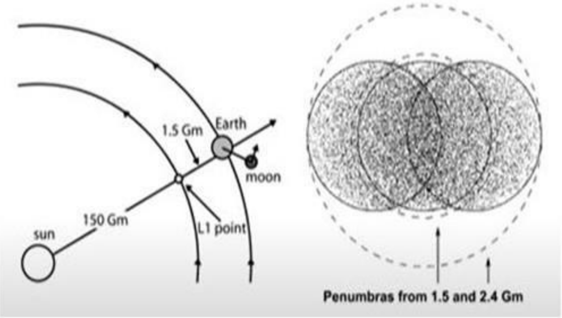

Fig. 16. Roger Angel's depiction of a swarm of satellites in the L1 Lagrange point [29]

C. *James Webb Telescope*

One of the most ambitious satellites from NASA, as illustrated in Figure 17, gives a more detailed bird's eye view of the Universe. Using the concept of complex origami, it can fold its sunshades into a compact structure, which is used to cool down its instruments into almost absolute zero to provide a more in-depth view of the Universe. Placed at L2 Lagrange point, it will have a field of view without the Sun or the Earth. Hence, it will help a much deeper analysis of the night sky [30].

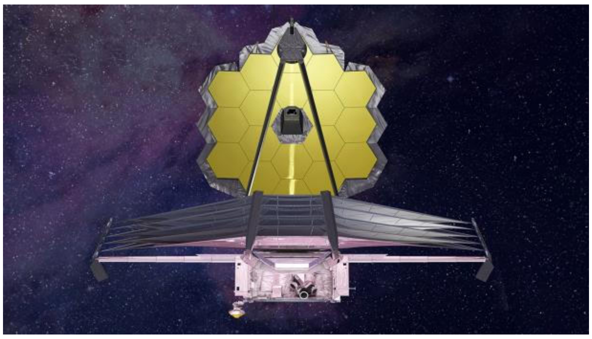

Fig. 17. James Webb Space Telescope [31]

D. *Space Transportation*

- Transit Hubs and Waystations at Lagrangian Points L1 and L2: Establishing spaceports at Lagrangian Points L1 and L2 proposes a strategic advancement in interplanetary travel infrastructure. These locations are uniquely suited to act as intermediary stations for spacecraft voyaging between Earth, the Moon, and more remote destinations within our solar system [32].

- Orbital Shipyards at Lagrangian Points: Lagrangian Points offer ideal sites for orbital shipyards, facilitating the construction, servicing, and dismantling of spacecraft in a stable, energy-efficient environment. These locations minimize the energy required for station-keeping and bypass the significant costs and limitations associated with launching structures from Earth. By constructing spacecraft in orbit, challenges such as Earth's gravity and atmospheric resistance are avoided, allowing for the assembly of larger and more complex structures. Lagrangian points, particularly L1 and L2, are areas of interest for space debris mitigation strategies due to their use as staging areas for missions and satellite constellations. Efforts to minimize debris generation and actively remove debris from these regions are essential to maintain their usability and prevent collisions with operational spacecraft [33].

- Gateway Stations for Deep Space Missions: The envisioned transit hubs and waystations at L1 and L2 would be multifunctional, providing essential services such as refueling, maintenance, and crew rest. These facilities would reduce operational energy costs by mitigating the need for continuous propulsion and decrease the frequency and cost of return trips to Earth by enabling on-site servicing and refueling.

- Strategic Utilization of L4 and L5 Lagrangian Points for Deep Space Propulsion: L4 and L5 Lagrangian Points, known for their stability, are prime candidates for launching deep space missions. These points are advantageous due to minimal orbital disturbances and a consistent position relative to Earth and the Moon. Utilizing L4 and L5 for such purposes capitalizes on their inherent stability. It enhances the logistical capabilities for missions to outer planets and interstellar probes, making these points integral to the infrastructure of deep space exploration.

- Quarantine and Research Stations at Lagrangian Points: Due to their isolation and stable orbital characteristics, Lagrangian Points are proposed as optimal locations for quarantine and research facilities. These stations would be critical for handling and analyzing samples returned from other celestial bodies, providing a secure environment that minimizes the risk of biocontamination to Earth.

- Asteroid Redirect Ports at L1 and L2 Lagrangian Points: The L1 and L2 Lagrangian Points are strategically suited for serving as asteroid redirect ports. These locations can act as preliminary staging areas for asteroids that are potential terrestrial threats. Once positioned at these points, asteroids can be safely processed for valuable minerals or redirected into stable orbits around the Moon or Earth for further mining operations. Microwave Electrothermal Propulsion Systems (MEPS) offer a promising approach for satellite propulsion, particularly for missions to Lagrangian points where precise station-keeping is crucial. By efficiently converting electrical energy into thrust, MEPS can help maintain the position and orientation of spacecraft at Lagrange points with minimal propellant mass [34].
- Development of Residential and Tourist Space Colonies at L4 and L5 Lagrangian Points: The L4 and L5 Lagrangian Points, recognized for their stable orbital relationships with Earth, present ideal locations for constructing large space colonies. These colonies could serve a multifunctional purpose, providing residential facilities for space workers and their families and accommodating research staff engaged in long-term projects.
- Zero-Gravity Manufacturing Facilities at Lagrangian Points: The unique zero-gravity conditions at Lagrangian Points offer significant opportunities for establishing manufacturing facilities in space. Such an environment could enhance product quality and efficiency, leveraging space's distinctive properties to optimize production processes.

E. *Other Applications*

- A satellite in the L2 region can help in better lunar expeditions because it is about 85% of the Earth to the moon distance, so this could be used as a substation for frequent moon visits. A Space elevator is a transportation system to and from planets, asteroids, and other heavenly bodies. Due to its stability, an Earth-Moon space elevator is possible at the L2 Lagrange point.
- The temperature at L2 is also subzero. Edward Strum of Harvard University proposed using this spot as a cryogenic freezing zone to store food for astronauts. Storing food at the Lagrange point would cut fuel costs substantially for space food transportation.
- L1 and L2 also allow immense bandwidth, as the transmission speeds are very high over traditional Ka-band radio [35].
- The Lagrange points are of much higher importance than just placing a spaceship; they also play a crucial role in a system that drifts around the solar system without using much firepower. These are Megastructures called the InterPlanetary Superhighway (IPS).

V. CONCLUSION

The current paper overviewed the importance of Lagrange Points. This natural phenomenon helps humans develop into a higher solar system-wide civilization. There are five equilibrium points in a system of two bodies. When the mass of the third object is negligible compared to the mass of the other two objects, one primary requirement for dealing with Lagrange points is when the mass of the third object is negligible: Sun-Earth and an object with a negligible mass compared to the earth system will have well-defined Lagrange points, but there will be no Lagrangian points for Sun, Earth, and another entity of the same Earth mass. These points also have significant astronautical uses and are feasible for positioning a satellite or a space station. Overall, the theory and science behind these points are interesting. Several satellites and spacecraft have been deployed to these points, with more planned for the future. Scientists and astronomers continue to develop new ideas and methods to exploit this phenomenon.

REFERENCES

[1] "WMAP Observatory: Lagrange Points," map.gsfc.nasa.gov. https://map.gsfc.nasa.gov/mission/observatory_l2.html

[2] Rahman, M. I. (2019). Deep space communication and exploration of solar system through inter-Lagrangian data relay satellite constellation. 8th Interplanetary CubeSat Workshop (pp. pp. 1-19)). iCubeSat.

[3] Bond, Victor R, Steven J Sponaugle, Michael F Fraietta & Shonn F Everett. 1991. Cislunar libration point as a transportation node for lunar exploration. En AAS/AIAA Spaceflight Mechanics Meeting, 91–103.

[4] Farquhar, Robert W. 1969. Future missions for libration-point satellites. Astronautics Aeronautics 7. 52–56

[5] C, Neil J. 1998. What is a Lagrange point? https://solarsystem.nasa.gov/ resources/754/what-is-a-lagrange-point/

[6] NOAA. 2015. Points of Lagrange: A satellite a million miles from home. https://www.nesdis.noaa.gov/content/points-lagrange-satellite-million-miles-home

[7] "Can a system of three stars exist?," Astronomy Stack Exchange. https://astronomy.stackexchange.com/questions/33214/can-a-system-of-three-stars-exist (accessed Apr. 30, 2024).

[8] Gurfil, Pini. 2006. Modern astrodynamics. Elsevier

[9] McInnes, Colin R & Matthew P Cartmell. 2006. 7 orbital mechanics of propellantless. Modern Astrodynamics 189

[10] "Why future astronauts may be sent to 'gravity holes,'" New Scientist. https://www.newscientist.com/article/dn17713-why-future-astronauts-may-be-sent-to-gravity-holes/ (accessed Apr. 30, 2024).

[11] Burnett, DS. 2013. The genesis solar wind sample return mission: Past, present, and future. Meteoritics & Planetary Science 48(12). 2351–2370

[12] Armano, M, Matteo Benedetti, J Bogenstahl, Daniele Bortoluzzi, Paolo Bosetti, N Brandt, A Cavalleri, Giacomo Ciani, Ilaria Cristofolini, AM Cruise et al. 2009. Lisa Pathfinder: the experiment and the route to lisa. Classical and Quantum Gravity 26(9). 094001

[13] Jiang, Jonathan H, Albert J Zhai, Jay Herman, Chengxing Zhai, Renyu Hu, Hui Su, Vijay Natraj, Jiazheng Li, Feng Xu & Yuk L Yung. 2018. Using deep space climate observatory measurements to study the Earth as an exoplanet. The Astronomical Journal 156(1). 26

[14] Tyson, Neil deGrasse. 2002. The five points of Lagrange. Natural history 111(3). 44–48

[15] McInnes, Colin R & Matthew P Cartmell. 2006. 7 orbital mechanics of propellantless. Modern Astrodynamics 189

[16] Howell, Elizabeth. 2017. Lagrange points: Parking places in space. Space. https://www. space. com/30302-lagrange-points. Html

[17] "Lagrange Noktaları Nelerdir? Dünya Etrafındaki Bu 'Park Noktaları', Astronomi ve Gök Mekaniği İçin Neden Önemlidir?," Evrim Ağacı, Jan. 07, 2022. https://evrimagaci.org/lagrange-noktalari-nelerdir-dunya-etrafindaki-bu-park-noktalari-astronomi-ve-gok-mekanigi-icin-neden-onemlidir-11324 (accessed Apr. 30, 2024).

[18] Pirani, Simona, Anders Johansen & Alexander J Mustill. 2019. On the inclinations of the Jupiter trojans. Astronomy & Astrophysics 631. A89

[19] "DSCOVR (Deep Space Climate Observatory) - eoPortal," www.eoportal.org. https://www.eoportal.org/satellite-missions/dscovr (accessed Apr. 30, 2024).

[20] Mainzer, Amy. 2009. Neocam: The near-earth object camera. Bull. Am. Astronomy. Soc 38. 568

[21] "File:WMAP spacecraft.jpg - Wikipedia," commons.wikimedia.org. https://en.m.wikipedia.org/wiki/File:WMAP_spacecraft.jpg

[22] Adrian Cho, "Mission to capture the big bang afterglow launches," New Scientist. https://www.newscientist.com/article/dn921-mission-to-capture-the-big-bang-afterglow-launches/ (accessed Apr. 30, 2024).

[23] "Lagrange Points-the kevbase," kevbase.com. http://kevbase.com/site /gallery/misc/lagrange-points.html (accessed Apr. 30, 2024).

[24] B. P. Kondratyev, "Milestones in the Development of Celestial Mechanics," Astronomy Reports, vol. 67, no. 7, pp. 742–757, Jul. 2023, doi: https://doi.org/10.1134/s1063772923070041.

[25] McMurtry, Craig W., et al. "Development of passively cooled long wave infrared detector arrays for NEOCam." American Astronomical Society Meeting Abstracts# 221. Vol. 221. 2013.

[26] Menzel, M, M Davis, K Parrish, J Lawrence, A Stewart, J Cooper, S Irish, G Mosier, M Levine, J Pitman et al. 2023. The design, verification, and performance of the james webb space telescope. Publications of the Astronomical Society of the Pacific 135(1047). 058002

[27] Angel, Roger. 2006. Feasibility of cooling the Earth with a cloud of small spacecraft near the inner lagrange point (l1). Proceedings of the National Academy of Sciences 103(46). 17184–17189

[28] "US detects huge meteor explosion," BBC News, Mar. 18, 2019. Accessed: Apr. 30, 2024. [Online]. Available: https://www.bbc.co.uk/news/science-environment-47607696

[29] Baum, Chad M. & Low, Sean & Sovacool, Benjamin. (2022). Between the Sun and us: Expert perceptions on the innovation, policy, and deep uncertainties of space-based solar geoengineering. Renewable and Sustainable Energy Reviews. 158. 10.1016/j.rser.2022.112179.

[30] Gardner, Jonathan P., et al. "The James Webb space telescope." Astrophysics in the Next Decade: The James Webb Space Telescope and Concurrent Facilities. Dordrecht: Springer Netherlands, 2009. 1-29.

[31] Penoyre, Zephyr Sandford. 2019. & Emily The spaceline: practical space elevator a alternative achievable with current technology.

[32] "James Webb Space Telescope: NASA's new telescope gets hit by micrometeoroid in space- What was the impact?," Jagranjosh.com, Jun. 10, 2022. https://www.jagranjosh.com/current-affairs/james-webb-telescope-nasas-new-telescope-gets-hit-by-micrometeoroid-in-space-what-was-the-impact-1654836935-1 (accessed Apr. 30, 2024).

[33] M.V.H. Khan and E.L. Ntantis, "Space Debris: Overview and Mitigation Strategies," in Proceedings of the 8th International Conference on Research, Technology and Education of Space, H-Space, 25-26 Apr. 2024.

[34] R.R. Mulki and E.L. Ntantis, "Study of Microwave Electrothermal Propulsion System," in Proceedings of the 8th International Conference on Research, Technology and Education of Space, H-Space, 25-26 Apr. 2024.

[35] C. Zhao et al., "A K-/Ka-Band Broadband Low-Noise Amplifier Based on the Multiple Resonant Frequency Technique," in IEEE Transactions on Circuits and Systems I: Regular Papers, vol. 69, no. 8, pp. 3202-3211, Aug. 2022.

Circular food production in space environment

Insect protein production by supplementing green biomass in feed

Orsolya Meier
Faculty of Medicine
UniSpace Hungary, University of Debrecen
Debrecen, Hungary

Éva Domokos-Szabolcsy
Faculty of Agricultural and Food Sciences and
Environmental Management
University of Debrecen
Debrecen, Hungary

Milán Fehér
Faculty of Agricultural and Food Sciences and
Environmental Management
University of Debrecen
Debrecen, Hungary

Abstract— *This study aims to assess the effect of combining semolina with dried green duckweed, alfalfa, and green pepper as feeding substrate for yellow mealworm larvae (Tenebrio molitor). The research extended to examining production parameters (individual body weight, growth rate, survival rate, feed conversion ratio: FCR) and the dry matter, carbon, sulfur, nitrogen, and crude protein content of the larvae. The results show that all feed supplements used had a positive effect on the protein content of yellow mealworm larvae. The highest protein content was realized in the larvae fed with the alfalfa supplemented diet. In addition to increasing the larvae's protein content, the plant substrates also increased their organic carbon content compared to the control group. The larvae fed with the pepper supplement with the lowest mean individual weight were associated with the highest FCR, whereas larvae fed with the duckweed supplement with the highest mean individual weight were associated with the lowest FCR. In terms of survival rate, all treatments achieved a value above 90%. Our experiment also suggests that a high protein content in feed does not necessarily ensure high protein content in the larvae. This research highlights the potential of integrating innovative agricultural techniques and entomophagy to increase the efficiency and sustainability of food production in terrestrial and possibly extraterrestrial environments.*

Keywords—insect protein, circular food system, space food, yellow mealworm, alfalfa, duckweed, green pepper

I. INTRODUCTION

As humanity discovers more and more remote parts of the universe, the food supply for long-term space missions becomes an increasingly critical issue, and thus the need for sustainable food systems becomes more obvious. In space environments, where resources are limited and recycling is essential, insects can play a vital role as valuable actors in a circular food system. They can serve as a sustainable alternative protein source due to their low environmental impact, rapid reproduction, and efficient conversion of organic matter into high-quality proteins. Based on EFSA's expert opinion, the yellow mealworm larva is one of the four insects currently suitable for human consumption in Europe. Mealworm larvae can be properly preserved by lyophilization, but they can also be used in other forms as food during deep space missions. In a 2023 study, the 3D printability of protein gel derived from mealworm larvae was investigated. Guar gum was added to the insect protein as a stabilizer and the resulting gel proved to be suitable to produce food in space [1]. The role of mealworms in protein supply is anticipated to expand, owing to their high feed conversion efficiency and the capacity to utilize various types of plant biomass, including waste materials, as feed. Alfalfa, pepper, and duckweed are promising candidates for cultivation in extraterrestrial environments. Alfalfa, a crucial leguminous fodder plant for sustainable farming, produces significant quantities of green and dry biomass rich in protein, carotene, and minerals. Its high feed value is primarily attributed to the superior biological value of its protein. According to Apostol et al. [2], its protein content is approximately 35 g per 100 g of dry matter, while Domokos-Szabolcsy et al. [3] reported that the leaf protein concentrate contains about 40 m/m%. Alfalfa is particularly suited to the nutrient-poor Martian soil, and its ability to enrich the soil can facilitate the growth of various vegetable plants [4]. Peppers have been successfully harvested multiple times from the Advanced Plant Habitat grow chamber aboard the International Space Station. Not only do they provide an excellent source of fresh food and vitamin C, but the stems and leaves of the plant may also serve as suitable feed for insects. At the University of Debrecen in Hungary, within the framework of the DE SPACE program, researchers compared the NuMex Espanola Improved variety with the domestically bred Hungarian Enigma Sweet (hereinafter HES) pepper, during which they found that since HES is optimized for yield and is a smaller-growing variety, so it can be more suitable to fit in a small space and have a higher yield. Domokos-Szabolcsy et al. [5] detected ~55 phytochemicals not only from the fruit of HES, but also from the green juice obtained by processing green leafy shoots. Green juice has been shown to be a rich protein source, containing 24-27 m/m%. Consuming 100 grams of this juice can provide male astronauts with approximately 43.0-49.2% of their daily recommended protein intake, while female astronauts can achieve 52.4-59.9% of their recommended intake. Additionally, duckweed, with its wastewater purification ability and high protein content, holds potential for use in space-based agricultural systems. It is able to grow in a medium with a relatively high nitrogen, phosphorus and potassium content, while concentrating minerals and synthesizing protein [6]. Duckweed has one of the highest protein content of any plant and also contains many vital micronutrients. Duckweed leaves contain 92-94% water, ~45% of their dry weight is protein and 30-35% carbohydrates. Under ideal conditions, its fiber content is low, ~5%. Dried duckweed with less than 10% moisture content can be stored for at least five years without deterioration if kept in a place shielded from light and moisture, and it can be pelletized without binders, as noted by Skillicorn, Spira and Journey [7]. Due to its growth rate and high protein content, its protein productivity can be ten times higher than that of soybean [8]. Additionally, the drying process eliminates pathogens, and the wax coating on the surface of the leaves inhibits fungal growth, further extending shelf life, according to Ansal, Dhawan and Kaur [9].

II. MATERIALS AND METHODS

2.1. Materials

The alfalfa green biomass came from an alfalfa experiment ('Tápiószelei' variety) grown under field conditions in the Demonstration Garden of the Agricultural Science Center of the University of Debrecen. For the feeding experiment, alfalfa was processed as follows: after harvesting, the green biomass was wet fractionated with a twin-screw vegetable and fruit press (Green Star GS 3000, Anaheim, Canada). The green juice fraction obtained during pressing was frozen at -20°C and prepared by lyophilization (Alpha 1-4 LSC Christ).

The green pepper (a mixture of varieties) as a plant substrate came from a hydroponic experiment set up in the Research Glasshouse (Biodrome) of the MÉK Applied Plant Biology Department of the University of Debrecen. The harvested green biomass was frozen at -20°C and then used after lyophilization (Alpha 1-4 LSC Christ) and pulverization.

The duckweed was harvested from a pond at the Aquaculture Laboratory of the University of Debrecen. The duckweed was dried at a temperature between 40 °C and 43 °C in an ALPFRIGO CFD 700 dryer for 3 days before use.

The yellow mealworm larvae (*Tenebrio molitor*) required for the experiment was provided by the Aquaculture Laboratory of the University of Debrecen from its own culture. The insect larvae were raised on wheat semolina as a basic feed, and they were given raw carrots to cover their water needs. We started our experiment with approximately 6-week-old insect larvae.

2.2. Substrate Composition

During the experiment, four types of substrate combinations were used. 100% semolina was set as a control group (commercially available wheat semolina), while throughout the different feed treatments the weight ratio of semolina: plant substrate was constant (75%: 25%), as shown in Table 1.

TABLE I. SUBSTRATE COMPOSITIONS

Group Label	*Dried Green Biomass*	*Semolina*	*Total weight of substrate*
C	0%	100%	20 g
P	25% pepper	75%	20 g
A	25% alfalfa	75%	20 g
D	25% duckweed	75%	20 g

2.3. Experimental Set-Up and Research Environment

Four different treatments were applied in the experiment (C, P, A, D), and each were repeated four times, in a total of 16 units. The experiment was set up in a transparent 0.15 L box, which initially contained 20 grams of feeding substrate and 40 insect larvae. The initial individual average body weight of the experimental larval stock was 0.0719 ± 0.0036 g.

During the feeding experiment, the samples were kept in a programmable incubator (Memmert HPP110ECO, Büchenbach, Germany) at 23°C, 60% relative humidity, and 0% light intensity for 20 days. On the 7th, 14th, and 20th days of the experiment, samples were removed from the incubator. The larvae were extracted from the sample boxes, and their weight was subsequently measured. Additionally, on these dates, both the survival rate and pupation stages of the larvae were systematically monitored. On the last day of the experiment, we measured the feed consumption of the larvae to calculate the feed conversion ratio. Afterwards, the larvae samples were frozen at -20°C and then freeze-dried for 48 hours in a lyophilizer (Alpha 1-4 LSC Christ).

2.4. Feed Conversion Ratio

Equation (1) was used to calculate the feed conversion ratio (hereinafter FCR), where the weight gain is the difference between the initial and final weight of the larvae. To determine the total feed consumption, we measured the weight of the remaining feed at the end of the experiment. This approach allowed for an accurate assessment of FCR, revealing the effectiveness of the feed strategy in promoting growth within the experimental conditions.

$$FCR = \frac{Feed\ consumed}{Weight\ gain}\ g/g \tag{1}$$

2.5. Crude Protein Content

The crude protein content of the larvae was determined using two methods. According to the Kjeldahl method, lyophilized, powdered samples were prepared and measured in 1-gram increments, conducted in triplicate. The crude protein content was then determined with a Tecator Digestor device (VELT, VWR), according to the MSZ EN ISO 5983-2:2009 standard. The crude protein content of the larvae was also determined using the Dumas method. This technique involved measuring the nitrogen, carbon, and sulfur content of the samples with the Elementar Vario Max Cube (Elementar Analysensysteme GmbH, Germany). In this method, 250 mg of the sample was placed in porcelain cartridges and burned in the combustion tube of the device, heated to 925 ºC, in an environment rich in oxygen and free from ambient air. During the combustion process, the nitrogen content was transformed into N_2, and the carbon content into CO_2. The device's reduction tube further converted nitrogen oxides into N_2. After combustion and reduction, CO_2 was captured in separate adsorption columns. The device then measured the amount of N_2, followed by the determination of carbon content through consecutive heating of the CO_2 columns and desorption of the gases. Throughout this process, helium was used as the carrier gas. From the nitrogen content, the crude protein content was estimated using a nitrogen conversion factor of 6.25.

2.6. Statistical Analysis

IBM SPSS 22 software was used for statistical evaluation of production parameters and protein determination data. The homogeneity of the variances was checked with Levene's test. In order to compare the results, we used one-way analysis of variance (ANOVA). Significant differences were established with the Tukey test ($p<0.05$).

III. RESULTS

3.1. Production Parameters

3.1.1. Growth Rate

Fig. 1, shows the growth rates of mealworm larvae. The larvae in Group D exhibited the highest growth rate, followed by Group C. Group P initially displayed a decrease in weight; subsequently, however, there was a rapid increase in larval growth starting in the second week.

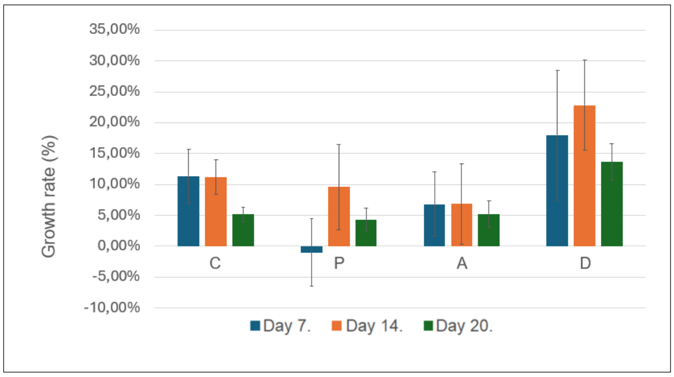

Fig. 1. Growth rate of yellow mealworms at different substrate compositions: C: 100% semolina; P: 75% semolina + 25% green pepper; A: 75% semolina + 25% alfalfa; D: 75% semolina + 25% duckweed.

3.1.2. Individual Average Body Weight

The largest growth in individual average body weight occurred in Group D, with final measurements surpassing 0.11 grams. In contrast, the individual average body weights for the P and A groups did not exceed 0.09 grams. Group C's final individual average body weight was slightly above 0.09 grams. Variations in the individual average body weight of the larvae across the experimental groups are detailed in Table 2.

TABLE II. INDIVIDUAL AVERAGE BODY WEIGHT OF YELLOW MEALWORM LARVAE AT DIFFERENT SUBSTRATE COMPOSITIONS

	Average of individual body weights (g)			
Group	***Day 0.***	***Day 7.***	***Day 14.***	***Day 20.***
C	0,0702± 0,0021^{a}	0,0781± 0,0018^{ab}	0,0868± 0,0009^{b}	0,0912± 0,0008^{ab}
P	0,0724± 0,0019^{a}	0,0717± 0,0058^{a}	0,0784± 0,0032^{a}	0,0818± 0,0038^{b}
A	0,0715± 0,0060^{a}	0,0762± 0,0050^{ab}	0,0813± 0,0041^{ab}	0,0855± 0,0031^{ab}
D	0,0736± 0,0034^{a}	0,0867± 0,0063^{b}	0,1061± 0,0030^{c}	0,1206± 0,0049^{a}

There is a significant difference between values marked with different letters in the same column ($p < 0.05$). Mean ± standard deviation. C: 100% semolina; P: 75% semolina + 25% green pepper; A: 75% semolina + 25% alfalfa; D: 75% semolina + 25% duckweed.

3.1.3. Biomass Average Weight

Fig. 2, shows the change in the average weight of the biomass during the experiment. Group D had the highest increase in biomass average weight, followed by Group C. In Group P, an initial drop in the average mass of the biomass was observed in the first third of the experiment.

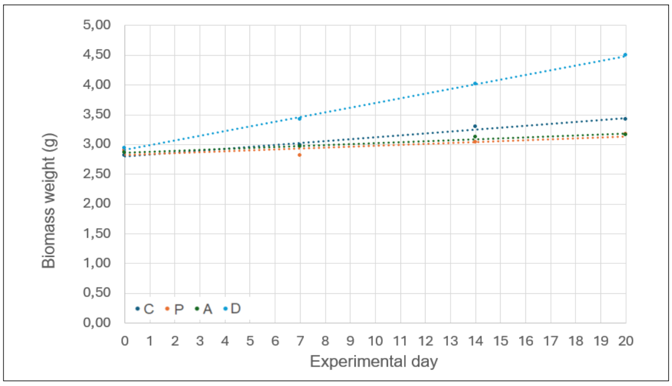

Fig. 2. Changes in the biomass weight of yellow mealworms at different substrate compositions: C: 100% semolina; P: 75% semolina + 25% green pepper; A: 75% semolina + 25% alfalfa; D: 75% semolina + 25% duckweed.

3.1.4. Survival rate

The survival rate was the highest when feeding with P, reaching a 96.9% survival rate, followed by C at 93.8%, D at 93.1%, and A at 92.5%. No significant differences were observed in the survival rates between the different groups. Pupation occurred during the feeding experiment; however, the pupae were not included in the survival rate assessment, and thus were not considered as living larvae in the analysis.

3.1.5. Feed Conversion Ratio

Fig. 3, shows the FCR of yellow mealworms reared on different substrates. Feeding on duckweed resulted in the lowest FCR, while feeding on pepper had the highest FCR. There was no significant difference between the control and alfalfa groups. The FCR value of each tested group is below 6.1 g/g. During our experiment, we did not achieve a feed conversion ratio below 3 g/g.

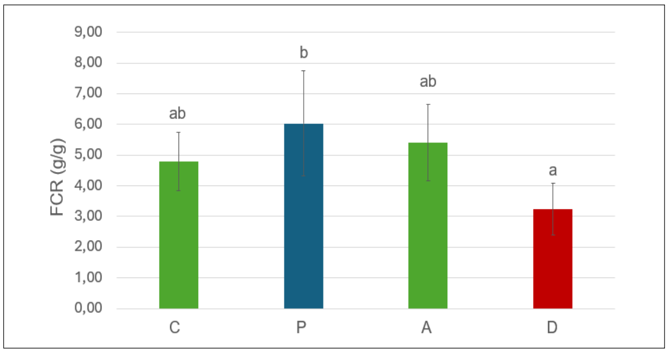

Fig. 3. FCR of yellow mealworms at different substrate compositions: Bars with different alphabets differ significantly ($p < 0.05$). C: 100% semolina; P: 75% semolina + 25% green pepper; A: 75% semolina + 25% alfalfa; D: 75% semolina + 25% duckweed.

3.2. Composition

3.2.1. Dry-matter and Carbon, Sulfur, Nitrogen Content

An elevated dry matter content was observed in Group D compared to Group C, whereas it was lower in the pepper and alfalfa groups. The sulfur content across the experimental groups displayed minimal variation. However, it was noted that the organic carbon content was higher in the treated larvae than in the control group. Regarding nitrogen content, Group A exhibited the highest levels, followed in descending order by groups P, D, and C. Table 3. shows the dry-matter content of the larvae measured after lyophilization, as well as the organic carbon, sulfur and nitrogen content of the different mealworm larval groups examined.

TABLE III. DRY-MATTER AND ORGANIC CARBON, SULFUR AND NITROGEN CONTENT OF YELLOW MEALWORM LARVAE AT DIFFERENT SUBSTRATE COMPOSITIONS

	C	***P***	***A***	***D***
Dry-matter (g)	1,84±0,22	1,50±0,13	1,45±0,20	2,25±0,08
Carbon (%)	44,12±0,27	53,49±0,01	53,39±0,18	50,50±0,07
Sulfur (%)	0,23±0,001	0,21±0,01	0,23±0,003	0,22±0,004
Nitrogen (%)	5,85±0,004	6,27±0,06	6,73±0,04	5,90±0,01

Mean ± standard deviation. C: 100% semolina; P: 75% semolina + 25% green pepper; A: 75% semolina + 25% alfalfa; D: 75% semolina + 25% duckweed.

3.2.2. Crude Protein Content

Based on the Kjeldahl method, the control group had the lowest crude protein content. The crude protein content of mealworm larval groups consuming feed supplemented with pepper, alfalfa and duckweed green biomass showed significantly higher values. In the case of these larvae, we were able to realize crude protein contents above 35 m/m%. The results of the mealworm larvae's crude protein content according to Dumas showed a similar trend as the values measured according to Kjeldahl. The alfalfa group had the highest crude protein content with a value above 40 m/m%. Fig. 4, shows the crude protein content according to Kjeldahl and Dumas, where the similarity between the trends of the results obtained with the two different measurement methods can be observed.

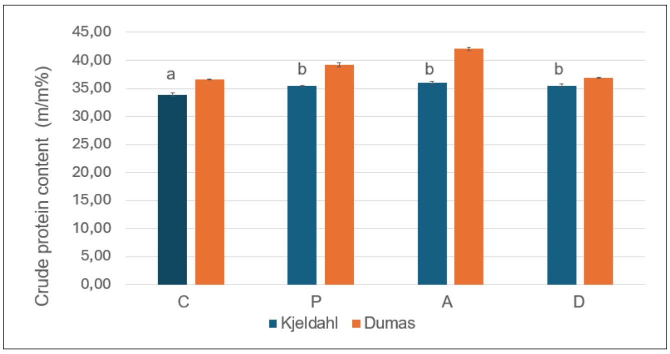

Fig. 4. Crude protein content of yellow mealworms at different substrate compositions determined according to the Kjeldahl and Dumas methods: Bars with different alphabets differ significantly ($p < 0.05$). C: 100% semolina; P: 75% semolina + 25% green pepper; A: 75% semolina + 25% alfalfa; D: 75% semolina + 25% duckweed.

IV. DISCUSSION

4.1. Production Parameters

During the feeding experiment, a higher rate of mass growth of mealworm larvae in the duckweed group was clearly observed. As a result, these larvae moulted more than the others. The weight of the duckweed group increased by 18% in the first week, 23% in the second week, and 14% in the third week, reaching the highest average biomass weight and the highest individual average weight by the 20th day. The duckweed group was significantly different from the pepper group, which at the end of the feeding experiment had the lowest average individual weight and biomass weight, but also the highest survival rate. During the change in the average mass of the biomass, we found that the pepper group lost its mass in the first week. This phenomenon was only observed in this group. After that, however, in the second week, it had a higher growth rate than the alfalfa group, which, on the other hand, developed at almost the same rate in the first 2 weeks. In general, in all experimental groups, it was observed that the growth rate decreased in the third week. There was no significant difference in survival rates between the groups; each group exhibited a survival rate higher than 90%. Liu, Masri, Perez, Maya and Zhao [10] reported similar findings, with survival rates of 91.7%, 92.5%, 89.3% and 89.7% using wheat bran alone and using a combination of wheat bran with red cabbage, carrots, and oranges, respectively. Literature sources indicate that the FCR values for mealworm larvae vary widely. Broekhoven, Oonincx, van Huis and van Loon [11] reported FCR values ranging from 2.62 to 6.05 in their study. They observed the lowest FCR value with feeds high in protein and low in starch, while the highest FCR was associated with feeds low in protein and high in starch. This finding aligns with our experiment, where the lowest FCR value was observed in the duckweed group. According to literature, duckweed contains the highest protein content among the three tested plant substrates. The FCR was inversely proportional to the average final individual weight of the larvae. At the experiment's conclusion, Group P, which had the lowest individual average body weight, exhibited the highest FCR value. Conversely, Group D, with the highest individual average body weight, demonstrated the lowest FCR value. There was a significant difference between the FCR values of the pepper and duckweed groups. In a study by Toviho, Imane, Pusztahelyi and Bársony

[12], an FCR value of 2.58 g/g was observed after an experimental period of 6 weeks on a feed with a composition of 75:25 wheat semolina and duckweed, which in our case was 3.24 g/g after 20 days in group D with the same composition. The pepper group recorded an FCR of 6.04 g/g, whereas the control group and the alfalfa group registered values of 4.79 g/g and 5.40 g/g, respectively. Melis et al. [13] observed an FCR value almost identical to the pepper group during keeping only on wheat bran, where they measured an FCR value of 5.48 ± 0.197.

4.2. Crude Protein Content

According to the Kjeldahl method, the crude protein content in groups P, A, and D was significantly higher than that in the control group. Utilizing both the Kjeldahl method and the Dumas method for determining crude protein, the highest values were observed in the alfalfa group, measuring 36.00 m/m% and 42.06 m/m% based on dry matter, respectively. The lowest crude protein content occurred in the control group, also determined by both methods (Kjeldahl: 33.91 m/m%; Dumas: 36.57 m/m%). Tan, Lai and Loh [14] reported similar crude protein contents in their 28-day study of mealworm larvae fed various substrates including watermelon peel, eggshell, banana peel, and a 1:1:1 mixture of these. Specifically, the banana peel group registered the lowest crude protein content at 38.53±1.43%, while the watermelon peel group exhibited the highest at 43.38±2.71%. They also observed that the banana peel group with the lowest crude protein content had the lowest FCR value. It is interesting to note that even in the experiment we conducted, the duckweed group with the lowest FCR value, which utilized the feed with the highest protein content in the best proportion, was not the group with the highest crude protein content. From this we can conclude that the high protein content of the feed does not necessarily ensure the high protein content of the larvae.

V. CONCLUSIONS

This experiment shows that all feed supplements used had a positive effect on the protein content of yellow mealworm larvae. If our primary objective is to produce protein suitable for human consumption, alfalfa emerges as the most suitable substrate for inclusion in feed, as it demonstrated the highest crude protein content among the substrates tested in our experiment. Conversely, if the goal is to maximize biomass production, duckweed should be utilized, as it has proven effective in achieving higher biomass yields. Our feeding experiment highlights that it can be useful to use pepper, alfalfa and duckweed substrates for the production of insect protein, which can be integrated into a circular food supply system in extraterrestrial environment, and by which the protein supply of long-term space missions would become more sustainable and economical. Nevertheless, further investigation is required to elucidate the impact of green biomass-based supplements on the quality of larval proteins, particularly in terms of amino acid composition, as well as to determine their effects on the larvae's fat content.

ACKNOWLEDGMENT

The present work is supported by the 2021-1.2.4-TÉT Plant species targeting for green biorefining purposes in Brazil and the Carpathian Basin, their processing technologies and product development possibilities entitled project. Project no. TKP2020-NKA-04 has been implemented with the support provided from the National Research, Development, and Innovation Fund of Hungary, financed under the 2020-4.1.1-TKP2020 funding scheme.

REFERENCES

[1] W. Chancharoen, Y. Kaewkumpha, W. Chansataporn, P. Ngamkajornwiwat and J. Wannakee, "Printability Properties of Protein Gel Obtained from Mealworm (Tenebrio molitor) in the 3D Food Printing of Deep-Space Food," *Preprints,* 2023.

[2] L. Apostol, S. Iorga, C. Mosoiu, R. C. Racovita, O. M. Niculae and G. Vlasceanu, "ALFALFA CONCENTRATE – A RICH SOURCE OF NUTRIENTS FOR USE IN FOOD PRODUCTS," *Journal of International Scientific Publications - Agriculture & Food,* vol. 5, pp. 66-73, 2017.

[3] É. Domokos-Szabolcsy, S. R. Yavuz, E. Picoli, M. G. Fári, Z. Kovács, C. Tóth, L. Kaszás, T. Alshaal and N. Elhawat, "Green Biomass-Based Protein for Sustainable Feed and Food Supply: An Overview of Current and Future Prospective," *Life,* vol. 13, no. 2, 2023.

[4] P. Kasiviswanathan, E. D. Swanner, L. J. Halverson and P. Vijayapalani, "Farming on Mars: Treatment of basaltic regolith soil and briny water simulants sustains plant growth," *PLoS One,* vol. 17, no. 8, 2022.

[5] É. Domokos-Szabolcsy, T. Alshaal, J. Koroknai, S. Kovács, C. Tóth, G. Csilléry, Z. Jókai, A. Matkovits, P. Makleit, S. Veres and M. G. Fári, "Phytochemical evaluation of the fruits and green biomass of determinate-type sweet pepper (Capsicum annuum L. fasciculatum) grown in terrestrial bioregenerative life-support research facilities," *Journal of Plant Interactions,* vol. 18, no. 1, 2023.

[6] C. Escobar and A. Escobar, "Duckweed: A Tiny Aquatic Plant with Enormous Potential for Bioregenerative Life Support Systems," *47th International Conference on Environmental Systems,* 2017.

[7] P. Skillicorn, W. Spira and W. Journey, "Duckweed Aquaculture: A New Aquatic Farming System for Developing Countries," *The World Bank,* 1991.

[8] L. Landesman, N. C. Parker, C. B. Fedler and M. Konikoff, "Modeling duckweed growth in wastewater treatment systems," *Livestock Research for Rural Development,* vol. 17, no. 6, 2005.

[9] M. D. Ansal, A. Dhawan and V. I. Kaur, "Duckweed based bio-remediation of village ponds: An ecologically and economically viable integrated approach for rural development through aquaculture," *Livestock Research for Rural Development ,* vol. 22, no. 7, 2010.

[10] C. Liu, J. Masri, V. Perez, C. Maya and J. Zhao, "Growth Performance and Nutrient Composition of Mealworms (Tenebrio Molitor) Fed on Fresh Plant Materials-Supplemented Diets," *Foods,* vol. 9, no. 2, 2020.

[11] S. v. Broekhoven, D. G. A. B. Oonincx, A. v. Huis and J. J. A. v. Loon, "Growth performance and feed conversion efficiency of three edible mealworm species (Coleoptera: Tenebrionidae) on diets composed of organic by-products," *Journal of Insect Physiology,* vol. 73, no. 1-10, 2015.

[12] O. A. Toviho, M. Imane, T. Pusztahelyi and P. Bársony, "Effect of Duckweed (Spirodela polyrhiza)-Supplemented Semolina on the Production Parameters and Nutrient Composition of Yellow Mealworm (Tenebrio molitor)," *Agriculture,* vol. 13, no. 1386, 2023.

[13] R. Melis, A. Braca, R. Sanna, S. Spada, G. Mulas, M. L. Fadda, M. M. Sassu, G. Serra and R. Anedda, "Metabolic response of yellow mealworm larvae to two alternative rearing substrates," *Metabolomics,* vol. 15, no. 8, 2019.

[14] S. W. Tan, K. S. Lai and J. Y. Loh, "Effects of Food Wastes on Yellow Mealworm Tenebriomolitor Larval Nutritional Profiles and Growth Performances," *Examines in Marine Biology & Oceanography,* vol. 2, no. 1, 2018.

Testing Clock Synchronization with GPSDOs and a Free-Space Laser Communication System

Máté Galambos
Department of Networked Systems and Services
Budapest University of Technology and Economics
Budapest, Hungary
galambos.mate@vik.bme.hu

Márton Czermann
Department of Networked Systems and Services
Budapest University of Technology and Economics
Budapest, Hungary
marton.czermann@edu.bme.hu

Gergely Jánosi
Department of Networked Systems and Services
Budapest University of Technology and Economics
Budapest, Hungary
janosi@hit.bme.hu

Barna Kirchhof
Department of Networked Systems and Services
Budapest University of Technology and Economics
Budapest, Hungary
kirchhof.barna@edu.bme.hu

László Bacsárdi
Department of Networked Systems and Services
Budapest University of Technology and Economics
Budapest, Hungary
bacsardi@hit.bme.hu

Abstract— **Precise clock synchronization is a cornerstone of many applications. An example is entanglement-based quantum key distribution, where knowing the precise arrival times of heralding photons at the transmitter side and arrival times of signal photons at a remote receiver side allows us to select the corresponding photon pairs even through a lossy and noisy channel. Here we report on testing various methods of clock synchronization between two ground stations. We used GPS disciplined oscillators (GPSDOs) and a free-space laser communication system to synchronize remote clocks. We tested our system at various distances, from 60 meters to 500 meters and even 3 km. We found that our optical transmission system can be very precise, especially at short distances, although it is highly sensitive to optical turbulence. GPSDOs on the other hand had larger phase noise at short distances yet remain operational even under less-than-ideal weather conditions.**

Keywords—component; formatting; style; styling; insert (key words)

I. INTRODUCTION

Several applications require accurate synchronization between endpoints (e.g., indoor positioning systems [1], 5G-6G technologies [2] or special ICT areas, such as quantum key distribution (QKD) [3]). QKD is an emerging technology that uses a small number of photons (often single photons) to generate symmetric keys between endpoints, enhancing IT security in the forthcoming era of quantum computers [4]. By transmitting photons via dedicated quantum channel, information is carried by quantum states, like the state of the polarization or the phase of the complex wavefunction. If an attacker tries to gain information about these keys, the communicating parties are alerted due to the principles of quantum mechanics, and the leaked key can be discarded [5].

At Budapest University of Technology and Economics, an entanglement based free-space QKD system is being developed [6] as part of the Hungarian QNL and QCIHungary (being part of the European EuroQCI [7]) initiatives. In such a system (like in [8]), knowing the precise arrival times of heralding photons of the generated entangled photon pairs at the transmitter side and the arrival time of the signal photons at a remote receiver side allows us to select the corresponding photon pairs, growing a symmetric key between the parties.

Monitoring the security of these systems i.e., verifying the channel being uncorrupted, requires measurements relying on statistical data processing, involving cross-correlation between arrival times of the photon pair counts at the two sides in real-time. Therefore, the security of these practical systems relies strongly on a continuous, stable, and accurate synchronization technique. However, in a free-space communication system several atmospheric disturbances can occur [9] that affect both the sync and quantum signal. Maintaining synchronicity between the communicating parties is one of the greatest engineering challenges to overcome when realizing these systems in practice.

Besides clock synchronization between computers at the endpoints, realizing QKD systems require target hardware devices which usually perform measurements or control the system. The list of these devices includes arbitrary waveform generators, electro-optic modulators, FPGA-based devices, and data acquisition instruments. As a practical example, time tagger devices are widely used as high-performance time-to-digital converters in these systems.

Today, the most accurate time measurement devices are the atomic clocks [10, 11]. For direct time source synchronization, the target devices receive signals from positioning satellites (GPS, GLONASS, Galileo, etc.) that have atomic clocks on board. Locking on to that signal with the help of a phase locked loop (PLL) design, one can generate a very stable clock signal of some tens of nanosecond accuracy. These clock generator devices are called GPS disciplined oscillators (GPSDOs) [12]. This method, however, needs complex devices and GPS coverage. Furthermore, applying multiple GPSDOs can result in a slow relative drift between the sync signals provided by them. The performance of this timing solution is investigated in [13].

The other proposed synchronization solution is the distribution of a master clock signal between endpoints. This solution needs only one reference (or local) oscillator (e.g., an atomic clock) with which all the other devices in the scheme are synchronized by PLLs. If there is no need to be synchronized with Coordinated Universal Time (UTC), then this technique can be a sophisticated solution, being independent of other systems. In [14], an electro-optical synchronization system was introduced, demonstrating 31.4 fs optical delay stabilization over 65 hours of operation in fiber. However, no investigation of the performance of the system in free space has been published yet.

In this paper we present our own method for free-space synchronization, developed to support entanglement based free-space QKD. In Section II, the clock transmission system (CTS) is introduced. To evaluate the performance of the CTS in the final part of the paper, Section III characterizes the time tagger devices applied in the measurements, while Section IV provides measurement results on the GPSDOs, at various distances from 30 m to 3 km.

II. OUR SYSTEM

Multiple devices were applied for the tests: two custom-built Global Positioning System Disciplined Oscillators (GPSDOs), a custom-built free-space laser Clock Transmission System (CTS), and multiple time tagging devices. The transmitter side of our laser CTS system consists of a GPSDO whose output is connected to a PLL pulse generator. This controls a laser driver integrated into a refracting telescope. On the receiver side a photodiode and receiver module are integrated into a similar telescope, whose signals are transmitted to a pulse regenerator. The block diagram of this system can be seen in Fig. 1.

Our GPSDOs are both based on a u-Blox LEA-M8F GPS receiver, which controls an Oven Controlled Chrystal Oscillator (OCXO). The signal of the OCXO is transferred to a clock fanout buffer from where it is both available as a 10 MHz output and used as feedback for the phase comparator of the LEA-M8F chip. The PLL pulse generator is based on a Microchip ZL30169. This is a dual PLL clock generator, where the first digital PLL is used for cleaning the incoming clock from noise and jitter, while the second analog PLL and the divider chain generate the output clock signal. The laser diode is driven by an Analog Modules 763 laser driver board. On the receiver side the photodiode is connected to a modified ZL30169 chip, that accepts a 1 MHz input and converts it into a 10 MHz output.

In our experiment we used two time tagging devices. One was a Swabian Instruments Time Tagger Ultra (Value). The other was a pair of PicoQuant Time Harp 260 NANO cards that were integrated into two PCs.

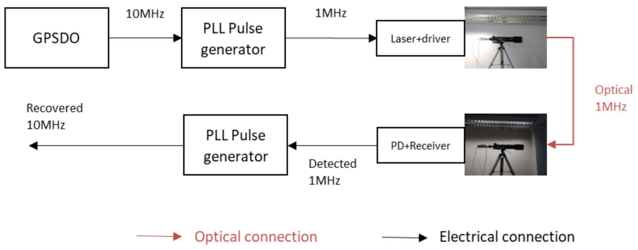

Fig. 1. Block diagram of our laser CTS system.

III. CHARACTERIZING OUR TIME TAGGERS

We tested the relative jitter between two input channels of these devices by splitting the output of a signal generator, connecting them to two inputs of the time tagger. Our signal generator was the 10 MHz output of one of our GPSDOs. We generated a two-sided start-stop histogram over a data collection period of 1 s using these channels and measured both the spread and standard deviation of the histogram.

Since we want to synchronize remote clocks for quantum cryptography both measures are important for us. The spread tells us about the maximum time window we should use in case of a largely noiseless environment while the standard deviation gives us more information about a coincidence window that we should use in case we need to find balance between the recorded coincidences and noise.

For the TimeHarp card the resolution was fixed to 250 ps. The average range was 708.33 ps and the standard deviation was 122.79 ps. For the Ultra time tagger device, we used two resolution settings: 1 ps and 50 ps. Using this time tagger and a finer resolution we also compared using our signal generator in two ways: splitting a single output and relying on the internal fanout buffer of the GPSDO. Comparing these gives us valuable insight into the performance of the fanout buffer.

For 50 ps resolution the average range was 400 ps and standard deviation was 55.43 ps. Splitting a single output of a GPSDO or using two outputs of the fanout buffers resulted in an average range of 414 ps and 415 ps and average standard deviation of 55.66 ps and 54.56 ps respectively. In each case the data collection time was 1 s. From these results, we conclude that there is no significant difference between these measurement setups and settings. However, the higher resolution provides a slightly clearer picture of the spread. We also conclude that the jitter of the fanout buffer is essentially immeasurable.

A. *The Effect of a Delay Line on Jitter*

We also examined the effect of using a longer coaxial cable, with a delay of 620 ns. We used two outputs of our GPSDO, one connected directly to our Ultra time tagger with a coaxial cable of about 1 m, the other through the longer coaxial cable. We measured the signal with 50 ps resolution. The average range was 416.67 ps while the average standard deviation was 57.25 ps, which shows a slight (about 2 ps) increase in standard deviation. We compared the jitters at multiple data collection times (namely 0.1 s, 1 s, 5 s, 10 s, and 30 s), and found that the data collection time had little to no effect on the measured jitters.

IV. JITTER BETWEEN GPSDOS

We compared our GPSDOs both in the laboratory when they were placed right next to each other, and outdoors on a university balcony when they were 85 m from each other. We used the long coaxial cable described before to directly transmit the signal from one GPSDO to the other which naturally limited the distance at which we could test our system.

TABLE I. EFFECT OF DATA COLLECTION TIME USING ULTRA VALUE TIME TAGGER

Resolution 50 ps two GPSDOs in the same laboratory		
Data collection time	Average range	Average st.dev.
0.1 s	450 ps	61.53 ps
1 s	550 ps	69.47 ps
5 s	2500 ps	499.85 ps
10 s	4100 ps	1140 ps
30 s	46050 ps	19952.17 ps

A. *Testing GPSDOs in the Laboratory*

First, we tested our GPSDOs in the same laboratory. We used different data collection times and found only a slight increase if the data collection time is under 1 s. For longer times however, we found a nonlinear increase of the jitter with data collection time (shown in Table I.)

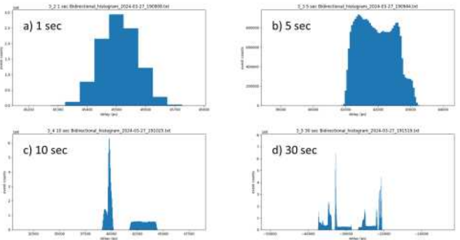

Fig. 2. The effect of data collection time on the start-stop histogram shape. The data was collected from two GPSDOs in the same laboratory over a) 1 s, b) 5 s, c) 10 s, and d) 30 s.

B. *Comparing GPSDOs Outdoors*

We also compared the jitter of our GPSDOs on the balcony, where we could place the GPSDOs 85 m apart from each other. We connected one of them to our Ultra Value time tagger with a 1 m long coaxial cable and the other with the long coaxial cable that we characterized in section III/A. Our results are shown in Table II. Comparing Table I. and Table II. we can see that in many cases the jitter doubled when we moved the GPSDOs from the laboratory to an outdoor environment and at a greater distance. Note that the cable connecting the two GPSDOs has negligible effect compared to the increase we are observing.

V. A. CHARACTERIZING OUR LASER SYNCHRONIZATION SYSTEM

We tested our free-space laser CTS in the laboratory, on a university balcony, and between two university buildings using a mirror to reflect the signal. We also tested it over 0.5 km and 3 km. The weather conditions during the tests were roughly the same: cold and still weather (close to zero degrees Celsius for the latter one with calm wind).

A. *Laser CTS in the Laboratory*

We characterized our laser CTS in the laboratory. Here we took two 10 MHz outputs of the same GPSDO, connected one directly to our time tagging device. We connected the other output to our laser CTS transmitter and sent the clock signal to the receiver which was about 5 m away. At the receiver we connected the recovered 10 MHz signal to the other input of our time tagging device. Our results are shown in Table III.

TABLE II. OUTDOOR EXPERIMENT OF COMPARING TWO GPSDOS ON A UNIVERSITY BALCONY USING OUR ULTRA VALUE TIME TAGGER

Resolution 50 ps two GPSDOs 85 m from each other		
Data collection time	Average range	Average st.dev.
1 s	950 ps	135.63 ps
5 s	2350 ps	652.94 ps
10 s	5633.33 ps	1771.44 ps
30 s	5875 ps	1603.29 ps
Resolution 1 ps two GPSDOs 85 m from each other		
Data collection time	Average range	Average st.dev.
1 s	831.83 ps	107.08 ps
5 s	2428.75 ps	567.56 ps
10 s	4578.33 ps	1184.18 ps
30 s	46119.67 ps	18525.43 ps

Comparing our laser CTS with two GPSDOs in the same laboratory (see Table II.), we can conclude that over 1 s data collection time they perform similarly. However, the laser CTS is largely insensitive to the data collection time over these distances (unlike two GPSDOs), so for longer measurements the laser CTS is preferable.

TABLE III. JITTER OF OUR LASER CTS IN THE LABORATORY MEASURED WITH OUR ULTRA VALUE TIME TAGGER

Resolution 50 ps GPSDO output compared to laser CTS 5 m link distance		
Data collection time	Average range	Average st.dev.
1 s	625 ps	66.18 ps

B. Laser CTS Outdoors on a University Balcony

To compare the performance of our laser CTS with two GPSDOs, we have placed the transmitter and receiver telescopes 85 m from each other on a university balcony. On the transmitter end we used two outputs of one of our GPSDOs. We connected one to our transmitter telescope. On the receiver side we connected our recovered 10 MHz signal to our time tagging device. We also used our long coaxial cable (characterized in section III/A) to transmit the GPSDO signal directly from one end of the balcony to the other. We compared the directly transmitted signal with the laser CTS transmitted signal over different data collection times and resolutions. Our results are shown in Table IV.

Comparing Table II. with Table IV. we can observe that our laser CTS system can be significantly better, especially for longer data collection times. However, the laser CTS system is sensitive to both alignment and turbulence. This leads to outliers, moments when the laser CTS system performs much worse than it otherwise would. (These outliers are included in the average.) As the data collection time increases the probability of these unlucky outliers increases. Note that in Table IV all data taken with 50 ps resolution happened to be narrow peaks (likely due to favorable weather conditions coupled with good telescope alignment). And for 1 ps resolution all data taken with 10 s data collection time also happened to be narrow peaks (hence the unusually low jitter).

TABLE IV. OUTDOOR EXPERIMENT OF COMPARING TWO GPSDOS ON A UNIVERSITY BALCONY USING OUR ULTRA VALUE TIME TAGGER

Resolution 50 ps **GPSDO output compared to laser CTS** **85 m link distance**		
Data collection time	Average range	Average st.dev.
1 s	1000 ps	138.17 ps
5 s	1033.33 ps	128.9 ps
10 s	1216.67 ps	147.48 ps
30 s	1550 ps	163.57 ps
Resolution 1 ps **GPSDO output compared to laser CTS** **85 m link distance**		
Data collection time	Average range	Average st.dev.
1 s	1339.83 ps	260.87 ps
5 s	1472.67 ps	227.45 ps
10 s	966.67 ps	103.05 ps
30 s	99999 ps	17357.98 ps

C. Laser CTS Between BME University Buildings

We performed a test between two neighboring buildings of the university. In this setup the transmitter and receiver were on the rooftop of the same building right next to each other. The overall optical path was varied between approximately 60 meters (when the mirror was 30 meters away) and 200 meters (when the mirror was about 100 meters away) with moving a mirror on top of the neighboring building to different places.

One of the GPSDO outputs was connected to the TimeHarp time tagger directly, while the other one was connected to the PLL of our transmitter telescope. We bounced the light back from the mirror on the other building to the receiver telescope. From the receiver we connected the regenerated 10 MHz clock signal to our TimeHarp time tagger. We chose this time tagger because at longer distances where direct electrical connection between the transmitter and receiver side is not possible, this time tagger was our only option for simultaneously measuring time tags at both sides.

We used 5 s data collection time at various distances and measured the jitter. These results are shown in Table V. However, due to the limited size of our mirror, the alignment process was difficult. The finite size of the mirror also meant that we lost some portion of the beam when we used the mirror. As a result, we only achieved a good alignment between the transmitter and receiver at the shortest 2x30 m link distance. This is reflected by the data where for longer distances we observed much worse jitter.

TABLE V. TESTING OUR LASER CTS BETWEEN TWO NEIGHBORING UNIVERSITY BUILDINGS USING OUR TIMEHARP 260 NANO TIME TAGGER

Resolution 250 ps **Signal generator compared to regenerated signal from laser CTS** **5 s data collection time**		
Link distance	Average range	Average st.dev.
2x30 m	8333.33 ps	404.86 ps
2x60 m	68250 ps	10406.51 ps
2x100 m	>99750 ps	22753.6 ps

We also examined how the complex start-stop histogram shapes arise, and how they relate to the distribution observed at short data collection times. We created an animation where we broke down the data collected over 5 s to smaller segments. Each frame of the animation represented data collected through roughly 0.01 s. A rapidly drifting narrow peak was observed on the animation, shaping the long-term cumulative pattern. We note that rapid drifts were also observed in other measurements, where the narrow short-term histogram peak flattened for a few frames and then remerged at a different position. Our speculation for the cause of this behavior is that the receiver may be completely losing the signal from the transmitter. These frames leave a telltale sign in the long-term cumulative histogram shape in the form of a uniform distribution added to the multiple peaks formed by the shift.

D. Laser CTS System Over 500 m Link Distance

Since we intend to apply our system at longer distances, we performed a test between building I of BME university and the nearby Schönherz dormitory building, located roughly 500 m from each other. Our setup consisted of a GPSDO on the transmitter side (located at BME building I) connected to the transmitter telescope through the PLL. On the receiver side we connected both our regenerated clock signal coming from the PLL of the laser CTS receiver and another GPSDO to the same TimeHarp 260 NANO time tagging card. We produced histograms between these two channels, meaning that the expected jitter is the added jitter of both the laser CTS and the relative jitter between the GPSDOs on the transmitter and receiver side.

TABLE VI. TESTING OUR LASER CTS BETWEEN THE UNIVERSITY AND A DORMITORY 500 M APART USING OUR TIMEHARP 260 NANO TIME TAGGER

Resolution 250 ps **GPSDO output compared to laser CTS transmitted clock signal** **500 km link distance, 5 s data collection time**		
First day		
Constellation used	Average range	Average st.dev.
Glonass	-	-
GPS	151763.89 ps	32306.18 ps
Second day		
Constellation used	Average range	Average st.dev.
Glonass	4916.67 ps	1194.91 ps
GPS	40291.67 ps	7922.71 ps

On the first day our GPSDOs were synchronized to both Glonass and GPS. However, during data collection one of the signals had a doubled frequency rate (due to reflected signal or improper trigger setting). This error only appeared in the measurements performed with Glonass, so we omit that data from our analysis. During this day both the transmitter and receiver telescopes were indoors: the transmitter was located inside a university and the receiver in a dormitory room. Note that the temperature difference between the room and the outside air may have caused additional optical turbulence.

On the second day we were able to achieve a better alignment and the measurements were performed with our GPSDOs synchronized to both satellite sources again. On this day the transmitter was set up on the rooftop of building I, and the receiver was located on the rooftop of the dormitory. The data collected during the second and third days are summarized in Table VI. and in Fig. 3.

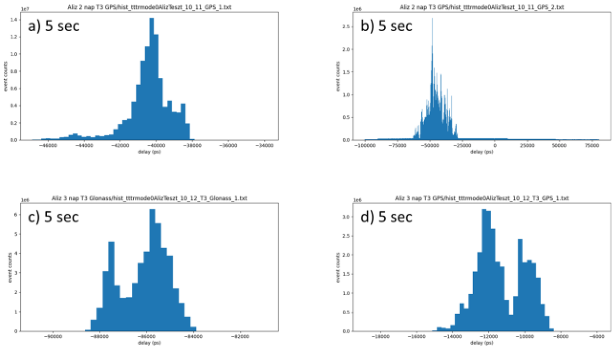

Fig. 3. Start-stop histogram comparing a local GPSDO with a remote GPSDO whose signal is transmitted through 500 m laser CTS link. a) the first day synchronized to GPS with a good lock, b) the first day synchronized to GPS with a worse lock, c) second day synchronized to GPS with a good lock, and d) the second day synchronized to GLONASS with a good lock.

VI. CONCLUSIONS

We conclude that for short range and short data collection time the GPSDOs and laser clock transmission system perform similarly. For more than a few seconds of data collection time and up to 85 m distance our laser CTS outperformed our GPSDOs. Over a 3 km distance we could not achieve a lock with the laser CTS but the GPSDOs remained operational.

ACKNOWLEDGMENT

This project has received funding from the European Union under grant agreement No 101081247 (QCIHungary project) and has been implemented with the support provided by the Ministry of Culture and Innovation of Hungary from the National Research, Development and Innovation Fund.

Special thanks to our students Ákos Uzonyi, Anna Veszely, Botond Horváth, Dániel Reményi, Gergely Déri, Gergő Csizmadia, Kitti Oláh, Petra Seres, and Viktor Zahorán for assisting with the measurements. We also thank the management of Schönherz dormitory and Vodafone Hungary for providing access to the measurement sites.

REFERENCES

[1] M. S. Lima Junior, M. Halapi, and E. Udvary, "Design of a realtime indoor positioning system based on visible light communication," Radioengineering, vol. 29, pp. 445‑451, 09 2020.

[2] F. N. Janky and P. Varga, "Time Synchronization Solution for FPGA-based Distributed Network Monitoring", Infocommunications Journal, Vol. X, No 1, March 2018, pp. 1-9. DOI: 10.36244/ICJ.2018.1.

[3] L. Gyongyosi, L. Bacsardi and S. Imre, "A Survey on Quantum Key Distribution", Infocommunications Journal, Vol. XI, No 2, pp. 14-21., June 2019, doi: 10.36244/ICJ.2019.2.2.

[4] S, Imre, "Quantum Communications – Explained for Communication Engineers," IEEE COMMUNICATIONS MAGAZINE, vol. 51, No 8, pp. 28-35., 2013.

[5] P. W. Shor and J. Preskill, "Simple Proof of Security of the BB84 Quantum Key Distribution Protocol," Phys. Rev. Lett. 85, 441, Jul 2000, doi: 10.1103/PhysRevLett.85.44.

[6] M. Galambos, and et al., "Building the First Hungarian Free-space Quantum Communication Device," Proceedings of the 5th International Conference on Research, Technology and Education of Space (H-SPACE 2019), pp. 20-21, 2019.

[7] European Commission, "The European Quantum Communication Infrastructure (EuroQCI) Initiative," April 18, 2024. [Online]. Available: https://digital-strategy.ec.europa.eu/en/policies/european-quantum-communication-infrastructure-euroqci. [Accessed: May 3, 2024].

[8] R. Ursin, and et al., "Entanglement-based quantum communication over 144 km," Nature Physics, vol. 3, no. 7, pp. 481–486, Jul 2007, doi: 10.1038/nphys629.

[9] M. Bass and et. al, "Handbook of Optics, Third Edition Volume V: Atmospheric Optics, Modulators, Fiber Optics, X-Ray and Neutron Optics," vol. 5., New York: McGraw Hill Professional, 2010.

[10] L. ESSEN, J. PARRY, "An Atomic Standard of Frequency and Time Interval: A Cæsium Resonator," Nature vol. 176, pp. 280–282, Aug 1955, doi: 10.1038/176280a0.

[11] "BIPM Annual Report on Time Activities," International Bureau of Weights and Measures, vol. 15, p. 9, 2020, ISBN 978-92-822-2280-5. ISSN 1994-9405.

[12] M. A. Lombardi, "The Use of GPS Disciplined Oscillators as Primary Frequency Standards for Calibration and Metrology Laboratories," NCSLI Measure 3, no. 3: pp. 56–65, 2008, doi: 10.1080/19315775.2008.11721437.

[13] M. A. Lombardi, "Evaluating the Frequency and Time Uncertainty of GPS Disciplined Oscillators and Clocks," NCSLI Measure 11, no. 3–4, pp. 30–44, 2016, doi: 10.1080/19315775.2017.1316696.

[14] J. Tratnik, and et al., "Electro-optical synchronization system with femtosecond precision," 2010 Conference on Optical Fiber Communication (OFC/NFOEC), collocated National Fiber Optic Engineers Conference, San Diego, CA, USA, 2010, pp. 1-3, doi: 10.1364/OFC.2010.OThH4.

Fast Routing in Entanglement-based Satellite Networks

András Mihály
Department of Networked Systems and Services
Faculty of Electrical Engineering and Informatics
Budapest University of Technology and Economics,
Műegyetem rkp. 3., H-1111 Budapest, Hungary
andras.mihaly@edu.bme.hu

László Bacsárdi
Department of Networked Systems and Services
Faculty of Electrical Engineering and Informatics
Budapest University of Technology and Economics,
Műegyetem rkp. 3., H-1111 Budapest, Hungary
bacsardi@hit.bme.hu

With the advent of quantum computers capable of handling thousands of logical quantum bits coming closer and closer, there is an increased need for high-security communication protocols. Due to Shor's algorithm, we can factorize primes in logarithmic time complexity instead of exponential, as with the best classical algorithms. The speedup of factorization is crucial in breaking today's most used public-key cryptographies, such as the RSA scheme. The RSA scheme is a vital part of modern Internet security and is used by many actors, from banks through virtual private networks to shopping websites. Using quantum communication, we can not only facilitate secure key exchange, whose security is backed by physical laws, but also provide a way for quantum computers to exchange non-classical information.

In our research, we developed a new algorithm based on our old REBSAN (Routing in Entanglement-Based SAtellite Networks) algorithm. With the use of our novel algorithm, it is possible to calculate all possible paths from a starting ground node to all other available ground nodes in O(deg(v)*O(V2)) time. This algorithm uses a novel approach in satellite-based quantum communication utilizing the unique properties of entanglement-based systems. Using these properties, we are no longer bound chronologically or in space in pathfinding. This means we could have routes where the first edge is the last chronologically or have paths like A → B ← C connecting A to C. This newfound freedom means we can find routes where previously it was impossible.

Keywords—Quantum communication; Satellite; Routing; QKD;

I. INTRODUCTION

As quantum computers grow more advanced and can handle thousands of logical quantum bits, there is a greater need for high-security communication protocols. This is due to a breakthrough quantum algorithm developed by Peter Shor [1] that allows for prime factorization in logarithmic time complexity instead of the exponential time complexity of classical algorithms. This speedup in factorization is essential in breaking today's most widely used public-key cryptographies, such as the RSA scheme. The RSA scheme is a crucial part of modern Internet security, and it is used by many entities, from banks and virtual private networks to online shopping websites. Quantum communication not only enables secure key exchange backed by physical laws but also provides a means for quantum computers to exchange quantum information.

Two main mediums for optical quantum communication networks are fiber-based and free-space optics (FSO). Both mediums have advantages and drawbacks. Fiber-based networks use a controlled medium (the fiber). This leads to a more predictable channel, which can be more easily characterized as a mix of quantum channels [2], at the cost of lower range and fixed links, but in some cases already built fiber networks can be used [3]. We call links free space if the primary physical medium between communication parties is non-controlled, e.g., atmosphere or deep space. Free-space links can change dynamically, and the only cost lies in creating the communication nodes, with the drawback of the chaotic medium. Using satellites as intermediary nodes, we can maximize the advantages of free-space links.

In the case of larger systems, FSO systems can be better because of their more extensive coverage and dynamism. Using satellites as intermediary nodes can bring out even more the advantages of FSO systems. Most modern research on satellite-based quantum networks focuses on Low-Earth Orbit (LEO) satellite-based systems. The main factor that makes LEO satellites attractive for quantum systems is their high coverage and relatively low Earth-satellite link attenuation. Not considering the cost of technology development, which is needed for high-reliability satellite-based quantum systems, one of the highest cost drivers for these networks is the cost of launching and maintaining satellites. Thus, reducing the number of satellites needed for maintainable quantum communication is a top priority in the field of satellite-based quantum communication.

The structure of our paper is as follows: in Section 2, we provide an overview of related research. In the third section, we explain how we model the satellite network and the workings of our algorithm. In Sections 4 and 5, we present and discuss our results.

II. Related works

The field of quantum communication via satellites is extensively researched. Regarding satellite-based quantum communication, we can refer to two types of systems. A simpler system can facilitate quantum key distribution (QKD) between parties, but this system, although it uses a quantum channel, in the end, creates classical information. A more complex system can not only create keys but also share quantum information between parties. In the second case, we talk about the quantum Internet.

Our research focuses on sharing entanglement between endpoints, as this will be a critical metric for the future quantum Internet. Sharing entanglement using satellites can lead to high-fidelity entanglements, as shown by researchers at the University of Science and Technology of China [4]. The next step in developing quantum Internet is to devise an algorithm for sharing and routing entanglement inside the network. Most modern research on routing in quantum networks assumes a static network with set entanglement links with set capacity [5], [6], which is perfect for fixed fiber-based network topologies. In the case of quantum satellite networks, there is not only a constant change in the network's topology, but we also need to choose which of the available links to use. There exist papers focusing on quantum satellite-based networks; for example, [7] provides an excellent overview of architectures and use cases, and [8] provides an algorithm that solves the dynamicity of the satellite networks. Both papers use multiple layered satellite networks for their proposed architectures, which can lead to better performance at the cost of using more satellites, which can incur extra costs. In our research, we use a single-layered satellite network, which, with our algorithm, can facilitate regional connections with as little as 16 and almost global connections with 64 satellites.

III. OUR ALGORITHM

We can break down our algorithm into six key ideas. Firstly, we use time-varying-graphs (TVG) to model the satellite network [9]. Next, we partition all edges of our graph into smaller, equal-duration edges. In the third step, we use a unique characteristic of quantum entanglement-swapping. With this, we can ignore the time order of edges in paths. Next, we account for the limited coherence time of quantum memories and take a subgraph of the whole TVG depending on the start time of the edge of the starting node. Thanks to the characteristics mentioned in the third step, from here we can simplify our TVG subgraph to a weighted directed graph, where the edge weights are the transmittances. From here on, the routing problem is reduced to a trivial problem that can be solved with any algorithm that takes in a weighted directed graph with no negative cycles (we used Dijkstra's algorithm [10]).

A. Modelling the network

We modeled the satellite network as a time-varying graph. As it can be seen in Figure 1, we did it by representing each visibility interval between two nodes with $[T; T+N]$: $\mu_1, \mu_2, \ldots, \mu_n$, where the nodes become visible for each other from timesteps T to T+N, and $\mu_1, \mu_2, \ldots, \mu_n$ are the transmittance values.

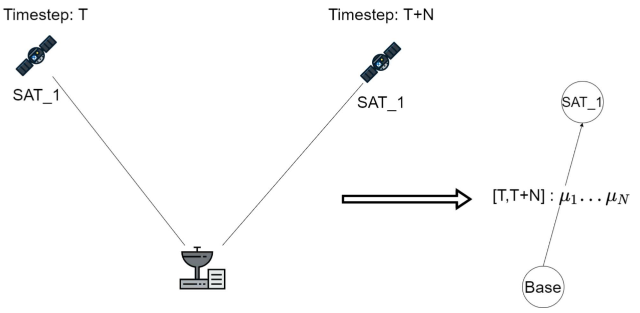

Figure 1. Modelling of the satellite network using time-varying-graphs.

B. Simplifying the graph

Our algorithm has two main input values: the maximal coherence time of the quantum memory (QMEM_LEN) and the maximal length or granularity (GRAN) for partitioning edges. GRAN is used as a maximal value when dividing the edges of our TVG into shorter edges.

C. Quantum entanglement swapping for paths with non-linear paths

Quantum entanglement swapping is a key [11] [12] part for any quantum network that wants to share quantum information across long distances. In Figure 2, an overview of the process of quantum entanglement swapping is illustrated. This is a crucial difference between quantum and classical networks. It is important to note that although the quantum link paths do not need to be linear in time, the process of entanglement swapping also utilizes a classical channel that will need to be routed accordingly.

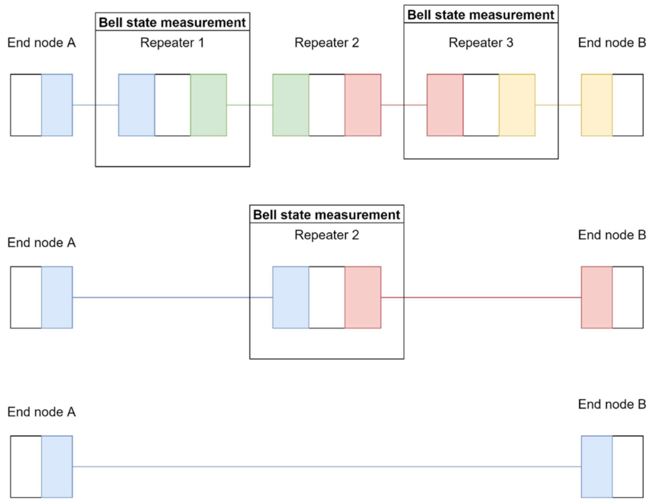

Figure 2. Quantum entanglement swapping based network. The colors here represent different entanglements between nodes.

D. Finding paths between nodes

Nodes are sorted into two categories: intermediary and end nodes. In our case, routing will only be considered between two end nodes. To find all the paths between the starting and destination nodes, we need to iterate over all the edges from the starting point, which are ordered in descending order depending on their transmittance. We generate a sub-graph of the TVG for all the edges, including only edges inside a QMEM_LEN interval. Next, we simplify the sub-graph by removing the timesteps, resulting in a weighted directed graph with no negative cycles. Lastly, we use our preferred routing algorithm to get the best route using our weight function. In our case, we used Dijkstra's algorithm and the weight considering the difference in the transmittance difference and the distance in time. After each cycle, we remove the edges that were used.

IV. RESULTS

We tested our algorithm with multiple satellite constellations along two main types of architectures. Table 1 shows that we created four constellations for each type of architecture, with the number of satellite nodes ranging from 16 to 64. The cross (CROS) architecture uses satellite orbits that are either parallel or perpendicular to each other in terms of inclination. Regarding the retrograde (RETRO) architecture, in terms of inclination, satellite orbits are parallel but have opposite orbital directions.

	LOW	LOWMID1	LOWMID2	MID
Satellites	16	32	32	64
Inclination	56.0568°			
Inclination shift (CROS)	90°			
Inclination shift (RETRO)	180°			

Table 1 Satellite systems used in our simulation.

Our simulation uses the transmittance calculated for the edges using QSCS 2.0 [13] as the main characteristic to optimize. Using this transmittance, we calculate the maximum sharable entangled photons between end nodes by multiplying it with a photonic entangled quantum bit generator output frequency. The efficiencies of quantum entangled generators have drastically increased in the last few years [14], [15], as these systems are highly complex, and there is no information on how they could be adapted to space systems. We use a significantly smaller 1MHz efficiency in our simulations. As it is shown later, even at this low rate of entanglement generation, we can reach high rates of entanglement sharing. For an easier comparison between different constellations and architectures, we will calculate the average of the maximal sharable quantum entanglements for all test ground stations, getting the average entangled bits per hour (AEQ/h) for most cases.

In our simulation, we used the following values:

- **Default satellite orbit:** a: 1000 [km], e: 0.0002090, i: 56.0568°
- **GRAN:** 25. 50, 100, 200
- **QMEM_LEN:** 100-2000 [s]
- **Starting ground station location:** Latitude: 0°, Longitude: 0°
- **Test ground station's locations:** Latitude: one for every 10°, Longitude: one for every 15°
- **Efficiency of the entangled quantum bit generator:** 1 [MHz]
- **Laser wavelength:** 860nm
- **Simulation time:** 10800 [s]

A. Reachability

As shown in Figure 3, when using a MID constellation along the CROS architecture, we reach a coverage of almost 100%. Here, it is important to note that the places unreachable from the start node were unreachable due to the orbital inclination of satellites, not because of a deficiency in our algorithm. The simulation was run for the Figure with the granularity set to 100 and maximal quantum memory coherence time set to 2000. Figure 3 shows these settings lead to a somewhat consistent AEQ/h over the covered area.

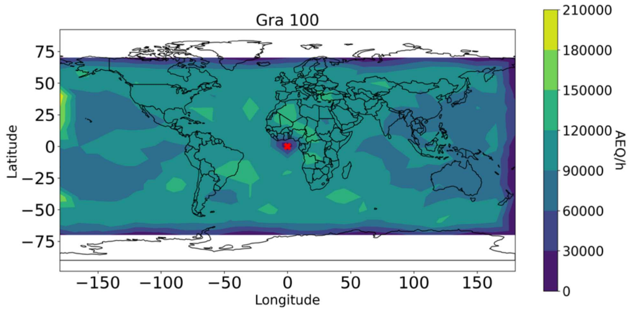

Figure 3. CROS MID constellations AEQ/h values over the globe. The output was generated using GRAN=100 and QMEM_LEN=2000.

In Figure 4, we can see that when decreasing the value for QMEM_LEN, the reach will also decrease, but by comparing Figures 4 and 5, we can see that the value used for GRAN plays a critical role. We can see that the QMEM_LEN, where we experience a drastic decrease, heavily correlates with the granularity. For GRAN values that are low enough, we won't even experience significant drops in reachability

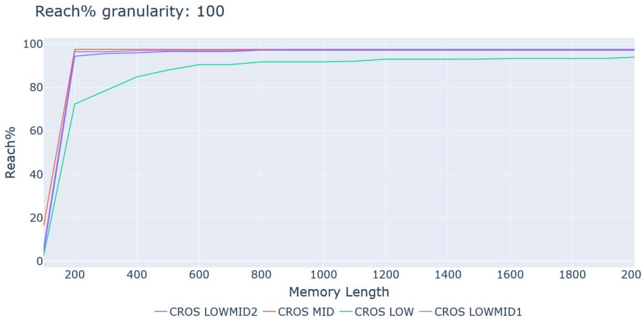

Figure 4. Plot for the CROS constellations reachability of the test ground stations with granularity set to 100. It is important to note that 100% shows that the algorithm reached all the reachable stations. This doesn't account for stations that are not reachable because of the satellite properties.

Figure 7. Plot for the CROS constellations reachability of the test ground stations with granularity set to 50.

B. Entangled bits shared

The focus of our algorithm is to provide entanglement-sharing routes depending on the architecture and other properties of the satellite network. Figure 6 shows that using only 64 satellites, we can share on entanglement at an average rate of 70kHz. It can be observed that just like in the case of reachability when QMEM_LEN starts nearing the value of GRAN, the network's throughput decreases drastically.

Figure 5. Plot for the CROS constellations average share entangled quantum bits per second with granularity set to 100.

Based on our simulations, while GRAN is at most half of the QMEM_LEN, the network will not experience drastic changes. It is important to note the fact, as seen in Figure 6, that using a small GRAN value will not counteract all effects of the smaller QMEM_LEN values. On the other hand, decreasing the values for GRAN will lead to a network that contains more edges, which will require more processing power; for example, the GRAN=25 calculation will use four times more edges than an algorithm with GRAN=100.

Figure 6. Plot for the CROS constellations average share entangled quantum bits per second with granularity set to 25.

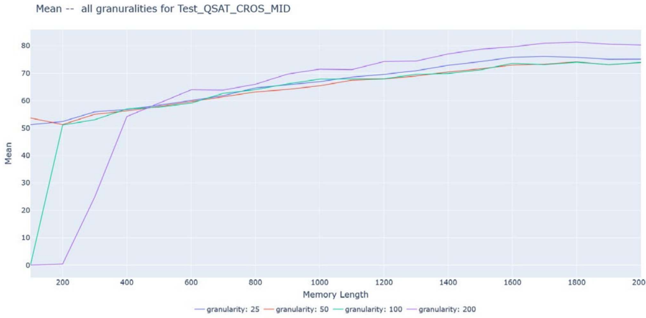

Figure 8. The plot of the mean transmittance of the CROS MID constellation across all granularities.

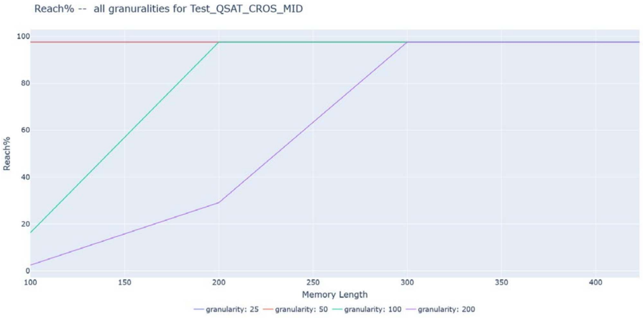

Figure 9. The plot of the reachability of the CROS MID constellation across all granularities.

V. CONCLUSSION

This paper presents our novel algorithm for finding optimal entanglement-sharing routes in small satellite networks. The algorithm could create optimal routes between two points and be customized with set granularity and quantum memory coherence lengths. This customizability enables our algorithm to be fine-tuned for specific needs. As we can see in Section IV, for a given coherence length QMEM_LEN, the maximal values should be around QMEM_LEN/2.

Looking at Figure 8, we can also see that the granularity value doesn't significantly influence the mean throughput of networks, apart from affecting the point where we experience a steep decrease. The steep decline's main reason is mainly the reduction in reachability; this can also be seen in Figure 9.

In conclusion, in this paper, we provide a novel algorithm for routing entanglement generations in satellite systems. We also show that it can support small satellite networks and quantum memories with varying coherence times. One next option to extend this algorithm would be the addition of a scheduler so it could support multiple connections with different priorities.

ACKNOWLEDGMENT

This research was supported by the Ministry of Culture and Innovation and the National Research, Development and Innovation Office within the Quantum Information National Laboratory of Hungary (Grant No. 2022-2.1.1-NL-2022-00004)

REFERENCES

[1] P. W. Shor, “Polynomial-Time Algorithms for Prime Factorization and Discrete Logarithms on a Quantum Computer,” *SIAM J. Comput.*, vol. 26, no. 5, pp. 1484–1509, Oct. 1997, doi: 10.1137/S0097539795293172.

[2] L. Gyongyosi, S. Imre, and H. V. Nguyen, “A Survey on Quantum Channel Capacities,” *IEEE Commun. Surv. Tutor.*, vol. 20, no. 2, pp. 1149–1205, 2018, doi: 10.1109/COMST.2017.2786748.

[3] E. Udvary, “Integration of QKD Channels to Classical High-speed Optical Communication Networks,” *Infocommunications J.*, vol. 15, no. 4, pp. 2–9, 2023, doi: 10.36244/ICJ.2023.4.1.

[4] J.-G. Ren *et al.*, “Ground-to-satellite quantum teleportation,” *Nature*, vol. 549, no. 7670, pp. 70–73, Sep. 2017, doi: 10.1038/nature23675.

[5] L. Gyongyosi and S. Imre, “Routing space exploration for scalable routing in the quantum Internet,” *Sci. Rep.*, vol. 10, no. 1, p. 11874, Jul. 2020, doi: 10.1038/s41598-020-68354-y.

[6] M. Pant *et al.*, “Routing entanglement in the quantum internet,” *Npj Quantum Inf.*, vol. 5, no. 1, pp. 1–9, Mar. 2019, doi: 10.1038/s41534-019-0139-x.

[7] L. de Forges de Parny *et al.*, “Satellite-based quantum information networks: use cases, architecture, and roadmap,” *Commun. Phys.*, vol. 6, no. 1, pp. 1–17, Jan. 2023, doi: 10.1038/s42005-022-01123-7.

[8] D. Huang *et al.*, “Quantum Key Distribution Over Double-Layer Quantum Satellite Networks,” *IEEE Access*, vol. 8, pp. 16087–16098, 2020, doi: 10.1109/ACCESS.2020.2966683.

[9] A. Casteigts, P. Flocchini, W. Quattrociocchi, and N. Santoro, “Time-varying graphs and dynamic networks,” *Int. J. Parallel Emergent Distrib. Syst.*, vol. 27, no. 5, pp. 387–408, Oct. 2012, doi: 10.1080/17445760.2012.668546.

[10] E. W. Dijkstra, “A note on two problems in connexion with graphs,” *Numer. Math.*, vol. 1, no. 1, pp. 269–271, Dec. 1959, doi: 10.1007/BF01386390.

[11] J.-W. Pan, D. Bouwmeester, H. Weinfurter, and A. Zeilinger, “Experimental Entanglement Swapping: Entangling Photons That Never Interacted,” *Phys. Rev. Lett.*, vol. 80, no. 18, pp. 3891–3894, May 1998, doi: 10.1103/PhysRevLett.80.3891.

[12] R. V. Meter and J. Touch, “Designing quantum repeater networks,” *IEEE Commun. Mag.*, vol. 51, no. 8, pp. 64–71, Aug. 2013, doi: 10.1109/MCOM.2013.6576340.

[13] “Quantum Satellite Communication Simulator.” Accessed: Jul. 12, 2022. [Online]. Available: https://www.mcl.hu/quantum-old/simulator/

[14] Z. Zhang *et al.*, “High-performance quantum entanglement generation via cascaded second-order nonlinear processes,” *Npj Quantum Inf.*, vol. 7, no. 1, p. 123, Aug. 2021, doi: 10.1038/s41534-021-00462-7.

[15] A. Chopin *et al.*, “Ultra-efficient generation of time-energy entangled photon pairs in an InGaP photonic crystal cavity,” *Commun. Phys.*, vol. 6, no. 1, pp. 1–9, Apr. 2023, doi: 10.1038/s42005-023-01189-x.

The role of entanglement in the development of satellite-based quantum internet

Kitti Oláh
Department of Networked Systems and Services
Budapest University of Technology and Economics
Műegyetem rkp. 3., H-1111 Budapest, Hungary
olah.kitti@edu.bme.hu

László Bacsárdi
Department of Networked Systems and Services
Budapest University of Technology and Economics
Műegyetem rkp. 3., H-1111 Budapest, Hungary
bacsardi@hit.bme.hu

***Abstract*— Nowadays, there is a growing trend on using the quantum technology in computing and communication. Although the focus is mostly on the development of quantum computers, the importance of quantum networks should not be forgotten. The aim is to connect these devices so they can communicate via a global quantum network, known as the quantum internet, following the protocols of quantum communication. There are two types of transmission channels: optical fibers and free-space systems (including satellites). Although satellite-based communications can be extended over long distances, atmospheric effects and fading must be considered. In our work, we investigated the application possibilities of quantum memories in satellite communication. We analyzed the impact of one or more quantum memories in a satellite-based quantum network through a simulation of a LEO satellite constellation.**

Keywords*— *Quantum memory; Quantum communication; Space communication, Nitrogen-vacancy centers, Quantum entanglement

I. INTRODUCTION

The 2nd Quantum Revolution is currently underway, where the focus is no longer on building quantum computers, but on connecting them through a global network as quantum internet [1]. In quantum communication, the information is carried by quantum bits, which can be physical implementations of polarization of photon, spin of electron or nuclear spin [2]. The communication channel between two nodes in a network can be based on optical fiber or satellite links. Fiber optics with increasingly high polarization stability are now available, but there are significant physical limitations over long distances [3]. The combined effect of these is already compromising the quantum bit state. As a result, there is a growing number of experiments in free-space quantum communications, one of the possibilities for further development of which is to extend it to satellite systems. To store quantum bits intact over long distances, we need quantum memories. The focus of our research has been to investigate quantum memory-based satellite communications by testing several protocols and system structures for Low Earth Orbit satellites.

II. QUANTUM MECHANICAL BACKGROUND

A. *Quantum bit*

In quantum computing, which is based on quantum mechanics, our basic unit of information is the quantum bit. It is an isolated, two-state (superposed) physical system whose state can be described by Dirac's formalism as follows:

$$|\psi\rangle = a|0\rangle + b|1\rangle\ ,$$

where

$$a, b \in \mathbb{C} \ \ and \ \ |a|^2 + |b|^2 = 1.$$

These complex coefficients also describe a state vector, which is interpreted in the Hilbert space and it is a unit vector. Furthermore, the state of the quantum bit can be described by Schrödinger's equation [4], which also gives its wave function:

$$\mathrm{i}\hbar \frac{\mathrm{d}|\psi\rangle}{\mathrm{dt}} = \mathrm{H}|\ \psi\rangle\ ,$$

where $\hbar$ is the reducated Planck's constant and H is the Hamiltonian operator of the closed system. During a superposition, it is in two separate states at the same time until a measurement is made on it. This is because at the moment of measurement, its wave function collapses into a defined eigenstate. Its value correlates with the absolute value squared of the complex probability amplitudes. After the measurement, it can be considered a classical bit.

B. *Quantum entanglement*

One of the most interesting quantum mechanical phenomena is entanglement, whereby two or more quantum bits correlate with each other. It means that if we measure one member of the pair after entanglement, we will know the state of the other quantum bit at that moment, because they are correlated. However, it is important to note that this does not mean that we can communicate faster than the speed of light. In 1935, Einstein-Podolsky-Rosen formulated the phenomenon of the distance effect, whereby the position or momentum of one quantum particle could be determined from the measurement of another particle, which also applies the principle of non-locality. We can create EPR pairs with a Controlled-NOT gate (CNOT gate), but in quantum optics we need a more complex system. First, we want to show under what physical conditions entangled quantum bit pairs can be created [1].

One implementation of EPR can be the cascade transition used by Alain Aspect et al. They were able to reach an excited state of the calcium atom from which they could only return to the ground state by emitting two photons. In turn, the photons moved in random directions, but if they were detected in opposite directions, they were polarization-correlated, i.e. entangled [5][6].

They then began to study the interaction between nonlinear crystals and lasers, which led them to another method for creating EPR. The other option is called spontaneous parametric down-conversion, which requires the use of nonlinear optical crystals (β-Barium Borate). Irradiated by a violet laser, it creates photon pairs in the infrared. Due to momentum conservation, EPR pairs can be detected in the opposite direction to the irradiated laser beam [7].

III. QUANTUM COMMUNICATION PROTOCOL

In this section, we present two quantum communication protocols, both based on entanglement. The technique was developed in 1993 [8], and the first successful experiment was carried out in 1998 [9]. In 2017, single-photon quantum bits were teleported between the Chinese Micius quantum satellite on the Low Earth Orbit and a ground-based observatory via an uplink channel [10]. This is a huge step towards the creation of a global-scale quantum internet.

A. *Quantum teleportation*

For the procedure, we need an EPR source and measuring equipment. In this protocol, both the classical and quantum channels have an important role to play. First, we distribute an EPR pair between Alice and Bob, then Alice interleaves it with the quantum bit to be transmitted (secret message). She performs a Hadamard gate operation on it, which puts the quantum bit in superposition. Alice then takes measurements on her quantum bits, the results of which she sends to Bob on the classical channel, since after the measurement, Alice will only have classical bits. However, Bob must wait for the measurement results because he must perform transformations on his quantum bit depending on them. After that, he will have the same state what Alice had originally. Figure 1. shows the steps of the protocol operation.

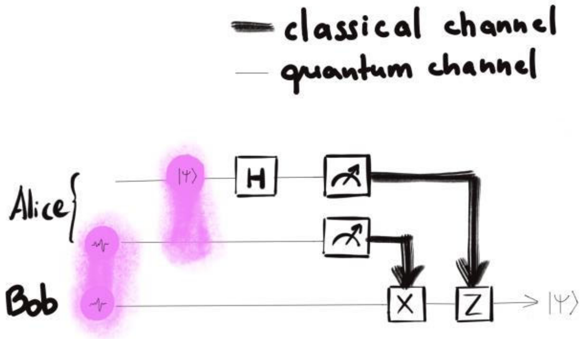

Fig. 1.
Visualization of quantum teleportation

B. *E91 protocol*

The E91 protocol, formulated by Artur K. Ekert, is one of the QKD protocols based on the entanglement phenomenon [11]. Figure 2. shows the elements of E91 protocol. The first EPR pair is split between Alice and Bob. First Alice measures the resulting quantum bit according to her own base directions, which in this case are:

$$[\uparrow, \nearrow, \longrightarrow]$$

Bob then measures according to his own base directions:

$$[\nwarrow, \uparrow, \nearrow]$$

Their measurement bases are known, but the specific measurement results are random. They then split the measurement results according to their base directions. There will be groups where the measurement direction was the same, and groups where it was not. The set of results for which different base directions have been applied is used to check whether there was an eavesdropper in the system, for which a Bell's test is performed. If the result shows that there was no third party in the communication, then the key bits can be detected from the results in the common baseline direction.

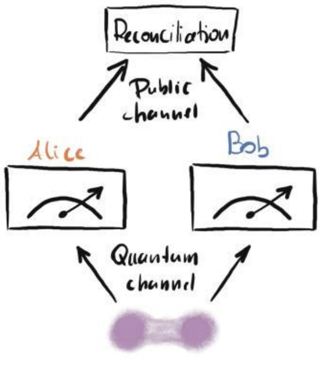

Fig. 2.
Visualization of E91 protocol

IV. QUANTUM MEMORY STRUCTURES

The main task of quantum memory is to store the incoming qubits with high fidelity for a given time and then enable their efficient read out. Its state is not measured during the read-in and read-out process because then its wave function would collapse and it would become a classical information-carrying unit. A schematic of this is shown in Figure 3.

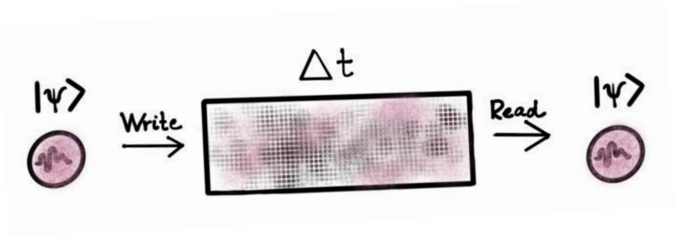

Fig. 3.
Visualization of quantum memory

From a quantum communication point of view, the most important properties are storage time, fidelity, efficiency [12]. By fidelity, we mean the degree of similarity between the quantum bits read out from quantum memory and the quantum bits read in. By efficiency, we mean that we read out the quantum bit we need it. As mentioned, qubits are very sensitive to decoherence due to interaction with environment, which has a big impact on the efficiency of quantum memory. We have also mentioned that we can encode quantum information into the polarization of a photon, the nuclear spin of atom or even electron spin. Therefore, one of the biggest challenges in the development of quantum memories is how to relate photon-based quantum information to atomic systems. The spin-photon effect can provide a solution to this problem, using an entanglement swapping protocol [13][14]. In this section, we present two quantum memory platforms.

A. Nitrogen-vacancy centers

One of the most promising quantum memory platforms is the NV center found in diamond, a solid-state defect. This defect in the crystal structure affects the optical and magnetic properties of the material. A vacancy means that there is a vacant atomic space between the carbon atoms of the diamond, to which a nitrogen atom is attached. It is also called color-center technology because it has a visible range of single-photon absorption and emission spectra [17].

The NV-center's electron spin-based quantum bits can be superpositioned by microwave and optical excitation. The coherence time can be up to $10\,ms$ for ^{13}C isotopes. Alternatively, the electron spin-based quantum bits can be entangled with a CNOT gate to the nuclear spin, i.e. this platform is capable of spin-photon interfacing.

It is one of the most likely candidates for quantum memory, as it already satisfies several criteria such as: scalability, universal gate operations, special measurement principle (Optically detected magnetic resonance), spin-photon interface and integrability.

To entangle new quantum bits to a photon-based system, we need the storage of quantum states during entanglement. This means that quantum bit coherence time must be longer than the time required to entangle new quantum bits. Also, one of the most important properties is scalability, i.e., storing as many entangled quantum bits as possible at the same time, since more complex tasks and error corrections mean that it is not sufficient to use only one quantum bit [15].

In Figure 4., we show a structure with ^{13}C nuclear spins interconnected by NV centers, where the nuclear spins are the data qubits and the electron spins are the communication qubits. The nuclear spins are written to preserve quantum information, while the electron spins are tasked with providing entanglement for the new qubits. Communication quantum bits are placed between two highly reflecting optical cavities to enhance the interaction of photons with quantum bits. The state of the electron spin can be transferred to the nuclear spin by hyperfine interaction excited by appropriate microwave or radiofrequency pulses [16].

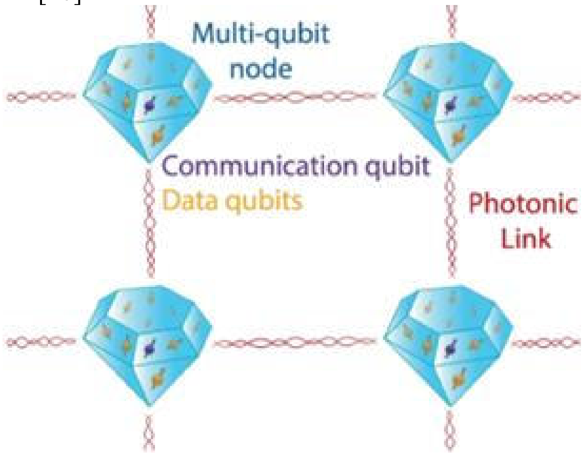

Fig 4.
NV-center based multi-qubit node in diamond [16]

B. Electromagnetically Induced Transparency

EIT is also one of a quantum memory platform that exploits optical nonlinearity. It shows quantum interference, i.e., the ability of light to propagate in the opaque atomic medium. It is commonly used for Bose-Einstein condensates and can be used to cool and store atoms. There are several models of EIT-based quantum memory, but in our case we stick to optically driven memory, as our research was on photon-based quantum communication.

In this case we need a strong optical field to trigger the absorption of photons in the memory. Figure 5. also clearly shows Λ structure where there are two ground levels and one excited [18].

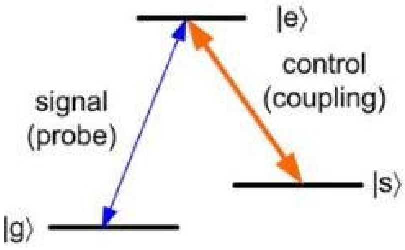

Fig. 5.
Λ-structure EIT [18]

First, initialization is performed, i.e., a coupling beam (strong control field) is used to bring all the atoms to the ground state. Next, the excited and ground levels are controlled [20]. Then the system receives the signal pulse (weak field), at which point the coupling beam power is reduced to zero and the states of the signal photons can be written into the nuclear spins of the atoms. So, in the absence of a strong field, the weak field is lost in the two-level system.

It has the advantage of having a long storage time (1s) for both cold/hot atomic sources. The state of the quantum bit can be read out at any time. However, it is not suitable for storing more than one photon. However, due to its rapid development, storage times of up to 40s have been achieved [19].

V. RESULTS OF SIMULATION

An important element of satellite quantum communication is the deployment of a channel with high quantum efficiency. It is worthwhile to prioritise both LEO and GEO orbital constellations in terms of channel quantum efficiency. In both cases, it is important to know whether the channel is uplink or downlink, since in the latter case the atmospheric attenuation of the channel will be much lower than in the uplink case. In the LEO orbit, the quantum bit has a shorter path to travel, but the LEO satellites much faster, unfortunately results in a short time window for the channel to be established. Conversely, GEO constellations at ~35786km altitude have an easier time to establish a continuous quantum channel, because the satellites are in a fixed orbit.

In this section, we present the quantum memory-based approach for one or more satellite constellations. For both models, we have chosen currently operating terrestrial optical receiver stations: Teide Observatory (Canary Islands), Helmos Observatory (Peloponnese), ESA-ESTEC (Noordwijk). For our research we used data from the Starlink TLE. Figure 6. shows a visualization of this system, where the satellite orbits at an altitude of 550 km and our aim was to see when and for how long the satellite is visible from the observatories. For optical communication, we specified a minimum elevation angle constraint of 30°. However, at angles lower than this, a bad signal-to-noise ratio would occur in optical communication, i.e., information loss could occur

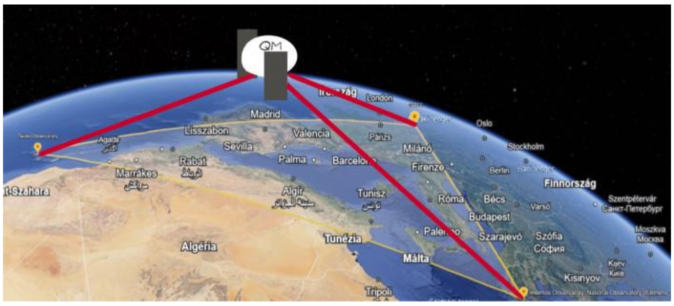

Fig. 6.
Visualization of a quantum memory-based satellite

To do this, we first examined the cases where at least two receiver stations are visible at nearly the same time instant, the results of which are shown in Table 1. Figure 7. shows that it starts to become visible from Noordwijk at time 13485s, continues until 13653s, and then becomes visible from Helmos observatory at time 13761s. This shows that if we want to install quantum memory on this satellite, it will have to store it with high fidelity for at least 108s from Noordwijk

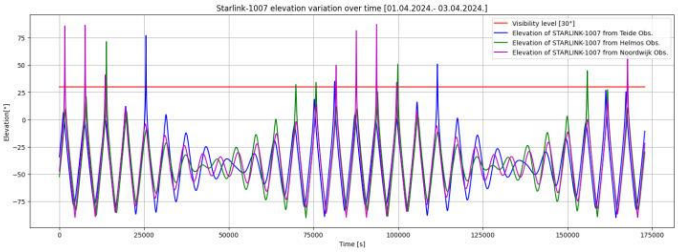

Fig.7.
Elevation of Starlink-1007 satellite from observatories

Observatory	**Teide**	**Helmos**	**Noordwijk**
Initial sampling time moments [s]	…	13761	13485
	81178	…	81586
	…	99794	99598

Table 1.
Sampling time of Starlink-1007 satellite

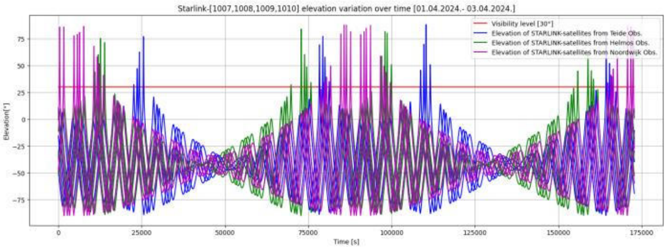

Fig. 8.
Elevation of Starlink - [1007,1008,1009,1010] satellites from observatories

Therefore, we have also explored the possibility of installing quantum memory on several satellites orbiting in LEO orbit, to reduce the storage time requirement. The result is shown in Figure 8. In this case, we can achieve longer coverage in time if we also consider the possibility of inter-satellite communication. Table 2. shows the moments of visibility of the 4 satellites when they reach a minimum elevation angle of 30° as seen from at least one of the receiving stations. There are several time instants associated with the sampling, but only the time instants close to each other, which would be necessary for the communication between the satellites, are considered in the table. However, we obtained the result that a minimum storage time of 525 s would be required, which is not yet feasible due to current technological limitations.

	Starlink-[1007,1008,1009,1010] satellites				**Observatories**
Initial sampling time moments[s]	25434	23545	22602	24198	**Teide**
	81178	79215	78225	79889	
	111468	109550	108576	110213	
	-	165251	164243	165939	
	13761	11857	10880	12519	**Helmos**
	69757	73745	72742	74423	
	-	97873	96887	98539	
	155726	159785	158771	160474	
	13485	11558	10561	12230	**Noordwijk**
	81586	79728	84632	80370	
	87535	85624	90608	86291	
	93512	91603	96587	92269	
	99538	97587	-	98260	

Table 2.
Sampling of Starlink-[1007,1008,1009,1010] satellites

CONCLUSION

The aim of our research was to investigate the conditions under which a quantum communication network could be built for a satellite system currently orbiting LEO, focusing on quantum memories. It is clear from our simulation results that with 1 LEO orbiting satellite we are not able to cover the given receiver stations for long time intervals. Therefore, we increased the number of LEO orbiting satellites tested, but unfortunately this was still insufficient, as it would require at least several minutes of storage time on the part of the quantum memory. Therefore, it would be worthwhile to extend this quantum network model to GEO satellites in the future. In parallel, further developments in the world of quantum memory platforms should be pursued.

ACKNOWLEDGMENT

K. Oláh would like to thank Ferenc Simon, who helped in the field of quantum memory. This research was supported by the Ministry of Culture and Innovation and the National Research, Development and Innovation Office within the Quantum Information National Laboratory of Hungary (Grant No. 2022-2.1.1-NL-2022-00004)

REFERENCES

[1] S. Imre, F. Balázs, Quantum Computing and Communications: An Engineering Approach, John Wiley & Sons Ltd. (2004) DOI:10.1002/9780470869048

[2] Á. Schranz, B. Solymos, and M. Telek. “Stochastic performance analysis of a time-of-arrival quantum random number generator”. In: IET Quantum Communication (2023) DOI:10.1049/qtc2.12080

[3] E. Udvary, "Integration of QKD Channels to Classical High-speed Optical Communication Networks", Infocommunications Journal, Vol. XV, No 4, December 2023, pp. 2-9., DOI: 10.36244/ICJ.2023.4.1

[4] D.J. Griffiths, Introduction to quantum mechanics, 2nd ed.Pearson Education. Inc., (2005), ISBN: 0131911759

[5] Freire Junior, O. Alain Aspect’s experiments on Bell’s theorem: a turning point in the history of the research on the foundations of quantum mechanics. Eur. Phys. J. D 76, 248 (2022). DOI: 10.1140/epjd/s10053-022-00542-z

[6] Alain Aspect, Philippe Grangier, and Gérard Roger, Experimental Realization of Einstein-Podolsky-Rosen-Bohm Gedankenexperiment: A New Violation of Bell's Inequalities, Phys. Rev. Lett. 49, (1982) DOI: 10.1103/PhysRevLett.49.91

[7] S. Karan et al., Phase matching in β-barium borate crystals for spontaneous parametric down-conversion, Journal of Optics, Vol.22, (2020) DOI: 10.1088/2040-8986/ab89e4

[8] C.H. Bennett, G. Brassard, C. Crépeau, R. Hozsa, A. Peres and W. K. Wootters Teleporting an unknown quantum state via dual classical and Einstein-Podolsky-Rosen channels, Phys. Rev. Lett. 70, (1993), DOI: 10.1103/PhysRevLett.70.1895

[9] D. Boschi, S. Branca, F. De Martini, L. Hardy, S. Popescu, Experimental Realization of Teleporting an Unknown Pure Quantum State via Dual Classical and Einstein-Podolski-Rosen Channels, Phys.Rev.Lett.80 (1998), DOI: 10.1103/PhysRevLett.80.1121

[10] Chao-Yang Lu, Yuan Cao, Cheng-Zhi Peng, and Jian-Wei Pan, Micius quantum experiments in space, Rev. Mod. Phys. 94, (2022) DOI: 10.1103/RevModPhys.94.035001

[11] Artur K. Ekert, Quantum cryptography based on Bell’s theorem, Phys. Rev. Lett. 67, (1991), DOI: 10.1103/PhysRevLett.67.661

[12] Simon, C., Afzelius, M., Appel, J. et al., Quantum memories. Eur. Phys. J. D 58, 1–22 (2010), DOI: 10.1140/epjd/e2010-00103-y

[13] Mario Mastriani, Simplified entanglement swapping protocol for the quantum Internet, Scietific Reports, (2023), DOI: 10.1038/s41598-023-49326-4

[14] J.Jin, M.li Grimau, L. Giner, J. Slater, M.R.Lamont, V.Verma, M.D. Shaw, F.Marsili, S.W.Nam, D.Oblak,W.Tittel, Entanglement swapping with quantum-memory-compatible photons, Phys. Rev. A 92, (2015), DOI: 10.1103/PhysRevA.92.012329

[15] Maximilian Ruf, Noel H. Wan, Hyeongrak Choi, Dirk Englund, Ronald Hanson, Quantum networks based on color centers in diamond, Journal of Applied Physics (2021), DOI: 10.1063/5.0056534

[16] C. E. Bradley et al., Robust quantum-network memory based on spin qubits in isotopically engineered diamond, npj Quantum Inf 8, 122 (2022) DOI: 10.1038/s41534-022-00637-w

[17] Ádám Gali, Ab initio theory of the nitrogen-vacancy center in diamond, Nanophotonics, De Gruyter (2019), DOI: 10.1515/nanoph-2019-0154

[18] Lijun Ma, Oliver Slattery, and Xiao Tang, Optical quantum memory based on electromagnetically induced transparency, Journal of Optics, Vol.19. (2017), DOI: 10.1088/2040-8986/19/4/043001

[19] Georg Heinze, Christian Hubrich, and Thomas Halfmann, Stopped Light and Image Storage by Electromagnetically Induced Transparency up to the Regime of One Minute, Phys. Rev. Lett. 111,(2013) DOI: 10.1103/PhysRevLett.111.033601

[20] R.K. Ramakrishnan et al, The Quantum Internet: A Hardware Review, J Indian Inst Sci 103, 547–567 (2022). DOI: 10.1007/s41745-022-00336

Study of Microwave Electrothermal Propulsion System

Rhea R. Mulki
Department of Aerospace Engineering
Amity University Dubai
Dubai, UAE
rhearanjit01@gmail.com

Efstratios L. Ntantis
Department of Aerospace Engineering
Amity University Dubai
Dubai, UAE
entantis@amityunivesity.ae

***Abstract*—Since 1960, the propulsion landscape for satellites and spacecraft has diversified significantly. While chemical rockets remain prevalent, alternative methods like nuclear power, electrostatic, and magnetic drives aim to enhance efficiency by boosting exhaust velocities and reducing fuel requirements. A notable innovation is beam-powered propulsion, or directed energy propulsion, which involves transmitting ground-based energy to spacecraft. Among these, electrothermal thrusters stand out, using electrical energy to heat propellant and generate thrust, with variants like resistojets and arcjets currently in use. One advanced iteration, the Microwave Electrothermal Thruster (MET), replaces electric arcs or heaters with plasma for propellant heating, addressing the limitations of older designs. MET performs better by converting a resonant cavity into a heating chamber and employing microwaves to induce plasma heating. A Bogazici University's Space Technologies Laboratory (BUSTLab) study tested a MET prototype using Helium gas, measuring chamber parameters, mass flow rate, power levels, thrust, and specific impulse (Isp). At 500 W power, they achieved a remarkable Isp of 347 seconds and 266 mN thrust. This experimentation showcases the potential of MET technology in achieving high-efficiency propulsion for future spacecraft, marking a significant step towards more sustainable and capable space exploration methods.**

Keywords—thrust generation, space exploration, microwave amplification, propellant efficiency, interplanetary travel

I. INTRODUCTION

Rocket propulsion is crucial for maneuvering aircraft and spacecraft across diverse environments. As Newton's third law of motion dictates, it operates on the fundamental principle of generating thrust through propellant acceleration. This thrust plays a pivotal role in navigating through atmospheric and space environments. However, space debris in orbit significantly challenges spacecraft navigation and safety [1]. Furthermore, specific orbital positions known as Lagrange points, where gravitational forces reach equilibrium, hold strategic importance for deploying and maintaining satellites and spacecraft due to their stable nature and reduced fuel requirements for station-keeping [2].

In rocketry, the traditional method of chemical propulsion achieves thrust through chemical reactions such as fuel combustion within a rocket engine's combustion chamber. This heated exhaust is directed through a nozzle to accelerate the gas, generating thrust. Unlike turbine engines and propeller-powered aircraft that use atmospheric air as a working fluid, rockets use hot exhaust gases generated from the combustion of enclosed propellants. This distinction allows rockets to function in space without atmosphere, unlike propeller-powered aircraft or turbines [3]. While chemical rockets dominate space exploration, navigation, and research today, other forms of rocket propulsion have been considered since the field's earliest days to improve spacecraft's efficiency. One such category of rocket propulsion is beam-powered propulsion. Beam-powered propulsion is a classification of aircraft or spacecraft propulsion in which energy from a remote power plant is beamed to spacecraft/aircraft. Beam-powered propulsion is classified as laser, microwave, and electric.

Nowadays, launching into orbit is still done the same way it was six decades ago. As assessed in the rocket equation, this is somewhat because of the structural limitations of current materials and the limited specific impulse (Isp) of chemical propellants that achieved the 460 second limit. Currently, the choices are bi-modal: high thrust with lower Isp, such as in chemical propulsion, or high Isp at the expense of low thrust, such as in electric propulsion. Electric propulsion technology, over the past 30 years, has made considerable advancements in propulsion. Electric propulsion can be classified as electrostatic, electromagnetic, and electrothermal. This research paper discusses electrothermal propulsion, which uses microwave power as the energy source [4].

Microwave Electrothermal Thruster (MET), a classification of electric propulsion, is currently considered to be utilized in space propulsion implementations such as satellites and spacecraft. The widely studied types of electrothermal systems are resistojets and arcjets. They are used in various fields on space platforms but also have limitations. Scientists have been looking into various other substitutes for arcjets and resistojets due to the cathode erosion problem and the limit of thermal endurance [5]. For these reasons, scientists have proposed using MET [6]. MET uses plasma in lieu of an electric arc generated by electrodes or heaters. This makes MET a better choice over arcjets and resistojets. Scientists have discovered that in MET, the temperature of the walls increases when used and can be overcome by using cooling gas.

MET thruster was first introduced in the 1960s when scientists used electrodeless microwaves to create discharge that heats the gas inside a cylindrical resonant cavity. They believed that electrodeless discharge would have high efficiency while heating gas and reduce erosion on the surface of the thruster [7]. However, in the 1980s, a simple electric thruster was in use because of the problems faced by MET. Despite these disadvantages, the interest in this topic started growing again during the 1980s because of the efficiency offered by microwave sources [8]. The Pennsylvania State University, under the guidance of NASA and AFOSR, researched MET [9]. NASA reached the peak on MET with their 11 kW thruster, which operated utilizing 0.915 GHz at NASA Glenn Research Center [10]. MET shows promise for spacecraft propulsion and maneuvering. MET promises advantages in operating life, efficiency, and propellant selection compared to other electrothermal thrusters.

II. LITERATURE REVIEW

Jack Mattingly's report in [11] highlights the fundamental operation of rocket engines, which expel a working fluid acting as reaction mass to generate thrust, adhering to Newton's third law. This principle underpins all electromagnetic propulsion systems. Martin Hawley et al. [12] elaborate on the potential of MET for spacecraft propulsion, citing advantages in operating life, efficiency, and propellant selection over other electrothermal thrusters.

Daniel Clemens notes in [13] the extensive use of electric propulsion systems in around 200 spacecraft, including resistojets, arcjets, ion thrusters, and Hall thrusters. Serhan Yıldız et al. in [14] stress the critical role of selecting propulsion systems for communication satellites, evaluating MET feasibility among other electrothermal thrusters like resistojets and arcjets. They also highlight MET's advantages over traditional thrusters like resistojets and arcjets, particularly in its use of plasma, making it more efficient and durable.

John Power discusses MET's suitability for medium to high-power spacecraft propulsion due to its electrodeless design and high-pressure capabilities [15]. John Brandenburg et al. in [16] mention MET's safety and ease of use for transfer missions. Mikhail Abaimov et al. mention a CubeSat employing MET propulsion to enhance mission possibilities [17]. They contrast MET with chemical rockets' complex plumbing and delicate components, Hall-effect thrusters' high power requirements, and Arcjets' electrode erosion issues, which limit their use in CubeSat missions [18].

III. THEORY OF MICROWAVE ELECTROTHERMAL THRUSTER

The MET utilizes an electromagnetic resonant cavity in which plasma is heated with propellants' help. The propellant gas heats up in the heating chamber, producing the thrust. After the plasma commences, it performs the resistive load function and increases the gas's temperature by absorbing microwave energy.

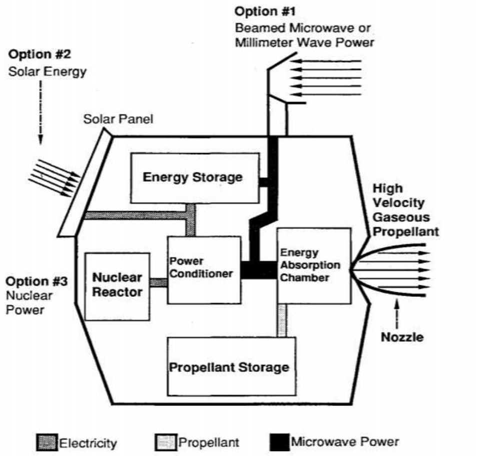

Fig. 1. Proposed MET system schematic [19]

Figure 1 shows a schematic of the system, including three options for the power source for the thruster. In option 1, microwave or millimeter-wave radiation is directed to the spacecraft from an external source like the planetary base or space station. The radiation is concentrated on the coupling system, which helps sustain and heat the plasma. Expansion of the working fluid as it passes through a nozzle produces thrust. Option 2 includes on-board solar panels in a self-contained arrangement. Option 3 is a nuclear reactor that generates electricity sent to the microwave-frequency oscillator.

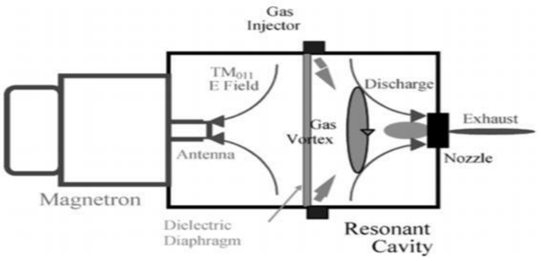

Fig. 2. Diagram of the MET thruster in its present form [6]

The plasma is produced by the microwave using MET. MET uses a converging-diverging type of nozzle to produce thrust. The gas produced goes through the nozzle and changes the heat energy into kinetic energy, leading to the gas's high-velocity release. A resonant cavity, as seen in Figure 2, is a structure that produces electromagnetic radiation with standing waves inside a closed system. The free electron accelerates and interacts with neutrals due to Lorentz's force, leading to elastic collision, which releases momentum. This process leads to plasma formation with the same energy as the microwave beam [15]. Interacting with the plasma heats the propellant gas. MET has two parts: a nozzle and an antenna. A nozzle at the nozzle plate is attached to the end of the cavity (*see* Fig. 2). The antenna design uses the concept of operating frequency. A quarter of the wavelength is used to maximize radiation [20].

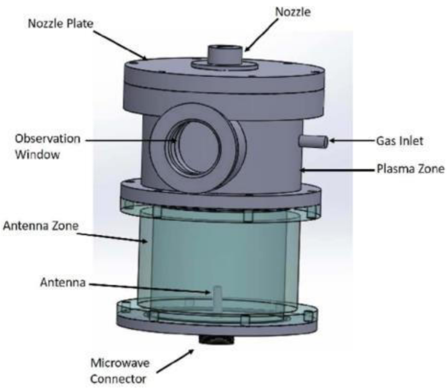

Fig. 3. Proposed MET system schematic [14]

A prototype MET illustrated in Figure 3 was developed at the BUSTLab. The operating frequency is 2.45 GHz. In this research paper, Helium gas is used as the working fluid at microwave power of 400 W and 500 W. This experiment is done to study the efficiency and performance of MET. The investigational figures, suitable equations, and values of the BUSTLab MET thruster are evaluated [21].

IV. Comparison of Electrothermal Propulsion Systems

The resistojet, arcjet, RF induction arcjet, and MET are alternative and competitive propulsion systems. Every system has advantages and disadvantages. Table I summarizes the comparisons between these systems.

TABLE I. COMPARISON OF COMPETITIVE ELECTROTHERMAL PROPULSION SYSTEMS [22]

System Type (Status)	**Advantages**	**Disadvantages**	**Thrust/Power (mN/kW)**
Resistojet [Flying]	DC/AC system well developed, Low risk	Deposition from hydrazine gas generators, Tortuous flow path	300-500[31]
Arcjet [Near-flight tests]	DC lab system is a well-developed, Uncomplicated power system	Electrode erosion limits life	70-110[35] 110-170[36]
Electrodeless Arcjet (RF Induction) [Under development]	Electrodeless, EM transport to gas, Lighter & cheaper power supply (than microwave)	Less efficient coupling	130[4]
Microwave electrothermal thruster [Under development]	Electrodeless, EM transport to gas, very efficient coupling	Low-power processor efficiency	400-500[6,14] 280[28]

A. *Resistojet*

The resistojet is considered the simplest electrothermal thruster (*see* Fig.4). This system is currently used in space applications. Its working fluid is heated over and around a resistance heating coil. Since the heater element must have a higher temperature than the working fluid, choosing the material is the major challenge to meet the mechanical strength and electrical performance requirements at operating temperatures. Material temperature constraints limit the temperature of the working fluid, which controls the specific impulse. Maximization of propellant temperature within these constraints requires a large contact area.

The resistojet is a low-risk propulsion system. The primary reliability concern stems from the possible deposition of nonvolatile residues downstream of the hydrazine gas generators, which form a significant element of the current flight-type resistojet system. Various gases can serve as propellants in these systems. Resistojet is an optimal choice for space exploration due to its straightforward power and propellant-feeding mechanisms. Additionally, it offers the advantages of being lighter and more compact. In the event of a heating system failure, a cold gas system can be employed as a backup. Notably, there is no need for electric charging like thrusters that emit ions. Resistojets also have drawbacks, such as their heater elements, where the melting point and thermal endurance are the limiting factors even when the walls are cooled.

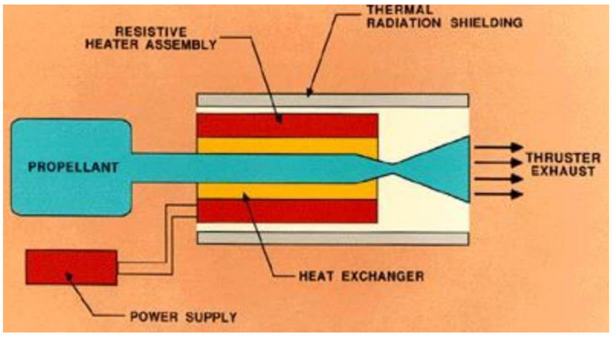

Fig. 4. Resistojet Assembly [23]

B. *Arcjet*

In an arcjet (refer to Fig.5), an arc forms between electrodes, heating the working fluid as it passes through. Unlike the resistojet, where heat transfer from surfaces to fluids is a concern, the arc serves as the primary energy transfer mechanism in the arcjet. This reduces the heat transfer problem, allowing higher working-fluid temperatures and specific impulses than resistojet. However, designing arcjet electrodes that interact with the working fluid presents a significant engineering challenge, akin to the materials issue in resistojet design. Laboratory model arc jets have reached a high maturity level, having passed life tests lasting hundreds of hours [24].

Arcjets use AC/DC arc discharge to attain high specific impulse and exit velocities. It was also found that these values are higher than those of other thrusters except ion or Hall effect thrusters. The anode is the nozzle, and the cathode is Tungsten or alloy. The discharge of the arc is produced at the constrictor region. Augmented Hydrazine arcjets provide two times increment in specific impulse. This helps reduce the spacecraft's mass, thereby increasing its lifetime.

The main limitation of arcjet thrusters is cathode erosion. Vaporization happens due to the striking of the ions on the cathode surface at a significant pace. In addition, the rupturing of the anode surface is caused by an electron current. This leads to a gap formed between the anode and cathode. The arc will not be formed due to the Coulomb law, and also, the high current of the arc affects the motion of the ion, leading to instability of the arc and splitting it due to the magnetic field effect. This also affects the gas energy transfer and electrode erosion. Erosion will be affected by cathode material, geometry, and propellant type. Erosion does not happen because of some errors but is already induced. It can be reduced by following some measurements, such as changing the flow pattern and selecting materials with higher thermal endurance. Arcjet has a heavier and more complex power processing unit than resistojet.

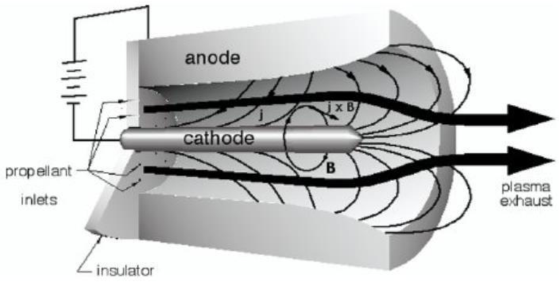

Fig. 5. Arcjet Assembly [25]

C. Electrodeless Arcjet (RF Induction)

A Radio-Frequency (RF) induction or electrodeless arcjet uses a radio-frequency induction coil to generate and sustain plasma and heat the propellant [26]. This eliminates the problems associated with arcjet electrodes. Material specifications for the plasma chamber wall require that it be transparent to radiation at the frequency used under operating conditions. The concept is similar in many respects to the microwave electrothermal thruster but operates at lower frequencies. The lower frequency use may permit a smaller, lighter power conditioning system than the microwave one. On the other hand, the energy coupling from the induction coil to the plasma may not be as efficient at lower frequencies as it is at microwave frequencies. A typical assembly of electrodeless arcjet is presented in Figure 6.

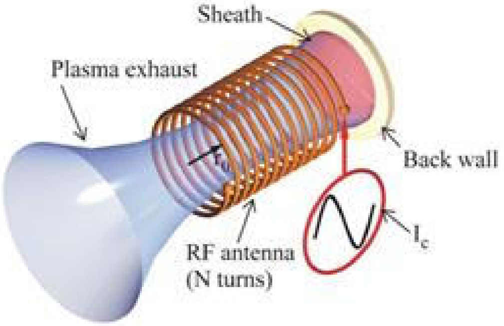

Fig. 6. Electrodeless Arcjet Assembly [27]

D. Microwave Electrothermal Thruster (MET)

The MET (*see* Fig.7) may have significant advantages over the three competitive systems listed in Table I. It may be considered a microwave-frequency version of the RF induction (electrodeless) arcjet and shares many features with the latter. Energy is transferred directly to the propellant by radiation rather than by conduction. No electrodes need to be in contact with the working fluid. Material specifications for the plasma chamber wall require that it be transparent to microwaves under operating conditions. The heat and chemical resistance used in MET are similar to those in the conventional rocket thrusters, so the traditional rocket layout and construction could also be used in the MET assembly. The distance between the plasma and the nozzle can be varied to provide operation with different propellants or under varying pressures and flows.

MET can overcome the drawbacks of resistojet and arcjet. The working fluid is heated using plasma. MET increases the temperature of the propellant by utilizing free-floating plasma. In resistojet, the propellant gas temperature limit imposes the filament heater's thermal endurance. This limit is eliminated in MET due to the absence of a solid heater element. Cathode erosions and arc instability limitation in arcjet thrusters will be eliminated due to the utilization of plasma. Another benefit of MET is that several gases can be used as propellants. Water vapor can be used as a working fluid and achieves a specific impulse of around 450 seconds. The dimension and impulse of MET can be reduced by varying the electromagnetic field frequency.

The MET systems have not been used in space yet, which does not provide adequate information about the spacecraft integration levels. The experimental models developed to date have power processors and microwave generators heavier than the thruster alone.

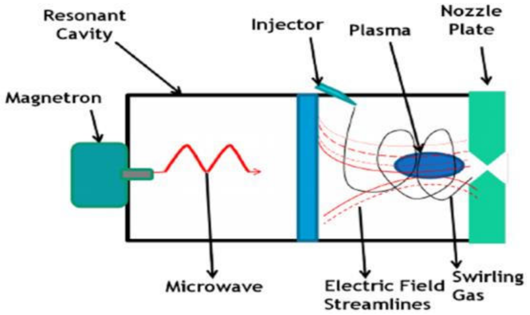

Fig. 7. MET Assembly [28]

V. EXPERIMENTAL SETUP

The MET prototype, developed by BUSTLab, was designed for a microwave frequency of 2.45 GHz power to 1200 W. The availability and cost-effectiveness are the reason for selecting 2.45 GHz as the microwave frequency. This MET comprises an antenna, nozzle, resonant cavity, and quartz separation plate, as seen in Figure 8. The inner diameter and length of the resonant cavity are 100 mm and 175 mm, respectively, and these are ideal for the operations conducted at 2.45 GHz. These dimensions are chosen for operating at 2.45 GHz frequency. Stainless steel is the material used for the body of the thruster. There are two holes for connection purposes: Gas feeding and measuring pressure. The coupling probe is made of copper and is a 31 mm long (λ/4) antenna. To separate the antenna zone from the plasma zone, a 10 mm thick plate of quartz is used. A window with a diameter of 50mm is situated at the cavity wall for plasma observation. A converging-diverging nozzle is placed in a section in the resonant cavity.

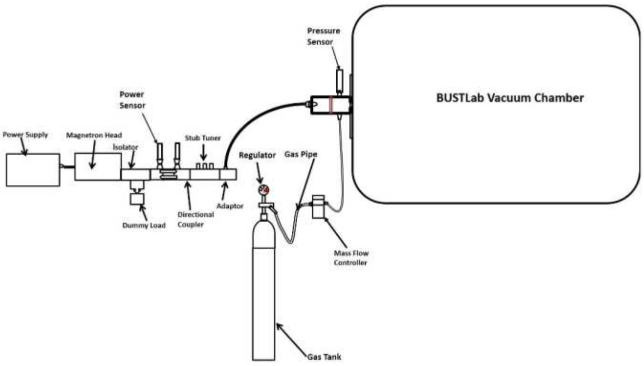

Fig. 8. Experimental Setup [21]

The main components in the setup used for this experiment are a thruster, microwave generating system, microwave transmitter, gas feeder, measuring system, and vacuum system. A vacuum chamber is attached to the MET thruster via a port for the experiment. A supply of power and a magnetron with a power of 1.2 kW are used for microwave generation. This allows power levels to be increased by 12 W for each observation. The function of a microwave transmitter is to transmit microwave energy to the resonant cavity. The microwave transmitter comprises a coupler, an isolator, and a waveguide to coax adaptor. The isolator can shield the magnetron from the damage of reflected power. By employing a tuning system, the power coupling can be strengthened, and reflections can be minimized. The function of the adaptor is to make the system flexible and to help move the waveguide to the coax cable. Two power sensors are utilized to measure the power levels that are delivered and reflected [29].

VI. EXPERIMENTAL RESULTS

In the current study, experimental data are used to evaluate thruster performance results. The chosen mass flow rates for the operation of this prototype MET are 30 to 84 mg/s and power values of 400 W and 500 W. The mass flow rate value is incremented for each power level until the plasma quenches. The experiments are conducted thrice for every mass flow rate. After attaining the proper pressure condition, microwave power is incremented to the required power. Before plasma formation, around 50% of microwaves are caused to reflect. The beginning of plasma discharge minimizes the reflections. As the mass flow rate increases, pressure also increases, which causes plasma volume to contract and the plasma to shift to the inlet region of the nozzle. If the backscattering is still high, the system is tuned by utilizing a tuner. The discharge chamber pressure reading for every mass flow rate is taken down.

Another set of experiments was conducted to determine cold gas conditions. Mass flow is brought in at required magnitudes for these tests, and the chamber pressure is noted down without microwave energy supply after the plasma cavity is cleared using the vacuum chamber. The chamber gas temperature is found using the chamber pressure values data and constant heat rocket equations.

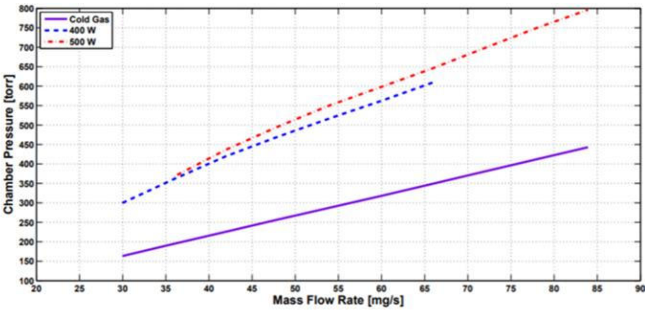

Fig. 9. Chamber pressure recorded values for cold gas, 400W, 500W microwave power

Data for chamber pressure is measured for power of 400 W, 500 W and cold gas. There is a linear relation between chamber pressure and mass flow rate for the three operations, as seen in Figure 9. Increasing power causes chamber pressure to rise. This happens because the propellant is heated electrothermally. The pressure level at 400 W is about two times that of cold gas condition. There is a slight increase in pressure with an increase in power level from 400 W to 500 W. The maximum pressure at which plasma can be sustained is about 800 torr at 500 W and around 600 torr at 400 W.

In Figure 10, a surge in chamber temperature is assessed in terms of input power for different mass flow rates. Before chamber temperature reaches the max value, the plasma volume decreases as pressure is incremented, so thermal losses decrease due to gas temperature increments. When the mass flow rate crosses its maximum value, the gas cannot be heated to a high temperature as the plasma and gas interaction time decreases. 1030 K and 1114 K at 400 W and 500 W, respectively, are the values of maximum chamber temperature, as shown in the graph of Figure 10.

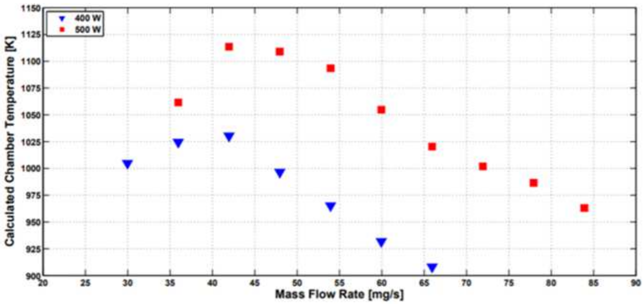

Fig. 10. Chamber temperature data for 400 W & 500 W microwave power

The values of exhaust velocity and specific impulse depend on temperature. In Figure 11, specific impulse (Isp) is similar to temperature values. The highest value of Isp is 334 seconds for 400 W and 348 seconds for 500 W, which is similar to resistojets [30]. Increasing power increases specific impulses. The specific impulse at 500 W is around 15 seconds greater than 400 W for the same mass flow rate.

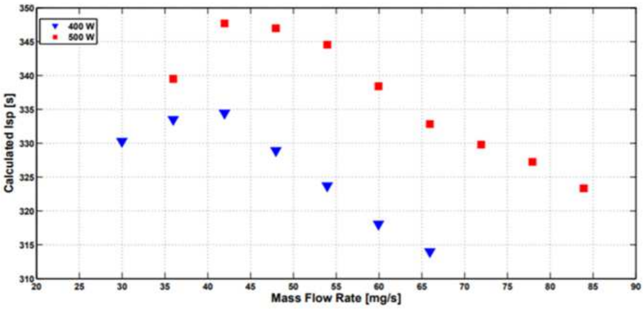

Fig. 11. Specific impulse values at 400 W & 500 W microwave power

It can be observed from Figure 13 that the values of thrust increase linearly for the increase in the mass flow rate value. The thrust value rises from 97 mN to 203 mN and 120 mN to 266 mN for 400 W and 500 W. The thrust value at 500 W has, to some extent, a greater value than 400 W.

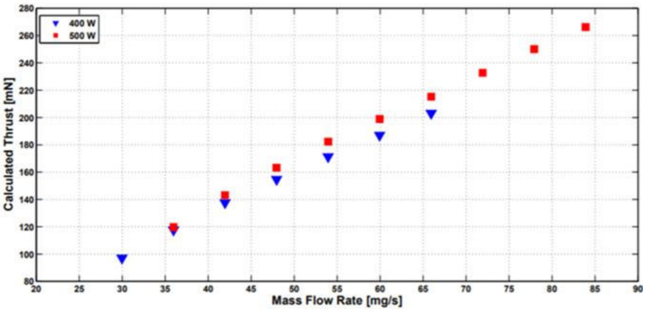

Fig. 12. Thrust values obtained at 400W and 500W power

The efficiency of coupling at these two power levels is around 97%. While the experiments were conducted, the system was tuned for each mass flow rate and power value. As observed in Tables 2 and 3, the incrementing mass flow rate is caused by the thrust efficiency increase. When the thrust efficiency keeps rising, the values of specific impulses drop after a peak. For ideal operations, diminishing specific impulses are required to gain efficiency, and vice versa.

TABLE II. OBSERVATIONS RECORDED AT 400 W INCIDENT POWER

mfr [mg/s]	p_c [torr]	T_c [K]	V_{ex} [m/s]	τ [mN]	I_{sp} [s]	n_c [%]	n_τ [%]
30	300	1005	3240	97	330	98	31
36	361	1025	3272	118	334	98	38
42	420	1030	3281	138	334	98	45
48	470	997	3227	155	329	98	50
54	517	965	3176	171	324	97	54
60	562	932	3120	187	318	97	58
66	609	908	3080	203	314	98	63

TABLE III. OBSERVATIONS RECORDED AT 500 W INCIDENT POWER

mfr [mg/s]	p_c [torr]	T_c [K]	V_{ex} [m/s]	τ [mN]	I_{sp} [s]	n_c [%]	n_τ [%]
36	368	1062	3330	120	339	97	40
42	436	1114	3411	143	348	97	49
48	496	1109	3404	163	347	97	56
54	550	1093	3380	182	345	97	62
60	598	1055	3320	199	338	97	66
66	646	1020	3265	215	333	97	70
72	698	1002	3235	233	330	97	75
78	749	986	3210	250	327	97	80
84	796	963	3172	266	323	98	84

VII. PROSPECTS FOR MICROWAVE ELECTROTHERMAL THRUSTERS

A highly efficient thruster that utilizes water as a propellant for several Lunar and Mars expedited orbital Technologies Corporation and the University of Alabama at Huntsville have proposed ions called Advanced Microwave Electrothermal Thruster (AMET). To improve existing designs, the proposed AMET will incorporate various innovations, which involve the utilization of low frequency (0.915 GHz) to allow high microwave generating efficiency using accessible magnetrons. The Advanced MET imparts a specific impulse around 800 seconds, much above the specific impulse of chemical propulsion. To keep transit times acceptably short, it provides high thrust per unit power and allows the utilization of easy storage of working fluid i.e., water, on the Moon and Mars. Thus, it will be an attractive option for this class of missions. The workforce is experienced in utilizing water vapor as a working fluid for the operation of AMET. In Phase I, AMET is revealed to exhibit practicality using water vapor as a propellant. In Phase II, AMET that has reached near flight is planned to be exhibited. A layout for the AMET propulsion system will also be developed [31].

The CubeSat MET (CμMET) system is currently under development (see Fig.13) to increase the operation potential of 3U, bigger CubeSats. The proposed thruster uses 17.8 GHz microwave frequency at a power of 10 W. Projects on CμMET systems include requisite expansion, electro-magnetic modeling, systems-level layout, and component choice for packing in 1U or 1.5U modules [32].

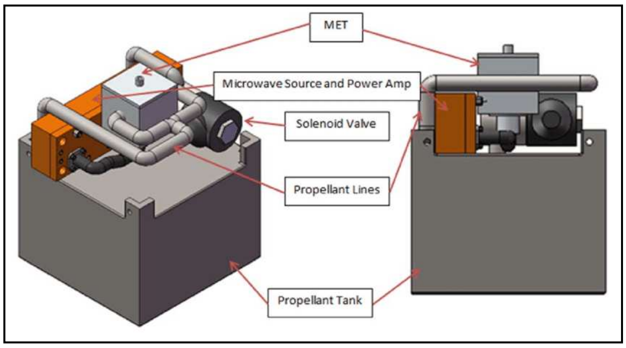

Fig. 13. CμMET Schematic [33]

VIII. CONCLUSION

The MET systems developed by BUSTLabs, operating at a frequency of 2.45 GHz, are evaluated at 400 W and 500 W power and for cold gas. Parameters such as the chamber's temperature, thrust, and specific impulse are calculated using suitable equations, whereas chamber pressure and power are obtained from the instruments. Maximum specific impulse of 348 seconds and thrust of 266 mN is assessed. The resistojets' specific pulse extent is similar to the evaluated specific impulse values at the specified power. It has been noted that incrementing power is beneficial for MET's performance. The MET has several potential advantages over the resistojet and arcjets and is assessed for feasibility as a spacecraft propulsion system. Progress of MET systems will eliminate the drawbacks of other electrothermal systems and provide a lifetime solution. The MET is uncomplicated and efficient and can efficiently reach high powers and high specific impulses that can also operate on water vapor, which is probably the most common chemical compound in the universe.

REFERENCES

[1] M.V.H. Khan and E.L. Ntantis, "Space Debris: Overview and Mitigation Strategies," in Proceedings of the 8th International Conference on Research, Technology and Education of Space, H-Space, 25-26 Apr. 2024.

[2] J. Eldo and E.L. Ntantis, "Review of Lagrangian Points and Scope of Stationary Satellites," in Proceedings of the 8th International Conference on Research, Technology, and Education of Space, H-Space, 25-26 Apr. 2024.

[3] Veris, A. "Fundamentals Concepts of Liquid-Propellant Rocket Propulsion System," Springer, Rome Italy 2020.

[4] Agarwal N. (2015) *Beam Powered Propulsion Systems*, Colorado: AIAA.

[5] Whitehair, S., "Experimental Development of a Microwave Electrothermal Thruster," Ph.D. Dissertation, Michigan State Univ., MI, 1986.

[6] Brandenburg, J.E., Kline, J., and Sullivan, D., "The Microwave Electrothermal (MET) Thruster Using Water Vapor Propellant". IEEE Transaction on Plasma Science, 33(2), 2005, 776–782.

[7] Jahn, R. G., Physics of Electric Propulsion, McGraw-Hill, New York, 1968, pp. 134-139

[8] S. Whitehair, J. Asmussen, and S. Nakanishi, "Microwave electrothermal thruster performance in helium gas," J. Propulsion, vol. 3, no. 2, pp. 136–144, 1987.

[9] D.J. Sullivan and M. M. Micci, "The effect of molecular propellants on the performance of a resonant cavity electrothermal thruster," presented at the 1991 Int. Electric Propulsion Conf., Viareggio, Italy, Oct. 1991.

[10] J.L. Power and D.J. Sullivan, "Preliminary Investigation of High Power Microwave Plasmas for Electrothermal Thruster Use," presented at the 29th Joint Propulsion Conf., Monterey, CA, Jun. 28–30, 1993.

[11] Mattingly, J.D., "Elements of Propulsion: Gas Turbines and Rockets" AIAA Education Series, USA, 2006.

[12] Hawley, M.C., Asmussen, J., Filpus, J.W., Whitehair, S., Hoekstra, C., Morin, T.J. and Chapman, R. (1989) Review of Research and Development on the Microwave Electrothermal Thruster, 5 edn., Illinois: AIAA.

[13] Clemens, D.E. (2008) Performance evaluation of the microwave electrothermal thruster using Nitrogen simulated Hydrazine and Ammonia, Pennsylvania: AIAA.

[14] Yildiz, MS, Celik, M. (2016) *Experimental Performance Analysis of the BUSTLab Microwave Electrothermal Thruster*, Istanbul, Turkey: AIAA.

[15] Power, J.L. (1992) *Microwave Electrothermal Propulsion for Space*, 6 edn., Ohio: IEEE.

[16] Brandenburg, J.E., Kline J., Sullivan D. (2005) The Microwave Electrothermal (MET) Thruster Using Water Vapor Propellant, 2 edn., Florida: IEEE.

[17] Abaimov, M.D., Sinha, S., Bilén S. G., Micci M.M. (2013) CubeSat Microwave Electrothermal Thruster (CμMET), Pennsylvania: IEPC.

[18] Agarwal N. (2015) *Beam Powered Propulsion Systems*, Colorado: AIAA.

[19] Whitehair, S., "Experimental Development of a Microwave Electrothermal Thruster," Ph.D. Dissertation, Michigan State Univ., MI, 1986.

[20] Mueller, J. and Micci, M.M., "Desing and Performance Characteristics of a New Microwave Electrothermal Thruster," 22nd Electric Propulsion Conference, Viareggio, Italy, July 1991, IEPC-91-033.

[21] Micci, M.M., Bil, S. G., and Clemens, D. E., "History and Current Status of Microwave Electro-thermal Thrusters," Progress in Propulsion Physics, Vol. 1, 2009, 425–438.

[22] McKevitt, F. X., "Design and Development Approach for the Augmented Catalytic Thruster (ACT)," AIAA Paper 83-1255, 1983.

[23] Crews PT 2013, *An analysis of current propulsion systems*, accessed February 10, 2024, <http://currentpropulsionsystems.weebly.com/ele ctrothermal-propulsion-systems.html>.

[24] Sankaran K., Cassady L., Kodys A.D., Choueiri E.Y., "A survey of propulsion options for cargo and piloted missions to Mars," Astodynamics, Space Missions and Chaos, 1017(1), 450-467, 2004

[25] Curran, F.M., Hardy, T.L., and Haag, T. W., "A Low-Power Arcjet Cyclic Lifetest," NASA TM-100233, 1987.

[26] Pollard, J.E., Lichtin, D.A., and Cohen, R.B., "RF Discharge Electrothermal Propulsion: Results from a Lab-Scale Thruster," AIAA Paper 87-2124, June 1987Martinez-Sanchez, M. and Pollard, J.E., "Spacecraft Electric Propulsion An Overview," Journal of Propulsion and Power, 14(5), 1998, 688–698.

[27] Bathgate S., Bilek, M.M.M., Mckenzie D.R., Electrodeless plasma thrusters for spacecraft: A review", Plasma Science and Technology, 19(8), 083001.

[28] Yildiz S., Unaldi, N., Celik, M., "Geometry Optimization of a 2.5 GHz Microwave Electrothermal Thruster Resonant Cavity", In Proceedings of Space Propulsion 2014, May 23, 2014, Cologne, Germany.

[29] Diamant, K.D., Zeigler, B.L., and Cohen, R. B., "Microwave Electrothermal Thruster Performance", Journal of Propulsion and Power, Vol. 23(1), 2007, 27–34.

[30] Martinez-Sanchez, M. and Pollard, J.E., "Spacecraft Electric Propulsion An Overview," Journal of Propulsion and Power, 14(5), 1998, 688–698.

[31] NASA Advanced Microwave Electrothermal Thruster (AMET). Space Technology Mission Directorate June 26, 2018, accessed March 10, 2024, https://data.nasa.gov/dataset/Advanced-Microwave Electrothermal-Thruster-AMET-Ph/by4w-sewy,

[32] Shiroma, Wayne A. et al., "CubeSats: A Bright Future for Nanosatellites," Central European Journal of Engineering, 2011.

[33] Abaimov, M.D., Sinha, S., Bilen, S.G., Micci, M., "CubeSat Microwave Electrothermal Thrsuter (CµMET)", 33rd International Electric Propulsion Conference, October 9-10, 2013, Washington D.C., USA

Fuel consumption optimization for suborbital solid fuelled rocket engines

Hegedűs András, Tölgyesi Gergely Márk
BME Suborbitals
Budapest University of Technology and Economics
Budapest, Hungary
andrewhegedus.1@gmail.com

***Abstract*—This study introduces a MATLAB–based motor optimization program developed by the BME Suborbitals Rocketry Team, tailored for suborbital rocketry applications. The program tackles the intricate task of identifying optimal grain geometries within a predefined size range, crucial for achieving diverse apogees efficiently. It is designed to handle both Bates and conical grains, chosen for their structural stability and ease of remanufacturing, enabling consistent performance due to relatively low tolerances. Furthermore, the program's flexibility allows for the exploration of various thrust curves, a result of the unique combination of Bates and conical grain geometries. This code can serve as the baseline for competent rocket engine development. Due to this, emphasis is placed on minimizing hardware costs, achieving the lowest rocket launch rail leaving velocity, and maintaining the rocket's acceleration within predefined limits. Engine parameters such as maximum pressure, average pressure, and minimum thrust are also considered, enhancing the program's adaptability to specific mission requirements. This research not only contributes to advancing propulsion systems for suborbital rockets but also underscores the significance of optimization methodologies in achieving cost-effective and efficient solutions. The findings hold implications for both academic research and practical applications within the aerospace industry, offering insights into the intricate balance between performance, cost, and manufacturability in rocket motor design and optimization.**

Keywords — rocket; engine; drag; pressure; isentropic; burn; grain;

I. INTRODUCTION

A MATLAB program was developed to optimize a low apogee rocket's solid fuel rocket motor (SRM) fuel consumption. This paper will outline key aspects of the program, including propellant geometry generation, inner ballistics of the motor, nozzle flow, and flight simulation. The focus is on cylindrical type grain design for low apogee applications due to its ease of manufacture and high precision.

II. GRAIN GEOMETRY

A. Generating geometries

The geometry generator can create various grain geometries with identical outer diameters. In the examples provided, we'll focus on one grain for clarity. This module utilizes specified limits, including the maximum outer diameter, minimum inner diameter, minimum and maximum total length of the grain assembly, and step sizes for radial and length adjustments. These parameters control the grain dimensions, resulting in diverse geometries. When working with more than two grains, the program restricts inner diameters to be larger than the previous grains, ensuring optimal gas flow within the inner cylinder.

B. Analytical model for grain consumption

Saint Robert's law [1] is used for calculating the one-dimensional burning speed: $r_{1D}(t)$

$$r_{1D}(t) = aP^{n}(t) \tag{1}$$

In (1) a is the burn rate coefficient, n is the pressure exponent and $P(t)$ is the chamber static pressure. Some applications require a higher factor and orthographic approach, which can describe erosive burning [3].

$$\dot{m}(t) = A_{burn}(t)\, \rho_{pr}\, r_{1D}(t) \tag{2}$$

The mass consumption $\dot{m}(t)$ can be calculated using (2), where the burning surface area (BSA) is A_{burn} and the propellant density is ρ_{pr}.

C. Geometry change during the burn

The program handles cylindrical grain geometries, commonly referred to as BATES [2] and Conical grain. Fig.(1) depicts the evolution of a BATES grain's geometry, displaying a section view with only the inner cylinder exposed to burning. It illustrates the change in burning surface area (BSA) as a function of the burned distance.

$$A_{burn}(t) = D_{i}(t)\pi L \tag{3}$$

$$A_{burn}(t + dt) = [D_{i}(t) + 2\, aP^{n}(t)dt]\, \pi L \tag{4}$$

$$A_{burn}(t) = \frac{\pi L[D_{i1}(t)+D_{i2}(t)]}{2\cos(arctg\frac{D_{i2}-D_{i1}}{2L})},\ if\ D_{i2}(t) \leqq D_{0}$$

$$A_{burn}(t) = \frac{[D_{0}-D_{i1}(t)][D_{i1}(t)+D_{0}]}{4\sin(arctg\frac{D_{i2}-D_{i1}}{2L})},\ if\ D_{i2}(t) \geqq D_{0} \tag{5}$$

For BATES grain the BSA is defined by (3), where L is the length of the grain, which does not change. During the burn, however, Di(t) changes due to the burning speed. By combining (1) and (3), we derive the combined burn rate–dependent change in BSA as shown in (4), employing a numerical approach. Fig.(2) illustrates the evolution of Conical grain geometry on the left, while on the right, it depicts the change in BSA as a function of burned distance. The same designations are used to describe the burn, with the addition of: $D_{i1}(t)$ and $D_{i2}(t)$, which are the two inside diameters of the Conical grain, while $L_{grpit}(t)$, is the hypotenuse of the grain. The Conical grain's burn is described in (5), which can be rewritten into a differential form.

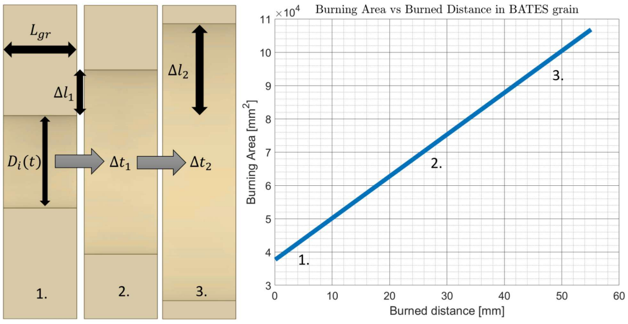

Fig 1. BATES grain's change in geometry

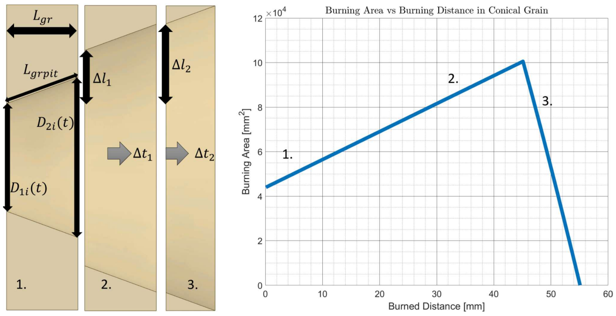

Fig 2. Conical grain's change in geometry

III. INNER BALLISTICS OF THE MOTOR

A. Chamber pressure

The change in BSA directly affects the burn consumption and the generated mass flow. We assume the mass flow rate of the motor is equal to the propellant consumption rate (2), simplifying the equations without sacrificing accuracy. As the mass flow rate passes through the nozzle throat, it chokes the flow, resulting in sonic velocity at the throat. This sonic condition increases the chamber pressure, as the velocity in the throat cannot exceed the local sound speed. Eq. (6) allows us to relate the chamber pressure to the grain consumption rate. The c^* is the so-called characteristic speed, which is the propellant's isentropic combustion property [4]. The A^* is the area of the nozzle's throat.

$$P(t) = \frac{\dot{m}(t)}{A^*} c^* \tag{6}$$

B. Maximum pressure

During the operation of the motor, the maximum pressure plays a significant designing point, thus during optimization, it needs to be predefined. For a specific grain geometry, a wide range of pressure can be reached by setting the optimal A^* in (6). To be able to set a desirable maximum pressure, one needs to be able to calculate the maximum BSA. The diameter at which the maximum BSA will take place can be calculated using the first derivative of (3) and (4).

C. Settings of the solver

The solver uses a numerical approach for solving the upper equations; it can use both Eulerian and fourth-order Runge Kutta approaches. The Eulerian and Runge-Kutta method was compared in terms of accuracy and computing performance. The conclusion was that the Eulerian method with a time step of: $dt = 0.01s$ gives the fastest, and yet acceptable results compared to finer time steps $dt = 0.0001\,s$.

D. Filtering the generated geometries

The geometry generator generates a wide range of grains, of which only some reach the desired flight profile. When simulating the Inner ballistics of the motor it is important in terms of computing time to filter the results before sending it forward to the next module of the optimization code. We designed predefined criteria for the code, that can be easily set, but the user can set any type of criteria during the filtering. One such criterion is the average pressure, which we want to be as close as possible to the maximum inner pressure, due to the problematic nozzle flow.

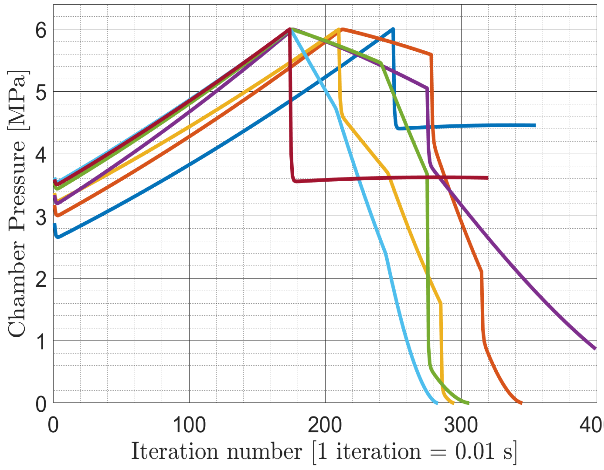

Fig 3. Pressure curves generated by the Inner ballistics module

In Fig. (3) we can see filtered results of the Inner ballistics module, where the initial number of generated geometries is: 224 532 (The maximum number of generated geometries can reach up to 20 million when using 32 GB of RAM), which decreased after the filtering to 74 422, and in Fig. (3), we only showed 7 of them, for better visualization. In this example, the time needed for generating the geometries was 0.86 s, while the time needed for running the Inner ballistics module was 103 s.

IV. SUPERSONIC FLOW SOLVER OF THE ROCKET NOZZLE

A. *Defining the nozzle geometry*

To be able to determine the thrust curve that the rocket motor can produce, the software must specify rocket nozzle geometry before it deals with the flow calculations for every potential pressure curve. Since only solid-fuelled rockets were considered and thus it is a particularly hard task to maintain a constant chamber pressure, the nozzle was optimized for the average combustion chamber pressure. This pressure was calculated in the internal ballistics section. It is important to keep in mind that both the geometry generator and the flow solver calculate with a one–dimensional, adiabatic process. To further specify our way of calculations, thereby we provided the assumptions we made before and during the calculations.

The working fluid is homogeneous in composition, and the phase distribution is isotropic throughout the exhaust composition. We do not negate the different phases during the exhaust process. We use modified variables to account for the multiphase flow. The exhaust composition obeys the perfect gas law. The heat transfer through the nozzle wall does not affect the exhaust flow itself, so we can consider the flow adiabatic. Any wall friction or boundary layer is considered non-appreciable. We do account for discontinuities in the flow in the form of separations at the wall. The inlet boundary condition is a steady and constant flow of the aforementioned isotropic exhaust composition. Any transient effect is negated (i.e. startup or shutdown). They are considered instantaneous. The gas composition, velocity, pressure, temperature, and density are uniform across a given cross-section and are normal to the longitudinal axis of the nozzle. The rocket nozzle operates at sea-level ambient conditions. The nozzle has a conical contour. The last assumption i.e. the nozzle must have a conical contour comes from the fact that this software was written with practical applications in mind. While a bell-shaped nozzle could offer some per cent improvement in terms of performance, the calculation of said nozzle would require huge amounts of computational power. Subsequently, the decision was made to consider the conical design suitable for comparison purposes.

The software used the average combustion chamber pressure to determine the expansion ratio and thus the exit area of every rocket nozzle. Using the considerations listed above the nozzle expansion needed for theoretically perfect exhaust composition expansion can be calculated.

$$\frac{A^*}{A_y(t)} = \left(\frac{k+1}{2}\right)^{\frac{1}{k+1}} \left(\frac{P_y(t)}{P(t)}\right)^{\frac{1}{k}} \sqrt{\frac{k+1}{k-1}\left[1 + \left(\frac{P_y(t)}{P(t)}\right)^{\frac{k-1}{k}}\right]} \tag{7}$$

In the case of adiabatic expansion, $A_y(t)$ is any cross-section area downrange from the throat section A^*. It is only the function of the combustion chamber pressure, the pressure of the downrange cross section and the adiabatic constant k of the exhaust composition. To calculate the ideal expansion we assume that the exit pressure of the exhaust jet equals the ambient pressure of the rocket motor at the exit cross-section area of the rocket nozzle. With this consideration $A_y(t)$ becomes the nozzle exit cross-section area $A_{e,n}$ and $P_y(t)$ becomes the ambient temperature P_0 in (7), thus the nozzle exit cross-section area can be calculated. It is also important to note that the nozzle exit cross-section area was calculated with the assumption that the exhaust jet separates exactly at the nozzle exit cross-section, but during the flow calculations, it is not necessarily the case, because the exhaust jet may separate earlier while flowing along the longitudinal axis.

At ideal conditions, the nozzle diverging half angle does not have a significant impact on the expansion if it is smaller than the maximum turning angle of the supersonic exhaust composition flow. It is usually a good practice to design a nozzle with the greatest divergence angle to minimize the mass of the nozzle. While this lowers the nozzle's performance, the performance of the whole system can be improved. According to Stephen A. Whitmore, the nozzle divergence half-angle can be calculated using the steps listed below. Equations are supported in [4] and [5].

$$\theta_e = \theta_{nozzle} = \theta_{max} = \frac{\nu_e}{3} \tag{8}$$

Where θ is the rocket nozzle divergence half angle and ν is the maximum turning angle that a supersonic flow can take at a given Mach number.

$$\nu_e = \sqrt{\frac{k+1}{k-1}} tan^{-1}\left(\sqrt{\frac{k-1}{k+1}\left(M_e^2-1\right)}\right) - tan^{-1}\left(\sqrt{M_e^2-1}\right) \tag{9}$$

Where M_e is the exit Mach number, which can be calculated with the equation below.

$$\frac{A_y(t)}{A^*} = \frac{1}{M_y(t)}\left(\frac{1+\left(\frac{k-1}{2}\right)M_y^2(t)}{\frac{k+1}{2}}\right)^{\frac{k+1}{2(k-1)}} \tag{10}$$

For the initial nozzle geometry calculations, $A_y(t)$ equals $A_{e,n}$ thus $M_y(t)$ equals M_e. Still, in this case, M_e can not be expressed explicitly so the software uses the MATLAB built-in solver to approximate the value of M_e.

B. *Calculating the exhaust jet flow properties*

As it was stated before, the software does not assume that the jet exhaust separation point is the same as the nozzle exit cross-section. To find the cross-section at which the flow separates from the wall of the rocket nozzle the software uses the formula established by Kalt & Badal [8] and [6]. This formula is explicitly made to determine the theoretical separation pressure of a supersonic flow inside a conical rocket nozzle.

$$\frac{P_{sep}(t)}{P_0} = \frac{2}{3}\left(\frac{P(t)}{P_0}\right)^{-\frac{1}{5}} \qquad (11)$$

By knowing the separation pressure the software can determine the separation cross section using (7). If the calculated theoretical separation cross-section is greater than the nozzle exit cross-section, then the nozzle and thus the flow are under-expanded. In this case, the software uses the nozzle exit cross-section as the actual separation cross-section for any further calculations. If the calculated theoretical separation cross-section is smaller than the calculated nozzle exit cross-section, then the nozzle and the flow are expanded, and the software uses the calculated theoretical separation cross-section as the actual separation cross-section. In both cases, the actual separation pressure equals the actual exhaust jet exit pressure.

C. *Thrust force calculation*

The thrust of any rocket nozzles can be determined by using the following equation.

$$F(t) = \dot{m}(t)v_e(t)\lambda + \left(P_{e,j}(t) - P_0\right)A_{e,j}(t) \qquad (12)$$

In (12) the mass flow is already known, the exhaust pressure and the exhaust cross section were calculated based on the previous section and the ambient pressure is considered a constant. The only two unknown data are the $v_e(t)$ jet exit velocity and the λ kinematic loss factor. Due to the fact that the software uses only conical nozzle designs, it has to include the kinematic loss factor that represents the kinematic performance losses.

$$\lambda = \frac{1}{2}\left(1 + \cos\theta_{nozzle}\right) \qquad (13)$$

This occurs because a conical nozzle can not create a flow perfectly parallel to the nozzle's longitudinal axis. In the case of the considerations listed in the first part of this chapter, the exit velocity can be determined by the equation shown below.

$$v_e(t) = \sqrt{\frac{2k}{k-1}RT_c\left[(1-\left(\frac{P_y(t)}{P(t)}\right)^{\frac{k-1}{k}}\right]} \qquad (14)$$

Where R is the specific gas constant of the exhaust gas composition and T_c is the combustion chamber temperature. (14) is only valid if the gas velocity at the nozzle inlet cross-section is infinitely small. Using (12) the software can determine the thrust for any given nozzle for every given time step. The resultant thrust curve was used to predict the flight characteristics of the rocket motor in a predefined rocket.

V. FLIGHT SIMULATION

A. *Defining the rocket*

For this software, it is important to define the rocket from an aerodynamic and dynamic point of view. These attributes can be set by the user before the simulation and include the dry mass, the cross-section area, and the theoretical Mach zero coefficient of drag. It is important to note that the software will yield different results for different rocket configurations because the merit of the theoretical rocket motors will be defined based on the performance that they provide in the rocket. Next to the properties of the rocket, the flight simulation takes the thrust force curves and mass flow curves of every theoretical rocket engine simulated before and runs the flight simulations for them respectively. The flight simulation is fairly simple and does not include special, flight-affecting conditions such as wind cocking, launching at an angle to the upward direction, etc. This is considered acceptable because the software is executing a comparison between the multiple hundred thousand theoretical rocket engines. This is not a final design process, but a preliminary design evaluation program.

B. *Simulating the flight*

To simulate the flight of the rocket and the rocket engines the software solves the differential equation shown below.

$$m_r(t)\frac{dv_r}{dt} = -m_r(t)g - \frac{1}{2}A_r\rho(t)c_d(M)v_r(t) + F(t) \qquad (15)$$

Where the first term on the left side of the equation is the sum of all forces acting on the rocket, and on the right side the different terms are the gravitational force, the air resistance and the thrust of the rocket engine. This equation negates two effects, namely the Coriolis effect and the change in the gravitational potential with altitude. We also ruled these acceptable, because this version of the software is aimed to simulate rocket flight at relatively smaller altitudes and for relatively shorter time frames. The software utilizes two different differential equation solvers. The first solver that was implemented was a relatively simpler Euler's method equation solver, but due to the uncertainty of the accuracy of the solver, another one was implemented. This solver was a fourth-order Runge–Kutta method. During development, it was revealed that upwards of 0.0001 seconds of timestep resolution the relative error of the two simulation results was under 0.1 per cent thus it can be considered negligible. Nonetheless, the user can set the solver before the simulation.

Important aspects of the flight that the software does not consider negligible are the change of drag and the change of air density during flight. The air density was calculated based on a standard metric atmosphere model developed by the American National Air and Space Administration (NASA).

The aerodynamic properties of a rocket are also subject to changes during flight because they are the function of the velocity. To consider them relatively accurately, the software uses the modified von Karman approximation to determine the drag coefficient of the rocket [9].

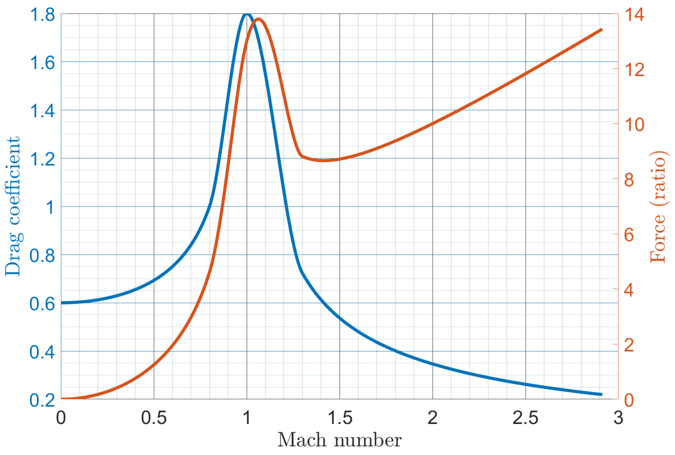

Fig. 5. Drag coefficient variation with Mach number

The figure shown below is some of the resultant velocity and altitude of the flight simulations.

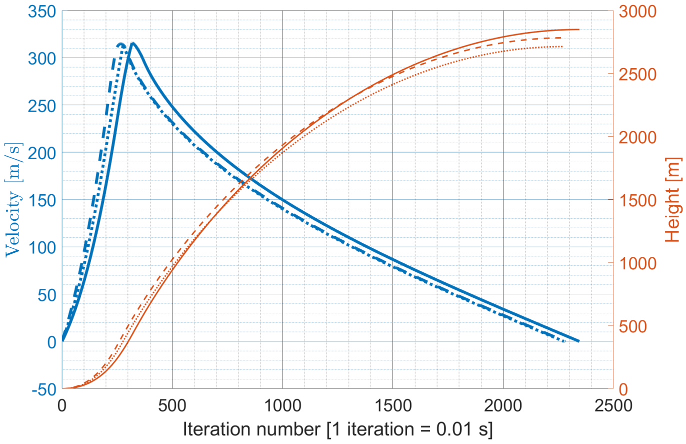

Fig. 6. Example altitude and velocity curves

VI. CONCLUSION

The results of the flight simulation are evaluated based on the criteria listed below.

- The initial thrust-to-weight ratio of the whole system must be over a user-defined value, typically 2–4 to avoid extended burn time on the launch pad.
- The rocket must reach a predefined speed at a predefined lower altitude (e.g. 30 m/s at 12 m) to ensure passive flight stability.
- The rocket must not exceed a user-defined acceleration, due to the potential sensitivity of onboard equipment or payload.
- The rocket must reach a user-defined altitude, with a user-defined percentage of error.

If the particular simulation fills all four criteria then the software saves the initial propellant grain dimensions, the nozzle dimensions, the pressure, thrust force, mass flow curves, total impulse, average thrust, average pressure and flight data.

ACKNOWLEDGEMENT

We would like to thank the contributions of Mihály Makovsky, Bence Kováts and Ákos Gyenge. Their help proved to be essential during the software development. We would also like to thank the support of the BME Suborbitals Rocketry Team highlighting the contributions of the Kratos Rocket Engine Development Project.

REFERENCES

[1] G. Derk, E. Boyer, G.A. Risha, R.A. Yetter, R.R. Dobbins, M.D. Smooke, "Experimental and numerical investigation of high–pressure nitromethane combustion, Volume 38, Issue 2, 2021, Pages 3325–3332, ISSN 1540–7489, https://doi.org/10.1016/j.proci.2020.06.201.

[2] Richard Nakka's Experimental Rocketry Web Site, Richard Nakka, Solid Rocket Motor Theory, Propellant Grain, Available at 2024.04.23 https://www.nakka–rocketry.net/th_grain.html

[3] Ma, Y.; Bao, F.; Sun, L.; Liu, Y.; Hui, W. A New Erosive Burning Model of Solid Propellant Based on Heat Transfer Equilibrium Propellant Surface. Int. J. Aerosp. Eng. 2020, 2020, 1–9.

[4] MIT, 16.50 Introduction to Propulsion Systems, Lecture 7, Subject: Modeling of rocket nozzles; effects of nozzle area ratio. Available at: https://ocw.mit.edu/courses/16–50–introduction–to–propulsion–systems–spring–2012/e2035e49d0312366d0772766f594b671_MIT16_50S12_lec7.pdf

[5] G. Shutton, O. Biblarz, "Rocket Propulsion Elements", 9th edition, Wiley, 2017.

[6] R. H. Stark. "Flow Separation in Rocket Nozzles, a Simple Criteria", German Aerospace Center, Lampoldshausen, D–74239, Germany, DOI:10.2514/6.2005–3940

[7] American National Air and Space Administration, Glenn Research Center, Standard Metric Earth Atmospheric Model. Available at: https://www.grc.nasa.gov/www/k–12/airplane/atmosmet.html

[8] Kalt S., Badal D., "Conical Rocket Nozzle Performance under Flow–Separated Conditions", Journal of Spacecraft and Rockets, Vol. 2, No. 3, page 447–449, 1965.

[9] Utah State University, MAE 6530, Propulsion Systems II, Lecture 3, Estimating the Launch Vehicle Drag Coefficient. Available at: http://mae–nas.eng.usu.edu/MAE_6530_Web/New_Course/launch_design/Section3.3.pdf

DCC Direct Current Converter development for PEP experiment of ESA's JUICE (Jupiter Icy Moons Explorer) mission

Pál Gábor VIZI
Space Technology Team
HUN-REN Centre for Energy Research
Budapest, Hungary
vizi.pal.gabor@ek.hun-ren.hu

Janos NAGY
Space Technology Team
HUN-REN Centre for Energy Research
Budapest, Hungary
nagy.janos@ek.hun-ren.hu

***Abstract* — JUICE - JUpiter ICy moons Explorer, the first major ESA (European Space Agency) mission to Jupiter [1], which was launched in April 2023, will arrive at the planet in 2031 and spend at least three years exploring the gas giant and its three large moons, Europa, Callisto and with detailed observation of Ganymede. Our group, the Space Technology Team of the HUN-REN Centre for Energy Research, developed the power supply for the Particle Environment Package (PEP) instrument. The PEP and its sensors explore the plasma environment in the Jupiter system. The PEP measures the density and flux of positive and negative ions, electrons, exospheric neutral gases, thermal plasma, and energetically neutral atoms. We were tasked with receiving onboard main and redundant 28V, and providing the suitable voltages to sensors and Data Processing Units of PEP.**

Keywords — ESA Jupiter Icy Moons Explorer (JUICE), Particle Environment Package (PEP), Direct Current Converter (DCC), EK HUN-REN, Centre for Energy Research

I. INTRODUCTION

European Space Agency (ESA) coordinated PEP development. European teams developed four sensors and NASA developed two ones of PEP. Our Direct Current Converter (DCC) provides the necessary voltages with high efficiency from the onboard 28V for European sensors and for their Digital Processor Units (DPU). The number of voltages required is between 3 and 6 for each sensor. A common Pulse Width Modulation (PWM) controller dedicated to each sensor generates required voltages, rather than separate converters, to save space and mass. The operation and design of DCC is described in detail in [2] The DCC contains partly redundancy. The onboard 28V comes from main and redundant sources and DPU is doubled to insure operation. Manufacturing and testing of the DCC in compliance with the technological requirements of ESA was our task too. SGF Ltd. prepared an EGSE (Electronic Ground Support Equipment) for test purposes.

II. JUICE MISSION AND BACKGROUND

A. Launch of JUICE

JUICE was launched from French Guiana on 14th April 2023. Two minutes after launch, Two minutes after launch, Ariane reached an altitude of 70 km and speeded up to leave the gravitational field of the Earth in 20 minutes.

The Ariane-5 rocket has a launch mass of 760 tons, and a payload of 6,150 kg. The space probe reaching the Jupiter contains 3,650 kg propellant for maneuvers. The flight time using the accelerating effect of the planets is nearly 8 years. The planned exploration time around the Jupiter system is 3.5 years. The research instrument with the high-gain antenna mass 2,450 kg. Tough negotiations were held for every gram of payload.

Figure 1 Launch of the JUICE mission onboard the 750-tons Ariane 5 rocket from the ESA base in Kourou, French Guiana, on 14th April 2023. (ESA Photo)

Jupiter is the fifth planet in our Solar System. Its mass is 2.5 times more than that of all planets.

In ancient times of mankind, this planet represented the main God of the Roman Empire. In 1610, Galileo Galilei was the first scientist who used a telescope in astronomy, to study Jupiter and discovered its moons. This discovery was a major contribution to shattering the Aristotelian worldview that the Earth was the center of the universe.

The Galilean moons are Io; Europa, Ganymede and Callisto. These moons can be considered planets by size, but they orbit Jupiter. They are larger than our Moon. Their surfaces are varied: Io has huge volcanoes, and Europa is covered with ice.

The JUICE mission aims to explore the Galilean moons and Jupiter system with remote sensors, geophysical and in situ instruments and the conditions that led to life formation in the Solar System. JUICE is developed to investigate the habitability of icy moons and measure if conditions for life are available. The JUICE mission will investigate possibility of life formation as NASA's Europa Clipper, will do this as a cooperative mission.

B. JUICE Space probe

The development of the probe started at the French company Airbus Defense & Space began in June 2015.

Total take-off mass (without fuel): 2,420 kg
Instruments: 280 kg
Bipropellant: 3,650 kg
Solar panel: 97 m^2 (~850 W at Jupiter)
Fixed high and one medium gain antenna (X, Ka Bands)
Data download capacity: ~ 1.4 Gbit/day
Probe is 3-axis stabilized.

C. Experiments of JUICE

The JUICE experiments are listed in [3].

III. PARTICLE ENVIRONMENT PACKAGE (PEP)

A. Background of PEP

The proposal for the Particle Environment Package (PEP) instrument was made in August 2010. The scientific instruments were selected in 2013. Both the probe and the instruments had undergone lot of examinations over a long period of time - for optimization and mass minimization – to insure reliability and maximum scientific results.

Originally, PEP was to contain 8 sensors, but was reduced to 6 in order to reduce mass. A set of 6 sensor are to investigate the plasma environment of Jupiter, the density and distribution of charged particles and high-energy neutral atoms. PEP particle spectrometer is to measure neutral and charged particles in the Jupiter system. The PEP-Instrument onboard JUICE consists of two units with a total of six different sensors. PEP-Lo (JEI, NIM, JNA, and JDC sensors) European unit and PEP-Hi (JoEE, JENI sensors) American unit. Purposes of the experiments are: imaging magnetospheres, moons and interactions; characterization of Jupiter's magnetosphere including aurora; characterization of the atmospheres of the Galilean moons and interactions of moons and the magnetosphere; furthermore, characterization of the Io and Europa torus, Ganymede's magnetosphere itself.

B. Sensors of PEP

Sensors of PEP are Jovian Energetic Electrons (JoEE) and Jovian Energetic Neutrals and Ions (JENI) APL, USA; Jovian plasma Dynamics and Composition (JDC) and Jovian Neutral Atoms (JNA) of Swedish Institute of Space Physics, Sweden; Jovian Electrons and Ions (JEI) Max-Planck Institute, Germany; Neutral and Ion Mass Spectrometer (NIM) University of Bern, Switzerland.

C. DPUs of PEP

PEP contains two Data Processing Units (DPUs) main and redundant one to control sensors, collect data and forward them to onboard telemetry.

D. Our group's task during development phase

-designing, manufacturing and testing (including a several qualification and a flight test model) an onboard common power supply system (DCC) for PEP-Lo experiment. The DCC provides power for sensors belonging to PEP-Lo.

-designing and manufacturing EGSE for PEP instrument sensors, (both software and hardware). DCC receives a main and a redundant onboard 28V and provides the required voltages to sensors and DPUs [Fig. 2].

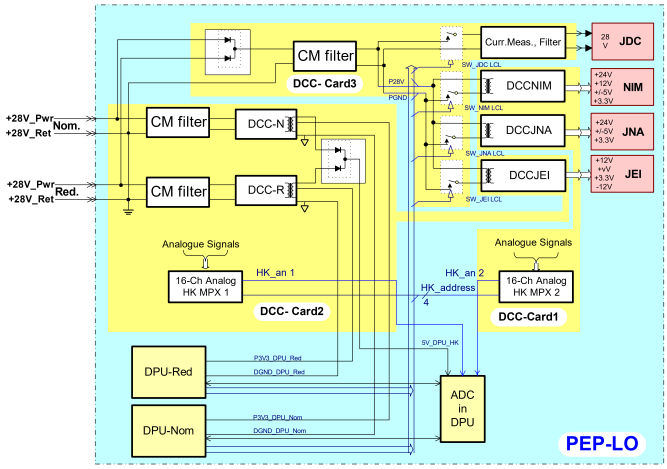

Figure 2 Block scheme of DCC Units is in yellow background, supplied sensors are in pink.

IV. OVERVIEW OF THE DCC UNIT OF PEP

Solar cells ensure the power supply of JUICE. The use of solar array power generation in combination with the large W/m^2, results in a large area solar arrays, typically about 60-75 m^2 charging onboard accumulators. The onboard voltage is 28 V for experiments, which is provided by a nominal line of 28 V and a redundant line. The block scheme of DCC Unit is depicted in Figure 2. It receives both onboard 28 V power by nominal and redundant lines, and the incoming power is transformed to voltages according to the requirements of the units, the main and redundant DPU and the sensors. If the nominal line drops, the onboard electronics switches DCC to the redundant power line to ensure the power for PEP-Lo experiment. The power requirements of the sensors for different operation modes were determined with 20% contingency for 6 modes of operation (see Table 1). During team meetings, a centralized DC/DC converter configuration was accepted, followed by individual, galvanically isolated DC/DC down converters for each subsystem and sensor (S&Ss).

This solution minimizes cross-coupling and the number of switching elements, thus the output units can be tested individually. Due to the 3 to 4 outputs typically required for sensor voltages, a flyback type converter topology is proposed.

The required output power level of the individual converters is between 5 - 15 W. In order to minimize the possible voltage drop between the converters and the supplied subsystems, special attention needs to be paid to the selection of the harness and cabling system. EMC requirements could be fulfilled easier by separation of DC/DC converters for subsystems and sensors.

The realized DCC was formed by a series of iterations with sensor teams, experiment PI (principal investigator), and by engineers responsible for the thermal balance and radiation shielding of instruments on space probe. DCC was initially aimed at containing full redundancy, which had to be reduced because mass reduction became more inportent in the meantime. Several circuit topologies were studied. With galvanic isolation requirement in view, only transformers with two or more windings should be used. The circuits can be of flyback topology, forward topology, push-pull and bridge. We choose the flyback topology, because it is advantageous for smaller power requirements and has fewer components. When used for multiple output, the individual output voltages follow each other quite well, when either the input voltage or the output load changes. They have the disadvantage that their main switching element, typically a MOSFET, is stressed by voltage spikes, higher than primary voltage. The degree of this stress varies depending on output voltage continuous and load. In the worst case, values can be several times the primary voltage. The voltage transient has to be neutralized by a so-called ”clamp network” which dissipates the transient energy to heat. This clamp circuits improve electromagnetic capability (EMC) and supress oscillations of signals as response to changes. Flyback transformers need a suitable gap in the core, which requires careful selection from the catalogue.

1-Off	**0.0 W**
2-Init	**34.7 W**
3-Standby	**18.2 W**
4-Service	**18.7 W**
5-Cal/Diag	**38.7 W**
6-Peak Science	**49.5 W**

Table 1: Total Power need of PEP-Lo experiment in different operation modes with 20% contingency

Figure 3. shows the configuration of a flyback converter in operation. In the on-state, energy is transferred from the input voltage source to the transformer (the output capacitor supplies energy to the output load). In the off-state, the energy is transferred from the transformer to the output load.

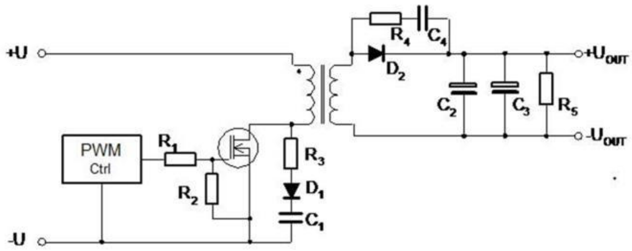

Figure 3 Simplified block scheme of flyback converter

The PWM [4] continuous conduction mode is achieved when the current in the charging/discharging coil never drops to or crosses 0. For continuous operation, the operation can be described by solving linear equations instead of differential equations.

$$Vo = N2/N1 * (ton/Ts) / (1 - ton/Ts) * Vi$$

where Vo and Vi are output and input voltages, and N2 and N1 are the windings of transformer.

Ton is the switch on time, and Ts is the period time. From this formula, we can determine the transmission ratio of PWM not only by transformer windings, but by duty cycle.

Even if the input voltage changes, the output voltage can be controlled by feedback from output. The transformer is an energy storage in the circuit. When the PWM output is on, it is charged with energy, which is released when the PWM output is off. Saturation point and linearity of a transformer can be set by air gap.

PWM converters were designed for a nominal load in continuous mode to reach better EMC performance. At low loads, they can operate in discontinuous mode. As the transformer for PWM has one common primary N1 and several secondary windings, N2, N3, ..Nx are designed for the required voltages. In the design, ISL78440 chip was used for switching element, a RadHard version of which exists for space application. The original manufacturer of this chip was Intersil, the present manufacturer is Renesas.

The task of the snubber is to reduce overshoot and spikes caused by inductors due to switching so as to protect semiconductors.

V. COMPONENT SELECTION

In the design for space application, reliability is an important factor, which is ensured by using high-reliability components to minimize the likelihood of failure events. The JUICE project applied components from the European Preferred Part List (EPPL) of ESA. The advantage of using components from the EPPL list is that these components have been tested for extreme applications; therefore, they survive environmental stress. Components (transformers and chokes) not on the EPPL list are ordered from a qualified manufacturer. These components go through a well-defined qualification process.

Materials used in the space probe have to be baked out, as evaporating materials would have negative effect on measurements by condensing at critical points. Not all materials are suitable for space use after baking out, so there is a list of materials that can be used for this purpose.

2.3 Detailed List of Requirements for High Reliability

After team meetings, the requirements for DCC were summarized in a document. The DCC has to fulfill approximately 150 requirements.

The most important areas covered are listed bellow:

- environmental: temperature, min/max operational temperature: -50 °C +50 °C -radiation: TID sensitive component tolerance ≥100krad and lifetime: at least 13.5 (Earth) years.
- telecommand & telemetry: DPU switches on/off sensor powers
- electrical design, applying ESA recommendations
- failure tolerance, safety inhibits should be independent, verifiable, stable and stay in a safe position even in case of energy failure.
- input power requirements, +26,5V to 31,5V, max 5A
- output power characteristics, different for each sensor
- current protection of individual sensors, different for each sensor
- power on and off transients, different for each sensor
- conversion efficiency, min 65% for DPU and 70% for sensors
- control loop stability, gain margin, phase margin, 10dB, 50deg
- switching frequency of PWM controllers, 200 kHz
- synchronisation I/F from DPU to DCC DPU board at 200kHz ±400 ppm/week stability
- control I/F from DPU to DCC Power switches
- active high requirements for EMC Testing, DM and CM conducted current and radiated emission according to requirements
- mechanical requirements (mass, size), 1.4kg, 48.5mm x 154.7mm x 149.2mm.

VI. MANUFACTURING FLIGHT MODELS

The ESA standards regulate the design and manufacture of flying PCBs (printed circuit board). As PCBs are an important part of flight hardware, extreme stress, e.g., vibration and extreme temperature cycles, or any humidity in PCB can cause failure in operation, radiation can damage hardware; therefore, PCB material requirements should minimize the risk of selection. Space agencies are developing recommendations for both PCB design and manufacturing and accepting the participation of qualified manufacturers to ensure reliable operation.

Once the PCB is ready, soldering components is a crucial task in flight assembly. During soldering, a pin is attached to a metal pad and an electrically conductive connection is made. The surfaces to be soldered must be clean. The tin solder has to cover the surfaces well. The tin, which can only be conventional lead, should flow properly during soldering and leave no residue of flux on the surface. Flux excess has to be cleaned after soldering is completed. During the assembly process, the space agency will accept certified manufacturers for space-qualified soldering. Soldering has to be qualified by the manufacturer on a package-by-package basis to ensure that any inclusions or cracks do not reduce reliability. The greatest stress for heavy parts is vibration, for others it is thermal expansion. The DCC was tested and calibrated according ESA standards during tests.

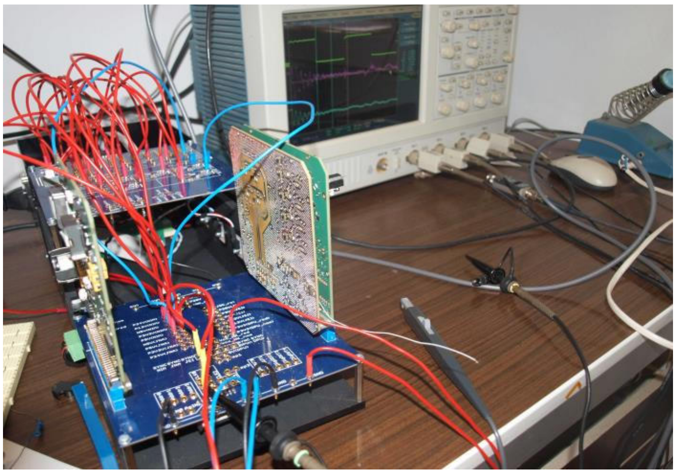

Figure 4 DCC (green cards) is tested with EGSE (blue cards)

VII. TASKS OF OUR GROUP DURING CRUISE PHASE

Our team supports the processing of the test, calibration and scientific data during the cruise phase.

In first year of flight PEP was switched approximately monthly for several hours. During operation DCC temperature values corresponded to simulated values with less than 5 °C deviation. The efficiency of DCC was between 70 and 80% depending on output power requirements, generally the efficiency was the higher at higher power.

These are regularly reported to PEP system developers. Scientific data will be forwarded to our physicist colleagues working on the exploration of the Solar System. It is also our task is to monitor DCC operation with DCC service data, and archive scientific and service data.

Ageing of components is also an important factor during a decade-long project. This has also been scaled up and tested in flight.

VIII. SUMMARY

Since the launch of the Ariane-5, the PEP sensors have been switched on as scheduled. The DCC we developed has been working well over the past year. Its temperatures have been in line with the values calculated in simulations and the DCC efficiency has been between 70% and 80%, depending on the load current.

REFERENCES

[1] Jupiter Science Enabled by ESA's Jupiter Icy Moons Explorer, https://doi.org/10.1007/s11214-023-00996-6

[2] Nagy J. et al., 2022, Hungarian Participation in JUICE Project of European Space Agency. *Acta Polytechnica Hungarica*, Vol. 19, No. 9, pp. 25-43, https://doi.org/10.12700/APH.19.9.2022.9.2

[3] https://www.esa.int/Science_Exploration/Space_Science/Juice/Juice_spacecraft_specs

[4] Intersil ISL78840 Datasheet https://www.alldatasheet.com/view.jsp?Searchword=ISL78840&sField=2

Remote sensing of hydrological parameters by GNSS reflectometry

J. Gaskó, D. Fátay
Faculty of Electrical Engineering and Informatics
Budapest University of Technology and Economics
Budapest, Hungary

B. Turák, Sz. Rózsa
Department of Geodesy and Surveying
Faculty of Civil Engineering
Budapest University of Technology and Economics
Budapest, Hungary

Abstract— **There is an increasing interest in the remote sensing applications of the Earth's surface environments with GNSS reflectometry (GNSS-R) including river gauging, ice sheet and snow cover analysis and soil moisture measurement. It provides a new, highly precise, continuous, all-weather and quasi-real-time remote sensing tool that can greatly increase the available data's spatial and temporal resolution, while providing redundancy for traditional methods. Existing GNSS-R methods for such measurements are often done with expensive or cumbersome equipment that require a significant investment of time, resources, and skilled workforce to install and evaluate data. During GNSS-R measurements the direct signal from the GNSS satellite and the reflected signal from the surroundings form an interference pattern. Changes in the environment and the satellites' positions result in a time dependent signal at a given receiver position, that is a source of noise under everyday use of GNSS positioning, but also carries relevant information about the environment that can be extracted.**

We have developed an easy to install, cost efficient measurement solution that automatically collects and evaluates GNSS-R data and determines water level and surface roughness. Via the prototypes installed around Lake Balaton, this solution is proven to be able to provide such data with sufficient reliability and precision.

Keywords— GNSS-R, remote sensing, reflectometry, water level, hydrology

I. INTRODUCTION

Traditional hydrology measurements are often done with tools that require precarious installation and maintenance and needs direct access to the body of water in question, and do not offer a convenient way to move the equipment, if necessary. Many of these are still analog and require manual labor to operate and suffer from reliability issues when facing geological changes, like seismic deformation, land subsidence and glacial isostatic adjustment. Long-term reliability of such systems is critical for data consistency and in case of such an extensively used water body as Lake Balaton, also for local businesses and environmental protection.

Solutions that do not require such labor to operate are rapidly spreading, among those are GNSS-based devices. These are either directly placed on the water surface for direct measurement, or next to the water body, using signals that are reflected from the water surface [1]. Such devices, if equipped properly, is able to determine basic properties of the water surface, mainly water level, and thus are used as tide gauges.

This method is generally called GNSS reflectometry (GNSS-R), and often use one or multiple geodetic receivers that puts a quite high price tag on these pieces of equipment. It needs an equipment that is sensitive enough, but as consumer-grade receivers are becoming more effective and higher quality, they are becoming sensitive enough for such tasks [2]. A case study with both types of receivers performed previously by Á. M. Ács et al. [3] showed that water level measurements are feasible with more simple setups by implementing a GNSS-R stream gauge over the river Danube, producing results that strongly correlate with traditional river gauges.

In the following chapters the principle of such systems is demonstrated, and an example is shown for a measurement device that is capable of providing reliable, quasi-real-time hydrology data using customer-grade receivers and supplementary equipment.

II. BASICS OF GNSS REFLECTOMETRY

Multipath is a phenomenon whereby signals from a source reach the receiver via multiple paths due to reflection or diffraction, causing interference and signal degradation due to phase differences and signal cancellations. This is a common source of positioning error in GNSS systems and is often suppressed or worked around in conventional use. This effect is the most severe when the angle of incidence of the electromagnetic wave on the surface causing the signal to reach the receiver via a non-direct route is relatively small, as in such cases, the reflected and the direct signal is more likely to have the same directional circular polarization. The angle at which signals with the original, right-handed and the reflected left-handed polarization match in energy is called the Brewster angle and is typically smaller than 30° for GNSS signals. The exact angle and reflected energy depend on the properties of the surface, such as its composition or water content.

Reflected signals below this angle, by having the same polarization as the direct signals, cause interference at the receiver that can be measured as a change in the signal-to-noise ratio (SNR) of the given signal. This change of measured signal strength is, besides other factors, determined by the angle of

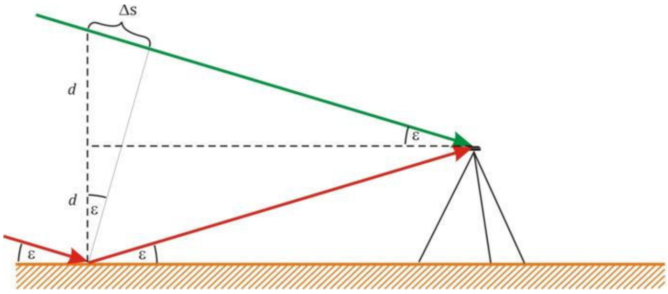

Fig. 1. Multipath geometry for a single horizontal reflecting plane [3].

incidence and distance of the surface relative to the receiver. Assuming that the reflecting surface is horizontal, the phase delay ($\Delta\varphi$) can be calculated as shown on Fig. 1:

$$\Delta\varphi = \frac{\Delta s}{\lambda} 2\pi = \frac{4\pi d}{\lambda} \sin(\varepsilon) \qquad (1)$$

where λ is the wavelength of the signal, d is the receiver's height above the surface and ε is the satellite's elevation angle. This means that there is a connection between the satellite's elevation, the receiver's height from the surface and the signal's strength:

$$SNR = A(\varepsilon) \sin\left(\frac{4\pi d}{\lambda} \sin(\varepsilon) + \phi\right) \qquad (2)$$

where A is an amplitude term dependent on elevation angle, surface roughness, and the dielectric constant of the surface, ϕ is the phase [2].

This gives a periodic dependence on the elevation angle whose period can be measured if the observation period covers a sufficient elevation range – hence is long enough in time. Furthermore, in case the receiver antenna's characteristics are known well enough, one can estimate all parameters that the amplitude term is a function of.

Reflections do not occur at a single point on the surface, but rather on an ellipsoidal footprint, called the Fresnel zone, as seen on Fig. 2. The eccentricity and area of this zone is a function of satellite elevation and can be calculated [4]. Unobstructed view to the entire area is key to data reliability.

Precise enough measurements of satellite SNR at low elevation angles (< 30°) therefore can be used to estimate certain parameters of the reflecting surface, mainly its height below the receiver, and also data on surface properties, snow accumulation, ice cover and thickness, soil moisture, vegetation cover and moisture content [3].

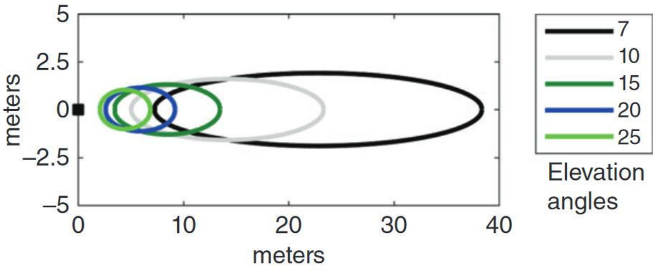

Fig. 2. Fresnel zone footprints as a function of satellite elevation [2]

Fig. 3. Inside the enclosure of the measurement unit (without antennas).

III. MEASUREMENT HARDWARE

The previously described measurement principles necessitate a device that is capable of measuring the targeted satellites' carrier waves' SNR and forwarding the data to the evaluation server.

Besides the support equipment providing the measurement unit with power and cellular connectivity, it is based on a Raspberry Pi 3B+ as the processing unit and a u-blox ZED-F9P-01B GNSS evaluation board with a u-blox ANN-MB series patch antenna. As seen on Fig. 3. (without the antennas that are mounted on the cover), the electronics were enclosed in an IP65 rated ABS box to provide environmental protection while allowing GNSS signals through, so even the antenna can be enclosed in a single unit. These are readily available, off-the-shelf, customer grade components that allow for easy installation at public locations without the fear of vandalism.

IV. EVALUATION

To limit the cellular data usage of the unit, observations are made in certain time windows, in which relevant data of a defined set of satellites is streamed to the evaluation server. These are calculated at most 5 days in advance, from the 5-day prediction ephemerides provided by the Center for Orbit Determination in Europe (CODE) [5], and then transferred to the unit. It can then put itself in power saver mode for longer gaps in between these windows or prepare if necessary: e.g. if the receiver module can be configured for the reception of certain satellites, the unit can start following those in advance. By adjusting certain parameters, like the minimum number of satellite transits in a window or whether to limit observations to descending satellites, it is possible to find a middle ground between temporal resolution and data reliability.

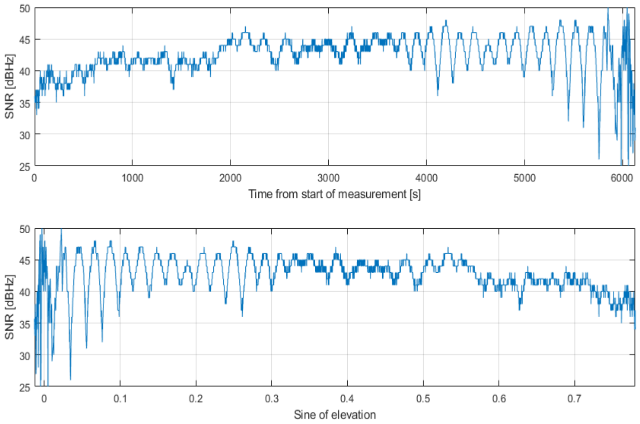

Fig. 4. SNR of L1 signal of R24 GLONASS satellite over time and elevation.

Following the acquisition of SNR-time logs utilizing the aforementioned measurement configuration (see Fig. 4.), the precise satellite elevations are determined for individual data points using ultra-rapid prediction ephemerides, also from CODE. We have chosen this product since it is the most accurate orbit solution available for real-time or near-real-time GNSS applications. The resulting SNR-elevation data is then scanned for dominant periods using the Lomb-Scargle periodogram (see Fig. 5.), that is proven to be able to determine the spectrum of the signal even on irregular or noisy data [4].

Finally, the characteristic frequency, that is defined as the peak with the highest amplitude of the periodogram, is determined. Using Eq. 2., the reflection height can then be calculated from that frequency, while the uncertainty of this value can be characterized by the proportions of the characteristic peak.

Due to various factors, like radio interference, ships passing through or anchoring within the Fresnel zones, or berthing within the marina causing secondary reflection surfaces, measurement reliability can degrade severely. The effects of these disturbances can often be seen as various artifacts at certain steps of the evaluation process. The exact filtering steps and parameters were determined over an extensive, 4 months long evaluation period, over which more than 5000 satellite transits were logged and analyzed. For the final results, there were filters in place for data point count and average sampling time, periodogram shape, minimum requirements for characteristic peaks, their own proportions and their height in comparison to second and third order peaks. In the evaluation software, all these filtering parameters can be fine-tuned for each station, depending on its hardware and environmental characteristics.

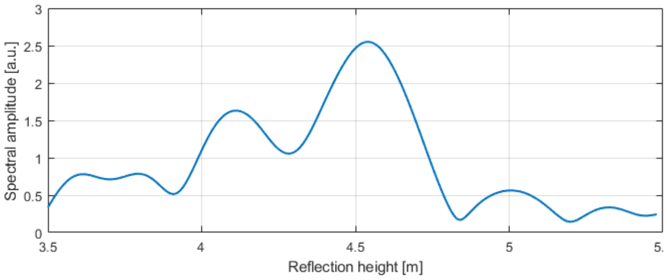

Fig. 5. Lomb-Scargle periodogram of L1 signal of R24 GLONASS satellite.

Fig. 6. Unit installations at the entry posts of the marinas.

This evaluation occurs subsequent to the observation window of each satellite, enabling the visual presentation of the calculated parameters to the user with minimal delay, without manual post-processing.

V. RESULTS

Dataset for the presented results cover a one-week period between 24-31 March 2024 and were taken at the pier of Balatonkenese marina, as seen on Fig. 6.

Fig. 7. shows the calculated and filtered reflection height over time. As seen, it is in good correlation with the official water gauge located at Balatonfűzfő, roughly 6km away. The discrepancy between the two data series is due to the fact that the zero point of official water gauge and the zero point of the reflectometry measurement unit are not the same. The difference (5.90m) gives the height of the GNSS antenna above the zero point of the water gauge. The calculated height is a negative

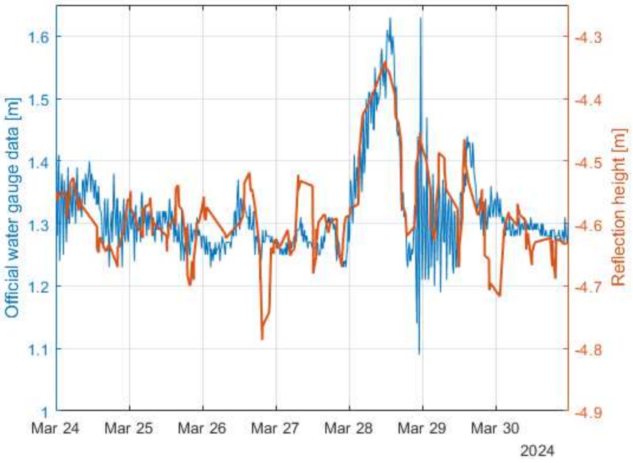

Fig. 7. Official water gauge data and calculated reflection height

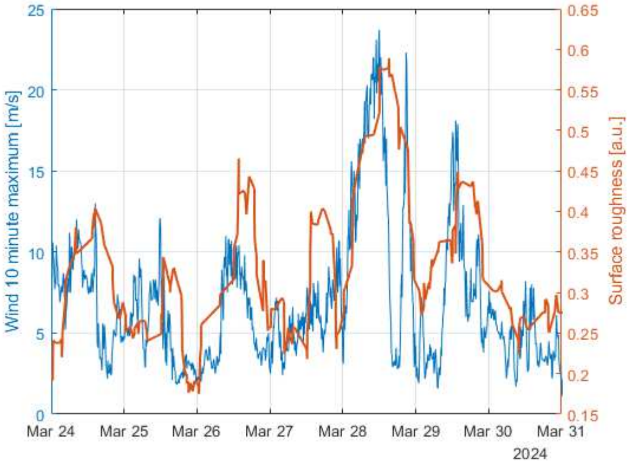

Fig. 8. Official wind meter data and calculated surface roughness.

number that decreases in absolute value with rising water levels, because then the vertical distance between the surface and the antenna decreases. On 28 March, a significant rise in water level (cca. 0.3m) can be seen, that is the result of the lake's surface tilt during high winds. That change can be very well seen on GNSS-R measurements as well. On that day, the official wind meter at Siófok (cca. 14km away) showed winds gusting to 23.5m/s that is proven to be sufficient for such phenomena [6].

Further investigating the effects of wind on reflectometry data, the height of the peak corresponding to the characteristic frequency, normalized by its width (distance between the two neighboring local minimums, if applicable), hereby called the assumed surface roughness, is plotted with wind data, as seen on Fig. 8. High winds cause the waves to get bigger, dispersing the reflection zone over a bigger area, causing the characteristic spectrum peak to spread out. This explains the correlation between the wind strength and the periodogram-based surface roughness.

This broadening of the periodogram peak also explains the uncertainty of the height determination, thus can explain some outlier data of Fig. 7., e.g. on 26 March, 19h, where the inaccurate results coincide with the peaks on the wind correlation plot (Fig. 8.).

VI. CONCLUSION

We developed a cost-efficient, easy-to-use GNSS-R-based hydrology measurement system that is proven to provide sufficiently reliable data on the water surface, including water level and wind-induced surface roughness, and is capable of serving as an alternative to traditional hydrological measurement methods.

ACKNOWLEDGMENT

The authors thank *HungaroMet* and *KDTVIZIG (Central Transdanubian Directorate of Water Management)* for providing us with the used meteorological and hydrological datasets. We are indebted to the staff of the marinas of Balatonkenese and Keszthely for providing the measurement sites and their assistance.

The research reported in this paper is part of project no. BME-NVA-02, implemented with the support provided by the Ministry of Innovation and Technology of Hungary from the National Research, Development and Innovation Fund, financed under the TKP2021 funding scheme.

REFERENCES

[1] N. T. Penna, M. A. Morales Maqueda, I. Martin, J. Guo, P. R. Foden, "Sea Surface Height Measurement Using a GNSS Wave Glider", Geophysical Research Letters, vol. 45, Issue 11, p. 5609-5616, 2018, doi: 10.1029/2018GL077950

[2] K. M. Larson, "GPS interferometric reflectometry: applications to surface soil moisture, snow depth, and vegetation water content in the western United States", WIREs Water, 2016, doi: 10.1002/wat2.1167

[3] Á. M. Ács, Sz. Rózsa, "The GNSS stream gauge", H-SPACE Proceedings, p. 51-55, 2020, ISBN 978-963-7367-26-7

[4] C. Roesler, K. M. Larson, "Software tools for GNSS interferometric reflectometry (GNSS-IR)", GPS Solutions, vol. 22:80, 2018, doi: 10.1007/s10291-018-0744-8

[5] https://www.aiub.unibe.ch/research/code___analysis_center, Accessed: 2024-03-24

[6] G. Kravinszkaja, "A Kyrill viharciklon hatása és lecsengése a Balatonon", Légkör, vol. 52., Issue 2, p. 9-11, 2007

Radiation characteristics measurement on a sounding rocket near the Kármán line

Szilárd Borsi, Richárd Huba Bezzegh, Dominik Gábor Nagy, Bence Csaba Kováts
Project TELLER
Budapest University of Technology and Economics
Budapest, Hungary
hello@project-teller.eu

***Abstract*— With the ongoing progress in the space industry, space travel has become more cost-effective and popular. However, it comes with inherent risks, particularly concerning radiation exposure, also including the ascent and descent through the atmosphere. Data on the radiation field in the altitude range of 30 km to 90 km is limited due to challenges with sustained balloon flights and the lower reach of Low Earth Orbit (LEO) satellites. With the increase in human spaceflight and the launch of complex space devices, the knowledge of radiation conditions in the atmosphere has become a more pressing issue.**

A new scientific payload will be implemented on board a sounding rocket to investigate the issue. Our project called TELLER (Three-axis Experimental Low-altitude Laboratory for Exploring Radiation) is an experiment developed by a team of students from the Budapest University of Technology and Economics (BUTE) in Hungary. The aim of the project is to assess the energy, density, and directional patterns of ionizing radiation in the atmosphere and to explore their correlation with altitude. The experiment will be launched up to the Kármán Line in the spring of 2025 to perform measurements, thanks to the Swedish-German student program called REXUS/BEXUS.

Our methodology involves integrating multiple measurements to enhance precision, utilizing a spatial arrangement of GM tubes and scintillator detectors. With this spatial placement, we are able to determine the direction of the incoming radiation. In the following article, we would like to describe the experimental set-up and the measurement process, the development and the progress so far.

Keywords: space — rocket — radiation — GM tubes — scintillator — REXUS/BEXUS

I. INTRODUCTION

Since the dawn of the space age, Hungary has been at the forefront of the development of various space dosimeters. Project TELLER (Three-axis Experimental Low-altitude Laboratory for Exploring Radiation) seeks to extend this heritage with its experiment. The project was founded in 2023 and has been selected for the European space education programme for university students, REXUS/BEXUS (Rocket/Balloon Experiment for University Students).

II. SCIENTIFIC BACKGROUND

Cosmic rays consist of high-energy particles that emanate from outer space and solar events, primarily including protons, along with alpha particles and heavier ions, gamma rays, and electrons. These primary particles seldom make it to the Earth's surface; they interact with atmospheric molecules, leading to the creation of secondary particles through a process called a nucleonic cascade, which manifests as air showers.

The air shower phenomenon has a strong effect at an altitude of 15-20 km, which has been repeatedly measured with balloons. This is called the Regener-Pfotzer maximum. Our experiment aims to investigate the characteristics of ionizing particles from this point up to the Kármán line. [1, 2]

Scintillators are materials that are able to convert high energy radiation such as X-rays or gamma rays to a near visible or visible light. (See fig. 1.) Detectors based on scintillators are essentially composed of a scintillator material and a photodetector that can be either photomultiplier tube (PMT) or a photodiode. The role of the photodetector is to convert the emitted light of the scintillator to an electrical signal. The obtained electrical signal is proportional to the number of photoelectrons generated by the scintillator [3].

Geiger-Muller tubes are one of the most well-known devices for measuring radiation. The wall of the GM tube is a thin metal (cathode) cylinder surrounding a central electrode (anode). The voltage between the anode and the cathode is 450-500 V. The GM tube is first evacuated and then filled with neon, argon or helium gas. Whenever an ionizing radiation goes through and creates a electron avalanche which in turn produces a narrow pulse with a steep rising edge (See fig. 2.) [4, 5].

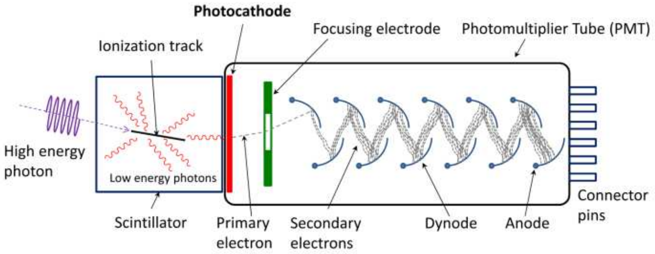

Fig. 1.: Principle of operation of scintillator crystals. [6]

We thank all sponsors and supporters for their help so far, with special thanks to: MANT - Hungarian Astronautical Society, RIVAIR Pilot Kft., VacuTec Meßtechnik GmbH.

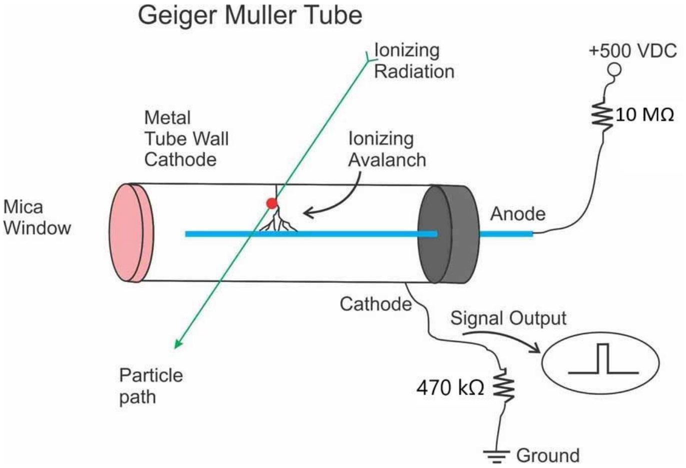

Fig. 2.: Principle of operation of Geiger-Müller tubes. [5]

III. THE EXPERIMENT

The mission statement of TELLER is measuring the intensity, direction and energy spectrum of ionizing radiation present in the atmosphere and its dependence on altitude, up to an altitude of 90 km. Experiment results will provide scientific insight into the radiation patterns that occur in the mesosphere. A preliminary design of the experiment can be seen on Figure 3.

A. *Geiger-Müller Module*

The Geiger-Müller Module (GMM) contains four parallel Geiger-Müller tubes (GM tubes). The layout allows us to divide the space into several regions. The rocket will rotate about its axis at 4 Hz during the flight, so the device will scan all directions. The measurement results are interpreted by the processing electronics using a coincidence detector, so that the relative direction of the detected particle with reference to the tubes can be determined (see fig. 4.).

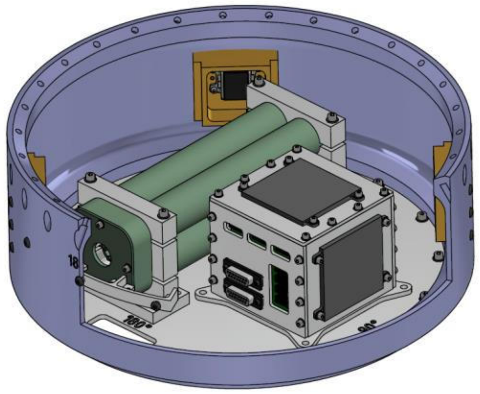

Fig. 3.: Preliminary design of the experiment. Green cylinders are the Geiger-Müller tubes, the yellow boxes in the bulkhead (purple-blue) are the cameras for optical orientation determination and the small box inside the bulkhead contains the electronics. On the sides of the box there are the scintillator crystals (black).

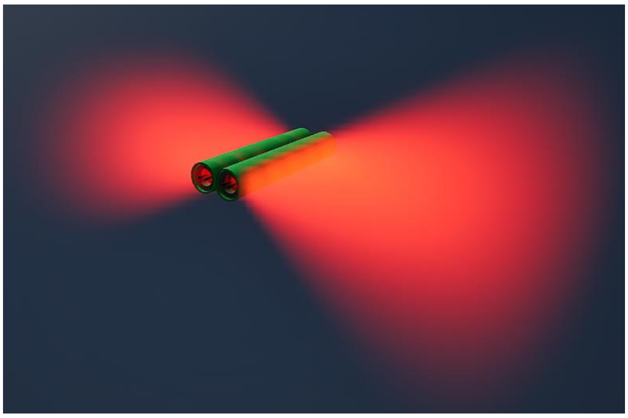

Fig. 4.: If a charged particle passes through two parallel Geiger-Müller tubes, its direction can be detected by the coincidence circuit. The incident region of these possible directions is indicated by the red area.

B. *Scintillator Module*

The other measurement instrument utilizes scintillator crystals composed of cesium iodide doped with Sodium. 3 crystal panels are installed orthogonal to each other. The direction of the detected particle cannot be accurately measured by this method, but it can complement and confirm the data measured by the GMM. The data is recorded with precise timestamps provided by the on-board computer (see fig. 5.).

C. *Optical Orientation Determination*

Four cameras are installed in the bulkhead to provide a continuous view of the outside world. The recordings will be processed to determine the position of the Earth and the Sun. Together with the Earth's position, the Sun's position and additional sensor data from the on-board computer, the orientation of the modules can be determined. The measured data can then be translated into an absolute frame of reference. In addition, interesting recordings are also provided.

D. *Electronics*

On-board electronics serve each of the experimental modules. This includes the power supply, which also provides the high voltage required by the GMM. The main task of the on-board computer is to store the data from each module for later processing. A real time clock is also available for synchronization. In addition, the on-board electronics include various sensors such as gyroscope, accelerometer, magnetometer and temperature sensor (see fig. 5.).

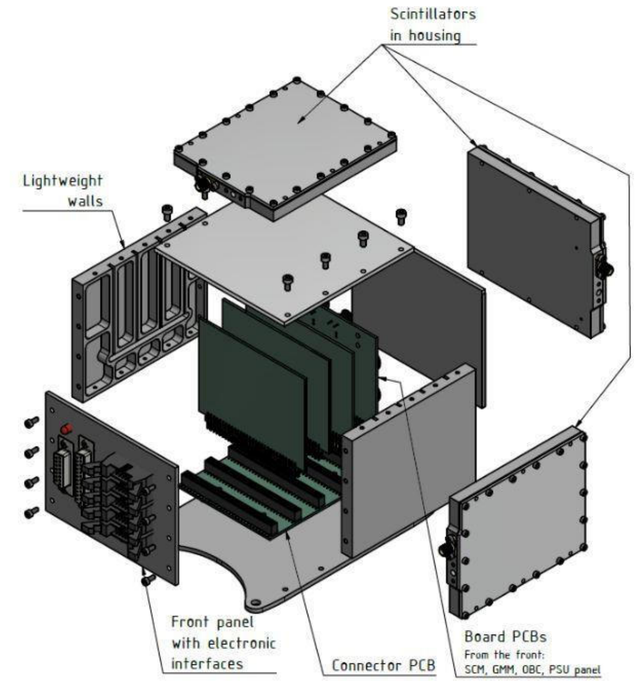

Fig. 5.: Preliminary design of on-board electronics and storage. The scintillator crystals are mounted on the side of the storage box.

IV. EXPECTED RESULTS

Based on previous experiments ([1, 3]) the count rate we are expecting is around 50 particles every second for the individual GM tubes. As for the co-incidence circuit and the individual scintillator crystals this value is about 10 to 20 based on the cross-section of these devices.

The typical energies detected should grow with the increasing altitude up until the point where the first air-showers are happening.

Regarding the directional distribution of radiation, the coming from Earth should be negligible. We are also expecting the radiation-field to be cylindrically symmetrical, with the symmetry axis being perpendicular to the surface of the Earth.

V. REXUS/BEXUS PROGRAMME

The REXUS/BEXUS (Rocket/Ballon Experiment for University Students) program is realized under a bilateral Agency Agreement between the German Aerospace Center (DLR) and the Swedish National Space Agency (SNSA). The Swedish share of the payload has been made available to students from other European countries through a collaboration with the European Space Agency (ESA). EuroLaunch, a cooperation between the Swedish Space Corporation (SSC) and the Mobile Rocket Base (MORABA) of DLR, is responsible for the campaign management and operations of the launch vehicles. Experts from DLR, SSC, ZARM and ESA provide technical support to the student eams throughout the project. REXUS and BEXUS are launched from SSC, Esrange Space Center in northern Sweden. Each year a new project cycle of about 1.5 years duration begins, starting with the call for proposals for two REXUS rockets and two BEXUS balloons [7].

ACKNOWLEDGMENT

A. The entire Project TELLER team would like to thank all academic supporters for their help. We would like to especially acknowledge the support of István Apáthy, Dr. Sándor Deme, Dr. András Pál and Zsolt Váradi, as well as the contribution of the members of the BUTE - Department of Broadband Infocommunications and the Electromagnetic Theory and BUTE - Departments of Electronics Technology.

REFERENCES

[1] Balázs Zábori, Attila Hirn, Sándor Deme, István Apáthy, and Tamás Pázmándi: Characterization of cosmic rays and direction dependence in the Polar Region up to 88 km altitude, Issue: J. Space Weather Space Clim. Volume 6, 2016, Article Number: A12, DOI: https://doi.org/10.1051/swsc/2016006
(J. Space Weather Space Clim., 6, A12 (2016))

[2] Walter, Michael & Wolfendale, A.. (2012). Early history of cosmic particle physics

[3] András Pál and his colleagues: GRBAlpha: the smallest astrophysical space observatory, Issue: Astronomy & Astrophysics, Volume 677, September 2023, Article Number: A40, DOI: https://doi.org/10.1051/0004-6361/202346182
(A&A 677, A40 (2023))

[4] Centronic: Geiger Müller tubes

[5] Images Scientific Instruments: How Geiger Counters Work and Detect Nuclear Radiation, https://www.imagesco.com/geiger, Retrieved: 2024.05.01.

[6] https://en.wikipedia.org/wiki/Scintillation_counter,
Retrieved: 2024.05.01.

[7] REXUS manual, version 7.17, Issued on and valid from: 26.11.2021, issued by Katharina Lesch and Stefan Völk, approved by Rainer Kirchhartz, Document ID: RX_UserManual_v7-17_26Nov21.docx

Radiocommunications with the international space station (ISS)

Katherine Alexandra Cazco Arguello
Széchenyi István University
SzeSat club
Gyor, Hungary
katalexa2014@gmail.com

Máté Péter Toth
Széchenyi István University
SzeSat club
Gyor, Hungary
tothpetermate@gmail.com

Abstract— **The conquest of space has been made possible thanks to technologically advanced telecommunications means. A great example is Earth-Moon-Earth communication, also known as lunar bounce. Our paper intends to study and summarize the knowledge that is necessary to establish radio transmission services between ISS and the Earth Station of the university. This communication will become important for us when we can welcome Hungarian astronauts on the board of ISS.**

It is our task to analyze the question whether the connection can be technically established from the roof of the university and the dormitory. We need to define the technical conditions which can guarantee the establishment of the connection with high reliability. In order to achieve this high reliability value, we need to design a geo-redundant earth station.

By the input technical parameters and expectations, we will have to carry out calculations in order to be able to determinate the adequate value of the power level.

Apart from the calculations we need to explore the area where we want to establish the earth station examining whether the technical conditions are given like power supply, line of sight etc.

In the chosen frequency band, we will measure the level of the noise, so that we can decide whether the given area is appropriate for the project.

Given the conditions, we will commence the planning of the scheme of the system of the station, including hardware and software elements. Following planning, we will commence the phase of implementation. As a first test, communication with a selected radio amateur satellite (repeater station) will take place. Using the results, we will continue the construction of the station so that we should be able to communicate with ISS in a similar way.

Based on scientific knowledge and utilization of engineering skills we would like to be the first to communicate with the astronauts on the board of ISS from the top of the University Győr.

Keywords—radiocommunication; international space station; spectrum; yagi antenna; satellite; automatization; automation.

I. INTRODUCTION

We are studying the radiocommunication with the International Space Station (ISS) to establish connection in the future with the Hungarian astronaut so that he can reply to the students' questions lives. This project is called Hunor-X. We expect four connections being established in Hungary; one of them would be ours from Győr. This is an unprecedent challenge for us both technically and as an experience as well since we rarely have the opportunity to speak to a Hungarian astronaut.

The ISS is a research centre and laboratory that synthesizes the scientific knowledge of 16 nations and is floating in space and revolving around the earth 330 kilometers to 420 kilometers above the earth's surface and has been home to a rotating international crew since November 2000. This station is under constant construction and repair and is often guided from stations on earth, so radio communications with this space station are very important. ISS is into the Low Earth Orbit (LEO) that is an orbit around earth.[1]

The radiocommunication between ISS and earth station is a way of wireless communication that uses electromagnetic waves to transmit information over long distances [2]. This communication is important for us because it is used for scientific investigation. The ISS uses these two wave lengths, one for uplink with 2 meters and the other one for downlink with 70 centimeters.

The hardware to establish communication with the satellites we have a set of base radiocommunication IC-9700, where we can receive and send messages and this station use both VHF and UHF bands, and it also includes D-STAR technology.

The software that was used in the automatization for sending and receiving messages and the analysis of the signals are as follows:

Firstly, we use the Gpredict software that is a real-time satellite tracking and orbit prediction application. Also, it can predict the time of future passes for a satellite and provide you with detailed information about each pass. It allows you to group the satellites into visualization modules [3]. In this program you can see the footprint of the satellites, too.

Secondly, we use node-red, a virtually programmable tool software, programmed in JavaScript and it was used to process the data we get from Gpredict.

Afterwards, the data are sent to the Programmable Logic Circuits that signals the rotors to change the azimuth and the elevation of the two Yagi antenna group.

II. RADIOCOMMUNICATION PLANNING

The technique of radiocommunication involves a generation of a modulated wave, and its spectrum contains a set of frequencies around the carrier. The modulated wave is transmitted into the propagation medium through a coupling device with the medium called an antenna.[4]

In radiocommunications planning there are the following terms:

A. *Frequencies*

In this investigation for space waves are used the frequency bands VHF with a typical range of 2000 km and UHF with a typical range of 600 km.

B. *Wave Polarization*

The antennas have an electrical field vector in a vertical plane; thus, the wave polarization is horizontal.

C. *Doppler effect*

Doppler effect involves the variation in the wavelength of any type of wave emitted or receiving by a moving object like the satellite.[5]

The following formula allows to calculate the maximum frequency shift with respect to the carrier frequency emitted or received by a satellite.

$$F_r = \frac{F_p}{V_l} . V_s \tag{1}$$

D. *Footprint*

Satellite footprints correspond to the regions of the Earth's surface encompassed by the signal transmitted by a satellite.

Most satellites as ISS, are to be found in low Earth orbit (LEO) that is an orbit around the Earth with an altitude that lies towards the lower end of the range of possible orbits, this is around 1200 miles or less.

In the Fig. 1, the footrpint of ISS satellite in Gpredict software, is observed.

In the Fig. 2, the prediction of ISS trajectory in N2YO.com website, is observed.

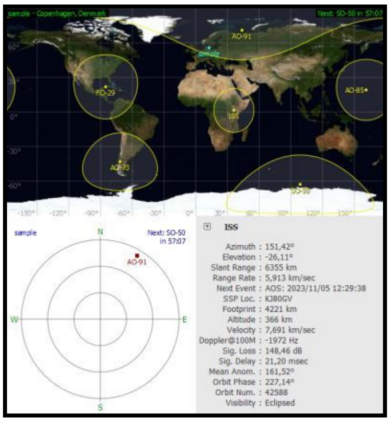

```
     Azimuth : 151,42°
   Elevation : -26,11°
 Slant Range : 6355 km
  Range Rate : 5,913 km/sec
  Next Event : AOS: 2023/11/05 12:29:38
    SSP Loc. : KJ80GV
   Footprint : 4221 km
    Altitude : 366 km
    Velocity : 7,691 km/sec
Doppler@100M : -1972 Hz
   Sig. Loss : 148,46 dB
  Sig. Delay : 21,20 msec
 Mean Anom. : 161,52°
 Orbit Phase : 227,14°
  Orbit Num. : 42588
  Visibility : Eclipsed
```

Fig. 1. Footprint of satellites.

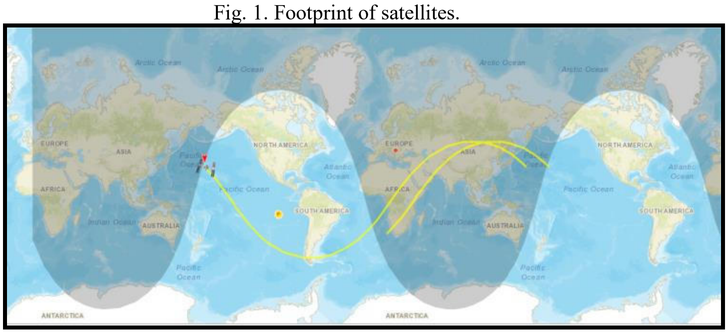

Fig. 2. Trajectory of ISS around the Earth.

III. SYSTEM COMPONENTS

The system design of the radiocommunication with ISS is the following:

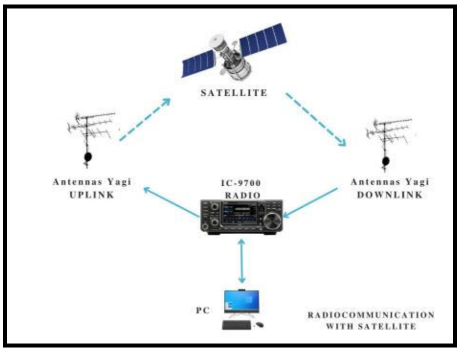

Fig. 3. System Design.

The system is made up of the following components:

A. *Earth Station*

The Earth Station is located in the top of the dorms building in the Széchenyi Istvan University. This station has the following components.

1) Transceiver Equipment: The transceiver Equipment is the Radio IC-9700 which can be seen in the Fig. 4.

Fig. 4. Radio IC-9700 implemented in the station.

2) Wave guide: In the Earth station there are an ECOFLEX-10 and ECOFPLEX-15 coaxial cables.

3) Yagi antennas: The earth station has two antennas, the downlink antenna receives messages and is made up of 4 antennas with 12 elements which you can see in the Fig. 5, and the uplink antenna send messages and is made up of 4 antennas with 19 elements.

Fig. 5. Yagi Antennas.

B. *International Space Station*

The ISS satellite like a repeater works with a frequency of 145,8 MHz for uplink and 437,8 MHz for downlink.

The system of communications is made up of the following:

1) Transceiver Equipment: The ISS uses Kenwood TM-D710E and a Kenwood TM-D710GA for amateur radio communication.

2) Wave guide: The wave guide in the ISS is the coaxial cable.

3) Antennas: A set of four UHF antenna systems is in place within the ISS Service Module to support the existing installation of the Kenwood TM-D710E radio.

C. *Trancking System Earth Station*

1) Rotator: The two-antenna group (4*12 Yagi @144MHz) and (4*19 Yagi @436MHz) have rotors that can move on 2 axels, elevation, and azimuth. This, it is possible to automate the tracking of a satellite's orbit with the antennas.

Fig. 6. Elevation-azimuth G5500 controller in the station.

2) Controller Software: With Gpredict we control the antennas according to the satellites current position over Node-Red.

IV. CALCULATIONS

The following calculations were made:

A. *Doppler effect calculation*

The calculation according to equation (1), for the maximum frequency shift due to the doppler effect at the downlink frequency of the ISS on the VHF band, it emits 145,8MHz, and at the uplink frequency of the ISS on the UHF band, it emits 437,8MHz, to a speed of 7777m/s, and the speed of light is 300.000km/s is as follows:

$$F_r = \frac{145\ 800\ 000Hz}{300\ 000\ 000m/s}.\frac{7777m}{s} = \ 3779Hz \tag{2}$$

$$F_r = \frac{437\ 800\ 000Hz}{300\ 000\ 000m/s}.\frac{7777m}{s} = \ 11\ 349Hz \tag{3}$$

.

B. *Noise Lever Measurement*

The noise levels in the roof of room D-800 and in the roof of the Radio Amateur Club, can be seen in the Table I.

TABLE I. NOISE MEASUREMENTS.

Roof of building D-800		**Radio Amateur Club roof**	
Uplink *145 MHz*	*Downlink* *436 MHz*	*Uplink* *145 MHz*	*Downlink* *436 MHz*
-69,78dBm	-69,61dBm	-127dBm	-124dBm

The noise for downlink from the Radio Amateur club roof of -154 dBW was used.

And the power noise from ISS is -186,84dBW.

C. *Free Space Attenuation Calculation*

The Free Space Path Loss is the loss on signal strength of a signal as it travels through free space.

For calculations we use the following equation from ITU. And 3dB were added by the polarization attenuation, humidify attenuation and atmospheric attenuation.

$$FSPL: 32{,}4 + \ 20\log_{10}(d) + 20\ \log_{10}(f) \tag{4}$$

For uplink:

$$FSPL: 32{,}4 + 20\log_{10}(412km)$$
$$+20\ \log_{10}(145{,}9\ MHz) + 3dB = \ 130{,}98\ dB \quad (5)$$

For downlink:

$$FSPL: 32{,}4 + 20\log_{10}(412km)$$
$$+20\ \log_{10}(437{,}8\ MHz) + 3dB = 140{,}52\ dB \quad (6)$$

D. Link Budget Calculation

This link budget calculates and provides information of losses and gains, available power at transmitter, antenna gain, propagation losses and performance losses due to noise and natural interference.

To calculate the link budget in Yagi antennas, the following equation is used.

$$P_s = G_t + G_r + P_t + 20\log_{10}\frac{\lambda}{4\pi R} \quad (7)$$

Uplink:

$$P_s = 15{,}75dB + 4{,}75dB + 20dB + 20\log_{10}\frac{2m}{4\pi(412000m)}$$
$$= -87{,}8\ dB \quad (8)$$

Link budget:

$$\left(\frac{C}{N}\right)^{dB} = -87{,}76\ dB - (-186{,}84\ dB) = 99{,}1\ dB \quad (9)$$

Downlink:

$$P_s = 4{,}75dB + 15{,}75dB + 16{,}99\ dB$$
$$+20\log_{10}\frac{0{,}70m}{4\pi(412000m)} = -99{,}9\ dB \quad (10)$$

Link budget:

$$\left(\frac{C}{N}\right)^{dB} = -99{,}89\ dB - (-154\ dB) = 54{,}1\ dB \quad (11)$$

TABLE II. LINK BUDGET TABLE.

Sensitivity	Signal-to noise ratio
Sensitivity transceiver earth station: -153,47 dB	Downlink C/N= -99,9 dB
Sensitivity transceiver satellite: -213dB	Uplink C/N=-87,8 dB

V. RESULTS

A. Test with Radio Amateur Satellites

1) Satellite SO-50: On 31 October 2023, there was successful connection with F1FPL, UR5FCC and LY4AA through of SO-50 cube satellite. The uplink frequency was at 145.847MHz, the downlink frequency was 436.803 MHz.

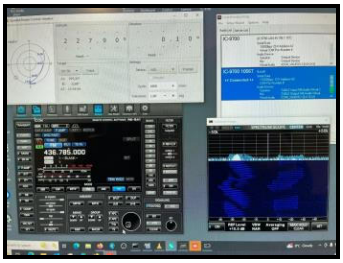

Fig. 7. Monitoring communication with SO-50.

2) Satellite RS-44: Another successful connection. The uplink frequency was at 145.962.829 Hz, the downlink frequency was 435.646.481 Hz.

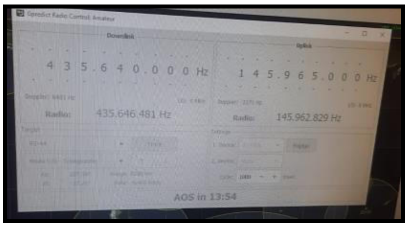

4 3 5 . 6 4 0 . 0 0 0 Hz

1 4 5 . 9 6 5 . 0 0 0 Hz

Radio: 435.646.481 Hz

Radio: 145.962.829 Hz

RS-44

AOS in 13:54

Fig. 8. Radio control to satellite RS-44.

B. Test with the ISS

On 17 October 2023, we were able to capture the ISS signal. In the Fig. 9, you can see the orbit of the satellite, the rotator control with the degrees of elevation and azimuth of the antennas and the spectrum scope.

On 18 October 2023, we were able to capture the ISS signal where this time the satellite passed almost above us.

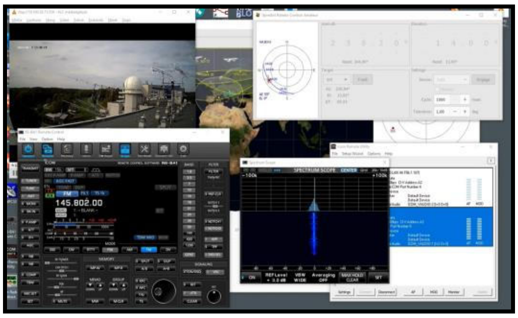

Fig. 9. Monitoring communication with ISS 17 October 2023.

On 18 October 2023, we were able to capture the ISS signal where this time the satellite passed almost above us.

Fig. 10. Monitoring communication with ISS ,18 October 2023.

On 20 October 2023, a connection was made through the repeater of the ISS. Downlink was measured 437,8 MHz with 10037 Hz of difference due to the Doppler effect and Uplink 145,99 MHz with of difference -3347 Hz, values close to the values calculated previously in the calculations of the Doppler effect. The movement of the antennas occurs with 236.05° azimuth and 0° elevation. Azimuth has a high trajectory starting with 236.05°and ending 34.67°.

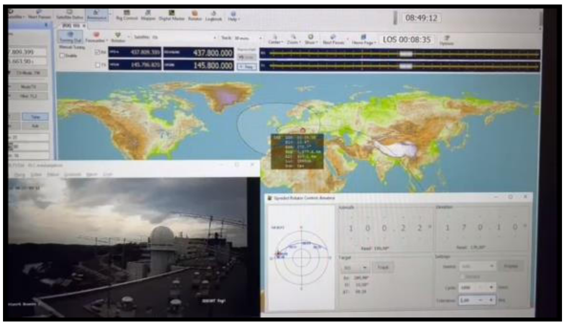

Fig. 11. Monitoring communication with ISS, 20 October 2023.

VI. CONCLUSION

Noise level of the top of the college is smaller than Room D.

Yagi antenna group has best size and stability for wind.

The link budget of Yagi Antenna is 99,08 dB for uplink and 54,11 dB for downlink. With a noise level of -186,84dBW for uplink and -154 dBW for downlink. We used Yagi antennas and with these the system is correct because provides better reception quality and greater overall communications accuracy and reliability.

The value of the free space attenuation with the distance and frequency for isotropic antennas is 130,98 dB with uplink and 140,52 dB with downlink, the connection can only be made if we have a better signal level according to our measurements, and the signal is stronger than the free space loss itself.

We decided choose Yagi antenna because it was already planted, it can fit the roof, it withstands stronger winds, with the Yagi antennas we can take advantage of the existing supports on the roof of the amateur radio club, these antennas have the frequency that we need, and have the good gain, and size and stability that support the strong wind.

The tests made it possible to prove our calculations. With the SO-50, which has a much lower signal power than the ISS, we made 9 successful connections.

Testing with ISS gave insights about the importance of the downlink power. All tests with ISS were successful proving that all our calculations were correct. The signal worsens when the ISS trajectory gets lower, and the best signal comes with the highest trajectory possible for the ISS. Everything is ready for the first connection with the ISS.

Testing with ISS was successful.

ACKNOWLEDGMENT

We thank Dr Péter Vári for guiding us in the completion of this thesis. Likewise, we thank Layos Keri, who taught us how to use the equipment and explained the entire communication process to us, we thank Péter Pataki and Anna Fabián Gertrúd, who help us with the measurement of the noise, also thank Dr Kolos Tibor for helping us with the calculations. And we want to thank all the people who made this project possible.

REFERENCES

[1] "International Space Station," *NASA website*, 2023. https://www.nasa.gov/reference/international-space-station/ (accessed Nov. 05, 2023).

[2] R. Union International Telecommunication Sector, "Handbook on Small Satellites," 2023.

[3] Alexandru Csete, *Gpredict User Manual*. 2017.

[4] J. M. Hernando Rabanos, *Transmision por Radio*, 6th ed. Madrid, 2008.

[5] C. Cao and S. Zhai, "The influence of LEO satellite Doppler effect on LoRa modulation and its solutio," *J. Phys. Conf. Ser.*, vol. 1883, no. 1, pp. 1–6, 2021, doi: 10.1088/1742-6596/1883/1/012071

[6] ITU-R P.525-3, "Calculation of free-space attenuation P Series Radiowave propagation," *Ser. ITU-R Recomm.*, vol. 3, pp. 1–3, 2016.

The perspective of launch capacity and strategic sovereignty of European space activity

Bence Kertész
Ludovika University of Public Service
MANT
Budapest, Hungary
kertesz.bence.official@gmail.com

Abstract— **This paper aims to analyse the European space launch capacity and its effects on the strategic sovereignty of European space activity (being the complex of ESA and EU member states). The analysis starts from the historical perspective of European space launch capacities which gives a brief introduction on the development and technological background of the sector and its potential. The research gives a conclusive review of current European space capacities, revealing the major issue of their temporary absence and analyses the effects of this phenomena on the strategic sovereignty of European space activity. Furthermore, this study draws the future perspective of European space launch sector and categorises the three main challenges that Europe has to solve to develop autonomous space launch capacities and to guarantee the future of European strategic sovereignty in space.**

Keywords—space launch capacity, strategic autonomy, current crisis, challenges, Europe

I. INTRODUCTION AND HISTORICAL PERSPECTIVE OF EUROPEAN SPACE LAUNCH CAPACITIES

Since the beginning of space research, key condition capacity to conduct space activity has always been the space launch capacity with the use of space launch vehicles (SLV). These capacities fundamentally limit the characteristics of space missions also by the mass of payload (small, medium, heavy) and its type (satellite, crew etc.). This way, the absence of launch capacity can be devastating to the autonomous access of space and for space activities. That is the reason why it is important to analyse the crisis of European space launch sector, and its possible future challenges and perspective.

Although European space research (which in this paper means the complex of ESA and EU member states) has always been in the forefront of global space research development, in the initial phase, space activity based on national level, and the formalised way of European space cooperation came alive only by the 1960's [1]. Signing the strategic importance of autonomous space launch capacities, one of the first institutional form that was created for united European space research was the European Launch Development Organisation (ELDO) in 1962 [2]. The first European space launch vehicle family was Europa, which was being developed and tested by the ELDO between 1964 and 1973 [3]. Although the project had many failures due to technical issues, it became the first step towards creating European space launch vehicle. As Europe still hadn't possessed the capacity for autonomous space launch, the dependency on the US SLV-s increased, moreover, the US conditions for launches became unacceptable, thus this way the fundamentals of European space activities were being threatened.[4] The solution for the challenge came by the creation of ESA in 1975,[5] which coordinated the new European rocket family, the Ariane series[6]. The Ariane rockets became the main pillar of European space transportation, only the Ariane 5 version in itself has made 117 launches between 1996 and 2023 [7]. Beyond being the general launch vehicle of European space sector, the Ariane series has been used for unique challenges, such as launching the Infrared Space Observatory, [8] James Webb Space Telescope and parts of the Galileo navigation system [9]. Meanwhile, a parallel rocket family was created with the name of Vega, which is designed for smaller capacity missions than the Ariane, being developed since 1998, and first launched in 2012 [10]. The third main rocket family to be used as launcher for European space research activity was the Soyuz series, being the most reliable launcher vehicle with a long historical background [11]. In European space activity, it was primarily used for launching medium size payloads and crewed missions [12].

In order to have autonomous space launch capacity, beyond space launch vehicles, the availability of launch site is also a fundamental condition. European space sector has its own major European launch site, located in French Guyana, since 1968 [13]. The Guyana Space Center consists of various facilities - including test pad for engines [14] – which can serve not only directly the launches, but potentially researches as well. However, it is important to notice that Europe's Spaceport doesn't have the capacity to provide the operational background for crew launches, thus Europe has not got the independent capacity for launching crewed missions, but participates in international cooperation to conduct this type of space missions [15]. Beyond that, for a period of time, there was also a potential future perspective of developing the necessary capacities for crew launches by using Soyuz rockets and creating necessary infrastructure at Europe's Spaceport [16].

Even though, Ariane, Vega and Soyuz rocket families have provided launch services for the European space sector, these three pillars of the system can be vulnerable. The following section of this research is going to reveal how the temporal unavailability of these launch services during 2023 has caused crisis and a threat to the autonomy of European space activity.

II. CRISIS OF EUROPEAN SPACE LAUNCH CAPACITY AND ITS EFFECTS ON EUROPEAN SPACE SOVEREIGNTY

In spite of the long and successful history of European launch services, in 2022, various negative events have showed the vulnerability of this sector and the potential danger of Europe losing its independent access to space by the temporary unavailability of launch capacity.

Until the second half of 2022, European space sector has based its activity on three main pillars. For heavy payload missions, the Ariane series was used, while Vega series provided launch capacity for smaller missions, and third pillar was the Soyuz series, providing launching capacity for medium payload and crewed missions.

From the Ariane series, the latest version in service was the Ariane 5, being the biggest capacity European heavy-lift space launch vehicle. This rocket could launch 10 tons of payload to Geostationary Transfer Orbit (GTO) or 20 tons to Low Earth Orbit (LEO) [17]. Beyond its heavy capacity, Ariane 5 had its unique characteristics that it could launch two different payloads separately, thus enabling flexible and cost-effective mission planning. Demonstrating its reliability and central role, between 1996 and 2023, 117 launches were made with this rocket (including its variants), providing launch service for a wide variety of missions [18]. As it was serving more than a quarter of a century, by the beginning of July 2023 with its last mission, the Ariane 5 became retired, being followed by its successor, the Ariane 6, originally planned to start its operation from 2020 [19]. But the tests of Ariane 6 delayed [20] and the successful inaugural flight was only made in July 2024 [21], this way breaking the constant provision of launch services, thus temporarily disabling the possibility for European heavy-lift launches.

The Vega series is the other pillar of European space launch capacities, providing cost-effective alternative for smaller capacity missions. The latest, upgraded version of this series is the Vega-C, which had its inaugural flight in 2022 [22]. This rocket can launch 3,3 tons of payload to LEO, and 2,2 tons to other orbits, and with its large fairing, it can carry larger payloads, such as one radar satellite or multiple nanosatellites [23]. Thanks to its SSMS (Small Spacecraft Mission Service) rideshare service, it can carry up to 50 small satellites in one mission, thus making lightweight launches more affordable [24]. But, as a consequence of a launch failure in December 2022, the services of Vega-C became suspended and due to the prorogation of investigations, it is planned to returning operational only by late 2024 [25].

As it was stated before, Europe does not have the independent capacity to launch crewed missions, but it has to rely on external partners. Between 2011 and 2020, the only available crew launch service globally was provided through the Russian Soyuz(-2) rocket [26]. In accordance with that, Europe also has been using Soyuz services for crewed missions and medium-sized satellites, this way covering diverse European launch needs together with Ariane and Vega [27]. At Europe's Spaceport, own launch-site was created for Soyuz as well, this way providing the possibility for uncrewed launches from (an overseas) European territory [28]. But in opposition to the decade of successful European collaboration with Roskosmos through Soyuz services, the political environment that changed due to the war in Ukraine, has caused the halt of this unique cooperation. Russia has suspended all Soyuz launches from Europe's Spaceport, and withdrew all of its service crew due to EU sanctions [29]. This abolished not only the possibility to launch medium size payloads, but the potential future perspective as well to create European crew launch capacity by using Soyuz rocket and integrating the necessary launch support into Europe's Spaceport.

This way, for a period, Europe has lost its capacity for heavy-lift, and lightweight launches, and its traditional partner for medium and crewed launches. This created a vulnerable position of Europe, making it dependent on the capacities of external actors, and threatening the fundamentals of European strategic autonomy and the activity of the whole space sector. The lack of capacities in itself can create hazard for the (national) security of Europe not mentioning the long-term consequences on various sectors, especially on the launch industry. A short-term example for the former argument is the fact that during the examined period, Europe had to launch the satellites of Galileo (as a GNSS, being a critical infrastructure and a direct guarantee of European strategic autonomy) by the capacities of an external actor, the United States of America, as ESA had to sign contract with SpaceX in October 2023 for launching Galileo satellites [30]. In overall, this short case study has proved that the European space launch sector is vulnerable, and a temporary absence of launch services can pose a major threat to the strategic autonomy of Europe and its space activities.

III. THE THREE MAIN CHALLENGES OF EUROPEAN SPACE LAUNCH SECTOR

As it has been proven, until now, the European launch capacity in the 21st century had a stable system for satisfying different needs for (heavy, medium, and lightweight) space missions by its three main pillars of launch rocket family (Ariane, Vega and Soyuz). However, this system has got structural vulnerabilities, which, as it was seen, can (temporarily) create deficiency in capacities, being a threat to European strategic autonomy. This study categorises three main deficiencies of the structure of European space launch sector, which challenges are needed to be tackled to guarantee the future of European space sector and to develop autonomous space launch capacities.

The first challenge is an economic challenge, which is the involvement of private actors in the launch industry by commercial needs. Even though, the main rocket families are created as a success of cooperation between private and state parties, there lies the threat that these companies can heavily depend on public support and demand, having rockets which might be too robust for the needs of the mass of small private space actors. In the future, ESA would like to change its approach to a competitive policy, in which, the private actors of a commercialised space launch sector would compete for launch contracts in spite of relying solely on Vega and Ariane rocket families [31]. In accordance with that, ESA has launched many programmes (such as the ESA Commercialisation Gateway) [32] to help (financially) the involvement of business entities in European space sector, this way fostering innovation and developing European space capacities at the same time.

The second challenge is a technological challenge, which is creating reusable European space launch vehicle. As the example of SpaceX has shown [33], the usage of reusable rockets can reduce massively the cost of flights thus enabling more affordable launch services, greater amount and more constantly available capacities. For developing these capacities, several initiatives have born, such as the Themis project (ESA reusable rocket prototype) [34] and Prometheus (ESA ultra-low cost, reusable rocket engine) [35]. In 2021, ESA launched the NESTS (New European Space Transportation Solutions) for awarding contracts to creating European space transport solutions [36]. ArianeGroup so far has presented a planned family of reusable, eco-friendly launchers in cooperation with diverse European companies, thus creating a potential concept for autonomous European reusable launch capacities [37].

The third challenge has economic, political and technological perspective, as it is the lack of European launch (and service infrastructure) capacity for crewed missions. As it was showed in the analysis, Europe traditionally relies on the external capacities of international partners in launching crewed missions, for a long time it was the Russian Soyuz, but now it changes to the US solutions, such as SpaceX [38] or the Axiom Space [39].

Politically, the option of returning to the Russian capacities is eroding, meanwhile the US perspective becomes stronger, which can also create dependency and threat to European autonomy (which scenario was also present during the Cold War as it was analysed in the first part of this research). In the political perspective, in order to guarantee the stability of using external capacities, Europe should create long-term accords with partners, having acceptable conditions to minimise the risks of a possible negative change in the future.

Technologically, the most plausible option of creating European capacity for crew launch is the development of Ariane-6, being the upcoming biggest European launcher rocket. According to the plans, the Susie upper stage compatible with Ariane-6 and serving as a reusable space transporter, is going to have the capacity of lifting and bringing back 7 tons of payload, that can be also a crew of 5 astronauts [40]. Parallelly, the concept of Athena project was raised in 2022, also with the aim of creating crew launcher applicable to Ariane-6 rocket [41]. However, beyond the development of launchers, the necessary ground support infrastructure should be created as well to comprehensively provide autonomous European crew launch capacity.

Economically, all of these perspectives should be taken into consideration, as the security interests, cost of technological solutions have to be in balance. This is a complex equation, as in short-term, contracts with external partners can be more cost-effective than developing own capacities, however, in the long-term, it can create devastating consequences on European competitiveness and autonomy.

IV. CONCLUSION

This research has presented the historical perspective of European space launch sector and analysed in detail the latest case of European launch capacity crisis, and its possible effects on European strategic autonomy (in space). Furthermore, it also categorised the three major challenges of European space launch sector as the need for commercialisation, for European reusable launch vehicles and for crew launch capacities. Due to technological, political challenges, and its structural vulnerabilities, Europe has lost temporarily its autonomous access to space as the three main pillars (Ariane, Vega, Soyuz rocket families) of launch sector became unavailable. This causes the forced reliance (and dependence) on the capacities of external partners, this way creating an existential threat to the (autonomy of) European space sector. To solve this crisis and to develop autonomous European space launch capacities the three challenges of commercialisation, European reusable launch vehicles and crew launch capacities need to be solved, considering political, economic, and technological dimensions. This way, the perspective of launch capacities is going to be a decisive factor in the future of European space sector, which also defines the strategic sovereignty of Europe in space.

V. REFERENCES

[1] ESA (no date - a). *History of Europe in space,* Available at: https://www.esa.int/About_Us/ESA_history/History_of_Europe_in_space (Accessed: 23 February 2024).

[2] ESA (no date - a). *History of Europe in space,* Available at: https://www.esa.int/About_Us/ESA_history/History_of_Europe_in_space (Accessed: 23 February 2024).

[3] ESA (2009). *The origins of Ariane,* Available at: https://www.esa.int/About_Us/ESA_history/The_origins_of_Ariane (Accessed: 10 April 2024).

[4] ESA (2009). *The origins of Ariane,* Available at: https://www.esa.int/About_Us/ESA_history/The_origins_of_Ariane (Accessed: 10 April 2024).

[5] ESA (no date - a). *History of Europe in space,* Available at: https://www.esa.int/About_Us/ESA_history/History_of_Europe_in_space (Accessed: 23 February 2024).

[6] ESA (no date - a). *History of Europe in space,* Available at: https://www.esa.int/About_Us/ESA_history/History_of_Europe_in_space (Accessed: 23 February 2024).

[7] ESA (no date - b). *Ariane 5,* Available at: https://www.esa.int/Enabling_Support/Space_Transportation/Launch_vehicles/Ariane_5 (Accessed: 10 April 2024).

[8] ESA (no date – c). *N° 50–1995: ISO successfully launched*, Available at: https://www.esa.int/Newsroom/Press_Releases/ISO_successfully_launched (Accessed: 30 September 2024).

[9] ESA (no date - b). *Ariane 5,* Available at: https://www.esa.int/Enabling_Support/Space_Transportation/Launch_vehicles/Ariane_5 (Accessed: 10 April 2024).

[10] ESA (no date - d). *Vega,* Available at: https://www.esa.int/Enabling_Support/Space_Transportation/Launch_vehicles/Vega (Accessed: 10 April 2024).

[11] ESA (no date – e). *Soyuz launch vehicle: The most reliable means of space travel,* Available at: https://www.esa.int/Science_Exploration/Human_and_Robotic_Exploration/Delta_Mission/Soyuz_launch_vehicle_The_most_reliable_means_of_space_travel (Accessed: 30 September 2024).

[12] ESA (2021a) Ten years of Soyuz at Europe's Spaceport, Available at: https://www.esa.int/About_Us/ESA_history/Ten_years_of_Soyuz_at_Europe_s_Spaceport (Accessed: 15 April 2024).

[13] ESA (no date - f) *Europe's Spaceport,* Available at: https://www.esa.int/Enabling_Support/Space_Transportation/Europe_s_Spaceport (Accessed: 10 April 2024).

[14] ESA (no date - g) *Overview of Europe's Spaceport,* Available at: https://www.esa.int/Enabling_Support/Space_Transportation/Europe_s_Spaceport/Overview_of_Europe_s_Spaceport (Accessed: 10 April 2024).

[15] HLAG (2023) *Revolution Space*, Available at: https://esamultimedia.esa.int/docs/corporate/h-lag_brochure.pdf (Accessed: 30 September 2024).

[16] ESA (2005) Soyuz at the Guiana Space Centre, Available at: https://www.esa.int/esapub/br/br243/br243.pdf (Accessed: 30 September 2024).

[17] Arianespace (no date - b) *'Ariane 5',* Available at: https://www.arianespace.com/vehicle/ariane-5/ (Accessed: 10 April 2024).

[18] ESA (no date - b) *Ariane 5,* Available at: https://www.esa.int/Enabling_Support/Space_Transportation/Launch_vehicles/Ariane_5 (Accessed: 10 April 2024).

[19] Dinner, Josh (2023) *Farewell, Ariane 5! Europe's workhorse rocket launches 2 satellites on final mission (video)*, *Space.com*. Available at: https://www.space.com/ariane-5-rocket-final-launch-success (Accessed: 10 April 2024).

[20] Foust, J. (2023b) 'ESA confirms Ariane 6 debut to slip to 2024', *SpaceNews*, 9 August. Available at: https://spacenews.com/esa-confirms-ariane-6-debut-to-slip-to-2024/ (Accessed: 15 April 2024).

[21] ESA (2024a) *Europe's new Ariane 6 rocket powers into space*, Available at: https://www.esa.int/Enabling_Support/Space_Transportation/Ariane/Europe_s_new_Ariane_6_rocket_powers_into_space (Accessed: 28 September 2024).

[22] ESA (2022) Vega-C successfully completes inaugural flight, Available at: https://www.esa.int/Newsroom/Press_Releases/Vega-C_successfully_completes_inaugural_flight (Accessed: 15 April 2024).

[23] Arianespace (no date - b) *'Vega C',* Available at: https://www.arianespace.com/vehicle/vega-c/ (Accessed: 15 April 2024).

[24] ESA (2020) *Rideshare service for light satellites to launch on Vega,* Available at: https://www.esa.int/Enabling_Support/Space_Transportation/Rideshare_service_for_light_satellites_to_launch_on_Vega (Accessed: 15 April 2024).

[25] Foust, J. (2023c) 'ESA delays Vega C return to flight to late 2024', *SpaceNews*, 2 October. Available at: https://spacenews.com/esa-delays-vega-c-return-to-flight-to-late-2024/ (Accessed: 15 April 2024).

[26] Mohanty, Susmita (2023) *Soyuz: the world’s most reliable human spacecraft*. Available at: https://www.stirworld.com/think-columns-soyuz-the-world-s-most-reliable-human-spacecraft (Accessed: 15 April 2024).

[27] ESA (2021a) *Ten years of Soyuz at Europe's Spaceport,* Available at: https://www.esa.int/About_Us/ESA_history/Ten_years_of_Soyuz_at_Europe_s_Spaceport (Accessed: 15 April 2024).

[28] ESA (2021a) *Ten years of Soyuz at Europe's Spaceport,* Available at: https://www.esa.int/About_Us/ESA_history/Ten_years_of_Soyuz_at_Europe_s_Spaceport (Accessed: 15 April 2024).

[29] Malik, Tariq (2022) *Russia halts Soyuz rocket launches from French Guiana over European sanctions on Ukraine invasion*, *Space.com*. Available at: https://www.space.com/russia-halts-soyuz-launches-french-guiana (Accessed: 15 April 2024).

[30] Wall, Mike (2023) *SpaceX inks landmark deal to launch European navigation satellites: report*, *Space.com*. Available at: https://www.space.com/spacex-launch-european-galileo-navigation-satellites (Accessed: 15 April 2024).

[31] Foust, J. (2023a) 'European launch deal praised despite competition questions', *SpaceNews*, 15 November. Available at: https://spacenews.com/european-launch-deal-praised-despite-competition-questions/ (Accessed: 18 April 2024).

[32] ESA (2024) *Commercialisation,* Available at: https://www.esa.int/ESA_Multimedia/Images/2024/01/Commercialisation (Accessed: 18 April 2024).

[33] Venditti, B. (2022) *The Cost of Space Flight Before and After SpaceX*, *Visual Capitalist*. Available at: https://www.visualcapitalist.com/the-cost-of-space-flight/ (Accessed: 18 April 2024).

[34] ESA (no date - h). *Themis,* Available at: https://www.esa.int/Enabling_Support/Space_Transportation/Themis (Accessed: 18 April 2024).

[35] ESA (2021b). *New ESA contracts to advance Prometheus and Phoebus projects,* Available at: https://www.esa.int/Enabling_Support/Space_Transportation/New_ESA_contracts_to_advance_Prometheus_and_Phoebus_projects (Accessed: 18 April 2024).

[36] Bibikoff, A.D. (no date - a) *ArianeGroup and ESA's NESTS initiative*, *ArianeGroup*. Available at: https://www.ariane.group/en/news/a-family-of-reusable-and-eco-friendly-launchers-for-europe/ (Accessed: 18 April 2024).

[37] Bibikoff, A.D. (no date - a) *ArianeGroup and ESA's NESTS initiative*, *ArianeGroup*. Available at: https://www.ariane.group/en/news/a-family-of-reusable-and-eco-friendly-launchers-for-europe/ (Accessed: 18 April 2024).

[38] Euronews (2024) *Meet the first all-European crew set to launch to the ISS,* Available at: https://www.euronews.com/next/2024/01/18/meet-the-first-all-european-crew-set-to-launch-to-the-international-space-station (Accessed: 18 April 2024).

[39] ESA (2023) *ESA and Axiom Space forge partnership for future space exploration,* Available at: https://www.esa.int/About_Us/Corporate_news/ESA_and_Axiom_Space_forge_partnership_for_future_space_exploration (Accessed: 18 April 2024).

[40] Bibikoff, A.D. (no date - b) *Susie, the new reusable rocket upper stage concept*, *ArianeGroup*. Available at: https://www.ariane.group/en/news/susie-the-reusable-space-transporter-european-style/ (Accessed: 18 April 2024).

[41] Parsonson, A. (2022) 'Project Athena: A challenge to ESA to develop crew launch capabilities', *European Spaceflight*, 16 February. Available at: https://europeanspaceflight.com/project-athena-a-challenge-to-esa-to-develop-crew-launch-capabilities/ (Accessed: 18 April 2024).

Assessment of Cooperation in the Space Sector

Don Koulaouzos
Skytrek Ltd.
London, United Kingdom
www.sky-trek.com

Abstract—**The phrase "united we stand, divided we fall" is often quoted to inspire unity and cooperation.**

The celebrated Apollo programme relied on over 20,000 different organisations to put humans on the Moon. Fifteen nations from five space agencies cooperated to build and maintain the International Space Station. The European Space Agency is another exemplar of successful cooperation at an international level.

Can we apply lessons from these and other historic achievements to the New Space era? Are there more advantages than disadvantages to cooperation, and what are the key factors that determine success? What are the barriers to entry for SMEs who try to grow alone?

Large enterprises are often reluctant to accept risk purchasing from small or startup companies held back by their size, restricted capital or limited history. Some of the benefits from cooperation include reduced costs and risks, sharing of financial and human resources, greater buying power, and improved supply chain assurance (especially for scarce components), as well as the efficiency benefits from economies of scale and market reach.

One of the main challenges competing companies face is determining whether growing the whole pie cooperatively will generate greater financial and strategic benefits than just their segment of the pie.

It is possible for firms to simultaneously exist as competitors and partners through a Coopetition framework. Analysing the strengths and weaknesses within a country or industry using Porter's Diamond model can help determine if there is a competitive advantage or disadvantage. Business clusters are one method for competing companies to work together to achieve goals that would not be possible independently. However, to achieve any measurable impact, clusters need to be more than just a passive catalogue of entities and capabilities.

Examples of successful cooperation in the space sector between emerging and well established companies include the European New Symphonie consortium, led by Unseenlabs and Euroconsult which has 22 members from 8 countries. Unio Enterprise operates with 14 companies including SES. Large conglomerates such as Airbus and Thales have grown through effective cooperation.

It is important to adopt the most appropriate collaborative model to be effective in the space sector. However, success will depend on having a clear common purpose, with well-structured and managed governance working with a true spirit of trust and employing effective communications.

Keywords— collaboration; consortium; competition; coopetition.

I. HISTORY OF SPACE COOPERATION

Although the "Old Space" era was initially conceived from an ideological conflict during the Cold War, many of the accomplishments were made possible through the cooperation of many entities.

The collective efforts of more than 20,000 different enterprises at the peak of the Apollo programme [1] contributed to the successful landing of humans on the Moon in the late 60's early 70's. A few years later, ten nations pooled their resources to create the largest multinational space cooperation entity - the European Space Agency. Former Cold War adversaries joined a 15-nation consortium to create the largest spacecraft to orbit the Earth - the International Space Station, the scope, scale, and cost of which was unlikely to have been feasible for any single nation alone.

Global and regional satellite services were pioneered through cooperative frameworks of Intergovernmental Organisations (IGO) before they became privatised. The International Telecommunications Satellite Organization (Intelsat) began services in 1964 with ownership and control from over 100 national entities, delivering global voice, data, and television services to nearly 150 countries. In 1977, 17 countries established the European Telecommunications Satellite Organization (Eutelsat) and a few years later in 1979, the International Maritime (Mobile) Satellite Organization (Inmarsat) delivered maritime and mobile communications services globally through the cooperation of its 86 member countries.

Each of these IGOs was governed and funded by traditional telecommunications operators who were competitors in the open market while being collaborators in the IGO board rooms.

Are there any lessons we can learn from these successful collaborative space endeavours or other industries? What were the key success factors that made these ambitious programmes possible and in the context of the "New Space" era, what are the opportunities for small to medium enterprises who wish to grow in a globally competitive market?

II. COOPERATION ADVANTAGES

The end of the 20th and beginning of the 21st century conveniently delineates the Old and New Space eras. Estimated by McKinsey [2] to grow to $1 trillion in value by 2030, space was once considered an exotic domain reserved for only a few large economies. Now it is an industry pursued by over 90 nations [3] as an attractive contributor to many of their economies. Developing nations, particularly in Asia and Africa, are investing in and cooperating together with their space initiatives. In 2023 the African Space Agency was established with some 20 countries having active national space programmes. The Indian Space Research Organisation (ISRO) has a long and distinguished history, having signed 230 agreements with 60 countries and five IGOs [4]. Collaboration in the form of foreign technology inputs played an important role in accelerating ISRO's growth and success [5].

As space is becoming more crowded with a proliferation of space missions (and debris), the space marketplace is similarly becoming more crowded. This growth creates opportunities as well as threats (and risks).

There are clear economies of scale advantages for any enterprise. Large organisations have greater procurement order volumes and buying power to negotiate better pricing and supply chain assurance which can help to lower production costs and reduce critical component shortages. Access to scarce or high-demand components such as semiconductors can be substantially improved through collaborative buying to help make the group's purchase order value more attractive to suppliers leading to better pricing and priority delivery.

One study of 71 manufacturers who undertook collaborative purchasing, achieved material cost reductions between 2.6% to 50%, demonstrating how cooperation can benefit businesses [6].

Being able to tap into a substantial workforce also gives an advantage to larger entities that can exploit the diversity of knowledge and skills as well as the capacity to support vital orders. Finally, larger entities have access to more capital which increases the confidence of their prospective customers, especially when bidding for competitive tenders.

Despite some space organisations establishing policies to encourage participation from startups and small to medium enterprises (SMEs), large entities are often reluctant to accept the risk of purchasing goods and services from smaller companies. When large scale integrators are faced with purchasing mission-critical or long-lead time items from either a small or large entity, the competitive advantage of the latter can influence procurement decisions.

This risk aversion by large companies who are less willing to work with startups is especially acute in Europe where there is more of a business cultural bias against SMEs compared to the USA [7].

In a highly competitive environment, one of the many challenges and barriers to cooperation is the desire to grow national market share. The fundamental question that companies of all sizes should address is: would growing the total size of the pie rather than just their segment of the pie generate greater financial and strategic benefits?

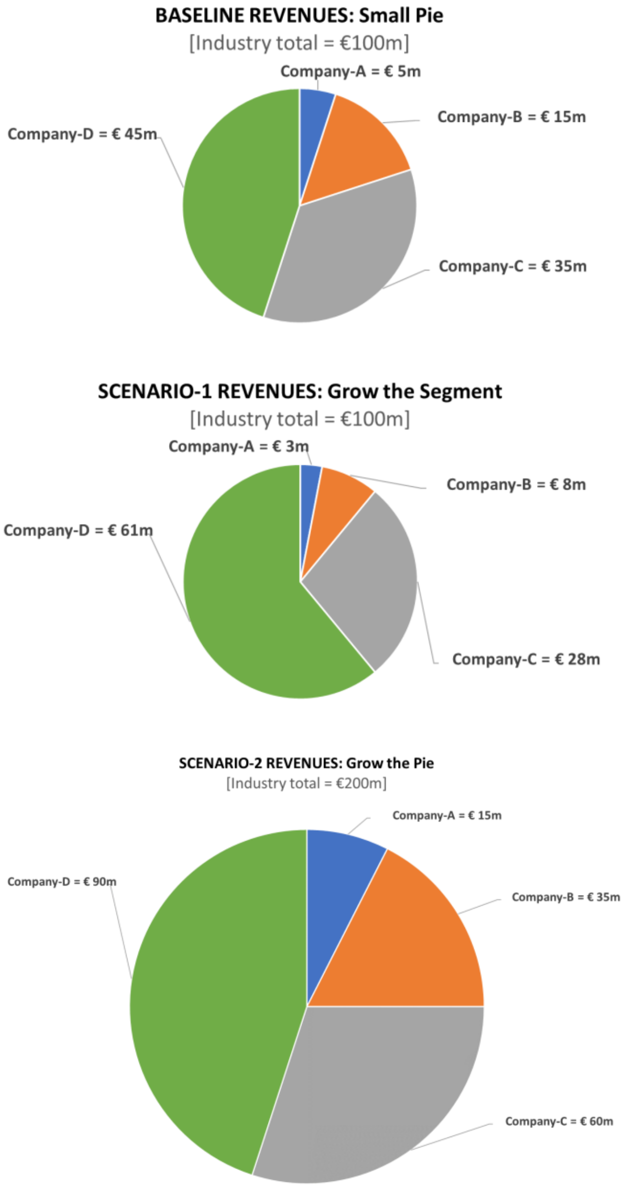

Fig. 1. Advantages of Growing the Pie

One way to address this question is to consider the simplified scenarios shown in Fig. 1. These illustrate a hypothetical small country's space industry that has four players dominated by two major companies. The baseline scenario has these four companies competing against each other, contributing a collective total of €100m in revenues to their national space economy.

In Scenario-1, the dominant player aggressively grows their €45m national segment of the pie by 16% to €61m at the expense of the three other companies, but the total national industry pie remains static at €100m. However, in Scenario-2, by establishing a mutually beneficial model of cooperation, this ambitious space-faring nation grows its international market share by collectively winning more higher value contracts regionally and globally. In this scenario, all the players enjoy increased revenues while the dominant player doubles their revenues to €90m while growing the entire national industry pie to €200m.

This collective growth was achieved from the benefits of cooperation. These benefits include lower material costs through collaborative buying, greater supply chain assurance and cross-fertilisation of innovation and human resources to cope with demand surges as well as standardisation and interoperability.

To demonstrate how this works with a real example from the space industry, consider Inmarsat, established with 28 member countries in 1979, and growing to 86 members prior to its privatization in 1999. The partners were simultaneously investors of capital, suppliers of satellite capacity, customers of bandwidth, as well as competing at the operating level. Inmarsat grew to be the largest global mobile satellite service provider at the time.

I witnessed this kind of cooperative working while serving as a board member on Inmarsat's Governing Council alongside strategic advisor Rosabeth Moss Kanter, professor of business at Harvard Business School [8].

When individual investor interests conflicted with the broader ambitions of the organisation, the advantages of growing the pie rather than the segment was used as a strategic argument to achieve consensus. This collaborative advantage principle was not dissimilar to the hypothetical example illustrated in Fig 1.

The benefit of cooperation is not limited to large firms. According to research on more than 9,000 SMEs in the UK between 2002 and 2014, the economic returns gained from knowledge exchange with external partners achieved higher returns to SMEs than larger firms [9].

III. SUCCESSFUL COOPERATION

The phrase "United we stand, divided we fall" was attributed to the ancient Greek storyteller Aesop more than two and a half thousand years ago but still rings true today.

An examination of cooperation in a wider context provides useful insights that could inform cooperation in the space sector.

In the animal world, many species depend on cooperation to survive. The diminutive Meerkats thrive in the harsh savanna of the Kalahari Desert by living in highly cooperative societies that share food foraging and predator scanning duties to support and protect their large family communities.

Although opinion is divided amongst some anthropologists, the social and technological advancements of humans largely relied upon cooperation and community support.

In the business world, cooperation can exist in many forms and models such as (i) strategic alliances, (ii) joint ventures, (iii) horizontal mergers, (iv) partner ecosystems, and (v) portfolio of collaborators, which can be applied within a national and international context.

To be successful, cooperation requires a shared vision with common goals, access to capital, infrastructure and expertise, as well as transparency, flexibility, trust and effective communications [10].

The acclaimed Harvard Business School guru, Michael Porter, created a model that describes how various factors within a domestic market can contribute to the competitive advantage of a nation to succeed globally.

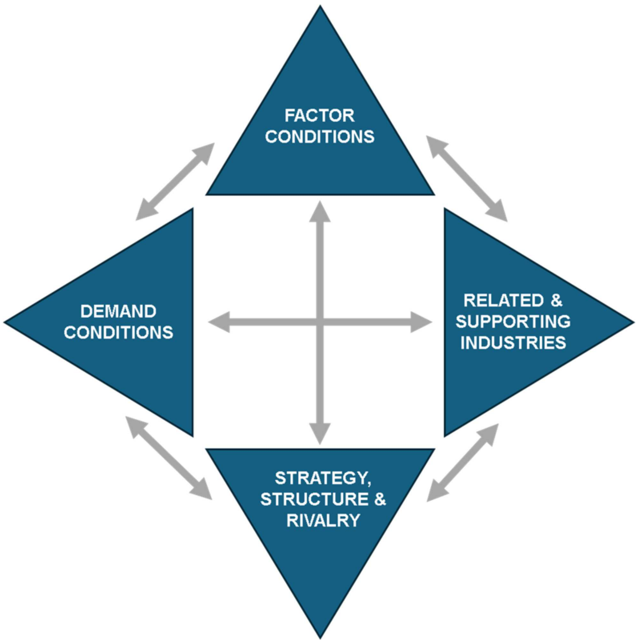

Fig. 2. Porter's Diamond Model

The Porter Diamond Model [11] shown in Fig. 2 illustrates four interrelated industry factors that span (i) Strategy, Structure & Rivalry, (ii) Demand Conditions, (iii) Factor Conditions, and (iv) Related & Supporting Industries. Corporate strategists use this analysis framework to assess investment and operational attractiveness for national markets.

When these factors or conditions are favourable, it encourages domestic companies to continuously improve and innovate, thus increasing their international competitiveness. Usually, competition amongst national firms is required to achieve this, but in some cases to excel in all these dimensions, two or more companies may need to join forces to improve their chances of winning business outside of their domestic markets.

A nation doesn't need to have a large population to successfully compete internationally. One case in point is Finland's Nokia which achieved market dominance in the mobile phone industry for years.

New Zealand, Singapore, Luxembourg, and Israel are examples of small nations with respectable and growing space industries and many smaller former soviet bloc countries are enjoying remarkable growth in the Space Sector.

The greater opportunities for smaller states can be realized by understanding and exploiting their comparative advantages and focusing on best-fit market niches, often by pooling resources.

Business collaboration through Porterian or business clusters can be established by geography, industry sector or through vertical and horizontal resources or supply chains. Business clusters span many diverse industries, with well-known examples such as Hollywood for the entertainment industry, Bangalore, Cambridge and of course Silicon Valley for information technologies. Bremen is known as the “City of Space” where 140 companies and 20 institutes provide jobs for 12,000 people generating billions of euros from the aerospace industry [12].

The Netherlands Aerospace Group (NAG) has a mission to support competitive international growth. They provide support to more than 100 Dutch aerospace members with international business development, networking, knowledge development, innovation, representation, and lobbying [13].

At the regional level, the European Aerospace Cluster (EACP) is a network of more than 45 European aerospace clusters in 18 countries that supports concrete projects in an informal, decentralised manner. EACP is structured as a partnership using Letters of Intent to allow continuous working groups, temporary project consortia as well as bi- or multilateral ad-hoc partnerships [14].

At the international cooperation level, a diverse group of 22 pan-European small and medium sized organisations representing 8 countries led by Unseenlabs and Euroconsult combined their ingenuity, resources, knowledge, and skills to successfully win a €1.4m study for the European Commission to shape future global connectivity by satellite [15]. This New Symphonie consortium demonstrates how the power of unity and cooperation between different sized companies across many nations can win competitive bids.

Another example of European cooperation is Unio Enterprise which operates with 14 companies including SES to develop an integrated space and 5G network providing global always-on connectivity.

The Airbus consortium, formed in 1970, operates under a unique and flexible form of partnership under French law. The partners have a dual role as both shareholders and industrial participants. It is one of the largest and most well-known consortiums that has succeeded in winning global market share in the aviation and aerospace industries.

The Artemis Accord, led by NASA, is a truly global collaborative framework to support lunar exploration. It involves the cooperation of 38 nations with Slovenia and Sweden having joined in April 2024. Some of the benefits to be realised from the Accord include sharing scientific information, interoperability standards for space-based infrastructure, and mitigation and disposal of space debris [16].

To be successful, cooperation requires an appropriate governance structure, the setting of clear individual and shared targets, a proper appraisal of the resources from each organization, and having very clearly defined Specific, Measurable, Achievable, Relevant, and Time-Bound (SMART) goals while maintaining effective communications.

IV. COOPERATING WITH COMPETITORS

Competition, in all its forms, is a natural and healthy part of a growing economy as companies seek to increase market share, profits and customer base. This often requires intellectual property and know-how to be jealously guarded. But as we have seen in the Old Space era, IGOs and companies were able to build and grow successful businesses with international rivals at the delivery level while cooperating at the shared strategic infrastructure level.

The term “Coopetition” which has gained popularity from the book of the same name [17] describes how companies can simultaneously cooperate while being competitors.

The concept is not new and dates back to the early 20th century. Intelsat, Eutelsat, and Inmarsat were classic examples of coopetition in the satellite communications industry. The high-profile coopetition between Pfizer and BioNTech helped to battle the COVID-19 pandemic. Other notable and successful coopetition examples include Apple and Samsung, Apple and Microsoft, UPS and DHL, as well as Delta and American Airlines.

Coopetition in the airline industry is well established and quite common. Many airlines often employ code-share agreements to ensure optimal load factors and efficient utilization of aircraft for various destinations.

There are many examples of successful coopetition in the space industry. The Boeing and Lockheed Martin United Launch Alliance (ULA) joint venture was established to compete with SpaceX. Their coopetition helped to successfully deliver the Curiosity rover to Mars in 2012.

V. CONCLUSION

Large enterprises and SMEs can benefit from cooperation, especially from knowledge exchange, shared resources, innovation, cost reduction and supply chain assurance.

There is no single cooperation model or blueprint that is universally applicable whether it be a consortium, joint venture, or simply a project-focused collaborative agreement.

To achieve real success, business clusters need to be more than just a passive directory or catalogue of eligible entities. A proactive and goal-driven program of active participation, contribution and cooperation among its members is not just desirable, it is essential.

Establishing cooperative and collaborative relationships is not without risk and success is not guaranteed. Corporate and national cultures as well as the scope and scale of the opportunity will determine what model works best. Successful cooperative ventures typically embrace the following four factors:

(i) Shared vision and common goals

(ii) National or location focus with access to capital and industry expertise

(iii) Effective communications, flexibility, transparency, and trust

(iv) Efficient use of shared resources, know-how, personnel, or infrastructure

Of course, the devil is always in the details, and much depends on proper execution.

Ultimately, successful cooperation will depend on the right entities working together at the right time using the right methods with the right resources for the right reasons.

REFERENCES

[1] NASA, (2019): The First Step: Langley’s Contributions to Apollo nasa.gov, 22 March 2019. Online: https://web.archive.org/web/20240423172015/https://www.nasa.gov/history/the-first-step-langleys-contributions-to-apollo

[2] MCKINSEY, (2024): The space economy is blasting off mckinsey.com, 11 January 2024. Online: https://web.archive.org/web/20240423172324/https://www.mckinsey.com/featured-insights/themes/the-space-economy-is-blasting-off

[3] CIA FACTBOOK, (2024): Space program overview cia.gov, 23 April 2024. Online: https://web.archive.org/web/20240423172635/https://www.cia.gov/the-world-factbook/field/space-program-overview

[4] S. KALHORO, (2024): Space 2.0: Developing nations lead the race for the final frontier trtworld.com, 23 April 2023. Online: https://web.archive.org/web/20240423172853/https://www.trtworld.com/opinion/space-20-developing-nations-lead-the-race-for-the-final-frontier-12796733

[5] A. BASKARAN, (2001): Technology accumulation in the ground systems of India's space program: the contribution of foreign and indigenous inputs, 2 April 2001. Online: https://doi.org/10.1016/S0160-791X(01)00009-4

[6] S. KIM, S. NETESSINE, (2012): Collaborative Cost Reduction and Component Procurement Under Information Asymmetry jstor.org, 24 October 2012. Online: https://www.jstor.org/stable/23359613

[7] J. POHLEN, (2019): Dynamics of startups in Europe: What are the critical success factors to put in place to help startups grow into scale-ups, especially in Belgium? handle.net, 2019. Online: http://hdl.handle.net/2078.1/thesis:19008

[8] R. KANTER, (1994): Collaborative Advantage: The Art of Alliances, August 1994. Online: https://hbr.org/1994/07/collaborative-advantage-the-art-of-alliances

[9] D. AUDRETSCH, M. BELITSKI, R. CAIAZZA, P. PHAN, (2023): Collaboration strategies and SME innovation performance, 17 May 2023. Online: https://doi.org/10.1016/j.jbusres.2023.114018

[10] FASTER CAPITAL, (2024): Key Factors For Successful Collaboration, 2024. Online: https://web.archive.org/web/20240919145842/https://fastercapital.com/topics/key-factors-for-successful-collaboration.html

[11] M.E. PORTER, (1990): The Competitive Advantage of Nations. New York: The Free Press.

[12] J RAVELING, (2021): 10 Bremen Companies in the Aviation and Aerospace Sector wfb-bremen.de, 12 August 2021. Online: https://web.archive.org/web/20240503175905/https://www.wfb-bremen.de/en/page/companies-aviation-aerospace

[13] NAG, (2024): Netherlands Aerospace Group (NAG) nag.aero, 2024. Online: https://web.archive.org/web/20240503180139/https://nag.aero/nag/about-nag

[14] EACP, (2024): EUROPEAN AEROSPACE CLUSTER PARTNERSHIP eacp-aero.eu, 2024. Online: https://web.archive.org/web/20240503183622/https://www.eacp-aero.eu/about-eacp/mission.html

[15] EUROCONSULT, (2021): New symphonie takes collaborative approach to european commission call for connectivity euroconsult-ec.com/, 9 December 2021. Online: https://web.archive.org/web/20240503180816/https://www.euroconsult-ec.com/press-release/new-symphonie-takes-collaborative-approach-to-european-commission-call-for-connectivity

[16] NASA, (2020): THE ARTEMIS ACCORDS, 13 October 2020. Online: https://web.archive.org/save/https://www.nasa.gov/wp-content/uploads/2022/11/Artemis-Accords-signed-13Oct2020.pdf?emrc=653a00

[17] A. BRANDENBURGER, B. NALEBUFF, (2011): Co-Opetition. New York: Doubleday.

Reproduction of the Lunar Radar experiment failure and success during implementation

Péter Pataki
Department of Telecommunications
Széchenyi István University
Győr, Hungary
patakip@tilb.sze.hu

Péter Németh
Department of Telecommunications
Széchenyi István University
Győr, Hungary
nemeth.peter@tilb.sze.hu

Abstract— **The first Lunar radar experiment was carried out in Budapest by Zoltán Bay, a Hungarian physicist, engineer and inventor, who and his team carried out a unique experiment at the time: he successfully detected a radar echo signal from the Moon. The experiment proved that radio waves can leave the Earth's atmosphere and reaches to the Moon, then bounce back to be detected from Earth. With this radar experiment, they even have been able to measure the Earth-Moon distance using radio waves. The resulting distance measurements made our knowledge of distances in the solar system much more accurate. This meant that Zoltán Bay not only launched radar astronomy, but also gave birth to a new discipline. Students at the Széchenyi István University of Győr set themselves the goal of repeating the radar measurement to commemorate the experiment. Given the possibilities of the present day, the instruments and settings had to be modified. After many challenges and trials to overcome, the Győr Lunar radar experiment was a success, a fitting tribute to our forefathers. Radar signal echo from the Moon has become accessible and commonplace in Győr thanks to the revival of old technology. Future plans include overcoming the noisy environment and conducting the experiment in other frequency bands.**

Keywords — Lunar radar, radiofrequency, communication, Zoltán Bay, Győr

I. INTRODUCTION

Zoltán Bay's achievement is the first successful Hungarian lunar radar experiment, and there have been several anniversaries in recent years: the 120th anniversary of his birth in 2020, the 75th anniversary of the successfull experiment which was celebrated in 2021, and the 30th anniversary of his death in 2022. On the occasion of these three anniversaries, the work of the renowned Hungarian scientist was commemorated at several event, and the experiment was repeated at the Department of Telecommunications of Széchenyi István University in Győr.

Thanks to the experiments and inventions of Zoltán Bay, in addition to radio astronomy, several important innovations were patented, which helped the development of electronics. Thanks to experiments carried out in the former United Glow laboratories, he was able to make a mark not only in the field of radio-frequency communication and measurement, but also in the development of fluorescent tubes, electron tubes and radio receivers.

The following lines are intended to commemorate the work of this eminent Hungarian scientist and to present the most important details of the first Hungarian lunar radar experiment. After the historical overview, we will show how the students of the Széchenyi István University in Győr succeeded in repeating the experiment.

II. THE FIRST SUCCESSFUL MOON ECHO EXPERIMENT

During the Second World War, bombing and air threats forced the Ministry of Defense to develop a suitable air defense system in Hungary, and in the last years of the war, research into microwave technology in Hungary was significantly increased. Many studies were carried out on the behavior and propagation of waves in different media until a hypothesis was born that these signals could leave the Earth's atmosphere. There was no way or possibility to prove this before, but previous experiments suggested that the phenomenon is not far from impossible. [1]

In March 1944, Zoltán Bay and his two colleagues, György Papp and Károly Simonyi, set up a working hypothesis to determine the conditions they would have to encounter in their tests to make the reflection of the signals as effective as possible. They knew in advance that the attenuations over the Moon's average distance of almost 380 000 kilometers from the Earth and the Moon's reflective properties would present a difficult test. Their knowledge suggested that radio frequency signals at wavelengths close to one meter penetrate the ionosphere with little loss and that the Moon's reflectivity might be somewhere around 10%. [1][2]

Under these circumstances, there was no technical solution available in Hungary at the time that could carry out a radio frequency experiment on such a scale. It seemed impossible to detect very small signals capable of the noise level, which prompted researchers to create new solutions. [2]

The idea was that the detection of such weak signals, almost one-tenth of the noise level, should not be detected separately, but should be summed up towards the noise level. To achieve this, Zoltán Bay came up with the idea of signal summation integration, for which he designed a new tool, the coulometer. The idea is that ten volt-ampere capillaries with a common anode are connected to a common glass vessel into which hydrogen is filled. With the multiplied repetition of the primary radar signal the reflected signal increases linearly with the number of repetition while the background noise increases with the square-root of this number, the useful signal was well above the noise limit. A rotary switch was used to connect the cathodes of the ten capillaries to the output of the receiver every three seconds. The timing of the emission of the signals was calculated to be consistent with the operation of this rotary switch, so that the incoming signal could always be applied to the cathode of the same capillary. During the fifty-minute measurement, the summed signal was already a good representation of the receiver levels, almost thirty times stronger than the original signal-to-noise ratio. [1][2]

By December 1945, with a small selection of electronic components available after the war, everything was ready for further experiments. In several cases, changes were detected in the coulometer tubes, but in mostly these were only reflections. After several weeks of trial and error, the first significant results were obtained on 6 February 1946. On that occasion the reflected radio signal rose by 4% above the calculated error limit, the experiment was considered a success. The results were presented at a press conference the following day.

The success of the tests was unquestionable, but they failed to win the world competition: on 10 January 1946, John H. DeWitt Jr. conducted a successful moon echo experiment in the United States of America as part of Project Diana, and he and his team were the first to demonstrate it. Nevertheless, the work of the Bay group is also recognized by science for its Hungarian developments and unique implementation. [3][6]

III. SETTING UP THE ORIGINAL EXPERIMENT

Creating the conditions for the lunar radar experiment was a real challenge for the Bay team. Hungarian research efforts were hampered by the lack of energy and equipment during and after the war. In addition to rebuilding the equipment in the research laboratories looted by the Soviets, the electrical power supply was not sufficient for an experiment of the power Zoltán Bay had envisioned. In the light of this, the equipment used for the tests also had to be selected and assembled as far as possible to produce the best results for the given possibilities. Zoltán Bay's manuscripts are still available today, and browsing through them gives a very interesting picture of the project. The precise, diary-like notes contain the most important calculations and sketches. [1][5]

The main units of the complete system consisted of the transmitter, the antenna system, the receiver-side amplifier and the coulometer. There was no suitable source or means for a klystron or magnetron-based oscillator, so the first transmission tests were carried out with signals of around half a meter wavelength and triode transmitting tubes instead of centimeter waves. The first successful detection of a lunar echo involved two 0QQ 500/3000 transmitting tubes, switched at three-second intervals. It was reported that this amplifier often got hot, so they had to find a solution that would transmit a sufficiently fast decay signal to the antenna even in pulsed mode.[1][4][5]

The proper adjustment of the pulses emitted by the transmitter at the antenna had to take into account that the receiver noise is proportional to the square root of the receiver bandwidth. Knowing this, it was necessary to find the optimum bandwidth value where the pulses would be as prominent as possible in the receiver noise. The most ideal approximation to this condition is to have a receiver bandwidth equal to $1/\tau$ of the pulse bandwidth. In this case, the pulse duration is not distorted and more accurate timing is possible. Thus, since τ is thus a short pulse in time, a higher peak power can be expected for the transmitter tubes. [5]

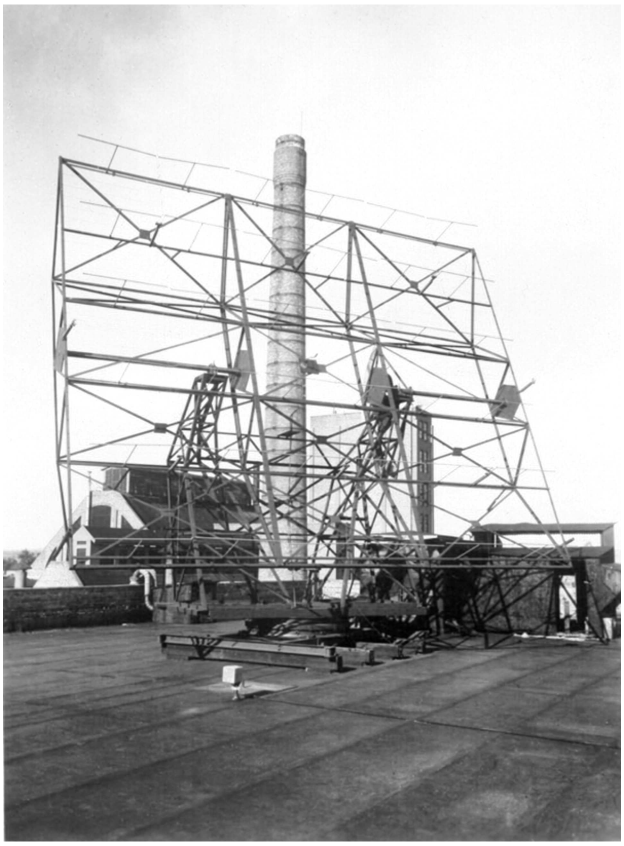

Fig. 1. The original antenna system for the tests [2]

The antenna – which served both transmitting and receiving purposes – is a system of 36 dipole elements, as shown in the Fig. 1. These were used to form three series of whole-wave dipole antennas. This system had a gain of approximately 19 dB compared with a single dipole and a directional azimuth of about 19°, which could be rotated in azimuth and elevation. The antenna could not be connected directly to the signal path due to its movement, and a 200 Ohm symmetrical wire of appropriate length and impedance was used. At the end of the signal path was a mechanical rotary switch to select between transmit and receive modes.[1][5]

To detect and summarize the signals they received, they created a novel instrument, the hydrogen coulometer (Fig. 2.), which later became an important tool in radio astronomy. For the experiment, a unique voltmeter was constructed, consisting of 10 individual tubes, all of which are connected to a common anode. The tubes were connected to the receiver amplifier in synchronism with the transmitter pulses using the rotary switch. According to the signal received, the hydrogen gas, which is superior to the current, always shifted the liquid-mesh in the thin capillaries in proportion to the current integral. This method with the rotary switch allowed the signal to always fall on the same tube according to the pulses and to be summed over the long test period. With the multiplied repetition of the primary radar signal the reflected signal increases linearly with the number of repetition while the background noise increases with the square-root of this number. [1][5]

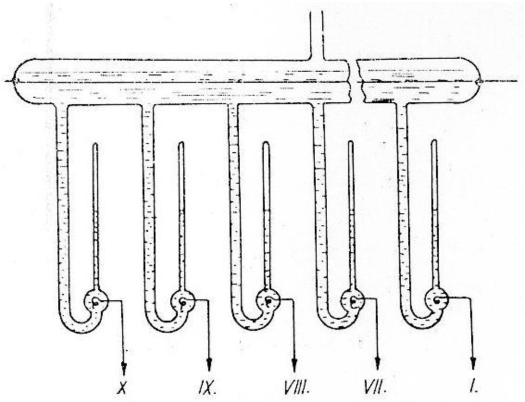

Fig. 2. Sketch of the coulometer [1]

IV. EXPERIMENT AND COMMEMORATION IN GYŐR

In the year 2022, the Department of Telecommunications at Széchenyi István University in Győr organized two events to commemorate Zoltán Bay and his experiment.

On the occasion of the World Telecommunications Day on 19 May, participants commemorated Zoltán Bay. Four students from the University worshipped the memorial statue of Zoltán Bay in Újpest.

In the run-up to World Telecommunications Day, members of the Honfy József Amateur Radio Department at the University, as well as some of their students, also wanted to experience the thrill of being connected to the Moon. The motivation to organize such a special form of communication would have been enough, but they thought they would repeat the experiment in a modern way to mark the 30th anniversary of Zoltán Bay's death.

Once we started researching how we could make the original experiment as credible as possible, we ran into several obstacles. First of all, the 120 MHz frequency - originally used 75 years ago - is now in a completely different use, and disturbing it for scientific purposes could have serious consequences. Then came the idea of moving to an amateur radio frequency band close to the radio spectrum, since the radio club has a license for this. The frequency band between 144-145 MHz was chosen.

The main obstacle to reproducing the antenna system was its size, which was mainly 6×8 meters. The implementation of a 36-element antenna system would have posed a serious risk to the safety of the building due to the large size and wind load. In the last 75 years, antenna improvements have been made to such an extent that a similar design to the original is no longer justified. As shown in Fig. 3, a Yagi antenna system was chosen because of its profitability and lightweight construction. The antennas are connected to a power divider with a 1 kW amplifier, which is responsible for distributing the power from the output stage evenly between the four antenna elements. Several measurements preceded its assembly, since power sharing requires that the signal paths to all four antennas have the same electrical length, avoiding phase differences that distort the signal.

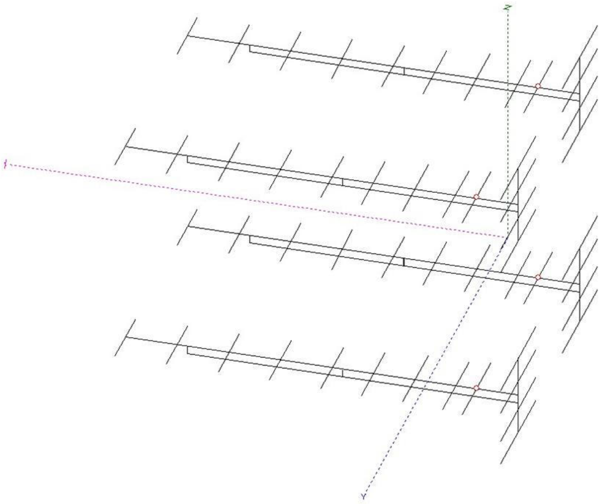

Fig. 3. The schematic of the antenna system for the 144-145 MHz frequency band

During the lengthy tests, it was necessary to see how the urban environment of Győr affected the experiment. As Győr is a major industrial city, there is a lot of radio frequency interference that can suppress the weak signals reflected from the Moon. In Zoltán Bay's day, the United Incandescent Lamp and Electric Co. production lines also interfered with measurements, so they were able to get results at night when the factory went quiet. In the 21st century, with day and night factory production, this is no longer feasible, so it was necessary to find the directions where the noise levels were highest and to communicate in a way that would avoid the direction of the main or side beams of the antenna. This involved a series of compromises. In order to determine the direction of the interference, several measurements were made continuously for a week with the antenna array presented.

V. CALCULATIONS FOR THE LINK BUDGET FOR THE EARTH-MOON-EARTH COMMUNICATION

The experiments of Zoltán Bay and John H. DeWitt Jr. play a major role in calculating the radio frequency field loss of the Earth-Moon-Earth connection today. The calculation of the loss in this path, ignoring the effects of the atmosphere and ionosphere:

$$\mathrm{L_0[dB]} = 10\log\left(\frac{P_T}{P_R}\right) = 10\log\left(\frac{64\cdot\pi^3\cdot R^2}{\lambda^2\cdot\sigma\cdot\chi}\right) = 10\log\left(\frac{64\cdot\pi^2\cdot R^4}{\lambda^2\cdot \mathrm{a_L^2}\cdot\chi}\right)$$

where P_T is the power of the transmitter, P_R is the received power λ is the wavelength in m, $\sigma = \pi\cdot\rho_1\cdot\rho_2$ is the effective reflecting surface of the moon in m^2, $a_L = 1738\cdot 10^3$ is the radius of10 the Moon according to the following relation $a_L = \rho_1 = \rho_2$, χ is the radio frequency reflection coefficient between 0.06-0.07, $R = 354\cdot 10^6$ m is Moon Perigee distance from the Earth. [7] Based on the calculation in our case the path loss in 144 MHz is 250 dB.

The receiving signal power is calculated from the losses between the Earth-Moon-Earth way added to the transmitter Effective Isotropic Radiated Power (EIRP): [7][8]

$$P_R = EIRP - L_0 - L_a - L_P - L_i - L_{DP}$$

where P_R is the received power in logarithmic scale, EIRP is the effective isotropic radiated power from transmitter in logarithmic scale, L_0 is the path loss, L_a is the atmospheric loss, L_p is precipitation loss, L_i is the antenna inaccuracy and L_{DP} is the depolarization attenuation.

The reflected, reduced power signal at the point of reception can be detected with very low power. To check the useful part of the reception signal level, it is necessary to check its value relative to the noise level at the point of reception.

$$\mathrm{SNR} = \mathrm{P_R} - \mathrm{P_N}$$

Where *SNR* is the Signal-to-noise ratio in dB, P_R is the received signal power in dB and P_N is the noise power in dB on the receiving point and same frequency as the communication. The calculated *SNR* is including the attenuations and losses from the full Earth-Moon-Earth path calculated with the received power.

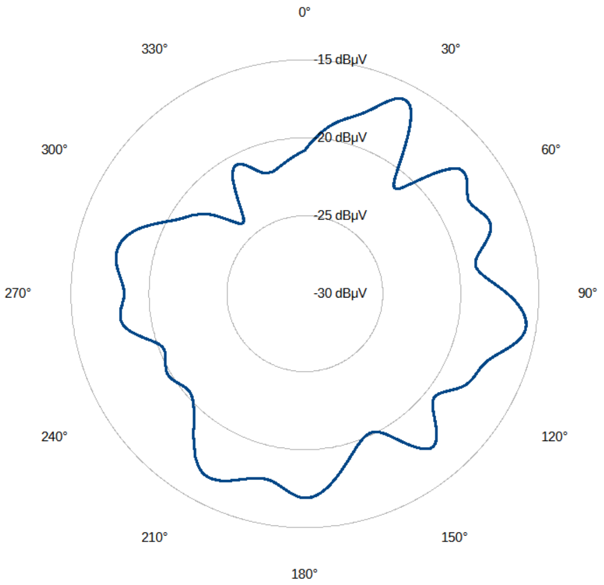

Fig. 4. The noise level around the antenna system in azimuth directions

The noise level is changed in the antenna azimuth and elevation degrees, so the calculation is repeating every antenna positioning. In preparation for the experiments we measured the noise levels in different directions of the antenna system. As shown in Figure 4, the noise level varies from direction to direction, explained by noise from the infrastructure around the antenna.

VI. EXPERIENCES FROM THE EXPERIMENT

The first unsuccessful attempts led us to realize that the biggest challenge of reception is the noisy environment. During the repeated tests, we determined Moon positions in which the antenna picks up the least amount of ambient noise. In these positions, we tried to justify our idea by receiving transmitted signals of other radio stations.

Fig. 5. The antenna system in use on the top of the University

During the first successful reception, although we were not yet prepared to transmit, we responded to the received station with an improvised setup. The connection was excellent with the new antenna system (Fig 5), and even another station receiving our signal established a two-way connection with us.

The experiments did not stop. We are currently working on perfecting the antenna and receiver system as well as possible noise elimination. We would like to perform the experiment on several frequencies, so that we can learn more about the possibility of radio communication with the help of the Earth's faithful companion.

REFERENCES

[1] Z. Bay, “Reflection of microwaves from the Moon”, Hungarica Acta Physica 1, 1-22 (1947) (received 18th Novembre 1946)

[2] P. J. Szabó, “Radarokkal a lopakodók ellen: a magyar katonai légtérellenőrző és radarrendszer története 1917-2014.” Zrínyi Kiadó, 2014, pp.87-93.

[3] C. Makamson, “Project Diana: To The Moon And Back,” https://www.nationalww2museum.org/war/articles/project-diana-moon-and-soviet-union, (Accessed 28. April 2024)

[4] Z. Bay, “Kísérleti Jegyzőkönyv 1944-1946”, unpublished

[5] Z. Bay, “Visszaemlékezés a magyar holdvisszhang kísérletre,” Fizikai szemle, vol. XXIV(4), 1974, pp.41-53.

[6] S. Mészáros, “A Hold válaszolt: Bay Zoltán radarvisszhang-kísérlete,” Természet Világa, vol. 127(2), February 1996, pp.66-68.

[7] V. A. Loshakov, “Experience of using antenna systems in earth-moon-earth communications,” *2013 IX International Conference on Antenna Theory and Techniques*, Odessa, Ukraine, 2013, pp. 541-543, doi: 10.1109/ICATT.2013.6650840.

[8] X. Wang, C. Wang, Q. Zhu and X. Chen, "Design and Application of Moon-Earth Communication Link Budget," 2011 International Conference on Internet Technology and Applications, Wuhan, China, 2011, pp. 1-4, doi: 10.1109/ITAP.2011.600626

The educational and awareness-raising activities of BME Suborbitals

Ádám Nagy, Bence Ujhegyi, Bence Csaba Kováts

BME Suborbitals
Budapest University of Technology and Economics
Budapest, Hungary
kovats.bence@bmesuborbitals.com

Abstract—**BME Suborbitals, an initiative by the Budapest University of Technology and Economics, exemplifies the integration of practical aerospace projects into higher education, bridging the gap between theoretical knowledge and their real-world application. This paper presents an in-depth analysis of flagship projects of BME Suborbitals: Project Prometheus, a high-altitude rocket designed to reach the stratosphere; Project Kratos, a breakthrough in rocket propulsion technology; and Project Athena, an endeavor to enhance satellite communication capabilities. Each project embodies the innovative spirit and technical prowess of the team, providing students with invaluable hands-on experience in aerospace engineering.**

This comprehensive exploration of projects, educational initiatives, and competitive accomplishments of BME Suborbitals reveals a multifaceted approach to enhancing space science education. By merging hands-on project work with competitive engagement and outreach activities, BME Suborbitals not only advances the technical skills of its members but also plays a crucial role in inspiring a new generation of engineers and scientists. The success of these initiatives advocates for a broader adoption of experiential learning models across the educational spectrum, ensuring future professionals are well-equipped to address the challenges and opportunities of the space industry.

Keywords — education; space; rockets; Hungary; BME; competition

I. INTRODUCTION

In the field of aerospace engineering, practical experience is of paramount importance. The BME Suborbitals competition team is designed to meet this need through three flagship projects: Project Prometheus, Project Kratos, and Project Athena. These projects not only focus on solving scientific and technical challenges but also on preparing students to handle the complex problems of the real world. Thus, the initiative serves as a bridge between academic education and engineering practice, facilitating the transition of students from theoretical studies to practical life. [1]

Moreover, the team is the co-organizer of the CanSat competition in Hungary which serves as a cornerstone for promoting space science and engineering among high school students. This competition challenges participants to design, build, and launch a miniature satellites within the constraints of a soda can, fostering a practical understanding of satellite technology and mission design. Through this initiative, BME Suborbitals not only contributes to the academic enrichment of participants but also stimulates a broader interest in aerospace careers even in the younger generations.

The participation and achievements of the team in the European Rocketry Challenge [2] (EuRoC) 2022 further underscores their role as pioneers in amateur rocketry. Their performance at EuRoC, marked by innovative design and engineering excellence, highlights the practical impact of their projects on the global stage, offering a testament to the value of project-based learning in inspiring the next-generation aerospace professionals.

In the following article, the achievements of the BME Suborbitals will be presented in the areas of education and training, as well as raising awareness of the space industry among young people.

II. PROJECT PROMETHEUS

The flagship project of BME Suborbitals, Project Prometheus, is developing a rocket aimed at reaching the stratosphere. This project is particularly important for team members as it provides a direct opportunity to apply aerospace and system engineering principles and rocket science in real-world conditions.

A. Educational Impact

The Prometheus project serves as an excellent practical educational tool. Students learn the fundamentals of design, simulation, and manufacturing while developing real-time problem-solving skills. During the project, students have the chance to participate in optimizing the aerodynamics of rockets, designing, and testing the engines, and developing avionic systems. This hands-on approach (see Fig. 1.) improves creative and critical thinking, as they gain a deeper understanding of the fundamentals of rocket technology.

During Project Prometheus, students develop the research rocket according to the EuRoC standards system, thus learning about the European Space Agency (ESA) ECSS [10] standards. They also acquire valuable systems thinking and systems engineering kills.

Fig. 1.: Gaining practical knowledge is important when working in a team. The picture shows the production of one of the rocket bodies. The team's knowledge of polymer technology is outstanding.

B. Technical Challenges

The technical challenges of Project Prometheus are numerous. Students must address problems related to thermal protection, aerodynamics, engine efficiency, and rocket stability, along with various other challanges. Special attention is given to safe design practices during the project, including the development of emergency shutdown systems and recovery techniques. [12] These challenges test not only engineering knowledge but also develop teamwork and project management skills, which are crucial for the professional development of students.

C. Practical Education and Development

The focus on practical education in Project Prometheus allows students to gain real project experience during their studies. The project provides not just theoretical knowledge but also involves students in every stage of design, construction, and testing, thus ensuring a deeper understanding of engineering decision-making processes. Consequently, the Prometheus project contributes to the development of engineering competencies, preparing them for future challenges in the field of space technology.

D. Technical Challenges and Innovations

Project Prometheus, focused on the development of a high-altitude rocket, presented several significant technical challenges. One critical issue was thermal management during the rocket's ascent through the stratosphere. The design of a robust thermal protection system (TPS) was necessary to mitigate the effects of frictional heating. The team addressed this through the application of ablative materials and FEM simulations aligned with ESA's ECSS standards. The rocket's aerodynamic design also required careful optimization, balancing minimal drag with flight stability at high velocities. This was achieved using custom polymer composites for the rocket's fuselage, supported by computational fluid dynamics (CFD) simulations to fine-tune the aerodynamic profile.

Another technical focus was on the avionics system, which had to maintain functionality under extreme conditions, such as low temperatures and high altitudes. The team developed a triple-redundancy system to enhance the reliability of telemetry and recovery systems, ensuring operational integrity throughout the mission.

III. PROJECT KRATOS

Within the framework of the BME Suborbitals competition team, the aim of Project Kratos is to open new dimensions in the world of rocket propulsion. This project focuses on the development and testing of innovative propulsion technologies that could significantly increase the efficiency and reliability of future spacecraft. Project Kratos participants will also gain insight into the design and implementation of safety-critical systems. (see Fig. 2.)

A. Educational Impact

Kratos is not just a technological project; it is also an educational platform where students can familiarize themselves with the latest solid rocket propulsion technologies. Throughout the project, students participate in the design, experimental development, and testing processes, providing them the opportunity to deepen their knowledge in this highly specialized area. The practical experience offered by the Kratos project facilitates the development of engineering thinking, problem-solving abilities, and innovative skills. In addition, as a research project, participants will be familiarized with basic scientific methods: from the process of hypothesis setting to testing, including drawing conclusions, and eventually publishing the results.

B. Technical Challenges

The technical challenges faced by Project Kratos are diverse, including the development of high-efficiency propulsion systems [3], selecting the optimal mix of propellants, and testing engines under extreme conditions [6]. Within the project, students must develop innovative solutions for thermal management, vibration damping, while ensuring the long-term stability of the propulsion systems. These challenges require not only technical competencies but also emphasize creativity and teamwork.

C. Practical Education and Innovation

The Kratos project is another outstanding example of practical education, where students directly participate in research and developments shaping the future of rocket technology. The project allows students to develop and test new propulsion systems hands-on, thereby contributing to innovation in the field of space technology. Thus, the Kratos project not only pushes the boundaries of propulsion technology but also supports the professional and personal development of students. [9]

D. Technical Challenges and Innovations

Project Kratos, which explored advancements in rocket propulsion, encountered significant challenges regarding solid rocket fuel performance. The goal was to develop an optimal propellant mixture that could offer high energy output while maintaining stability. The team focused on experimenting with composite propellants, which allowed for a precise balance between thrust and safety.

Thermal control in the rocket nozzle was another significant consideration, as the extreme temperatures during combustion risked erosion. To counter this, the team introduced high-temperature resistant materials, such as ceramics and carbon composites, using advanced finite element analysis (FEA) to test and validate the nozzle design.

Kratos also required sophisticated solutions for vibration management due to the high levels of thrust-induced vibration, which posed a risk to the structural integrity of the rocket. To mitigate this, the team implemented damping systems and strategically integrated vibration isolators in critical structural areas. Extensive structural analysis was carried out to optimize material distribution and reduce potential weaknesses.

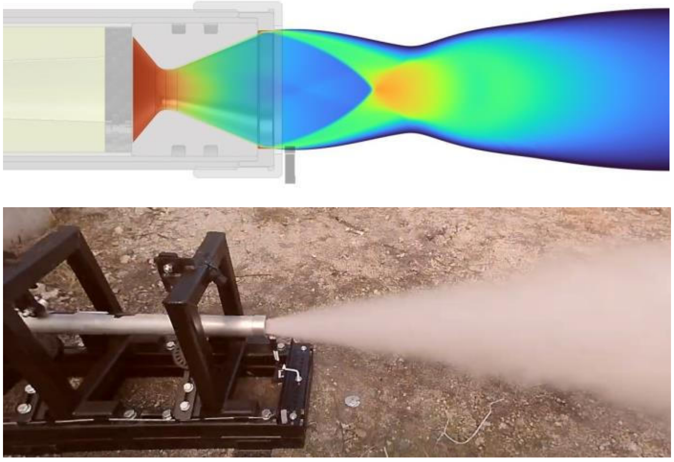

Fig. 2.: Thermal simulations of the Kratos engine (above) and during tests. In safety-critical systems, the hypothesis is validated in several ways. [3,6]

IV. PROJECT ATHENA

BME Suborbitals supplies the launch vehicles for the CanSat Hungary competition, as a co-organizer, [4] for the middle-schoolers in the framework of Project Athena. These rockets are capable of carrying the experiments of the participating teams to 1.5 km above ground level.

A. Educational Impact

The Athena project and CanSat competition offer an exceptional educational opportunity for students to participate in the development and application of satellite technology. Throughout the project, students can gain an in-depth understanding of satellite communication systems design, including signal transmission techniques, antenna design, and communication protocols. This practical experience not only deepens the knowledge of students but also enables them to directly contribute to the development of future communication technologies.

Participants will also gain an insight into the world of space development, as well as the challenges of system integration, as a launch requires three different teams to put together a system (see Fig. 3.). To be successful, each team must adhere to the ECSS-based standards required by CanSat.

B. Technical Challenges

The technical challenges of Project Athena include developing high-speed data transmission systems, improving the signal-to-noise ratio, and enhancing energy efficiency and reliability. Students must tackle specific problems of satellite communication, such as signal attenuation in atmosphere, and find innovative solutions to these challenges. Thus, the project encourages critical thinking, creativity, and engineering innovation among students.

Fig. 3.: The experiments of student teams are integrated into Athena rockets. Photo made by SPOT.

C. Practical Education and Development

The Athena project is a central element of BME Suborbitals, which gives secondary school students the opportunity to learn about space industry processes. It also offers the competitors the opportunity to apply and extend their knowledge in the field of telecommunications in a practical environment. The experience gained during the project not only aids in the professional development of the participating students but also contributes to making their skills directly applicable in the rapidly evolving industry of space technology and satellite communication.

V. ACHIEVEMENTS

BME Suborbitals has achieved several educational and training achievements in its history. [5]

During the lates application period, the team experienced a signifantly increased interest in membership. BME Suborbitals currently has over 80 members (see Fig. 4.), making it one of the largest organizations of young people with an interest in the aerospace industry in Hungary today. Compared to other European teams in terms of numbers and results, BME Suborbitals is of a similar size and has a similar influence in its field [2, 5, 7, 8, 11]. Although, as a young team, their results and publications are still below those of the old, big European teams. Last year the team received more than 100 applications, including even teachers and professors. The team has managed to reach people from primary school to industry players, raising awareness of opportunities and careers in the space industry in multiple demographic groups simultaneously.

Beside the outreach, internal training programs for members have also been launched. These lectures and sessions cover different areas of engineering. They give students from other disciplines an insight into the subject area and allow more experienced members to deepen their knowledge and share their experiences. These topics include, but are not limited to, aeronautics, fluid dynamics and finite element simulations, manufacturing processes, electronic design, and soldering technology.

Inter-organizational and international cooperation has been established recently as well. BME Suborbitals work together and share their knowledge with other BME competition teams and university organizations (Wigner College, Cosmos College). It also maintains good relations with other European rocket development teams (Aerospace Team Graz, Endevour), with whom the team fosters a great professional relationship and practices technological transfer as well [7,8].

Industry attention and recognition is also prevalent in connection to the team. The first generation of the memebers have recently left to take up careers in industry. The feedback is that they are developed into highly skilled engineers, greatly aided by their membership of the BME Suborbitals, where they have been able to put into practice the engineering knowledge they learned at university and have gained systems thinking and management skills firsthand.

Scientific results were published regularly. Several of the members have embarked on academic careers by publishing their developments or research in the team. This has created a demand for work using scientific methods. The team has already delivered more than 10 conference papers (like references [3] and [6], theses and publications.

Fig. 4.: The BME Suborbitals team

VI. CONCLUSION

The BME Suborbitals initiative within the Budapest University of Technology and Economics is an excellent example of how education and practical engineering work can be combined. Through Project Prometheus, Kratos, and Project Athena, BME Suborbitals not only deepens knowledge and practical skills of students but also provides them with the opportunity to face real engineering challenges and develop solutions for them.

These projects and activities contribute to the personal and professional development of students, preparing them to face the engineering challenges of the future. The practical experience gained by students within the ranks of the BME Suborbitals framework is indispensable for becoming successful engineers who can take on leadership roles in the field of space technology.

The success of BME Suborbitals highlights how project-based learning and active participation in competitions can effectively complement academic education. This not only to expand knowledge in the field of space technology but also to enhance critical thinking, problem-solving ability, and teamwork. Such a type of education encourages students to be more adaptable and innovative, ready to contribute to solving global challenges.

Overall, BME Suborbitals can serve as a model for other educational institutions, demonstrating how practical project work and participation in competitions can be valuable in engineering education. This type of integrated educational approach promotes scientific and technological innovation while inspiring the next generation to explore the endless possibilities of the engineering profession.

ACKNOWLEDGMENT

On behalf of the entire BME Suborbitals, we would like to thank all the supporting academic teachers who gave of their free time to the team, helping us with their professional knowledge and expertise.

REFERENCES

[1] Website of BME Suborbitals, https://suborbitals.bme.hu/, Retrieved: 2024.05.01.

[2] Portugal Space: European Rocletry Challange EuRoC'22 Classification, Reference: Portugal Space Reference PTS_EDU_EuRoC_RC_000914, Ver. 01. https://euroc.pt/, Retrieved: 2024.05.01.

[3] A. Hegedűs, G. Tölgyesi: Solid fueled rocket motor development with advanced simulating and measurement tools, Faculty of Mechanical Engineering TDK - 2023

[4] Hungarian Astronautical Society: Website of CanSat Hungary, https://www.cansatverseny.hu/, Retrieved: 2024.05.01.

[5] https://raketa.hu/magyar-raketaepito-csapat-europa-elvonalaban, Retrieved: 2024.05.01.

[6] B. Cs. Kováts, B.Szabó: Self-developed rocket engine production technology, Faculty of Mechanical Engineering TDK – 2023

[7] Website of Team "Aerospace Team Graz" (ASTG) – TU Graz, https://astg.at/ Retrieved: 2024.09.30.

[8] Website of Team "Endevour" – University of Edinburgh, https://www.endeavourockets.com/, Retrieved: 2024.09.30.

[9] George P. Shutton – Oscar Biblarz: Rocket Propulsion Elements. 2017, John Wiley & Sons Inc.

[10] ESA: ECSS Handbooks (Identification codes: ECSS-E-HB-XX-XX), Aviable under the link: https://ecss.nl/hbs/active-handbooks/, Retrieved: 2024.09.30.

[11] Website of Team "Aris" – ETH Zürich, https://aris-space.ch/, Retrieved: 2024.09.30.

[12] B. Ujhegyi, K. Molnár, Atmospheric rocket launch safety requirements and the challenges of meeting them, University of Óbuda, Faculty of Safety Engineering, TDK - 2023

Engineering and Management of Space Systems

- an International Joint Master's Double-Degree Programme

Jasminka Matevska
Faculty of Electrical Engineering and Computer Science
Bremen City University of Applied Sciences, Germany
jasminka.matevska@hs-bremen.de

Marek Chodnicki[1]
Faculty of Mechanical Engineering and Ship Technology
Zbigniew Łubniewski[2]
Faculty of Electronics, Telecommunications and Informatics
Gdańsk University of Technology, Poland

marchodn@pg.edu.pl[1]
zbigniew.lubniewski@pg.edu.pl[2]

Abstract— **Dynamic development of the European space sector results in a necessity for suitable Higher Education Institution graduates. Current study programs of Aerospace Technology are focused on the field of mechanical engineering. Although engineering methods for design, construction and assembly of mechanical systems are covered, interdisciplinarity and life cycle aspects are not considered in a sufficient degree. Due to the increasing digitalization, interconnection and distribution of technical systems, there is a high necessity to consider the systems with their interdisciplinarity during the entire life cycle from the initial idea through conception, design, production, integration, verification and validation to operation, maintenance and disposal in such a way that it best meets the expectations of the stakeholders and successfully accomplishes the planned mission. Current systems require different competencies depending on the characteristics of the application domain. The increasingly dynamic market requires an adaptation of traditional approaches and the introduction of agile methods in order to meet the requirements for greater flexibility and creativity. This, supplemented by management and social competencies, forms a future-oriented basis for mastering the ever-growing complexity of technical software-intensive systems. Our international interdisciplinary joint Master's double-degree program - Engineering and Management of Space Systems (EMSS) established as a cooperation of Bremen City University of Applied Sciences, Germany and Gdańsk University of Technology, Poland addresses all the above-mentioned systems engineering aspects and imparts competencies necessary to comprehend complex space missions as a "system of systems" during their entire life cycle. It is conducted in cooperation with the local space industry, in particular OHB, Airbus Defence and Space, and Ariane Group.**

Keywords*— Systems Engineering, Interdisciplinarity, Industry Cooperation, Master's Study*

I. INTRODUCTION AND MOTIVATION

In the course of the increasing digitalization, interconnection and distribution of technical systems and their growing complexity, a systems engineering approach has emerged. It takes a networked and interdisciplinary view of the scientific expertise of individual engineering disciplines. Systems engineering brings together all the disciplines involved in a structured process. This can include various technical, business, legal, logistical and also social or communicative aspects and should take into account the entire life cycle of the systems. The aim is to develop and adapt the respective system from the initial idea through conception, design, production, integration, verification and validation to operation, maintenance and disposal in such a way that it best meets the requirements of the respective stakeholders.

Business requirements are incorporated throughout the entire product life cycle in order to achieve an optimal balance of functions and interactions within the project budget, schedule, technical and other expectations and constraints. The increasing dynamics on the market require an adaptation of traditional procedures and the introduction of agile methods in order to meet the requirements for more flexibility and creativity.

In many branches of industry that usually recruit from the classical engineering sciences such as mechanical engineering, computer science and electrical engineering, there is an increasing need for specialists and managers who are trained to meet the requirements of systems engineering. This applies in particular to the aerospace industry, which is an interdisciplinary engineering science that combines various technical disciplines such as electronics, computer science, robotics, mechanical engineering and materials technology, and which is of particular importance in the state of Bremen as an economic cluster "aerospace" with more than 140 companies and 20 scientific institutions in this field.

Existing well-designed aerospace degree programs focus primarily on the mechanical engineering aspects and disciplines and are quite successful in teaching the necessary skills to successfully develop a space system, particularly from a mechanical and physical perspective. However, a space system increasingly consists of monitoring and commanding electronic and software components that enable intelligent and autonomous functionality. A space mission also includes all ground systems that make the conception, design, simulation, verification, validation and operation of the flight systems and thus the mission with all its phases possible at all. Many of the ground systems are de facto complex software systems with very high requirements in terms of end-to-end consistency and transferability of huge amount of partly real-time data.

The "Engineering and Management of Space Systems (EMSS) M.Sc." program offers an interdisciplinary course of study for this promising industry including the monodisciplinary engineering sciences in the fields of computer science, electrical engineering and mechanical engineering and combines these with overarching interdisciplinary system skills. Based on the fundamental idea of systems engineering, students acquire technical know-how at the cutting edge of research and application skills for practical space-related projects on specific systems (e.g. satellite systems). In addition to technical skills, management and social skills are taught.

II. STUDY PROGRAM STRUCTURE

The “Engineering and Management of Space Systems” study program is set up as an interdisciplinary course designed as a strategic cooperation between Bremen University of Applied Sciences (HSB), Germany and the Technical University of Gdańsk (Gdańsk Tech), Poland [1]. On HSB side the study programme is assigned to the Faculty of Electrical Engineering and Computer Science and conducted in cooperation with the Mechanical Engineering Department of the Faculty of Nature and Technology. On Gdańsk Tech side this study program is assigned to the Faculty of Electronics, Telecommunications and Informatics and conducted in cooperation with the Faculty of Mechanical Engineering and Ship Technology. The teaching language is English.

The international orientation of the course in cooperation with the two partner cities Bremen and Gdańsk strengthens the intercultural and linguistic skills of the students. These skills are an important prerequisite for successful positioning on the job market in times of globalization, converging markets and internationally active companies with transnational development teams.

The course is structured as a "joint double degree" program, in which one semester is completed in Gdansk and one in Bremen. The credits earned are credited to the curricula of the respective courses at both universities. The third semester comprises the Master's thesis and the Master's seminar and can be completed either in Bremen or Gdansk. The overall study program comprises at least 90 ECTS (European Credit Transfer System).

During the preparation phase, three pilot runs were run. The program was successfully accredited in December 2023 and has started the first official run in the current summer semester 2024.

The degree (as a double degree with one degree from each of the two participating universities) enables students to take up a qualified career as well as a doctorate. In addition to subject-related technical competences and management skills, the course concept also integrates the acquisition of skills in the areas of communication, cooperation and academic self-image. Thus, this degree program also lays the foundation for the ability to learn throughout life and strengthens graduates for the perception of social roles and effectiveness as professionals as well as responsible citizens.

III. ADMISSION CRITERIA

The EMSS study programme includes 90 ECTS. Therefore, applicants establishing a proof of a Bachelor's, German "Diplom" or an equivalent first academic degree including 210 ECTS in a discipline according to the course specializations (Computer Science, Electronics Engineering or Space Technology) or related STEM (Science, Technology, Engineering, and Mathematics) academic degrees can be accepted. As an exception, candidates holding a bachelor’s degree of 180 ECTS can also attend the programme upon completing the missing 30 ECTS in parallel.

A final grade corresponding to German mark good or very good (min. of 2.5), for international students a Grade Point Average of at least 3.00 / 4.00 or 7.50 / 10.00 or first class with distinction or with percentage larger 70%) is necessary in order to be accepted.

Since the programme is completely held in English, good knowledge of English, minimum of B2 Level according to Common European Framework of Reference Level Descriptions, equivalent certificate (e.g. TOEFL, IELTS), a university certificate, if English was the main language of instruction during studies or an interview with the admission board is necessary.

If a visa is required, applicants should consider that it may take several months to obtain. Visa applications are made to the Polish or/and German Embassy or consular mission in the corresponding home country.

IV. ADMISSION PROCESS

The application for the EMSS study programme is possible annually for the summer semester. It shall be performed within the application period at one of the partner universities, which is assigned as the home university. Responsible representatives from both universities build an admission board which decides on admission of all applicants. Each partner university can accept only limited number of candidates (15 per year).

Upon positive decision, the candidates are first enrolled at the home university and nominated for enrollment to the guest university. For the complete study programme and additionally for the semester abroad a corresponding Erasmus+ Learning Agreement is signed by both parties.

V. CURRICULUM

The content and objectives of the course take into account the international standards of systems engineering, based on the certification programs of the International Council on Systems Engineering (INCOSE) and the German chapter of the Gesellschaft für Systems Engineering (GfSE), core curriculum for SE-ZERT®, level D [4]. A mapping of the curricula is shown in table I. The proof of academic equivalency and certification are already being discussed with the INCOSE and GfSE colleagues.

TABLE I. MAPPING OF CURRICULA

SE-ZERT® C/D	*EMSS*
Systems Engineering Foundations Interfaces across Projects Cross-cutting Functions within Development Projects	Space System Management Space Systems Engineering
Cross-Project Interfaces Inferfaces among Systems Engineering and Project Management Conflict Mananagement and Social Skills	Project Management Space System Management Interdisciplinary Project, Part 1 & 2
Requierements Management Validation & Verification Realisation Processes Operational and Disposal Aspects	Interdisciplinary Project, Part 1 & 2 Engineering Foundations of Satellite Systems Special Mandatory Modules Elective Modules

The curriculum includes compulsory modules and compulsory elective modules. Each module comprises a workload of 180 hours, which corresponds to 6 ECTS credits. The Master's thesis including the Master's seminar comprises 30 ECTS. Due to the interdisciplinary orientation, it is possible to specialize in the following disciplines through a dedicated selection of compulsory elective modules:

- Computer Science
- Electronics Engineering
- Space Technologies

The following modules are mandatory:

- Mechanics, Mechatronics and Avionics in Space Systems
- Satellite Technologies
- Space Systems Engineering
- Project Management (incl. Teamwork and Communication)
- Law and Security in Space
- Interdisciplinary Project 1 & 2 (Satellite Mission)

A selection of the planned compulsory elective modules is listed as follows:

1. Model-based Systems Engineering
2. Design and Modelling of Space Propulsion Systems
3. Non-Chemical Space Propulsion Systems
4. Methods for the Development of Complex Software Systems
5. On-board Software Engineering
6. Satellite Communications
7. Measurement and Instrumentation
8. Space Mission Operations
9. Ground Segment Engineering

An exemplary selection for the Computer Science specialization could be as follows: 1, 4, 5 and 9. In order for the profile to be completed in sufficient depth, the technical tasks within the interdisciplinary projects and the Master's thesis should have a Computer Science or Software Engineering focus.

VI. DEVELOPMENT OF COMPETENCES IN COOPERATION

Students who already have a Bachelor's degree first learn the technical basics of the application domain (Mechanics, Mechatronics and Avionics in Space Systems and Satellite Technologies) at the Gdansk University of Technology. This technical knowledge is then expanded with competencies in space systems engineering, project management, communication, teamwork and social skills at the Bremen City University of Applied Sciences. Students can apply these knowledge in two consecutive semesters (Interdisciplinary Project 1 & 2). A realistic satellite mission is planned as an overall project and developed up to a "Preliminary Design Review" level in teamwork. A scientific approach is taught in particular within the modules Space Systems Engineering, Interdisciplinary Project 1 & 2 and in the Master's seminar and is assessed by corresponding achievements (scientific project report or Master's thesis).

Numerous colleagues from the local aerospace industry in Bremen (e.g. OHB, Airbus Defence and Space, Ariane Group, ZARM) are actively contributing to this transfer of skills. They are involved through company visits, guest presentations, active support in teaching and project work. Long-term cooperation is planned.

Each winter semester various experienced colleagues form from different disciplines and space companies in Bremen are presenting different technical disciplines and aspects of the space domain. During the winter semester 23/24 the following guest presentations took place:

- Straightforward Research - 6 Minutes of Microgravity with TEXUS
- Engineers' Calculation Models – from Analytical Models to Digital Twins
- Ground Segment for Space Applications - Overview of operational Ground Segment engineering in DLR and ESA environment
- Launcher Electrical System: A Generalized Functional Description of the Ariane Launcher's Avionics

- Software related Space Systems Engineering
- ESA OPS-SAT Presentation
- Spacecraft On-Board Software Engineering
- Programme Management Office - Key-Player in Space Exploration Projects
- Bremen, the City of Space, Space Coordinator Bremen State

Furthermore, the second part of the Interdisciplinary Project at HSB was conducted in cooperation with OHB. The Head of the Department of Satellite Systems Engineering was the main lecturer.

VII. SUMMARY

The international double degree Master's degree program in Engineering and Management of Space Systems provides a future-proof basis for mastering the constantly growing complexity of software-intensive technical systems in the space industry and space missions in their entirety as a "system of systems", thus offering potential graduates very good career perspectives.

During the preparation phase the program has also met with an extremely positive response from the international specialist community: At the “ESA Space Educational Activities Symposium” in Barcelona, Spain, at the end of April 2022, the course project [2] was presented and acknowledged with great interest by the specialist community, including the director of the ESA Space Academy, also with regard to possible collaborations. Furthermore, the Systems Engineering community acknowledged the concept at the “Tag des Systems Engineering” in November 2022 in Paderborn, Germany.

With the interdisciplinary international double degree Master's program EMSS, Bremen University of Applied Sciences and Gdansk University of Technology offer an innovative and future-oriented study program that has a unique selling point throughout Germany and Poland conducted in a strong cooperation with the local space companies. Thus, we can make an important contribution to securing skilled staff in the aerospace industry, especially in the Bremen region.

The concepts of this degree program are easily transferable to other (systems) engineering programs. In particular, the consideration of both the interdisciplinary aspects and the entire life cycle of the systems, supplemented by the teaching of social and management skills, form a good basis for meeting the current requirements in systems engineering.

ACKNOWLEDGMENT

The realization of this program was only possible thanks to the support of many academic and non-academic staff members of both universities, as well colleagues from the space industry, namely:

HSB: Andreas Teufel, Anne Brümmer-Kock, Yana Yerofeyeva, Thomas Trittin, Antonio Garcia, Uwe Apel, Sören Peik, Lars Braubach, Friedrich Fleischmann, Ludger Kempen, Christian Dierken, Thorsten Teschke, Indulis Kalnins

Gdańsk Tech: Justyna Szostak, Edmund Wittbrodt, Aleksandra Wiśniewska, Paulina Strakowska, Marcin Jasiukowicz

Airbus (incl. Airbus Defence & Space): Maik Purrmann, Temenushka Manthey, Christina Jetzschmann, Ingo Möller, Andreas Schütte, Anna Chrobry

Ariane Group: Celen Nil

OHB: Raphaël Lescouzères, Erik Dehnhardt

ZARM: Marcel Bernauer

The City of Bremen Space Coordinator: Siegfried Monser

REFERENCES

[1] Z. Łubniewski, P. Falkowski-Gilski, M. Chodnicki, A. Stepnowski, “Three Editions of Inter-University Studies on Space and Satellite Technology. Candidate and/vs. Graduate, a Case Study”, 3rd Symposium on Space Educational Activities, Leicester, U.K., Sept. 2019.

[2] J. Matevska, J. Szostak, Z. Łubniewski, S. Krawczuk, M. Chodnicki, “Engineering and Management of Space Systems (EMSS) - an international joint Master's double-degree Program”, 4th Symposium on Space Educational Activities, Barcelona, Spain, Apr. 2022.

[3] J. Matevska, “Engineering and Management of Space Systems: Neuer Internationaler Double Degree Masterstudiengang an der Hochschule Bremen”, Tag des Systems Engineering (TdSE), 2022, Paderborn, Germany, Nov. 2022.

[4] S.-O.Schulze, A. Rudolph, S. Stangl, F. Regge, „Kernkurrikulum für SE-ZERT® Ebenen C und D, GfSE-ZD-004“, Version 2, 03.07.2020

Promoted and organized by

BME VILLAMOSMÉRNÖKI ÉS INFORMATIKAI KAR

BME Faculty of Electrical Engineering and Informatics

MANT
Hungarian Astronautical Society

Hungarian Astronautical Society

Sponsors

MŰEGYETEM 1782

Budapest University of Technology and Economics

KÜLGAZDASÁGI ÉS
KÜLÜGYMINISZTÉRIUM

Ministry of Foreign Affairs and Trade

NMHH
Nemzeti Média- és Hírközlési Hatóság

National Media and Infocommunications Authority

Partners

Egyetemi
Kozmosz
Szakkollégium

BME Cosmos College for Advanced Studies

SPACE GENERATION
ADVISORY COUNCIL

Space Generation Advisory Council

Invitation to H-SPACE 2026

The 1st International Conference on Research, Technology and Education of Space was the opening event of the conference series. It was held on February 13, 2015.

The 2nd International Conference on Research, Technology and Education of Space was held on February 25-26, 2016.

The 3rd International Conference on Research, Technology and Education of Space was held on February 9-10, 2017.

The 4th International Conference on Research, Technology and Education of Space was held on February 15-16, 2018.

The 5th International Conference on Research, Technology and Education of Space was held on February 27-28, 2019.

The 6th International Conference on Research, Technology and Education of Space was held on February 26-27, 2020.

The 7th International Conference on Research, Technology and Education of Space was held on April 7-8, 2022.

The 8th International Conference on Research, Technology and Education of Space was held on April 25-26, 2024.

H-SPACE 2026, the 9th International Conference on Research, Technology and Education of Space' is planned to be organized in April 2026 in Budapest, Hungary.

The Call for Papers will be available from October 1, 2025 on the http://space.bme.hu website.

Index of the authors

Matolcsy	Balázs	2
Meier	**Orsolya**	**9**
Mihály	**András**	**11**
Mulki	**Rhea R.**	**13**
Nagy	**Ádám**	**22**
Nagy	Dominik Gábor	17
Nagy	Janos	15
Németh	Péter	21
Ntantis	Efstratios L.	7, 8, 13
Oláh	**Kitti**	**12**
Pál	Bernadett	5
Pataki	**Péter**	**21**
Patrik	Ábrók László	3
Petrovics	Zoltán	3
Rózsa	Sz.	16
Schranz	Ágoston	2
Sódor	Bálint	4
Steinmann	**Vilmos**	**6**
Szabo	M.	5
Szalai	Sándor	4
Tóth	Máté Péter	18
Tölgyesi	Gergely Márk	14
Tróznai	Gábor	4
Turák	B.	16
Udvary	Eszter	2
Ujhegyi	Bence	22
Velich	Csaba	3
Vizi	**Pál Gábor**	**15**